SAND2018-13494R

Evaluation of Spent Fuel Disposition in Crystalline Rocks: FY18 Progress Report

Spent Fuel and Waste Disposition

Prepared for
US Department of Energy
Spent Fuel and Waste Science Technology
Y. Wang, T. Hadgu, E. Kalinina
Sandia National Laboratories
J. Jerden, V. K. Gattu, W. Ebert
Argonne National Laboratory
H. Viswanathan, H. Boukhalfa, S. Chu, J. Hyman, S. Karra,
N. Makendonska, P. Reimus, K. Telfeyan
Los Alamos National Laboratory
L. Zheng, H. Deng, S. Nakagawa, K. Kim, T. Kneafsey,
P. Dobson, S. Borglin, C. Doughty, M. Voltolini
Lawrence Berkeley National Laboratory
M. Zavarin, E. Balboni, C. Atkins-Duffin
Lawrence Livermore National Laboratory
September, 2018
M2SF-18SN010302051

Revision 4
07/05/2017

APPENDIX E

NTRD DOCUMENT COVER SHEET [1]

Name/Title of Deliverable/Milestone/Revision No.	Evaluation of Spent Fuel Disposition in Crystalline Rocks: FY17 Progress Report M2SF-18SN010302051
Work Package Title and Number	Crystalline Disposal R&D – SNL SF-18SN01030205
Work Package WBS Number	1.08.01.03.02
Responsible Work Package Manager	Yifeng Wang (Name/Signature)

Date Submitted 9/24/2018

Quality Rigor Level for Deliverable/Milestone[2]	☐ QRL-1 ☐ Nuclear Data	☐ QRL-2	X QRL-3	☐ QRL 4 Lab-specific

This deliverable was prepared in accordance with Sandia National Laboratories
(Participant/National Laboratory Name)

QA program which meets the requirements of
X DOE Order 414.1 ☐ NQA-1 ☐ Other

This Deliverable was subjected to:

☐ Technical Review
Technical Review (TR)
Review Documentation Provided
☐ Signed TR Report or,
☐ Signed TR Concurrence Sheet or,
X Signature of TR Reviewer(s) below
Name and Signature of Reviewers
Carlos Jove-Colon

☐ Peer Review
Peer Review (PR)
Review Documentation Provided
☐ Signed PR Report or,
☐ Signed PR Concurrence Sheet or,
☐ Signature of PR Reviewer(s) below
Name and Signature of Reviewers

NOTE 1: *Appendix E should be filled out and submitted with each deliverable. Or, if the PICS: NE system permits, completely enter all applicable information in the PICS: NE Deliverable Form. The requirement is to ensure that all applicable information is entered either in the PICS: NE system or by using the NTRD Document Cover Sheet.*

- *In some cases there may be a milestone where an item is being fabricated, maintenance is being performed on a facility, or a document is being issued through a formal document control process where it specifically calls out a formal review of the document. In these cases, documentation (e.g., inspection report, maintenance request, work planning package documentation or the documented review of the issued document through the document control process) of the completion of the activity, along with the Document Cover Sheet, is sufficient to demonstrate achieving the milestone.*

NOTE 2: *If QRL 1, 2, or 3 is not assigned, then the QRL 4 box must be checked, and the work is understood to be performed using laboratory specific QA requirements. This includes any deliverable developed in conformance with the respective National Laboratory Participant, DOE or NNSA-approved QA Program.*

This page left blank intentionally

EXCUTIVE SUMMARY

The U.S. Department of Energy Office of Spent Fuel Waste Disposition (SFWD) established in fiscal year 2010 (FY10) the Spent Fuel Waste Science & Technology (SFWST) Program (formerly the Used Fuel Disposition Campaign - UFDC) program to conduct the research and development (R&D) activities related to storage, transportation and disposal of used nuclear fuel and high level nuclear waste. The Mission of the SFWST is:

> *To identify alternatives and conduct scientific research and technology development to enable storage, transportation and disposal of used nuclear fuel and wastes generated by existing and future nuclear fuel cycles*.

The work package of Crystalline Disposal R&D directly supports the following SFWST objectives:

- Develop a fundamental understanding of disposal system performance in a range of environments for potential wastes that could arise from future nuclear fuel cycle alternatives through theory, simulation, testing, and experimentation.
- Develop a computational modeling capability for the performance of storage and disposal options for a range of fuel cycle alternatives, evolving from generic models to more robust models of performance assessment.

The objective of the Crystalline Disposal R&D control account is to advance our understanding of long-term disposal of used fuel in crystalline rocks and to develop necessary experimental and computational capabilities to evaluate various disposal concepts in such media.

Significant progress has been made in FY18 in both experimental and modeling arenas in evaluation of used fuel disposal in crystalline rocks, especially in model demonstration using field data. The work covers a wide range of research topics identified in the R&D plan. The major accomplishments are summarized below:

- **Model development for spent fuel degradation and its coupling with metal corrosion:** The fuel matrix degradation (FMD) model that calculates the degradation rate of spent UO_2 fuel is being developed to predict radionuclide source term values based on fundamental electrochemistry and thermodynamics. The FMD model has been implemented in a manner that facilitates its integration with the geologic disposal safety assessment (GDSA) model. A preliminary integrated FMD-GDSA model has been successfully tested. The specific focus of on-going work is to accurately and quantitatively represent the generation of H_2 in a breached waste package and model its effect on the degradation rate of the spent fuel so that this key process can be accurately represented in PA models. A recent sensitivity analysis shows that the dissolved H_2 concentration is the dominant environmental variable affecting the UO_2 spent fuel dissolution rate. The anoxic corrosion of metallic engineering materials will be the main source of H_2 in crystalline rock repository systems, including stainless steel and carbon steel internal waste package components and possibly the Zircaloy fuel cladding. A steel corrosion module has been added to the FMD model to account for these H_2 sources and couple the H_2 generation rate with fuel degradation processes. There is a need for experimental data from electrochemical corrosion experiments with relevant steel, Zircaloy and UO_2 electrodes to parameterize and validate the steel corrosion module in the FMD model with regard to key environmental variables and alloy compositions.

- **Model development for glass waste form degradation:** The reactivity of silicate glasses and minerals is important to numerous engineering applications including nuclear waste disposal. Silicate dissolution exhibits complex temporal evolution and rich pattern formations. In FY17, we showed how observed complexity could emerge from a simple self-organizational mechanism: dissolution of the silica framework in a material could be catalyzed by the cations released from the reaction itself. This mechanism enables us to systematically predict many key features of a silicate dissolution process including the occurrence of a sharp corrosion front (vs. a leached surface layer), oscillatory dissolution and multiple stages of the alteration process (e.g., an alteration rate resumption at a late stage of glass dissolution). In FY18, through a linear stability analysis, we showed that the same mechanism could also lead to morphological instability of an alteration front, which, in combination with oscillatory dissolution, could potentially lead to a whole suite of patterning phenomena, as observed on archaeological glass samples as well as in laboratory experiments, including wavy dissolution fronts, growth rings, incoherent bandings of alteration products, and corrosion pitting. The result thus further demonstrates the importance of the proposed self-accelerating mechanism in silicate material degradation.
- **Understanding radionuclide interaction with metal corrosion products:** The main interest in radionuclide sequestration by corrosion products stems from (1) the potential for this process to significant inhibit radionuclide release during canister breaching and (2) from the absence of such processes in most repository performance assessments. The objective of this work is to quantify radionuclide sequestration as a result of canister breaching and near field corrosion processes. In FY18, molecular and crystallographic behaviors of Pu associated with ferrihydrite and goethite iron oxide phases were investigated. It was shown that the timing of Pu release and ferrihydrite corrosion product formation could lead to differences in Pu association: formation of PuO_2 versus coprecipitated Pu. Alteration of amorphous ferrihydrite to a more crystalline goethite phase would retain Pu association with the solid phase. However, the nature of Pu association would be affected by the characteristics of Pu associated with the precursor ferrihydrite. The molecular nature of Pu association with iron oxide phases affects the leaching behavior of Pu. EXAFS and TEM data confirm that in Pu association with goethite as a surface precipitate is more labile than the coprecipitate. This has implications to the longterm stability of Pu associated with corrosion products.
- **Understanding colloid-facilitated Cs transport:** Batch and column transport experiments were conducted to interrogate the effects of colloid aging on colloid-facilitated transport of ^{137}Cs through crushed analcime columns. The batch experiments were conducted to quantify the effect of colloidal aging on Cs partition coefficients and characterize the colloids injected into the columns. The column experiments were designed to characterize the desorption of Cs from strong sites on colloids. This was accomplished by using a very low concentration of total Cs (~10^{-10} M) so that ^{137}Cs would preferentially sorb to the fewer but stronger sorption sites. The first set of column experiments involved spiking a solution of FEBEX colloids with ^{137}Cs and letting the colloids age for a few hours, whereas the second set of experiments let the colloids age for 1200 hours prior to injecting through the analcime column. For both sets of column experiments, the eluent that passed through a first analcime column was collected and injected into a second fresh analcime column. The sequential injection method allows characterization of the ^{137}Cs bound to the strong sites on the colloid, and the use of a strongly sorbing column material (analcime) promotes desorption from the colloids. Both batch and column experiments demonstrate analcime's ability to outcompete colloids for ^{137}Cs sorption. In the presence of analcime, 12-23% of ^{137}Cs sorbed to the colloids and only 2-6% was in the dissolved phase, with the remainder sorbed to the analcime. The partitioning of ^{137}Cs between colloidal and dissolved phases in the absence of analcime was approximately 60:40. The column experiments had a much lower ratio of solid to liquid and demonstrated even greater loss of the Cs to the analcime. The ^{137}Cs eluted through the first column of the first set of experiments was only about 5%, and through the second column, no measureable ^{137}Cs eluted.

Conversely, through the first column of the second set of experiments (aged colloids), only ~2% of the initially injected ^{137}Cs was recovered through the column, but ~10% was recovered through the second column. Additionally, the second set of experiments also showed greater colloid recovery (~40%) through the second column compared to the second column (~20%) from the first set of experiments. These results suggest that aging the colloids prior to injection through analcime columns allows the ^{137}Cs to find the strong sorption sites on the colloids. Compared to previous batch experiments, the experiments of the present study report a higher K_d value for sorption of Cs onto colloids owing to the lower total Cs concentration and aging effects. Additionally, the present batch experiments demonstrate that the sorption rate onto the strong sorption site of the colloid is very slow compared to the sorption rate onto the weaker colloid sorption site. Furthermore, the desorption rate constant of the strong colloid sorption site had to be lowered for the aged colloid column experiment relative to the un-aged column experiment, suggesting that with a progressively smaller Cs concentration, the remaining Cs is proportionally more sorbed to the stronger sites. This work also suggests that there are greater than 2 sorption sites with progressively stronger affinity for Cs but less abundant.

- **Micro Fracture Flow Simulation Using Discrete Fracture Network Model:** The main focus of this year fracture simulation work was to simulate the Long-Term Sorption Diffusion Experiment (LTDE), conducted at the Äspö Hard Rock. The field test characterized tracer transport in the stagnant pore water of the rock matrix. A cocktail of both sorbing and non-sorbing tracers were allowed to contact fractured surface, as well as the unaltered rock matrix, for a time period of 200 days. The penetration profiles obtained by 1D simulation of tracer diffusion and measured during experiment do not agree and show different behavior. A Discrete Fracture Network (DFN) model was used to validate the hypothesis, which states that LTDE results were strongly influenced by heterogeneity in the micro-structure and the major diffusion of injected tracer into crystalline rock occurs through multiple micro fractures, which are observed in the rock samples. The DFN simulations of micro-fractures were performed using the dfnWorks simulation tool. Three numerical experiments were performed, where micro fracture intensity in DFN configurations varied representing different microstructure at the experimental sample. In each DFN configuration steady state pressure solution was evaluated and transport was evaluated through particle tracking transport. Time Domain Random Walk technique was used to simulate tracer movement through micro fractures, where a particle's travel time is controlled by both processes, advection and diffusion. The simulated penetration profile of particles shows similar behavior with LTDE experimental penetration plot when the advection term plays a significant role in the TDRW simulations. The conclusion from the performed numerical simulations is that microstructure is

present in the experimental sample and the injected tracer is driven by both, diffusion and advection.

- **Flow-transport model demonstration using Mizunami site data:** Through the Development of Coupled Models and their Validation against Experiments (DECOVALEX-2019) project, we obtained a comprehensive set of hydrologic and chemical data from a research tunnel at 500 m depth, at the Japan Atomic Energy Agency (JAEA) Mizunami Underground Research Laboratory (MIU). The objectives of this work are to develop a general workflow or methodology to synthesize field observations and measurements into a flow and transport model. In FY18, modeling analyses were conducted for DECOVALEX19, Task C, Step 2a and Step 2b. For Step 2b, the analysis was based on a larger domain to reduce boundary effects. The analysis also included fracture characterization using the new domain. The fracture model produced 10 DFN realizations which were upscaled to a continuum mesh for use in flow and transport. Boundary and initial conditions specified by the project were applied to flow and transport simulations for Step 2b. Project experimental data of excavation progress were also used. The simulation method previously developed to simulate excavation progress by continuously removing material from the excavated area was utilized. The DAKOTA statistical analysis and optimization code and the PFLOTRAN numerical flow and transport code were used. Predictions of inflow into the inclined drift for the 10 realizations are reasonable when compared with the experimental data. Inflow of the combined inclined drift and Closure Test Drift (CTD) were largely overpredicted. The simulations provided statistical data with uncertainty range. Future simulations will attempt to improve the predictions by using additional fracture data from Borehole 13MI38. Step 2b preliminary flow modeling was also conducted to simulate water filling of the plugged CTD and pressure recovery. The excavation process resulted in pressure drawdown in the vicinity of the experimental area. An experiment was conducted with the aim of pressure recovery by closing the CTD using a concrete plug and water filling. Preliminary blind simulations were carried out using project data with initial conditions at the CTD and 6 observation points in Borehole 12MI33. The simulation results were compared with project experimental data. The pressure predictions at the CTD and the observation points did not match the experimental data. Further modeling will incorporate the leakage.
- **Multi-Scale Characterization of Crystalline Rocks:** A series of laboratory experiments were conducted on granite slabs with a special geometry to replicate the stresses and rock deformation responses that are expected to occur in larger circular excavations of the excavation damage zone (EDZ) in a mined crystalline repository. Specifically, microcracks generated by applying stress to the shaped rock samples were observed both visually and through a pronounced decrease in seismic velocity. The stressed samples were also used to assess the changes in rock permeability as an indicator how these microcracks could affect hydraulic properties of rock in the EDZ. Preliminary modeling studies of flow and transport coupled process and the effects of the rock deformation on hydrological and transport properties were initiated using a rigid body spring network modeling approach. In addition, rock samples and data were collected from a crystalline basement analogue site in central Sweden, the 2.5 km deep “Collisional Orogeny in the Scandinavian Caledonides” (COSC) scientific borehole. This study is aimed at gaining insights into the flow characteristics of crystalline basement rocks. The first part of this task included a series of laboratory experiments on fractured cores that were selected based on the correlation with the borehole inflow zones identified from flowing fluid electrical conductivity (FFEC) logs. These core flow measurements were conducted using a unique laboratory apparatus that can measure multi-directional transmissivity to assess fracture anisotropy under confining stress conditions. One challenge that was observed is that some of the core appears to have been damaged during recovery from the borehole, so that the core transmissivity measurements are significantly higher than the field scale values calculated from the FFEC logging runs. The second part of this task involved the evaluation of the nature of the fractures that appear to be linked to the borehole inflow zones, which were identified from the FFEC field measurements. Acoustic borehole televiewer images of the COSC-1 borehole indicated that there were two distinct sets of fractures: (a) steeply dipping fractures that

were generated by current tectonic stresses, and (b) shallow fractures parallel to rock foliation. Based on new depth correlations of the core and well log datasets, it appears that the majority of the inflow zones are associated with the foliation-parallel fractures.

Based on the work accomplished in FY18 and the prior years, the future work is recommended to:

- Continue to focus on two key topics related to deep geologic disposal of spent fuel in crystalline rocks: better characterization and understanding of fractured media and fluid flow and transport in such media, and designing effective engineered barrier systems (EBS) for waste isolation. Specific attention will be given to the development of next-generation buffer materials for waste isolation and to a mechanistic understanding of alteration products (e.g. iron oxides) of EBS components as secondary waste forms for radionuclide retention.
- Help the geologic disposal safety assessment (GDSA) team to develop a total system performance assessment (PA) model and provide the parameter feeds to the model. One goal of this effort is to have a PA model matured enough over next two years to be able to simulate a typical thermal-hydrologic-chemical evolution history of a repository in a crystalline medium. Once such as a model becomes available, various disposal concepts will be explored.
- Continue to synthesize technical results obtained in FY17 and prior years in a few selected areas to demonstrate tangible progress in the research. The focus areas will include the stability of bentonite and the modeling approach for fluid flow and transport in fractured geologic media.
- The modeling work will move towards model demonstrations and applications using actual field data. For the process model development, an emphasis will be placed on the integration with total system model development.
- Fully leverage international collaborations, especially with Sweden Underground Research Lab and DECOVALEX.

In Appendix A, we briefly summarize the major accomplishments over the past five years and provide a perspective for future research for each research topic area identified in the R&D plan.

This page left intentionally blank

CONTENTS

ACRONYMS

AE	Acoustic emission
ANL	Argonne National Laboratory
CCDF	Complementary cumulative distribution function
COSC	Collisional Orogeny in the Scandinavian Caledonides
CTD	Closure Test Drift
DECOVALEX	Development of Coupled Models and their Validation against experiments
DFN	Discrete fracture network
DOE	U.S. Department of Energy
EBS	Engineered barrier system
EDS	Energy dispersive X-ray spectroscopy
EDZ	Excavation damage zone
EXAFS	Extended X-ray absorption fine structure
FEBEX	Full-Scale Engineered Barriers Experiment
FEPs	Features, Events, and Processes
FFEC	Flowing fluid electrical conductivity (FFEC
FMD	Fuel matrix degradation
FMDM	Fuel matrix degradation model
GDSA	Geologic Disposal Safety Assessment
GREET	Groundwater Recovery Experiment in Tunnel
HLW	High-level radioactive waste
IC	Ion chromatography
ICP-OES	Inductively couple plasma optical emission spectrometry
JAEA	Japan Atomic Energy Agency (JAEA)
KAERI	Korean Atomic Energy Research Institute
KURT	Korean Atomic Energy Research Institute Underground Research Tunnel
LBNL	Lawrence Berkeley National Laboratory
LDTE	Long Term Sorption Diffusion Experiments
LLNL	Lawrence Livermore National Laboratory
LANL	Los Alamos National Laboratory
MIU	Mizunami Underground Research Laboratory
NEA	Nuclear Energy Agency
PA	Performance assessment

PD	Potentiodynamic
PS	Potentiostatic
RBSN	Rigid Body Spring Network
SEM	Scanning electron microscopy
SNF	Spent Nuclear Fuel
SNL	Sandia National Laboratories
SFWD	Spent Fuel Waste Disposition
SFWST	Spent Fuel Waste Science & Technology
SSRL	Stanford Synchrotron Radiation Light Source
TDB	Thermodynamic database
TDRW	Time Domain Random Walk
TEM	Transmission electron microscopy
TSPA	Total system performance assessment
UFDC	Used Fuel Disposition Campaign
XANES	X-ray absorption near edge structure
XRD	X-ray diffraction
XAS	X-ray adsorption spectroscopy

1. GOALS AND OUTLINE

The U.S. Department of Energy Office of Spent Fuel Waste Disposition (SFWD) established in fiscal year 2010 (FY10) the Spent Fuel Waste Science & Technology (SFWST) Program (formerly the Used Fuel Disposition Campaign) program to conduct the research and development (R&D) activities related to storage, transportation and disposal of used nuclear fuel and high level nuclear waste. The Mission of the SFWST is:

> *To identify alternatives and conduct scientific research and technology development to enable storage, transportation and disposal of used nuclear fuel and wastes generated by existing and future nuclear fuel cycles*.

The work package of Crystalline Disposal R&D directly supports the following SFWST objectives:

- Develop a fundamental understanding of disposal system performance in a range of environments for potential wastes that could arise from future nuclear fuel cycle alternatives through theory, simulation, testing, and experimentation.
- Develop a computational modeling capability for the performance of storage and disposal options for a range of fuel cycle alternatives, evolving from generic models to more robust models of performance assessment.

The objective of the Crystalline Disposal R&D control account is to advance our understanding of long-term disposal of used fuel in crystalline rocks and to develop necessary experimental and computational capabilities to evaluate various disposal concepts in such media. The main research topics identified for this control account are summarized in a research plan developed by Wang et al. (2014). FY18 work is aligned with the following considerations and project goals (Figure 1.1):

- This control account would focus on two key topics related to deep geologic disposal of spent fuel in crystalline rocks: (1) better characterization and understanding of fractured media and fluid flow and transport in such media, and (2) designing effective engineered barrier systems (EBS) for waste isolation.
- This control account would assist the geologic disposal safety assessment (GDSA) control account to develop a total system performance assessment model and provide the parameter feeds to the model. One goal of this effort is to provide the GDSA with a basic “minimal” set of process models and model feeds in next two years to support the GDSA 2020 goal.
- The modeling work would move towards process model development and demonstration using actual field data. For the process model development, an emphasis will be placed on the integration with total system model development.
- The work planned for this control account would fully leverage international collaborations, especially with Sweden Underground Research Lab and DECOVALEX.
- Closely collaborate and integrate with other work packages, especially those on disposal in argillite, deep borehole disposal, and DOE-managed HLW and SNF Research.

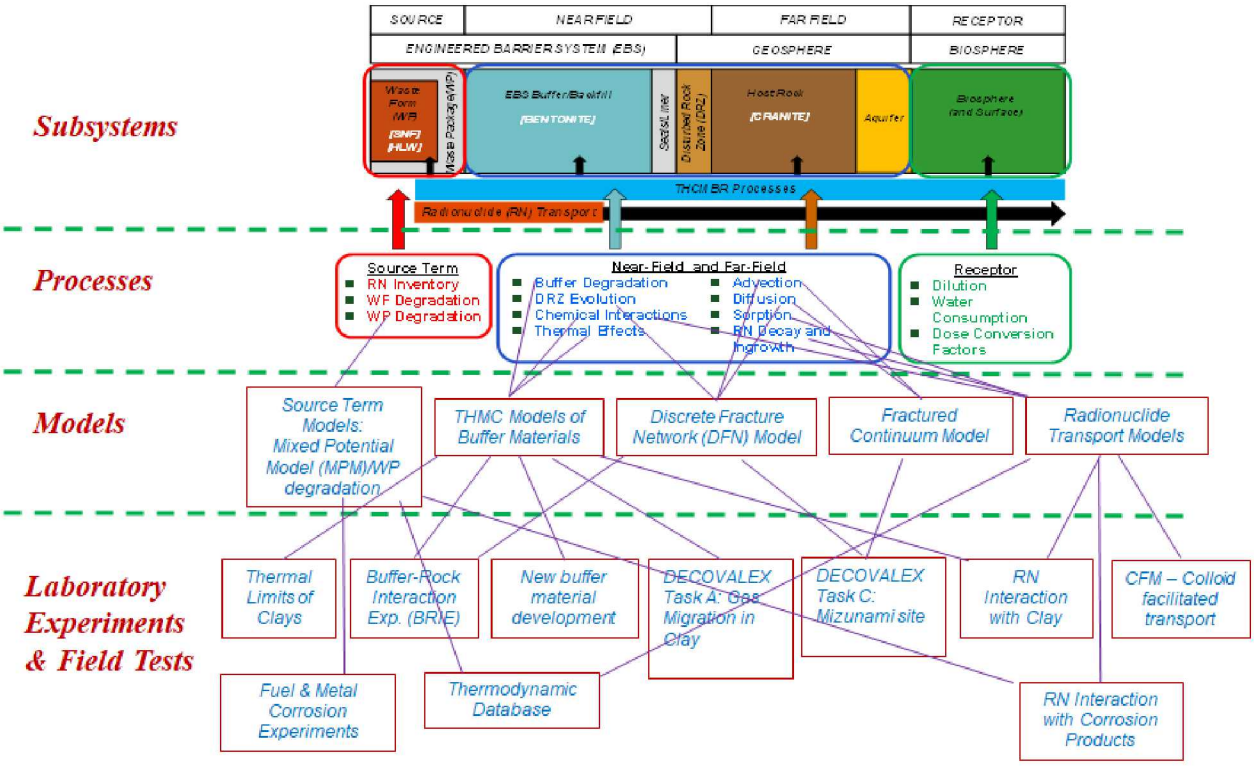

Figure 1.1. Integration of laboratory experiments, field tests and process model development to support a generic safety case analysis for deep geologic nuclear waste disposal in crystalline rocks.

The FY18 work for the Crystalline Disposal R&D control account is structured into the following tasks:

- Task 1: Supporting the development of a total system performance assessment model for crystalline media. FY18 activity would help the GDSA work package to improve the existing performance assessment (PA) model for crystalline rocks. The potential improvements would include an upgraded far field transport model for multiple realizations and an improved Engineered Barrier System (EBS) model with a preliminary representation of waste package degradation and failure.
- Task 2: Development of spent fuel degradation and waste package degradation model: This task would continue the model development for fuel matrix degradation and waste package degradation as well as for the coupling of the two material degradation processes.
- Task 3: Development of Engineered Barrier System (EBS) materials: Engineered buffer materials in the EBS are an important component for waste isolation in a crystalline repository. This task would try to understand the performance of various candidate buffer materials under a range of disposal conditions and to develop a new generation of buffer materials that can be tailored to various disposal environments for effective waste isolation.
- Task 4: Modeling of fluid flow and transport in fractured crystalline rocks: The task would continue to demonstrate the potential application of the discrete fracture network model and the fracture continuum model to actual field testing data obtained from international collaborations. Develop a strategy to integrate these types of process models into a total system performance assessment model.
- Task 5: Experimental investigation of radionuclide interactions with natural and engineered materials: Continue the work on radionuclide interactions natural and engineered materials and aim to develop a comprehensive process model for total system performance assessment (TSPA).

- Task 6: International collaborations: International collaborations are crucial for the activities proposed for this work package.

This report summarizes work accomplished in FY18 for the Crystalline Disposal R&D control account. The report is outlined as follows, covering topics from near-field waste form degradation, to engineered barrier material performance, and finally to far-field flow and transport:

- Chapter 2 documents the model development for fuel matrix degradation (FMD) and its coupling with package material degradation. The work documented is a jointed effort between the Crystalline and the Argillite control accounts. (Research topics addressed: S2, S3 and P19; see Wang et al., 2014).
- Chapter 3 presents the further development of the new model we proposed in FY17 for aqueous degradation of silicate glasses and minerals. (S2, S3 and P19).
- Chapter 4 presents a preliminary result on radionuclide sorption and sequestration by metal corrosion products. (P20 and P22)
- Chapter 5 presents a column study of colloid-facilitated Cs transport with respect to high sorption affinity sites and slow desorption from colloidal particles (P10 and P11).
- Chapter 6 presents the work using a discrete fracture network model to simulate the Long-Term Sorption Diffusion Experiment (LTDE) conducted at the Äspö Hard Rock, Sweden. (P1, P8, and P9)
- Chapter 7 presents the work using a continuum fracture model (CFM) to simulate fluid flow and transport at Japanese Mizunami site. (P1, P8, P9 and P12)
- Chapter 8 provides multiple scale characterization of crystalline rocks related to an excavation-damage zone (EDZ) and field logging tests. (S5, S6 and P1).
- Chapter 9 provides an overall summary of FY18 accomplishment for Crystalline Disposal R&D control account.
- Appendix A briefly summarizes the major accomplishments over the past five years and provides a perspective for future research for each research topic area.

The results documented in this report represents the major portion of the work conducted in FY18 for the Crystalline Disposal R&D control account but not all the work. The work not reported includes the experimental study of smectite-to-illite conversion and the development of a new generation of buffer materials. Either being at an early stage of data synthesis or due to a concern with intellectual properties, the related work will be reported later as it becomes appropriate for public release.

Wang Y. et al., (2014) *Used Fuel Disposal in Crystalline Rocks: Status and FY14 Progress*, FCRD-UFD-2014-000060, SAND2014, Sandia National Laboratories, Albuquerque, NM.

2. VALIDATION AND INCORPORATION OF A NEW STEEL CORROSION MODULE INTO FUEL MATRIX DEGRADATION MODEL

2.1 Introduction

The activity documented in this section is aimed to develop, test and implement a process model for the degradation rate of spent nuclear fuel that can be readily incorporated into the generic disposal system analyses (GDSA) performance assessment (PA) code to provide reliable radionuclide source terms over the service life of a deep geologic repository. The fuel matrix degradation (FMD) model (or FMDM), which is an electrochemical reactive-transport model based on fundamental redox kinetics and thermodynamics, was developed for this purpose and is currently being updated and tested. The FMD model was originally based the Canadian Mixed Potential Model (CMPM) of Shoesmith and King (1998) and King and Kolar (2003) but has been expanded to account for key phenomena and customized for application in the ongoing spent fuel and waste science and technology (SFWS) campaign.

The continuing development and implementation of the FMD model address two high level Features, Events, and Processes (FEPs) that are recognized as high R&D priorities for the SFWS campaign (Wang et al., 2014). The FEPs addressed by this model are 2.1.02 (waste form) and 2.1.03 (waste container), which correspond to the high priority research topics P19 (Development of waste form degradation model) and P20 (Development of new waste package concepts and models for evaluation of waste package performance for long-term disposal) identified by Wang et al. (2014).

Specifically, the FMD model uses mixed potential theory to calculate the degradation rate of UO_2 by accounting for all major anodic and cathodic interfacial reactions. Other major phenomena accounted for in the FMD model include:

- Effect of hydrogen generated from steel corrosion within a breached waste package,
- Alpha radiolysis and the generation of radiolytic oxidants as a function of fuel burn-up,
- Growth a porous layer of uranyl oxyhydroxide and/or uranyl peroxide corrosion phases.
- Complexation of dissolved uranium by carbonate.
- Temperature variations of reaction rates (by Arrhenius equations),
- One-dimensional diffusion of all chemical species to and from the fuel and steel surfaces.

The most important process that the FMD model accounts for that was not addressed in the original CMPM is the oxidation of dissolved hydrogen at the spent fuel surface (Jerden et al., 2015). Leaching experiments with spent fuel and simulated spent fuel have shown that the presence of hydrogen generated during the corrosion of steel added to a test can decrease the fuel degradation rate by 4 orders of magnitude relative to tests performed with no steel present (e.g., Röllin et al., 2001, Ollila, 2008). The means by which the effect of hydrogen is accounted for in the FMD model is discussed in Section 2.2 below.

Jerden et al., 2017(a) and Jerden et al., 2017(b) discussed the addition of a corroding steel surface as a source of hydrogen to the FMD model (FMDM version 3). One of the main findings of that work is that the extensive coupling between the corrosion of waste package components and the spent fuel that must be taken into accounted to accurately predict radionuclide source terms. As discussed in Jerden et al., 2017(b), the Eh and pH conditions within a breached waste package will evolve with time due to coupled reactions of alloy corrosion, radiolysis, and spent fuel dissolution. The latest FMD model includes a first step towards accounting for the coupled processes by linking steel corrosion kinetics and fuel degradation rates; however,

more extensive experimental and modeling work is needed to accurately model the fuel dissolution rate because the in-package solution chemistry evolves due to the corrosion of engineering materials.

The present report updates the work discussed in Jerden et al., 2017(a) and Jerden et al., 2017(b) and provides discussion of ongoing experimental validation work for the latest version of the FMD model (FMDM version 4). The electrochemical experiments that are being performed to parameterize and validate the FMD model (V.4) are discussed in Section 2.3 below.

As summarized in Jerden et al., 2017(b), the FMD model has been successfully integrated with the GDSA-PA code PFLOTRAN; however, there is a need to optimize the integrated code to improve computing speed. This optimization work is ongoing and will be summarized in a March 2019 milestone report. The flow of information within the integrated FMDM – GDSA-PA model is summarized in Figure 2.1.

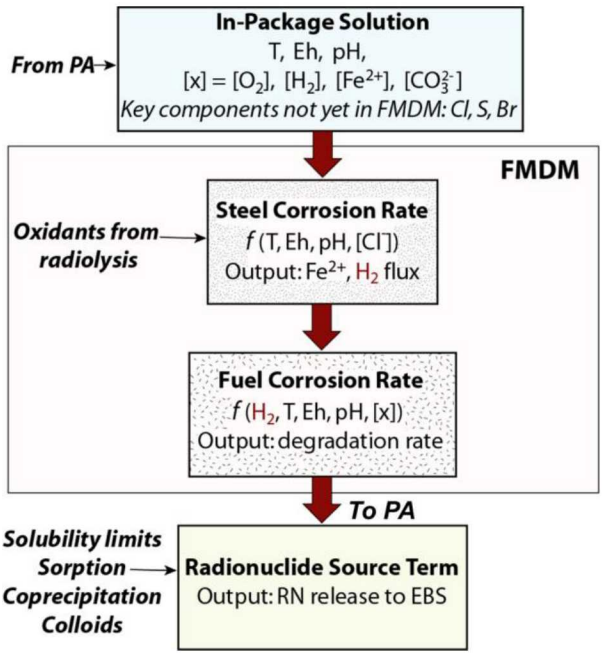

Figure 2.1. Summary figure showing the context of the FMDM within the source term calculation information flow (adapted from Jerden et al., 2017a).

2.2 Update on Validation of Fuel Matrix Degradation Model Version 4

The chemical and physical processes accounted for in the FMD model are shown schematically in Figure 2. In the model, spent fuel is exposed to an aqueous solution that has entered the waste package following a canister breaching event. The model conservatively assumes that the Zircaloy fuel cladding (not shown in Figure 2.2) is also breached at the time of water infiltration into the canister. The canister breaching process will be modeled separately; however, the breaching model will be coupled with the FMDM through the dependence of the spent fuel degradation rate on the concentration of hydrogen generated from the corrosion of canister steels.

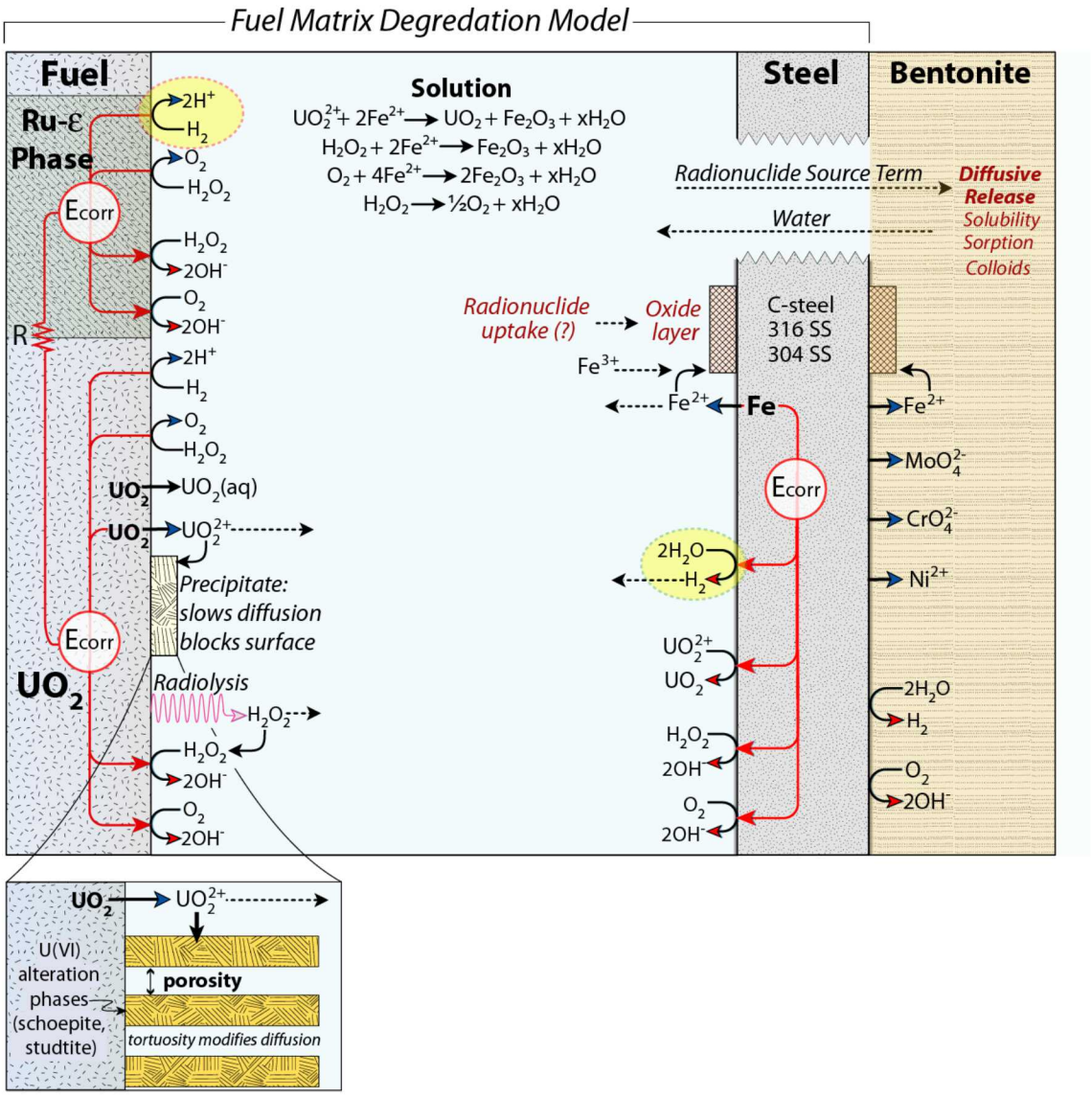

Figure 2.2. Schematic diagram showing the reaction scheme for the FMD model and identifying other key processes that influence in-package chemistry and radionuclide mobilization. (adapted from Jerden et al., 2017a).

Of the processes shown in Figure 2.2, H_2 generation and oxidation reactions (highlighted in yellow in the figure) have the most important impact on the fuel dissolution rate and radionuclide source term (Jerden et al. 2015). In the absence of H_2 generation, the dominant process is the oxidative dissolution of the fuel by the radiolytic oxidant H_2O_2 and its decomposition product O_2. In the FMD model, the H_2O_2 concentration is calculated using an analytical form of the radiolysis model developed at PNNL (Buck et al., 2014) and the burn-up/dose rate function that was derived from MCNPX dose rate modeling of Radulescu (2001).

When sufficient H_2 is present, the radiolytic oxidation of the fuel is counteracted by the oxidation of H_2 at the fuel surface. As shown in Figure 2.2, hydrogen oxidation occurs both on the UO_2 surface and on the

Ru-Mo-Pd-Rh-Tc bearing, fission product alloy commonly referred to as the ε phase. The reaction of H_2 with the ε phase is the dominant mechanism for the H_2 effect on spent fuel dissolution due to the catalytic properties of this noble metal-bearing phase. The assumption that the ε phase catalyzes H_2 oxidation at the fuel surface is supported by the electrochemical experimental work of Broczkowski et al. (2005) and Shoesmith (2007). Their results, which are summarized in Figure 2.3, show that the presence of dissolved H_2 lowered the corrosion potential of simulated spent fuel specimens containing the ε-phase relative to specimens that did not contain ε phase particles. Furthermore, increasing the amount of ε-phase in the specimens (simulating higher burnup: BU 2% vs 6% in Figure 2.3) further decreased the measured corrosion potential for the same H_2 concentration.

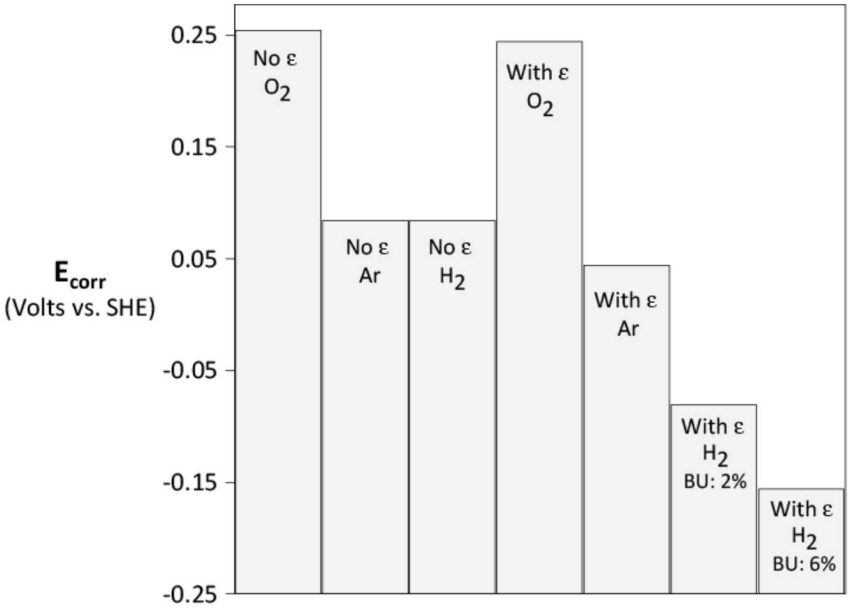

Figure 2.3. Summary of results from Shoesmith (2008) showing measured corrosion potentials for simulated spent fuel specimens with and without the fission product alloy Ru ε-phase. The conditions for the tests included bubbling either O_2, Ar or a gas mixture of 5% H_2 in Ar through the electrochemical cell solution. All tests were at 60°C. BU denotes simulated burnup, where higher burnup indicates a higher surface area coverage of the ε-phase (adapted from Shoesmith, 2008).

The FMD model calculates the net effect of all redox reactions occurring in the system based on the fuel and steel corrosion potentials (E_{corr}). The corrosion potential is the voltage at which the rates of the anodic and cathodic reactions are equal, that is, at E_{corr} the anodic dissolution current density is balanced by the cathodic oxidant reduction current density (participating reactions are shown schematically in red on Figure 2.2). Steel corrosion rate at the E_{corr} value established by a particular environmental condition (Eh, pH, chemistry) will depend on whether it corrodes actively or passivates. Under anoxic conditions, the steel corrosion rate is directly proportional to the rate of H_2 generation at the steel surface, since the only cathodic reaction occurring under anoxic conditions is the reduction of water to form H_2. The corrosion rate can be measured electrochemically as a corrosion current, which can be converted to a surface area-normalized mass dissolution rate by using Faraday's law for implementation in the FMD model.

All of the processes shown in Figure 2.2 are quantified in a parameter database that is updated as new experimental results are obtained. The FMD model parameter database is summarized in Table 2.1 and the specific parameters updated for FMDM V.4 are shown in Table 2.2.

Table 2.1. Summary of FMDM parameters and data gaps that need to be addressed in experimental work to improve the accuracy of the model (adapted from Jerden et al., 2017b).

Parameter	Description	Data needs to improve accuracy
Dimension of fuel environment	(mm – cm)	To be updated when dimensions of waste package are known
Nodes in fuel environment	(log-space grid: fine-spacing near surface)	To be updated when dimensions of waste package are known
Fuel surface coverage by NMP	(~1%)	From literature
Dimension of steel environment	(mm – cm)	To be updated when dimensions of waste package are known
Nodes in steel environment	(log-space grid: fine-spacing near surface)	To be updated when dimensions of waste package are known
Number of FMDM time steps	(100 – 1000)	Use to optimize PA interface
Fuel alteration layer porosity	(~50%)	From literature
Fuel alteration layer tortuosity	(~0.01)	From literature
Fuel alteration layer radiolysis factor	(*not used*)	*Could be activated to account for radionuclide uptake by U secondary phases*
Alpha particle penetration depth	(35μm)	From literature
Fuel burnup	(25 – 75 GWd/MTU)	**Input from PA**
Age of fuel (time out of reactor)	30 – 100 yrs	**Input from PA**
Resistance between fuel and NMP domains	(10^{-3} Volts/Amp)	Interpretation of literature
Temperature history	function	**Input from PA**
Dose rate history	function	Based on MCNPX results of Radulescu, 2011
Spatial dose rate	function (decrease in dose rate with distance from fuel)	Based on MCNPX results of Radulescu, 2011
Rate constants for interfacial reactions in fuel and steel domains	See Figure 2.2 for summary of specific reactions	**Data need:** experiments needed due to lacking or inconsistent data in current literature on H_2 reactions on fuel and NMP and steel corrosion under relevant conditions
Charge transfer coefficients for interfacial half-cell reactions in fuel and steel domains	See Figure 2.2 for summary of specific reactions	**Data need:** experiments needed due to lacking or inconsistent data in current literature on H_2 reactions on fuel and NMP
Activation energies	T dependence: See Figure 2.2 for summary of specific reactions	**Data need:** experiments needed due to lacking or inconsistent data in current literature on H_2 reactions on fuel and NMP and steel corrosion under relevant conditions

Table 2.1. Continued.

Parameter	Description	Data needs to improve accuracy
Standard potentials for interfacial half-cell reactions: fuel and steel	See Fig. 2.2 for reactions	From literature
Relative area of fuel domain	Default 1:1, depends on waste package design	To be updated when dimensions of waste package are known
Relative area of steel domain	Default 1:1, depends on waste package design	To be updated when dimensions of waste package are known
Environmental leak rate (diffusion barrier factor)	Depends on waste package design, breach	Interpretation of literature
Environmental concentrations	(O_2, H_2, CO_3^{2-}, Fe^{2+}, Cl^-)	**Input from PA**
Rate constants for bulk solution reactions in fuel, steel environments	See Figure 2.6 for summary of specific reactions	From literature
Activation energy for bulk solution reactions	T dependence, See Figure 2.8 for reactions	From literature
Passivation potential of steel surface	(75 V_{SCE}) as place-holder	**Data need:** experiments needed due to lacking or inconsistent data in current literature. For example, C-steels may not passivate under repository relevant conditions. More data are needed to determine active corrosion rates and to quantify the role magnetite corrosion layers play in corrosion behavior at pH > 8.
Passivation corrosion current density	Calculated internally within FMDM	**Data need:** experiments needed due to lack of data in literature
Radiolytic oxidant (H_2O_2) generation value (G_{cond})	Analytical function for conditional G_{H2O2} value from PNNL radiolysis model	Values based on radiolysis model results, Buck et al., 2013. *Would need to be updated, expanded for brine solutions (Cl, Br)*

Table 2.2. Specific electrochemical parameters that are dominant in determining the rate of spent fuel degradation in the FMD model. The rate constants for the reduction of H_2O_2 and O_2 (bold) are newly updated values for the FMDM V.4, while all others are the same as FMDM V.3. The V.3 parameters were derived from King and Kolar 2004 except for the steel corrosion parameters which are alloy specific and need to be determined experimentally.

Reactions	**Equation**	**k*** (mol m^{-2} s^{-1} or mol s^{-1})	**α**	**E^0** (V)
$UO_2 \xrightarrow{k_{UO_2}} UO_2^{2+} + 2e^-$	$i^{UO_2} = nAFk_{UO_2}\exp\left[\frac{\alpha_{UO_2}F}{RT}(E_{corr}^{UO_2} - E_{UO_2}^0)\right]$	$5.0x10^{-8}$	0.96	0.17
$H_2 + 2OH^- \xrightarrow{k_{H_2}} 2H_2O + 2e^-$	$i^{H_2} = nAFk_{H_2}\exp\left[\frac{\alpha_{H_2}F}{RT}(E_{corr}^{\varepsilon-phase} - E_{H_2}^0)\right]$	$1.0x10^{-3}$	0.5	0.58
$H_2O_2 + \xrightarrow{k_{H_2O_2}} O_2 + 2H^+ + 2e^-$	$i^{H_2O_2} = nAFk_{H_2O_2}\exp\left[\frac{\alpha_{H_2O_2}F}{RT}(E_{corr}^{UO_2} - E_{H_2O_2}^0)\right]$	$7.4x10^{-10}$	0.41	0.12
$H_2O_2 + 2e^- \xrightarrow{k_{H_2O_2}} 2OH^-$	$i^{H_2O_2} = nAFk_{H_2O_2}\exp\left[\frac{\alpha_{H_2O_2}F}{RT}(E_{corr}^{UO_2} - E_{H_2O_2}^0)\right]$	**$2.0x10^{-14}$**	-0.41	0.97
$O_2 + 2H_2O + 4e^- \xrightarrow{k_{O_2}} 4OH^-$	$i^{O_2} = nAFk_{O_2}\exp\left[\frac{\alpha_{O_2}F}{RT}(E_{corr}^{UO_2} - E_{O_2}^0)\right]$	**$1.0x10^{-12}$**	-0.50	0.43
$Fe \xrightarrow{k_{Steel}} Fe^{2+} + 2e^-$	$i^{Steel} = nAFk_{Steel}\exp\left[\frac{\alpha_{Steel}F}{RT}(E_{corr}^{Steel} - E_{Steel}^0)\right]$	*Data Need*	*Data Need*	*Data Need*
$2H_2O + 2e^- \xrightarrow{k_{H_2}} H_2 + 2OH^-$	$i^{H_2O} = nAFk_{H_2O}\exp\left[\frac{\alpha_{H_2O}F}{RT}(E_{corr}^{Steel} - E_{H_2O}^0)\right]$	$5.0x10^{-7}$	-0.48	-1.1

Where (i) is the current density for a half-call reaction (proportional to the reaction rate), (k) is the half-cell reaction rate constant, (α) is the charge transfer coefficient and (E^0) is the standard potential.

#Values shown in bold are updated constants for FMDM V.4 that were derived by comparing the FMDM results to experimental data (see Figure 2.4 and 2.5).

*The rate constant and other parameter values for steels will vary depending on the alloy composition. Electrochemical experiments with relevant alloys such as 316, 304 and low carbon steels are needed to quantify these parameter values.

As indicated in Table 2.2, the parameter values that were updated for FMDM V.4 are the rate constants for the reduction of H_2O_2 and O_2 on the UO_2 surface. These rate constants are used in the Butler Volmer relationships on which the FMD model is based on (see Table 2.2 for details).

The comparison of model results from FMDM V.4 and experimental datasets for the dissolution rate of spent fuel, simulated spent fuel and UO_2 are shown in Figures 2.4 and 2.5. The purpose of the comparison of the FMD model results to the experimental data was not to fit the data in a statistical sense, but rather to improve the accuracy of the model results while maintaining a conservative margin of safety (i.e. model

should reasonably overpredict degradation rates). As shown in Figure 2.3 the newer parameter value for the H_2O_2 reduction give a more accurate conservative bound to the experimental data.

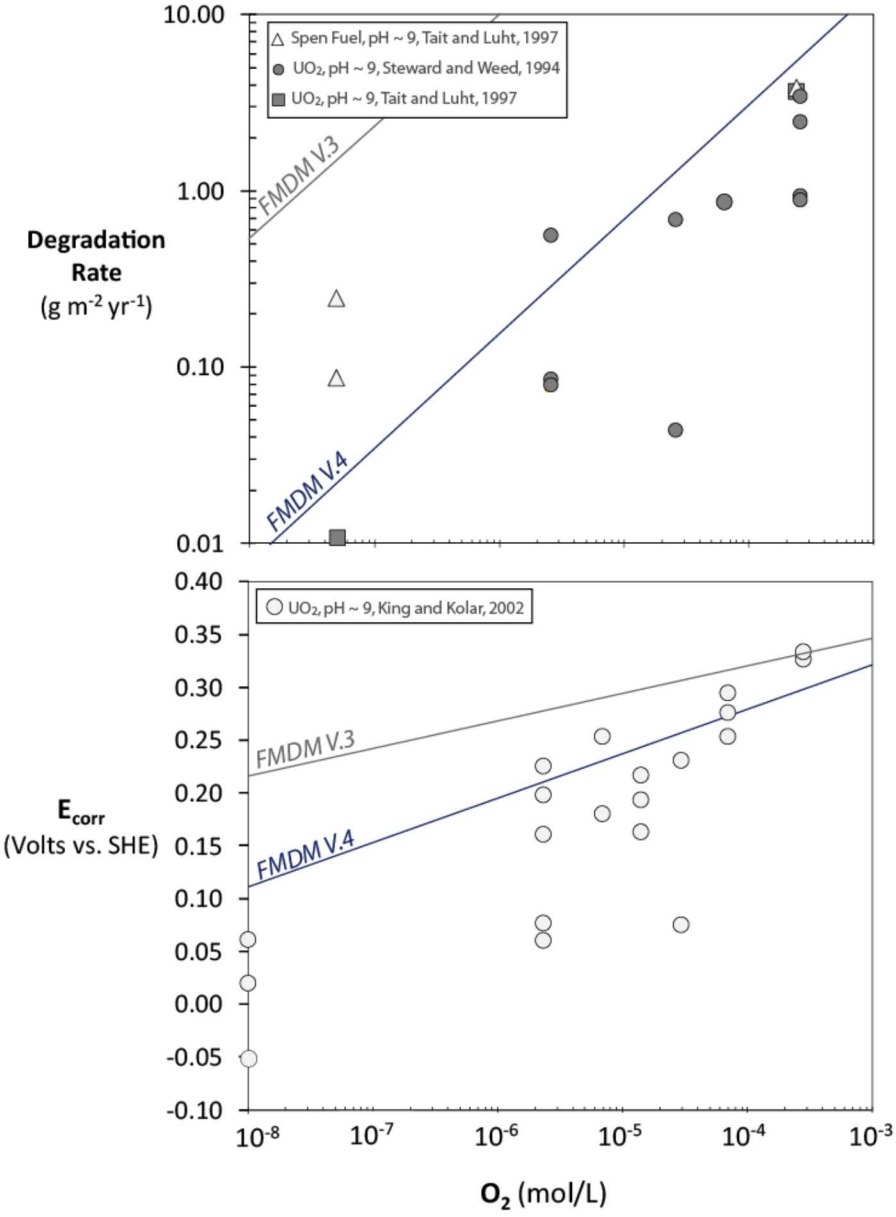

Figure 2.4. Comparison of results from the updated version 4 of the FMD model to experimental results. The model runs were for 25°C and no other oxidants were present.

Figure 2.4 shows the degradation rate (top plot) and E_{corr} (bottom plot) calculated by the FMDM V.3 and FMDM V.4 over a range of relevant dissolved concentrations of O_2 (no other oxidants present) and compares the model results to experimental data. The comparisons show that FMDM V.4 with the updated parameter value for O_2 reduction on the fuel (Table 2) is more consistent with the experimental results. The data points for spent fuel at ~$5x10^{-8}$ M O_2 in the degradation plot (top) are elevated relative to the general trend in the data due to the presence of radiolytic oxidants other than O_2 in those tests.

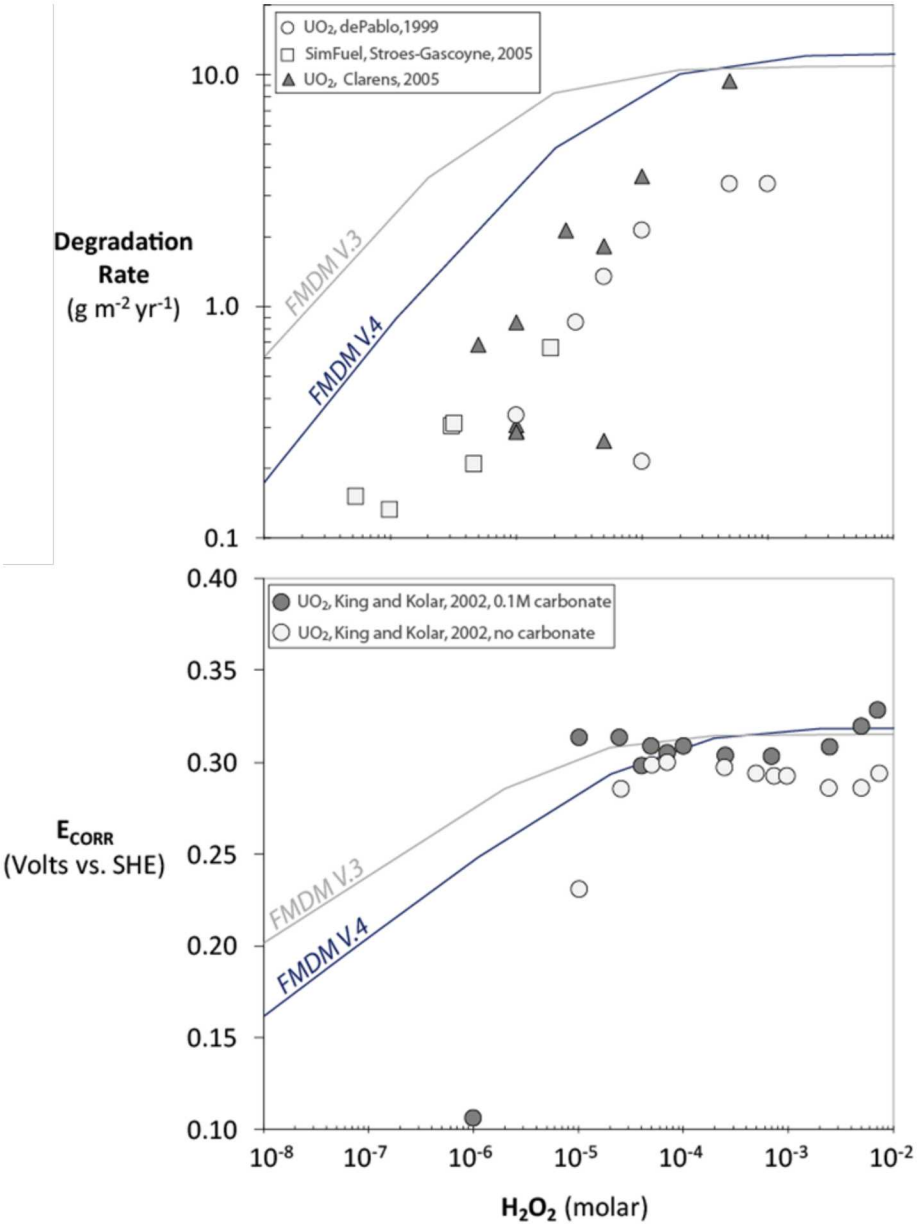

Figure 2.5. Comparison of results from the updated version 4 of the FMD model to experimental results. The model runs were for 25°C and an O_2 concentration of 10^{-9} molar.

Figure 2.5 shows the degradation rate (top plot) and E_{corr} (bottom plot) calculated by the FMDM V.3 and FMDM V.4 over a range of relevant dissolved concentrations of H_2O_2 and compares the model results to experimental data. In general, the FMDM V.4 with the updated parameter value for H_2O_2 and O_2 reduction on the fuel (Table 2.2) is more consistent with the experimental results. The model results for the degradation rate (top plot) are purposefully high as the goal is for the model to provide a conservative, but realistic, upper bound for the spent fuel dissolution rate.

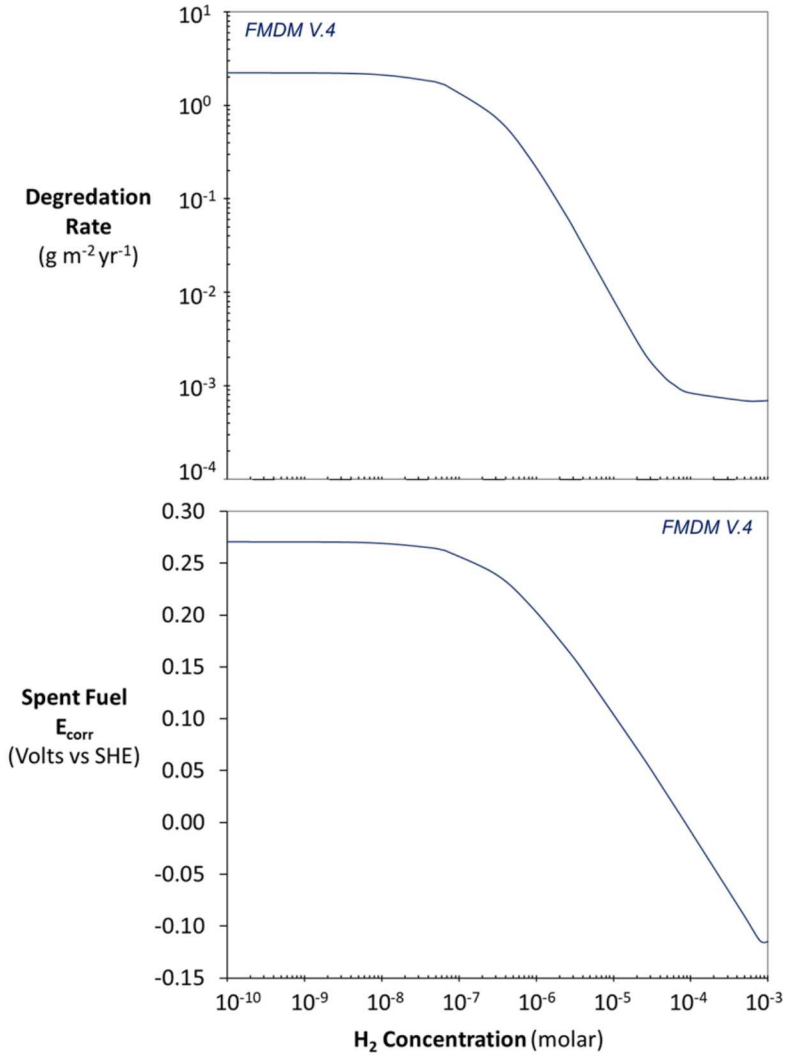

Figure 2.6. Results from version 4 of the FMD model showing the degradation rate and calculated E_{corr} as functions of the H_2 concentration at the spent fuel surface. For these runs the temperature was 25°C, the O_2 concentration was 10^{-9} M and the H_2O_2 concentration was 10^{-6} M.

Figure 2.6 shows the degradation rate (top plot) and E_{corr} (bottom plot) calculated by the FMDM V.4 over a range of relevant dissolved concentrations of H_2 concentrations at the spent fuel surface. The degradation plot (top) shows an inflection around 10^{-7} M H_2 indicating that the oxidation of H_2 begins to counteract the oxidative dissolution of the fuel at sub micromolar concentrations. When the H_2 concentration increases to around 10^{-4} M, the oxidation of H_2 becomes the dominant anodic reaction at the fuel surface thus effectively shutting off oxidative dissolution. Under the conditions for this model run the threshold E_{corr} for effectively shutting down the oxidative dissolution of the fuel is around 0.0 volts vs. SHE. As shown in Figure 2.6, after oxidative dissolution is shut down by H_2 oxidation the fuel continues to degrade at a rate of approximately 10^{-3} g m^{-2} yr^{-1}, which is the chemical dissolution rate of the fuel [UO2(s) → UO_2(aq)]. This lower degradation rate value is consistent with experimental results under reducing conditions (Jerden et al., 2017a).

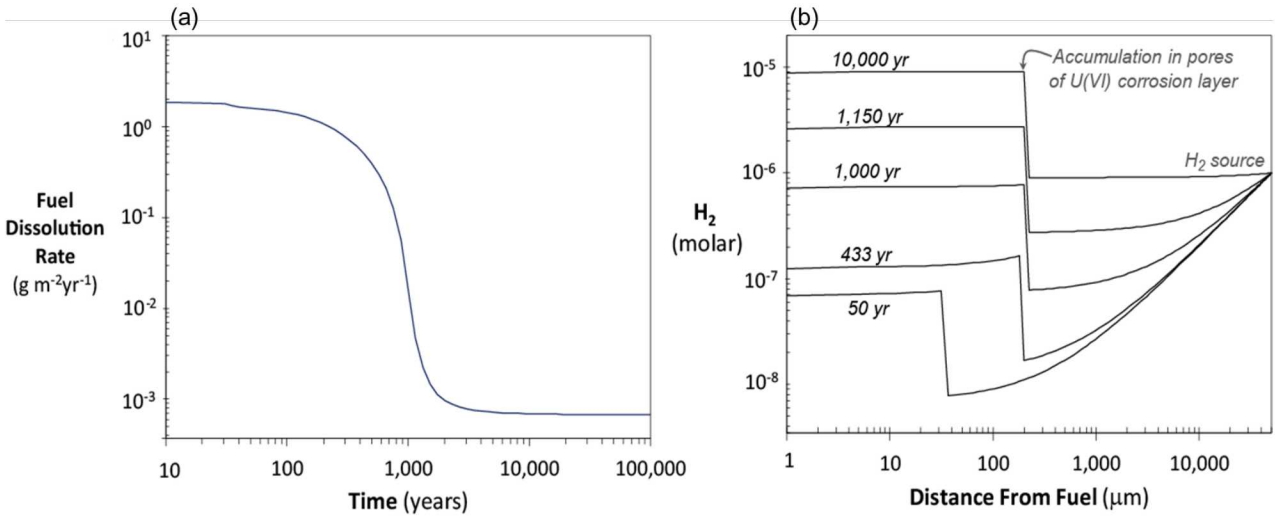

Figure 2.7. Model results using FMDM V.4 showing the fuel degradation rate as a function of time (a) and the H_2 concentration as a function of distance from the fuel surface (b). The temperature for these model runs was 25°C, the O_2 concentration was 10^{-9} M and the fuel burnup was 60 GWd/MTU.

Figure 2.7 shows the fuel degradation rate vs. time (a) and the H_2 concentration profiles at several times during a typical repository simulation. This example indicates the importance of the accumulation of H_2 near the fuel surface with time. This accumulation is accentuated by the presence of the porous U(VI) corrosion layer, which is modeled as a set of parallel tortuous pores that decrease species diffusion rates. In this example, a concentration of around $3x10^{-6}$ M H_2 is sufficient to counteract the oxidative dissolution of the fuel; however, this concentration is not achieved until around 1200 years. The H_2 source in this example is assumed to be a constant concentration of $1x10^{-6}$ M; however, in more realistic scenarios the H_2 source concentration will change depending on how changing repository conditions determine steel corrosion rates as a function of time. The addition of the steel corrosion module into the FMD model and the associated validation experiments will allow for the modeling of this more realistic scenario.

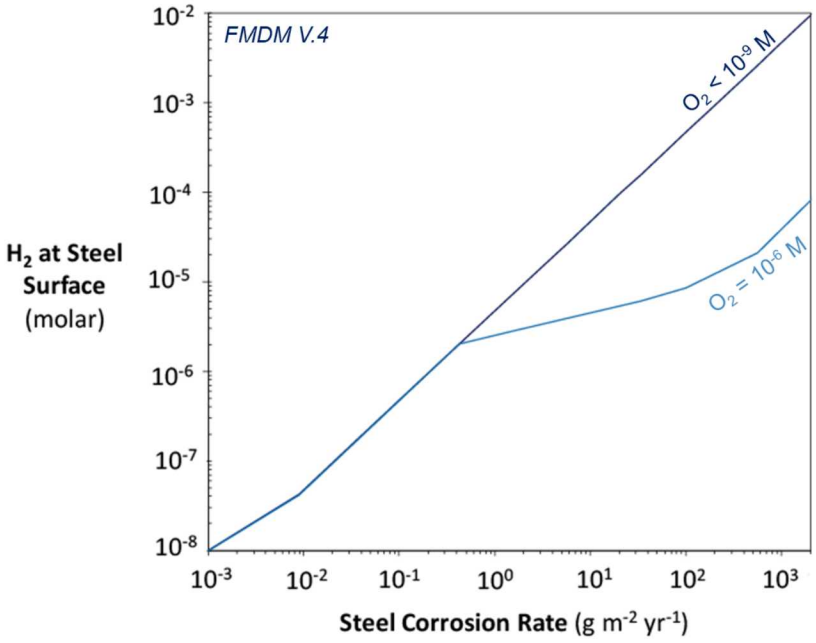

Figure 2.8. Model results using steel corrosion module of the FMDM V.4 showing the calculated H_2 concentration at the fuel surface as a function of the steel corrosion rate. The temperature for these model runs was 25°C, the O_2 concentration was 10^{-9} M and the O_2 concentration is indicated on the plot.

Figure 2.8 shows the concentration of H_2 produced by steel corrosion calculated by the steel corrosion module of the FMDM V.4 for different starting O_2 concentrations. This plot indicates how changes in dissolved oxygen concentrations can significantly affect the amount of H_2 produced by steel corrosion. For example, for a steel corrosion rate of around 100 g m^{-2} yr^{-1} and nanomolar O_2, the H_2 concentration due to steel corrosion would be around $5x10^{-4}$ M vs. a H_2 concentration of around $9x10^{-6}$ for solutions containing micromolar O_2. As shown in Figures 2.6, a concentration of $5x10^{-4}$ M H_2 is more than enough to shut down the oxidative dissolution of the fuel, while concentrations around 10^{-5} M H_2 do not completely counteract oxidative fuel degradation for 60 GWd/MTU fuels that are less than 1000 years old. Figure 2.8 highlights the need for an accurate and experimentally validated steel corrosion model that will provide a way to account for different alloy corrosion rates (i.e. different H_2 source concentrations) under changing repository conditions.

2.3 Electrochemical Experiments to Parameterize the FMDM Steel Corrosion Module

2.3.1. Background

As discussed above, establishing accurate steel corrosion rates for relevant disposal conditions is essential for accurate spent fuel degradation and source term modeling because of the dominant effect of H_2 on the spent fuel dissolution rate (as shown in Figures 2.6 and 2.7 above). The half-cell reactions of particular interest for H_2 generation are as follows:

$Fe^0 \rightarrow Fe^{2+} + 2e^-$ (Reaction 1)

$2H_2O + 2e^- \rightarrow H_2 + 2OH^-$ (Reaction 2a)
$2H^+ + 2e^- \rightarrow H_2$ (Reaction 2b)

with the overall steel corrosion reactions

$Fe + 2H_2O \rightarrow H_2 + Fe^{2+} + 2OH^-$ (Reaction 3a)
$Fe + 2H^+ \rightarrow H_2 + Fe^{2+}$ (Reaction 3b)

Reactions 3b and 3a indicate the fundamental coupling between steel corrosion and H_2 generation in alkaline and acidic conditions (respectively). The oxidation of other steel constituents (e.g., Cr, Mo, Ni, and Mn) will contribute to the anodic current, but the oxidation of Fe will be dominant.

To provide context for the experimental plan, Figure 2.9, which is a simplified version of the reaction FMDM reaction scheme shown above in Figure 2.2 above, that highlights the key H_2 consuming and producing reactions and shows schematically the potential importance of Zircaloy cladding as a source of hydrogen. Carbon steels, stainless steels and Zircaloly will all be corroding simultaneously with the spent fuel, therefore, our experiments will include representative specimens of each of these alloy types.

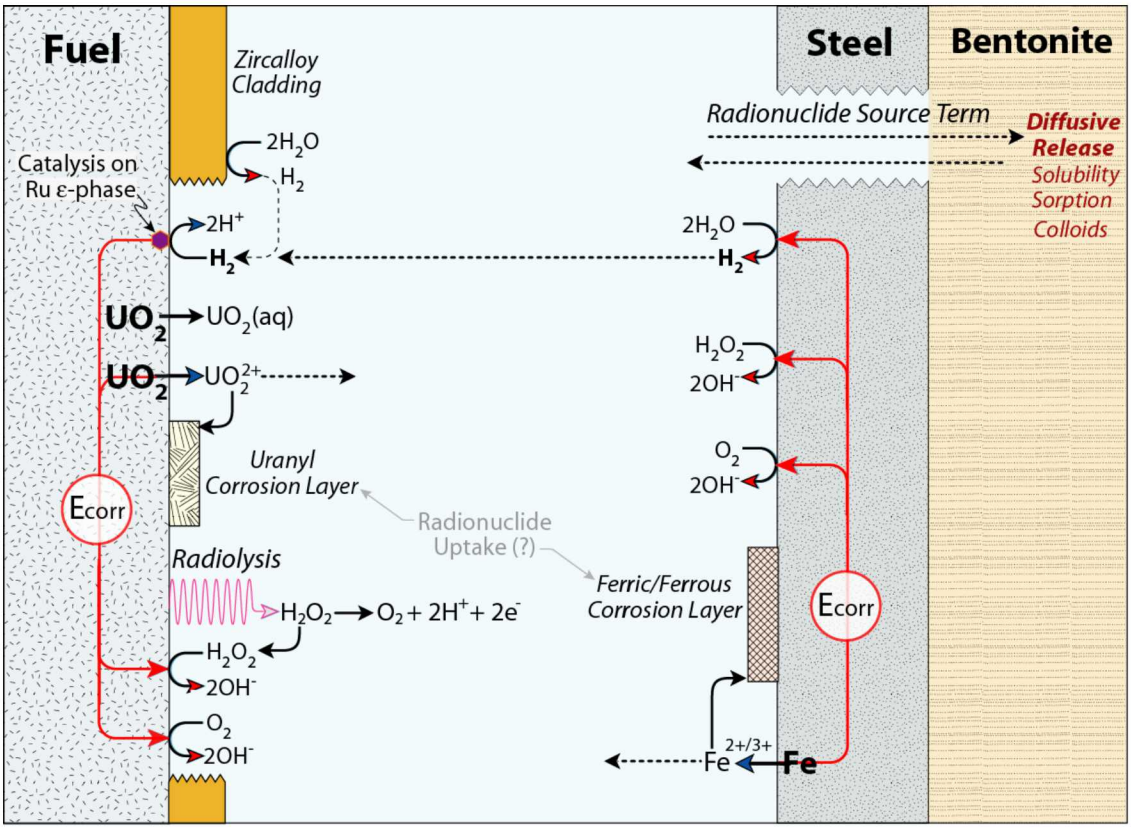

Figure 2.9. Schematic diagram of the FMD model reaction scheme highlighting the reactions that consume and produce H_2.

As discussed in Jerden et al., 2017(a), there is a wealth of literature on steel corrosion but much of the previous work was not done under conditions relevant for crystalline and argillite rock-type repositories. For example, Arthur has compiled corrosion rate data for a number of relevant alloys tested under a variety of conditions (Table 2.3); however, this compilation does not include the anoxic corrosion rates that that are more relevant to crystalline and argillite repository concepts. There is a significant amount of literature data on the corrosion of carbon steels, cast iron and forged steels (see reviews by Johnson and King, 2003 and King, 2007); however, much of these corrosion rate data are derived from batch style immersion tests that provide average cumulative rates rather than the instantaneous corrosion rates needed to represent the H_2 generation rates and to parameterize and validate the FMDM steel corrosion module.

Steel coupon immersion tests provide useful information on mineralogy and the evolution of the chemical system, but the Eh, pH and solution chemistry are not controlled and the surface conditions can change significantly over the test duration. Corrosion rates derived from immersion tests are based on cumulative mass loss measurements or corrosion layer thicknesses that do not indicate how the corrosion rate (and thus H_2 generation rate) varies with time or conditions (most importantly, with the solution Eh). Knowing these dependencies of the H_2 generation rate is essential for modeling spent fuel dissolution under evolving in-package chemical conditions.

Electrochemical tests can be used to quantify the effects of surface stabilization due to passivation and localized corrosion, such a pitting, that can only be qualitatively observed in coupon immersion tests. Furthermore, electrochemical methods can measure rates on the order of nanograms cm^{-2} d^{-1}. Thus, the use of electrochemical methods would provide reliable corrosion rates for durable EBS materials (including Zircaloy cladding) and provide dependencies on environmental conditions that could be used to predict the long-term generation of H_2 and attenuation of fuel degradation rates as the seepage water composition evolves.

Table 2.3. Statistical summary of immersion-type corrosion test results compiled by Arthur, 2004 (adapted). The anaerobic carbon steel corrosion rates are from King, 2007.

Metal	Conditions	Corrosion Rate (g m^{-2} yr^{-1})				Standard Deviation
		Min	Max	Median	Mean	
Stainless Steel Types 302/304/304L	Dilute groundwater[1] (25°C to 100°C)	0.01	12.56	1.03	1.71	2.38
	Saltwater (26.7°C)	12.70	313.18	40.64	91.53	89.07
	Saltwater (90°C)	5.28	127.20	16.24	46.53	47.62
Stainless Steel Types 316/316L/AM-350	Dilute groundwater (29.5°C)	0.01	0.38	0.02	0.07	0.11
	Dilute groundwater (50°C to 100°C)	0.30	4.08	1.83	1.98	1.17
	Saltwater (26.7°C)	0.01	118.30	5.89	15.51	26.77
Neutronit (borated stainless steel)	Dilute groundwater (29.5°C)	0.01	0.09	0.02	0.03	0.03
	Dilute groundwater (50°C to 100°C)	0.20	2.64	1.62	1.65	0.70
	Saltwater (26.7°C)	14.48	233.76	59.04	88.48	81.52
Stainless Steel Type 304 Alloyed with 0.3% Boron	Dilute groundwater (~25°C)	24.40	97.52	36.56	48.80	30.88
	Dilute groundwater (boiling)	24.40	219.44	134.08	126.00	63.92
Stainless Steel Type 304 Alloyed with 1.5% Boron	Boiling Dilute groundwater	1292.32	2023.84	1694.72	1682.48	262.16
Carbon Steel	Dilute groundwater (60°C)	629.68	1045.60	815.60	821.68	98.96
	Dilute groundwater (90°C)	464.64	1040.16	616.40	649.12	121.04
	Concentrated groundwater (60°C)	402.00	833.60	502.16	544.64	113.36
	Concentrated groundwater (90°C)	59.12	176.48	99.36	102.24	30.16
	Anoxic DIW in bentonite (80°C)	31.6	87.5	NA	NA	NA
	Anoxic brine in bentonite (80°C)	50.3	161.3	NA	NA	NA

[1]Dilute groundwater: dilute simulated ground waters with compositions similar J13 well water, a dilute sodium carbonate groundwater from the Yucca Mountain Site (see Arthur et al., 2004 for composition).
[2]Saltwater refers to sea water with ~17,000 ppm chloride.
[3]Concentrated groundwater: simulated J13 well water concentrated 1000x by evaporation.

NA: not applicable, no statistical analysis performed.

To provide instantaneous corrosion rates under controlled redox conditions, we have initiated a set of electrochemical experiments focused on providing parameter values and validation data for the FMD model for a range of relevant alloys.

2.3.2. Method and Results

The electrochemical corrosion experiments being performed at Argonne employ the standard three electrode method as described by Bard and Faulkner, 2001. The three-electrode cell used for the Argonne tests consists of a 20 mL jacketed, borosilicate glass vessel with a saturated calomel reference electrode (SCE), a graphite counter electrode and a steel, Zircaloy or UO_2 working electrode. A typical electrochemical cell and working electrode is shown in Figure 2.10. For these scoping experiments, an aggressive 10 mM NaCl solution adjusted to pH 4 with sulfuric acid was used as the electrolyte.

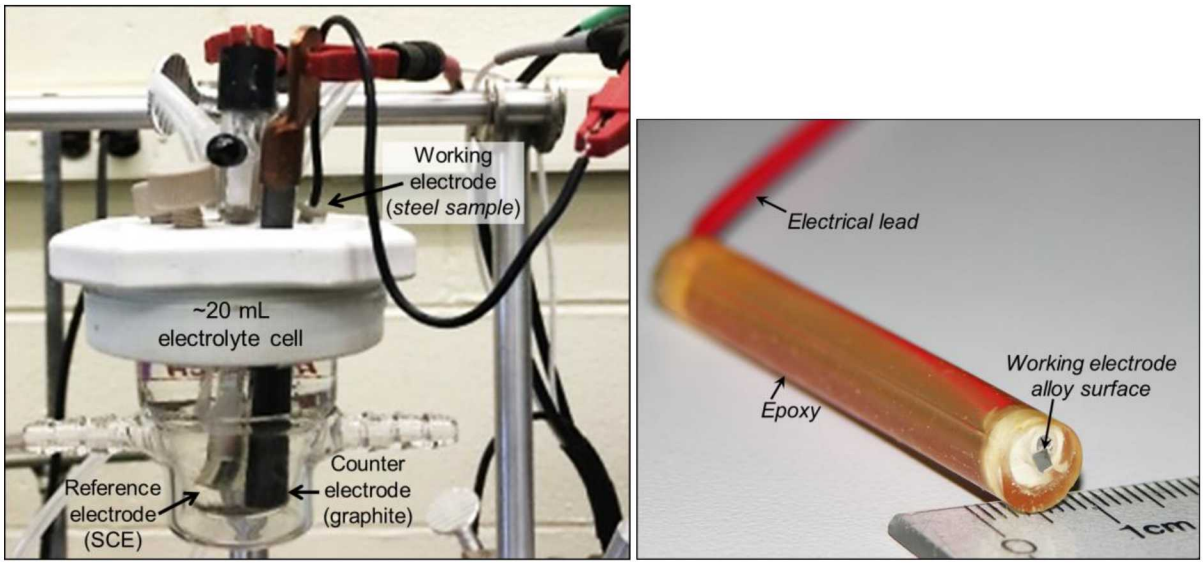

Figure 2.10. Three-electrode electrochemical cell used in Argonne electrochemical experiments (left) and an example alloy working electrode (right). The working electrode shown is made of Zircaloy-4, but the steel electrodes used for ongoing and future tests are the same size and mounted in the same way.

In the electrochemical tests, the electrolyte is used to impose chemical effects, including pH and Cl^- concentrations, and a potentiostat is used to impose a surface potential representing the solution Eh. The potentiostat can be used to impose a wide range of fixed potentials to efficiently determine the effect of the solution Eh on the steel corrosion and H_2 generation rate. In practice, a potentiodynamic scan is performed to measure E_{corr} for the polished surface in the test solution and identify regions of active and passive behavior to be studied in subsequent potentiostatic tests. The potentiodynamic scan indicates the propensity for active or passive corrosion, but the rapid scan rate does not allow stable passive layers to form. Potentiostatic tests are conducted to measure the corrosion currents as stable passive layers form or the constant currents are achieved with actively corroding metals.

Figure 2.11 (adapted from Jerden et al., 2017a) shows typical results for potentiodynamic (PD) scans (a) and potentiostatic (PS) measurements (b) in tests with the three main alloys of interest. These scoping tests

were performed under aggressive corrosion conditions (pH 4 for steels and pH 1 for Zircaloy) to optimize the methodology. These types of PD and PS analyses will be performed under a range of relevant repository conditions as part of the ongoing FY18 and future FY19 electrochemical tests. The test matrix for these ongoing and planned experiments is shown in Table 2.4.

Table 2.4. Test matrix for electrochemical experiments. Experiments will determine corrosion rates and mechanisms using standard potentiodynamic polarization, potentiostatic holds and electrical impedance spectroscopy techniques.

Solution Variables	2000 mg/L Cl^- No UO_2			4000 mg/L Cl^- No UO_2			2000 mg/L Cl^- UO_2 Pellet at OC			4000 mg/L Cl^- UO_2 Pellet at OC		
pH	4	7	10	4	7	10	4	7	10	4	7	10
316L SS	FY18	FY18	FY18	FY18	FY18	FY18	FY19	FY19	FY19	FY19	FY19	FY19
304L SS	Future work	Future work	Future work	Future work	Future work	Future work	Future work	Future work	Future work	Future work	Future work	Future work
Carbon Steel (4320)	FY18	FY18	FY18	FY18	FY18	FY18	FY19	FY19	FY19	FY19	FY19	FY19
Borated SS (Neutronit)	Future work	Future work	Future work	Future work	Future work	Future work	Future work	Future work	Future work	Future work	Future work	Future work
Zircaloy-4	FY18	FY18	FY18	FY18	FY18	FY18	NA	NA	NA	NA	NA	NA
Solution Variables	600 mg/L SO_4^{2-} No UO_2			1300 mg/L SO_4^{2-} No UO_2			600 mg/L SO_4^{2-} UO_2 Pellet at OC			1300 mg/L SO_4^{2-} UO_2 Pellet at OC		
pH	4	7	10	4	7	10	4	7	10	4	7	10
316L SS	Future work	Future work	Future work	Future work	Future work	Future work	Future work	Future work	Future work	Future work	Future work	Future work
304L SS	Future work	Future work	Future work	Future work	Future work	Future work	Future work	Future work	Future work	Future work	Future work	Future work
Carbon Steel (4320)	Future work	Future work	Future work	Future work	Future work	Future work	Future work	Future work	Future work	Future work	Future work	Future work
Borated SS (Neutronit)	Future work	Future work	Future work	Future work	Future work	Future work	Future work	Future work	Future work	Future work	Future work	Future work
Zircaloy-4	Future work	Future work	Future work	Future work	Future work	Future work	Future work	Future work	Future work	Future work	Future work	Future work

NA (not applicable) tests with UO2 and Zircaloy will not be performed.
Starting solution composition will from the middle column (3.8:1) shown in Table 1.
All tests to be performed at ambient temperature (will be measured and recorded for each test).
OC: Open Circuit.

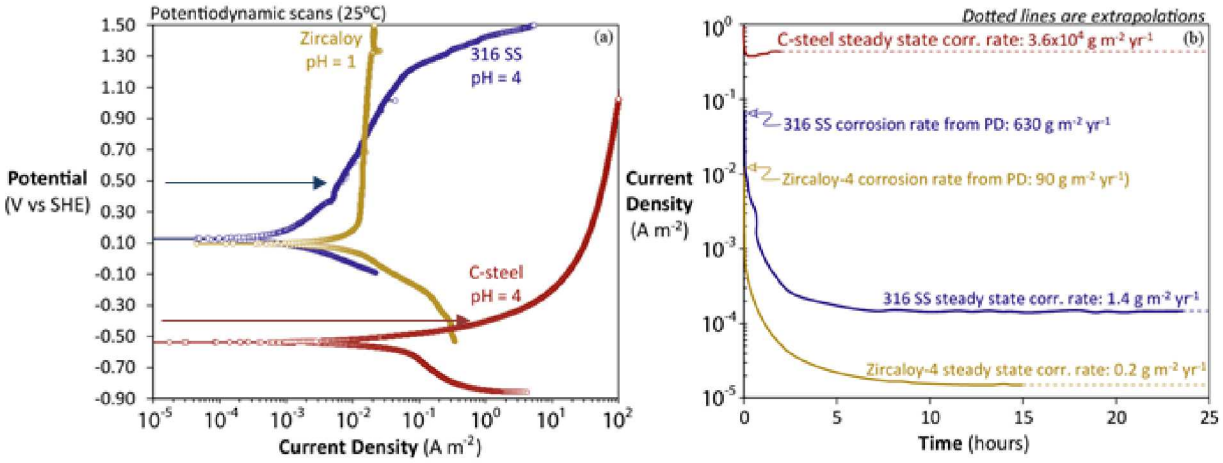

Figure 2.11. Example data from Jerden et al., 2017(a) showing they types of results obtained from electrochemical measurements: (a) potentiodynamic polarization and (b) potentiostatic corrosion of carbon steel at -0.4 V_{SHE} and pH = 4, 316L stainless steel at 0.5 V_{SHE} and pH = 4, and Zircaloy-4 at 0.5 V_{SHE} in pH 1 solution. The current densities measured in the PD scans are shown in (b) to illustrate the passive stabilization of 316 SS and Zircaloy-4 under these test conditions.

As shown in the scoping test data (Figure 2.11a) carbon steel, stainless steel and Zircaloy show significantly different corrosion behaviors (Jerden et al., 2017a). Carbon steel corrodes actively at very low potentials and does not passivate; while, stainless steel and Zircaloy-4 are noble at potentials below about -0.2 V and 316L passivates at moderate potentials, but corrodes actively above about 0.5 V. Zircaloy-4 passivates to high potentials in the absence of chloride (as shown), but passivation breaks down in the presence of even small amounts of chloride. As indicated by the arrows in Figure 11a, the potentiostatic tests (Figure 11b) were conducted at potentials above the E_{corr} values. The corrosion currents in the tests with Zircaloy-4 and 316L decrease as the surfaces are rapidly passivated in the pH 4 solution. Relative to the currents measured for the freshly polished clean surfaces in the potentiodynamic scans, the corrosion currents for Zircaloy-4 and 316L decrease about 1.5 and three orders of magnitude due to passivation, respectively. The initial corrosion rate of 316 SS is 630 g m^{-2} yr^{-1} (measured in the PD scan) but the steady state rate of the stabilized surface appropriate for calculating H_2 generation in the FMDM is only 1.4 g m^{-2} yr^{-1}. This rate is consistent with the 316 corrosion rates of 0.01 – 0.38 g m^{-2} yr^{-1} measured in dilute groundwater compiled by Arthur, 2004 (Table 2.3).

As pointed out in Jerden et al., 2017(a), the corrosion currents measured for the stabilized surfaces (Figure 2.11b) are appropriate for modeling the long-term H_2 generation rates in the FMD model. These passivated rates for Zircaloy-4 and 316L are readily measured electrochemically, but these are too low to have been measured by mass loss in coupon immersion tests. The corrosion behaviors and rates will be different under different environmental conditions, particularly for different Eh, pH, and Cl^- concentrations, and the differences must be taken into account in the FMD model. The electrochemical tests can provide the rate dependencies on these and other environmental variables.

Representative data from the solids characterization of corrosion phases produced during potentiostatic tests with 4320 carbon steel are shown in Figures 2.12 and 2.13. Figure 2.12 shows SEM micrographs of the freshly polished electrode surface (a) and (b) and the surfaces after potentiostatic corrosion at -0.45 V_{SCE} for different durations (c) and (d). The two distinct phases have different corrosion behaviors. The darker colored ferrite phase is the common body-centered cubic iron allotrope (α-iron) that corrodes preferentially

relative to the lighter colored pearlite, which is a two-phased, lamellar structure consisting of alternating layers of ferrite and a corrosion resistant iron carbide phase (Fe_3C). characterizing the steel microstructure is essential to understanding the corrosion behavior.

The 4320 alloy produced enough oxide corrosion products under the aggressive corrosion conditions (pH 4, potentiostatic holds at 0.1 and -0.45 V_{SCE}) for powder XRD analysis to be performed, and the results are shown in Figure 2.13. The major mineral phases identified in the corrosion layer were the ferric oxy-hydroxides maghemite (γ-Fe_2O_3) and lepidocrocite [γ-FeO(OH)]. For this experiment, ferric corrosion phases were favored over ferrous phases due to the presence of O_2 in the electrolyte solution. Future tests will focus on lower potentials and lower dissolved O_2 concentrations that are more representative of the reducing conditions anticipated to prevail within crystalline and argillite rock type repositories. A controlled atmosphere glovebox has been constructed to provide a low-oxygen environment for the electrochemical tests.

Most electrochemical tests will not generate enough corrosion phases for phase identification by powder XRD; therefore, electron diffraction by TEM may be used to characterize corroded alloys for selected tests. The TEM samples will be prepared using Argonne's FEI Strata 400 focused ion beam, field emission microscope with an AutoProb 200 sample extraction system (FIB). Specimens will be provided to collaborators within the SFWD campaign.

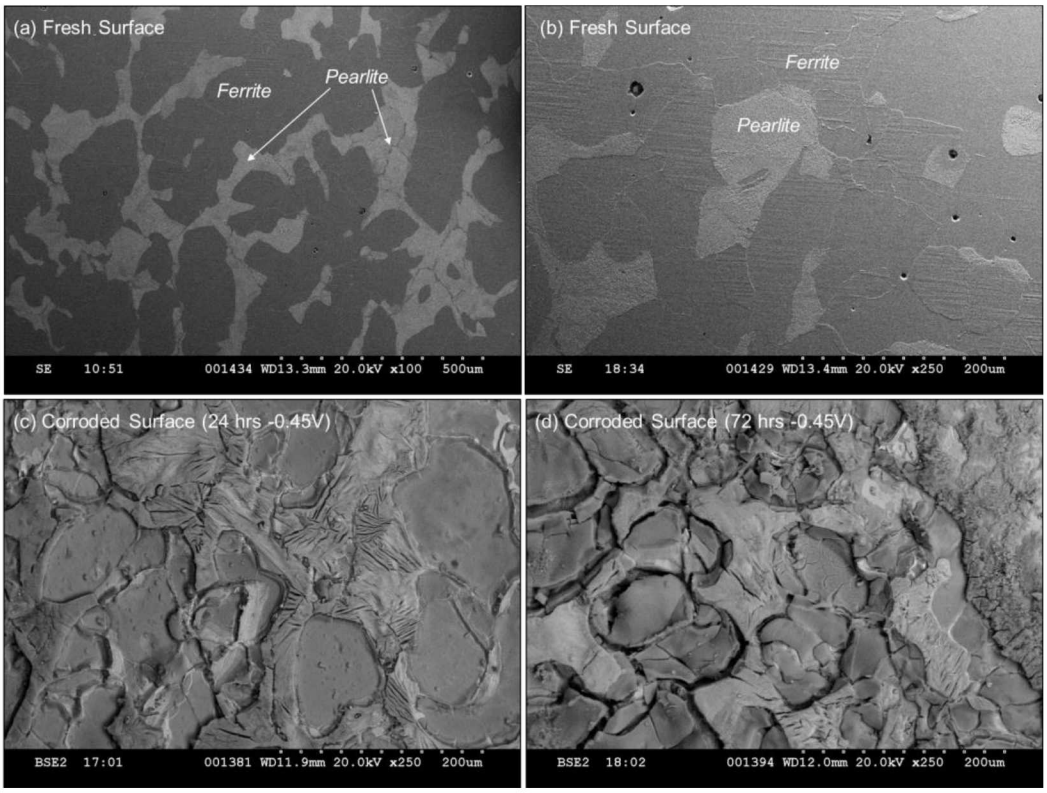

Figure 2.12. SEM micrographs of the polished unreacted 4320 steel electrodes (a) and (b) and the same electrode after 24 hours (c) and 72 hours (d) under potentiostatic conditions at 0.45 V_{SCE} and pH 4 [Gattu et. al. 2018, NACE].

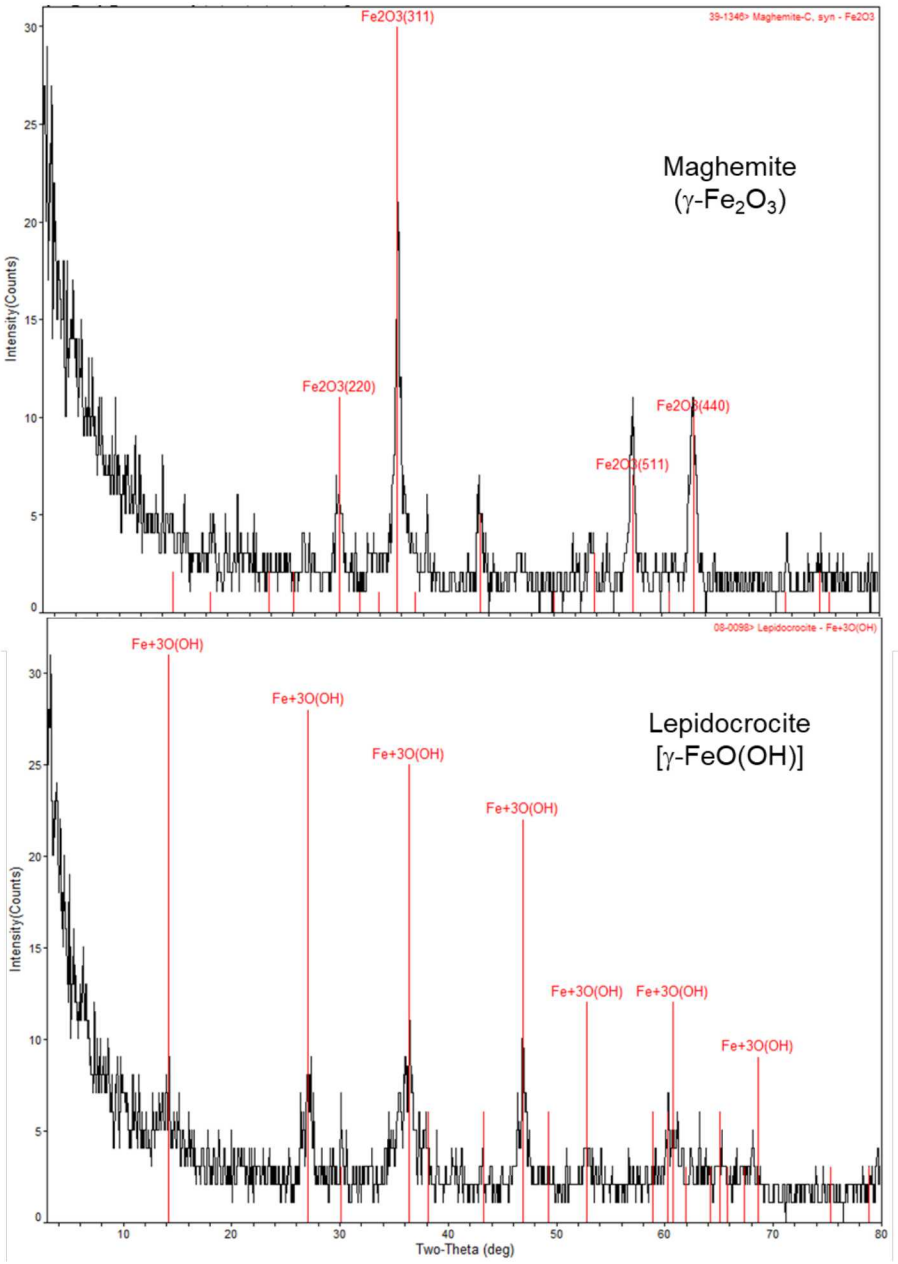

Figure 2.13. X-ray diffraction scans of oxide corrosion phases from the potentiostatic tests on 4320 carbon steel. The top diagram was for the -0.45 volt hold and the bottom diagram was for the 0.1 volt hold.

The test matrix shown in Table 2-4 calls for experiments to be performed in both sodium chloride and sodium sulfate solutions of varying concentrations to quantify the effect these anions have on steel and Zircaloy corrosion over a range of repository relevant Eh and pH conditions. The experimental concentrations for chloride and sulfate and other chemical variables such as pH and ionic strength are based on the chemical analyses of the bentonite pore waters presented in Fernandez et al., 2001 (Table 2.5).

As shown in Table 2-4, some experiments will be performed in the presence of a UO_2 (or lanthanide doped UO_2) electrode to provide a continuous source of uranium as the UO_2 dissolves at a rate established by the

solution chemistry and measured electrochemically. These tests involving the simultaneous corrosion of the alloy and UO_2 will produce samples that can be used to determine if the dissolved uranium is incorporated into steel corrosion phases. Detailed analytical electron microscopy will be required to both identify the corrosion phases present and to determine their uranium content and disposition. A range of different types of steel corrosion phases can be produced using the electrochemical approach described above as some tests will involve relatively oxidizing potentiostatic holds while others will be held at reducing conditions just above the alloy's corrosion potential in low O_2 environments.

Each electrochemical experiment will generally involve the following sequence of tests:

- Potentiodynamic scans to determine E_{corr} of alloy under conditions of interest,
- Potentiostatic holds over a range of relevant redox conditions,
- Standard electrical impedance spectroscopy to characterize the properties of passivating oxide layers,
- Detailed microscopy (reflected light, SEM/EDS) to characterize alloy microstructures before and after corrosion tests.

The results from these tests will provide the following information:

- Corrosion rates for stabilized surfaces under controlled environmental conditions,
- Electrical properties of the passivated surfaces to provide confidence in their long-term stability,
- Analytical expressions for key dependencies (Eh, pH, T, chloride concentration) to formulate rate laws for the corrosion of different materials required to calculate H_2 generation rates in the FMD model.
- Corrosion products for further analyses

Table 2.5. Bentonite pore water chemistry from FEBEX bentonite water extraction tests (adapted from Fernandez et al., 2001).

Measured Values	**Surface:Volume**		
	4.2:1	3.8:1	3.3:1
pH	7.49	7.29	7.38
Species *(mg/L)*			
Cl^-	2200	3600	4000
SO_4^{2-}	603	1100	1260
Br^-	4.9	4.9	9.1
HCO_3^-	67	131	133
$SiO_2(aq)$	10.9	14.4	N.D.
Al^{3+}	0.34	N.D.	0.12
Ca^{2+}	295	450	510
Mg^{2+}	385	410	390
Na^+	800	1725	2100
K^+	7.5	54	15
Sr^{2+}	6.2	6.9	7.5

N.D.: Not Determined

2.4. Conclusions and Future Work

The accomplishments and conclusions of this study are summarized as follows:

- The parameter database for the FMD model was updated based on comparisons between model results and existing spent fuel and UO_2 dissolution rate data.
- Results from sensitivity runs with the new model version (FMDM V.4) reiterate the need for experimental data to parameterize and validate the steel corrosion module added to the FMD model as discussed in Jerden et al., 2017(a) and Jerden et al., 2017(b). Electrochemical tests are in progress to support implementation of an improved steel passivation model in the FMD model by providing data sets with which the model can be calibrated for metals that will be present in the repository engineered barrier system (EBS) and key environmental variables.
- Results from scoping experiments demonstrated a straightforward electrochemical method that provides the electrokinetic information needed for model parameterization and validation.
- Model simulations using the FMDM V.4 agree with previous FMD model results showing that the presence of metals that corrode at different rates can extend the time over which H_2 generation will attenuate the fuel degradation rate. The materials used in the EBS can be selected to benefit the long-term performance of disposed fuel based on their measured corrosion behaviors and impacts on fuel durability as quantified by the FMDM calculations.

Model runs performed for this report demonstrate a number of important information gaps that need to be addressed by experimental work and in further model developments. These information gaps, which were also noted in Jerden et al., 2017(b), are as follows:

- Electrochemical corrosion experiments are needed to quantify the dependencies of spent fuel and steel corrosion rates on environmental variables under carefully controlled conditions. Most importantly, the dependencies of the steel corrosion rates on Eh, pH and the attenuating effect of passivation must be known to calibrate and validate the FMD model. Electrochemically determined corrosion rates are appropriate for calibrating the H_2 generation rates calculated with the FMD steel corrosion module because they quantify the electron transfer rate in the reduction reaction that generates the H_2. Examples of those electrochemical tests are summarized in this report.
- Experimental and modeling studies investigating the corrosion rates of different alloys that may go into the waste package design and waste form degradation are needed. Understanding the corrosion behavior of a variety of relevant engineering materials would provide important insights as to the types of steel that could be used to optimize the long-term performance of the waste package and canister materials. For example, using a combination of actively corroding and passive metals having a range of corrosion rates could be utilized to ensure H_2 would be generated throughout most of the regulated service life. The steel corrosion model developed to quantify H_2 generation from metal surfaces within a breached waste package can also be used to model the corrosion kinetics of external surfaces contacted by bentonite pore water and possibly to model container breaching.
- Electrochemical tests quantifying the kinetic parameters for individual reactions at the in-package solution – spent fuel interface are needed (e.g., see Table 2 above). Based on the use of robust canisters, it is likely that the majority of the spent fuel in a repository will not be contacted by groundwater until canisters begin to fail more than 1000 years after repository closure. More studies are needed to determine the effects of fuel aging on fuel dissolution rates by measuring dissolution rates of actinide oxide materials that simulate “aged” ~1000 year old fuel in the presence of H_2. Such materials can be represented by doping UO_2 with fission product oxides and actinides. Electrochemical tests to measure the dissolution rates of materials representing

aged fuel alone and in the presence of corroding steel will provide the dataset required for reliable model validation to add confidence to the rate predictions.

- Modeling studies that build on our successful model integration efforts are needed. These investigations should focus on the chemical evolution of the in-package solution in contact with degrading spent fuel following the breach of the waste package and Zircaloy cladding. This is particularly important just after a breach due to acid-producing reactions that occur when radiolytic oxidants from the fuel contact reducing groundwaters, as demonstrated in Jerden et al., 2017(b).

2.5. References

Arthur, S., Aqueous Corrosion Rates for Waste Package Materials, ANL-DSD-MD-000001 REV 01, October 2004, DOC.20041012.0003

Bard, A., Faulkner, L., "Electrochemical methods: Fundamentals and Applications", John Wiley and Sons, Inc., 2001

Broczkowski, M.E., Noël, J.J., Shoesmith, D.W., The inhibiting effects of hydrogen on the corrosion of uranium dioxide under nuclear waste disposal conditions, *Journal of Nuclear Materials,* 346, 16–23, 2005

Buck E., Jerden, J., Ebert, W., Wittman, R., "Coupling the Mixed Potential and Radiolysis Models for Used Fuel Degradation," FCRD-UFD-2013-000290, 2013.

Gattu, V.K., Ebert, W.L., Tehrani, N., and Indacochea, J.E. (2018). "Electrochemical Measurements of Steel Corrosion for Modeling H_2 Generation." *Corrosion 2018*, May 11-14, 2018, Phoenix, AZ. Paper No. 11370.

Jerden J. Frey K. Ebert W., "A Multiphase Interfacial Model for the Dissolution of Spent Nuclear Fuel, *Journal of Nuclear Materials*, 462, 135–146, 2015.

Jerden, J., Frey, K., Ebert, W., "Spent Fuel Matrix Degradation and Canister Corrosion: Quantifying the Effect of Hydrogen", Report for Spent Fuel and Waste Science and Technology Project, Report #: SFWD-SFWST-2017-000039, February 28, 2017(a)

Jerden, J., Gattu, V. K., Ebert, W., "Progress Report on Development of the Spent Fuel Degradation and Waste Package Degradation Models and Model Integration", Report for Spent Fuel and Waste Science and Technology Project, Report #: SFWD-SFWST-2017-000091, August 14, 2017(b)

King F. and Kolar M., "An Improved C-Steel Corrosion Model For the Mixed-Potential Model for Used Fuel Dissolution (MPM Version 1.4)," Ontario Hydro, Nuclear Waste Management Division Report No: 06619-REP-01300-l0027-R00, 2001.

King F. and Kolar M., "Validation of the Mixed-Potential Model for Used Fuel Dissolution Against Experimental Data" Ontario Hydro, Nuclear Waste Management Division Report No. 06819-REP-01200-10077-R00, 2002.

King F. and Kolar M., "The Mixed-Potential Model for UO2 Dissolution MPM Versions V1.3 and V1.4," Ontario Hydro, Nuclear Waste Management Division Report No. 06819-REP-01200-10104 R00, 2003.

King, F., "Overview of a Carbon Steel Container Corrosion Model for a Deep Geological Repository in Sedimentary Rock," Nuclear Waste Management Organization Report TR-2007-01, March 2007, 71 p.

Ollila, K., "Dissolution of Unirradiated UO_2 and UO_2 Doped with ^{233}U in Low- and High-Ionic-Strength NaCl Under Anoxic and Reducing Conditions," Posiva Working Report 2008-50, 2008.

Radulescu, G., "Repository Science/Criticality Analysis," Oak Ridge National Laboratory, Reactor and Nuclear Systems Division Report: FTOR11UF0334, ORNL/LTR-2011, Oak Ridge National Laboratory, Oak Ridge, TN., 2011.

Röllin S., Spahiu K., Eklunda U., "Determination of Dissolution Rates of Spent Fuel in Carbonate Solutions Under Different Redox Conditions with a Flow-through Experiment," *Journal of Nuclear Materials*, vol. 297, pp. 231–243, 2001.

Shoesmith, D.W. and F. King. 1998. A mixed-potential model for the prediction of the effects of α-radiolysis, precipitation and redox processes on the dissolution of used nuclear fuel. Ontario Hydro, Nuclear Waste Management Division Report 06819-REP-01200-0038- R00. Toronto, Ontario.

Shoesmith, D., "The Role of Dissolved Hydrogen on the Corrosion/Dissolution of Spent Nuclear Fuel," Nuclear Waste Management Organization, Toronto, Ontario, Canada, TR-2008-19, November 2008.

Wang Y. et al., "Used Fuel Disposal in Crystalline Rocks: Status and FY14 Progress," FCRD-UFD-2014-000060, SAND2014, Sandia National Laboratories, Albuquerque, NM., 2014.

3. NONLINEAR DYNAMICS AQUEOUS DISSOLUTION OF SILICATE GLASSES AND MINERALS: MORPHOLOGICAL INSTABILITY

3.1 Introduction

Chemical dissolution of silicate minerals and glasses - the most dominant component in the Earth crust - plays a critical role in global biogeochemical cycles and directly regulates the long-term climate evolution in our Earth system (Berner and Kothavala, 2001; Brady, 1991; White Blantley, 2003). Silicate dissolution and the induced carbonate precipitation have been investigated as a means for subsurface carbon sequestration (Matter and Kelemen, 2009). A recent field test where CO_2 was injected into a basaltic rock suggested that this carbonation process could happen far faster (< 2 years) than previously postulated (Matter et al., 2016), although the underlying mechanism is still unknown. Silicate materials have also been used in numerous industrial and technological applications such as molecular sieves for chemical separation (Kulprathipanja, 2010), catalysts for chemical conversion (Kulprathipanja, 2010), optical fibers for communication (Murata, 1996), biomedical devices (Hin, 2004), construction materials (Domone and Illston, 2010) and waste forms for nuclear waste disposal (Cailleteau et al., 2008; Gin, 2014). In many of these applications, the chemical durability of a material in the presence of liquid water or moisture directly determines the lifetime of the material in service. Therefore, understanding chemical alteration of silicate materials in aqueous solutions is of great importance to both Earth and materials sciences. Such an understanding is a prerequisite for a performance assessment of a silicate material as a waste form for nuclear waste disposal over a regulatory time period of up to hundreds of thousand years (Cailleteau et al., 2008; Gin, 2014), a time scale beyond any possible direct experimental test.

The underlying mechanism for silicate material degradation remains controversial. Aqueous dissolution of a silicate material was proposed to start with the formation of a silica-rich surface layer on a dissolution surface in which alkali and alkaline cations are partially leached out and replaced by hydrogen ions (Dran et al., 1986; Doremus, 1975; Petit et al., 1990). Recent experimental work suggests that, in a solution saturated with amorphous silica, the surface layer could form through a local structural arrangement involving little or no dissolution of silicate framework (Gin et al., 2015). The surface layer may continuously be subjected to *in-situ* silicate network repolymerization and reorganization, leading to the formation of a dense silica gel layer that may passivate a dissolving solid surface, resulting in a dramatic reduction in the dissolution rate (Gin et al., 2018). The traditional surface layer concept was challenged by recent observations of the existence of an extremely sharp interface between altered rims and pristine material domains, suggesting that material corrosion might be a direct dissolution-precipitation process (Putnis, 2015; Hellmann et al., 2015; Erui-Agudo et al., 2012; Geisler et al., 2015). Oscillatory zonings, commonly observed in altered rims, seem also difficult to reconcile with the traditional surface-layer concept (Putnis, 2015). However, the occurrence of a sharp interface is apparently not “universal”; as a matter of fact, in some cases, a gradient region (~500 nm thick) has been observed between altered rims and pristine material domains (Gin et al., 2015). The contradictory observations indicate the complexity of silicate material dissolution and call for a new theory to account for such complexity. Recently, we have shown how complex behaviors observed can emerge from a simple positive feedback between dissolution-induced cation release and cation-enhanced dissolution kinetics (Wang et al., 2016). This self-accelerating mechanism enables us to systematically predict the occurrence of sharp dissolution fronts (vs. leached surface layers), oscillatory dissolution behaviors, and multiple stages of glass dissolution (e.g., an alteration rate resumption at a late stage of a corrosion process).

Here we further show that the same mechanism can also lead to a morphological instability of an alteration front. Morphological instability refers to an evolution of an initially planar dissolution or growth surface

into a wavy or even fingered front through its own reaction-transport dynamics (Sekerka, 1973). This instability, in combination with oscillatory dissolution predicted by our previous work (Wang et al., 2016), can potentially give rise to a whole suite of patterning phenomena, as observed on archaeological glass samples as well as in laboratory experiments, including wavy dissolution fronts, corrosion pits, growth rings, and incoherent bandings of alteration zones. The result thus further demonstrates the importance of the proposed self-accelerating mechanism in silicate material degradation.

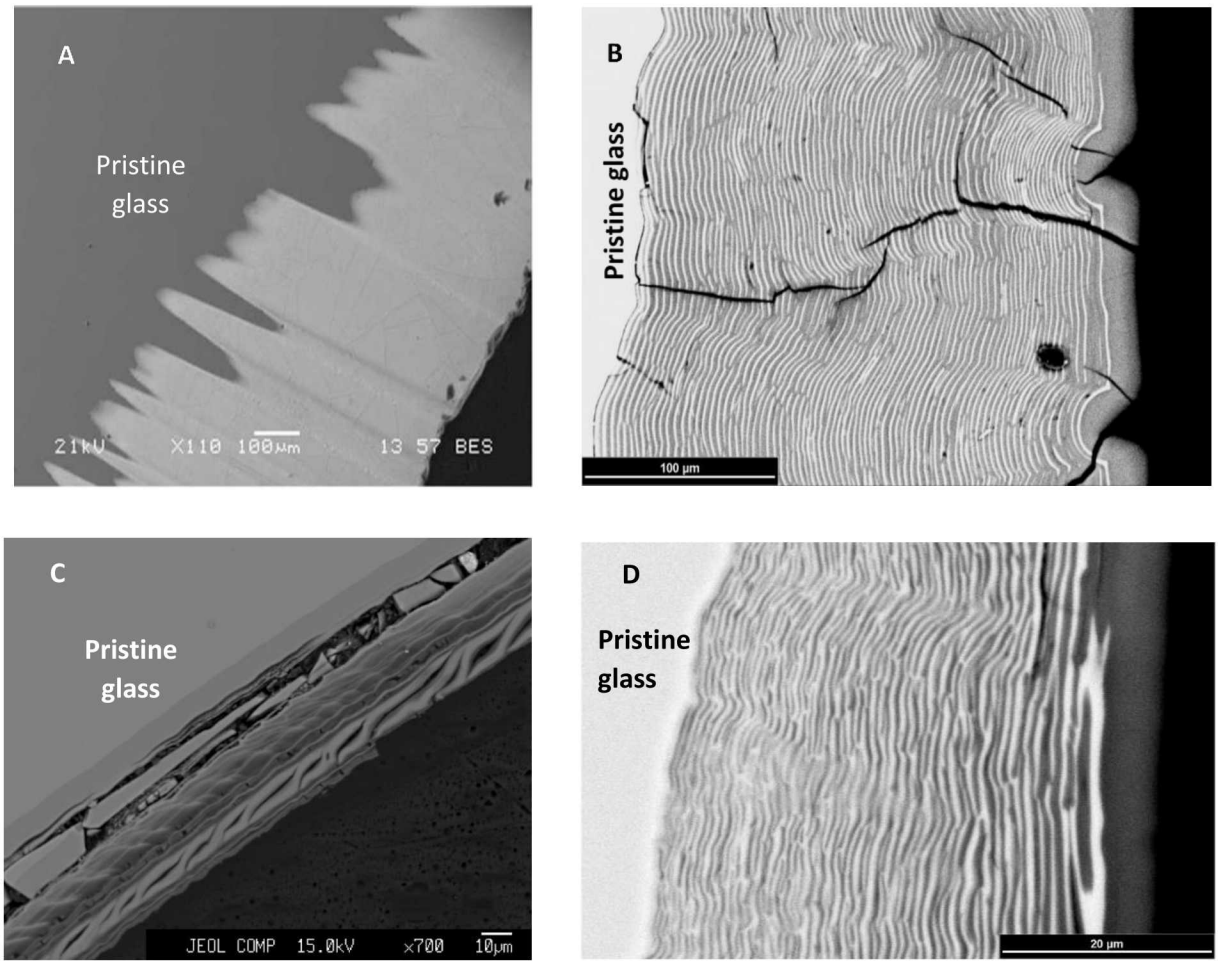

Figure 3.1. Backscattered electron images of corroded glass samples. A. Fingered dissolution front of an International Simple Glass (ISG) sample altered in deionized water at 90 °C and $pH_{25°C}$ = 9 under a flow-through condition for 55 days (scale bar – 100 µm). B. coherent wavy corrosion bands (chemical pattern) observed in corroded German WAK glass from an experimental series conducted at 150 °C, $pH_{init, 25°C}$ = 0, and S/V = 0.2 cm^{-1} (Geisler et al., 2010) (scale bar – 100 µm). C. Incoherent banding (bifurcations) at a glass dissolution surface and incoherent structures within individual bands in U-bearing, soda-lime glass beads corroded at 90 °C, $pH_{init, 25°C}$ = 7.1, and S/V = 0.6 cm^{-1}(Dohmen et al., 2013) (scale bar – 10 µm). D. Incoherent banding in German WAK glass from an experimental series conducted at 150 °C, $pH_{init,25°C}$ = 0, and S/V = 0.2 cm^{-1} (Geisler et al., 2010) (scale bar – 20 µm).

3.2 Results

Morphological instability and the underlying mechanism: Many excellent observations have been made on the structures and pattern formations of altered silicate materials. Dohmen et al. performed a detailed backscattered electron imaging study on two borosilicate glasses (Dohmen et al., 2013). They showed that among 16 dissolution experiments conducted, except one with an initial pH of about zero, all other experiments produced distinct lamellar layers with a thickness of 5 to 100 μm. Some of the layers form a coherent (i.e. parallel) wavy front with the convex side pointing toward a pristine glass domain. The wavy front seems to initiate from earlier-developed dissolution pits on a dissolution surface. Extensive pitting on a dissolution surface was observed on some samples (Dohmen et al., 2013, fig. 5). A gap seems to exist between an altered rim and a neighboring pristine glass domain, indicating an atomically sharp reaction interface. In addition to the coherent lamellar layers, incoherent wavy layers were also observed, in which two neighboring layers are not parallel (Dohmen et al., 2013, figs. 3c and 3g). In some occasions, hemispherical-shape incoherent layers penetrate deeply from a fracture surface into a pristine glass domain. Similar structural patterns were also observed on archaeological glass samples (Silvestri et al., 2005; Schalm and Anaf, 2016). On those samples, Silvestri et al. showed that within each individual wavy lamellar layer there occur spongy, distorted and branched structures (Silvestri et al., 2005, fig. 3), indicating complex dissolution and precipitation involved in the formation of each individual layer. Concentric growth rings were also observed on a view plane parallel to a material dissolution surface Schalm and Anaf, 2016, fig. 7b). Some of typical patterning phenomena in silicate glass alteration are shown in Fig.3.1.

We now want to show how these observed complex patterning phenomena in silicate material degradation can emerge from a morphological instability of a dissolution surface through the same mechanism we proposed earlier for oscillatory dissolution of silicate materials: the dissolution of a silicate material can potentially be catalyzed by the cations released from the reaction itself (Wang et al., 2016). This mechanism was postulated from the observed V-shape dependence of a far-from-equilibrium silicate material dissolution rate on solution pH (Wang et al., 2016; Rozalén et al., 2008; Skorina and Allanore, 2015; Wolery et al., 1996; Strachan et al., 1998). This mechanism operates on the right branch of the rate curve in Figure 2.2. Since the V-shaped pH dependence of the dissolution rate exists for a diverse set of silicate minerals including quartz (Wang et al., 2016; Rozalén et al., 2008; Skorina and Allanore, 2015; Wolery et al., 1996; Strachan et al., 1998), this dependence must be related to the dissolution of silica framework – a common structural component in all these minerals. In addition to the catalytic effect of hydroxyls, Rimstidt recently showed that a cation itself such as Na^+ could also catalyze quartz dissolution (Rimstidt, 2015). As elaborated previously (Wang et al., 2016), this self-accelerating mechanism can systematically account for the occurrence of multiple stages (or regimes) of silicate material degradation. For an illustration, let's assume that the material degradation starts in an acid solution (on the left branch of the dissolution curve in Figure 3.2), under which the dissolution rate of silica framework is higher than that for cation leaching, and as a result the material would dissolve congruently with no leached layer developed. As the pH of the solution increases due to the accumulation of the leached cations, the dissolution rate becomes lower than the leaching rate, leading to the formation a leached surface layer. As the pH continuously rises, the system moves from the left branch to the right branch of the dissolution curve. When the dissolution rate becomes on the same order of magnitude as the mass exchange rate with the bulk solution, oscillatory dissolution may emerge. As the pH of the solution further increases, the dissolution rate eventually overtakes the mass exchange rate, leading to a "runaway" situation with a sharp increase in the cation concentration at the interface as well as in the dissolution rate. The sharp increase in both cation concentration and pH inevitably causes zeolite precipitation. The whole dissolution process illustrated in Figure 3.2 would also be influenced by the dissolved silica concentration. As a matter of fact, it is the interplay between the cation and the silica concentrations that gives rise to oscillatory dissolution of silicate materials on (Wang et al., 2016).

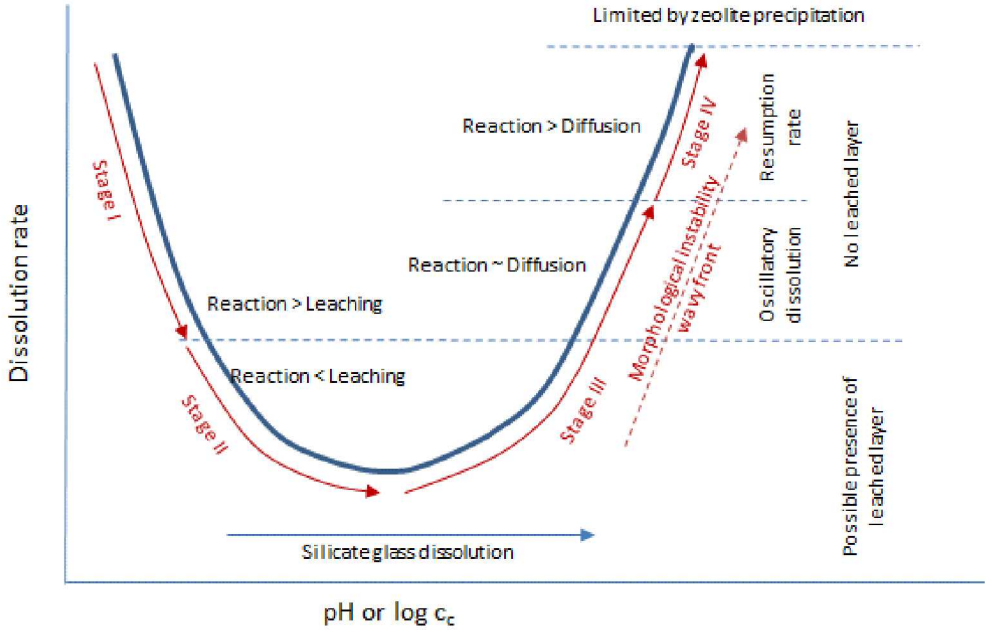

Figure 3.2. Pattern formation and transition in silicate material degradation as driven by the proposed self-organizational mechanism (Wang et al., 2016). In an acid solution (on the left branch of the dissolution curve), the dissolution rate of silica framework is higher than that for cation leaching, and as a result the material would dissolve congruently with no leached layer developed. As the pH of the solution increases, the dissolution rate becomes lower than the leaching rate, leading to the formation a leached surface layer. As the pH continuously rises, the system moves from the left branch to the right branch of the dissolution curve. When the dissolution rate becomes on the same order of magnitude as the mass exchange rate with the bulk solution, oscillatory dissolution may emerge. As the pH of the solution further increases, the dissolution rate eventually overtakes the mass exchange rate, leading to a "runaway" situation with a sharp increase in the cation concentration at the interface as well as in the dissolution rate. The sharp increase in both cation concentration and pH inevitably causes zeolite precipitation. $\Delta pH = pH - IEP$, where IEP is the isoelectric point.

An actual precipitation process of alteration products could be complex. Since we here focus on the morphological instability of a reaction front, for simplicity, we assume that the overall dissolution-precipitation reaction process can stoichiometrically be represented by reaction (3.1):

$$\text{Silicate} \xrightarrow{\text{Cations}} \text{Alteration products} + \alpha_s \text{SiO}_2(\text{aq}) + \alpha_c \text{Cations(aq)} \qquad (3.1)$$

where α_s and α_c are the stoichiometric coefficients of dissolved SiO_2 and cations, respectively, in the overall silicate alteration reaction. Since most of SiO_2 released from the dissolution is re-incorporated into the alteration products, α_s is expected to be relatively small compared to α_c. The cations in reaction (3.1) refer to alkali cations (mainly Na^+) and part of alkaline-earth cations that remain as dissolved cationic species in solution after their release from material degradation. Let's assume that the dissolution of a silicate material starts on a planar reaction front (Fig. 3.3). As the alteration reaction proceeds, the released SiO_2(aq) and cations accumulate at the front. In an actual dissolution process, the reaction front is inevitably subjected to environmental perturbations, resulting in small fluctuations in reaction rate on the dissolution

front. Based on the self-accelerating mechanism proposed above, in a faster dissolution region (labeled "a" in Fig. 3.3), more cations would become released and accumulated, which in turn further accelerates the dissolution at this location. The opposite happens at location "b", where the cations can be relatively easier to diffuse away due to a shorter diffusion distance through the alteration zone (Fig. 3.3). As a result, an environmental perturbation to the initially planar front could be amplified, leading to the formation of a wavy front. As a dissolution front becomes unstable, two other factors would come into play: surface tension, which tries to minimize the surface area of the front and therefore tends to restore the initial planar front, and diffusion, which tends to smooth out the concentration fluctuations on the dissolution surface. The final wave length of a wavy front would then be determined by the interplay between the morphological instability and these countering factors.

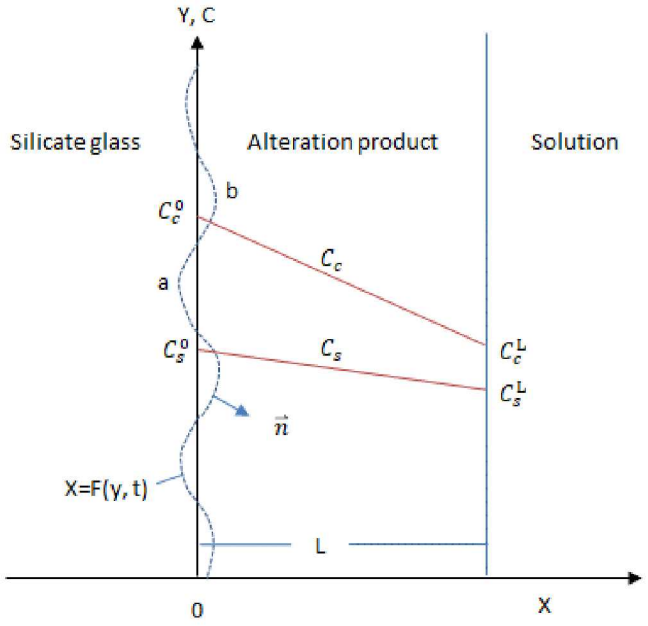

Figure 3.3. Schematic representation of the system for the morphological instability analysis. Vertical axis represents both Y coordinate and the concentrations of dissolved species.

Mathematical formulation: To further elaborate the morphological instability of a dissolution front, let's consider a modeling system as illustrated in Fig. 3.3. The system is divided into two physical domains: the pristine glass and the alteration zone. The dissolved species released from the alteration [reaction (3.1)] communicate with the bulk solution via diffusion through the corrosion products. The chemistry of the bulk solution outside the alteration zone is assumed to remain constant. Also assume that the position of the dissolution front at time t can be described by $X = F(Y, t)$.

Within $F(Y, t) < X < L$, the diffusion of the dissolved species across the alteration zone can be described by:

$$\frac{\partial C_s}{\partial t} = D_s \nabla^2 C_s \qquad (3.2)$$

$$\frac{\partial C_c}{\partial t} = D_c \nabla^2 C_c \qquad (3.3)$$

where X and Y are the spatial coordinates (Fig. 3); t is the time; C_s and C_c are the concentrations of dissolved SiO_2 and cations, respectively; D_s and D_c are the effective diffusion coefficients of the two species, respectively; and L is the thickness of the alteration zone.

At the dissolution front $X = F(Y,t)$, the reaction rate, R, and the diffusion fluxes are related by (Wang and Merino, 1995):

$$\alpha_s R = -D_s \vec{\nabla} C_s \cdot \vec{n} \tag{3.4}$$

$$\alpha_c R = -D_c \vec{\nabla} C_c \cdot \vec{n} \tag{3.5}$$

$$R = k\left[1 + \beta\left(\frac{C_c}{C_{IEP}}\right)^m\right](C_s^e - C_s) \tag{3.6}$$

$$C_s^e = C_s^e(\infty)(1 + \Gamma \mathrm{K}) \tag{3.7}$$

$$\mathrm{K} = -\frac{\partial^2 F}{\partial Y^2} \Big/ \left[1 + \left(\frac{\partial F}{\partial Y}\right)^2\right]^{3/2} \tag{3.8}$$

$$\vec{n} = \left(1, -\frac{\partial F}{\partial Y}\right)^T \Big/ \left[1 + \left(\frac{\partial F}{\partial Y}\right)^2\right]^{1/2} \tag{3.9}$$

where $\vec{n}$ is the normal vector of the dissolution front pointing toward the alteration zone; k is the reaction rate constant; β and m are constants characterizing the catalytic effect of cations on the dissolution rate of silica framework; C_{IEP} is the concentration of cations at the isoelectric point (IEP), at which the dissolution rate reach its minimum (Fig.3.2); C_s^e is the solubility of silica framework on a surface of curvature K; $C_s^e(\infty)$ is the solubility of silica framework on a planar surface; Γ is the surface tension of the interface between the pristine glass and the solution; and superscript "T" in Eq. (3.9) represents the transposition of a vector. Equations (3.7) and (3.8) capture the effect of surface tension on the solubility of silica framework.

At $X = L$, we have:

$$C_s = C_s^L \tag{3.10}$$

$$C_c = C_c^L \tag{3.11}$$

The kinematics of the dissolution front can be described by (Wang and Merino, 1995):

$$\rho \frac{\partial F}{\partial t} = \overline{R} - R\left[1 + \left(\frac{\partial F}{\partial Y}\right)^2\right]^{1/2} \tag{3.12}$$

$$\overline{R} = k\left[1 + \beta\left(\frac{\overline{C}_c}{C_{IEP}}\right)^m\right][C_s^e(\infty) - \overline{C}_s] \tag{3.13}$$

where ρ is the molar density of the silicate material; $\overline{R}$ is the reaction rate evaluated at the planar front; and $\overline{C}_c$ and $\overline{C}_s$ are the concentrations of dissolved SiO_2 and cations at the planar front, respectively.

Linear stability analysis: Equations (3.2) through (3.13) were first scaled, using:

$$x = X/L \qquad y = Y/L \qquad f = F/L \qquad \tau = t/T$$

$$u = C_s/C_s^e(\infty) \qquad v = \frac{C_c}{C_{IEP}} \qquad T = \frac{\rho L}{kC_s^e(\infty)} = \frac{L}{k\epsilon} \qquad r = \frac{T}{\rho L}R$$

$$\gamma = \Gamma/L \qquad \kappa = KL\,, \tag{3.14}$$

to lump model parameters to a minimum set of dimensionless parameters (see Methods):

$$\theta = \frac{kL}{D_s} \qquad \eta = \frac{C_s^e(\infty)D_s}{C_{IEP}D_c} \qquad \epsilon = C_s^e(\infty)/\rho \qquad \sigma = \frac{D_s}{D_c} \tag{3.15}$$

where parameter θ characterizes the relative importance between the reaction rate and the diffusional flux; η represents the diffusional flux ratio between dissolved SiO_2 and cations; ϵ is a smallness parameter characterizing the disparity in molar density between solution and solid, and σ is the ratio of diffusion coefficient between dissolved SiO_2 and cations. Assume the solubility of silica framework on a planar surface, $C_s^e(\infty)$, to be represented by that of amorphous silica (Neeway et al., 2014). The solubility of amorphous silica at 25 °C and neutral pH is $10^{-2.6}$ M (Eikenberg, 1990, fig. 1). This solubility increases with both temperature and pH and could reach ~ 0.5 M at pH 10.5 and 90 °C (Eikenberg, 1990, fig. 9). Given the density (2.52 g/cm^3) of international simple glass (ISG) and the weight percentage of SiO_2 (56.2%) in the glass (Gin et al., 2015), ρ is estimated to be 24 mole SiO_2/dm^3 glass. Considering the self-accelerating mechanism proposed above to be limited to the alkaline branch of the dissolution curve (Fig. 3.2), smallness parameter ϵ is therefore estimated to range approximately from 10^{-4} to 10^{-2}.

In the scaling analysis, we treat the thickness of the alteration zone (L) as a constant. In actual case, L evolves as a material degrades, depending on the relative rates of alteration product removal at the outer rim of alteration products and the dissolution of pristine silicate material at the inner rim. The rate of the former highly depends on specific experimental or environmental conditions. Mathematically, a linear stability analysis would be made much easier if it is performed around a steady state. Therefore, to facilitate the analysis, we treat our system as if it reaches a steady state, called a quasi-steady state, as the thickness of the alteration zone evolves. In other words, we treat L as a model parameter instead of a variable and then study the behavior of the system around a neighborhood of a given L value.

A linear stability analysis of scaled equations (3.2) through (3.13) was performed (see Methods). In the analysis, we first introduce a perturbation of non-dimensional wave number ω to an initially planar reaction front and then determine the growth rate (ζ) of the perturbation as a function of wave number (see Methods):

$$\zeta = \frac{\omega^3\gamma\frac{\partial\bar{r}}{\partial\bar{u}}\Big|_{s=0} - \omega\frac{d\bar{r}}{ds}\Big|_{s=0}}{\omega + \alpha_c\theta\eta\frac{\partial\bar{r}}{\partial\bar{v}}\Big|_{s=0} + \alpha_s\theta\frac{\partial\bar{r}}{\partial\bar{u}}\Big|_{s=0}} \tag{3.16}$$

where $s = x - f(y,\tau)$; $\bar{r}$, $\bar{u}$ and $\bar{v}$ are the scaled reaction rate and concentrations of dissolved SiO_2 and cations, respectively, all evaluated at the planar dissolution front (as indicated by the overbars). Note that all three derivatives in equation (3.16) depend on the concentrations and the concentration gradients of dissolved SiO_2 and cations at the surface. Therefore, as shown in equation (3.16), the stability of the dissolution front is controlled by (1) γ, θ, α_c and α_s, and (2) the concentrations and the concentration gradients of dissolved species at the front. For a silicate glass, assuming the thickness of an alteration zone (L) to be about 1 mm, and using the surface energy (E_s) of ~ 4 J/m^2 (Rimsza et al., 2017) (= 10^{-7} m), γ is estimated to be ~ 10^{-4}, based on the relationship of $\Gamma = 2v_mE_s/R_gT_k$ (see footnote 3 in Wang and Merino, 1995), where v_m is the molar volume of silica (24 cm^3/mol), R_g is the gas constant (8.314 J/mol/K) and T_k

is the absolute temperature (298 K). A typical growth rate ζ of perturbation as a function of wave number ω is shown in Fig. 3.4A. Over a limited range of wave number, the growth rate of perturbation becomes positive, implying that the perturbations with these wave numbers would be amplified and the dissolution front then becomes unstable. The wave number ω_{max} with a maximum growth rate determines the wave length of an actual pattern formed. The wave length ($2\pi L/\omega_{max}$) is estimated to range from a few to hundreds of micrometers, consistent with observations (Putnis, 2015; Hellmann et al., 2015; Ruiz-Agudo et al., 2012; Dohmen et al., 2013; Silvestri et al., 2005; Schal and Anaf, 2016; Geisler et al., 2010). Thus, our model provides a natural explanation for the formation of a highly wavy dissolution front as shown in Fig. 3.1A.

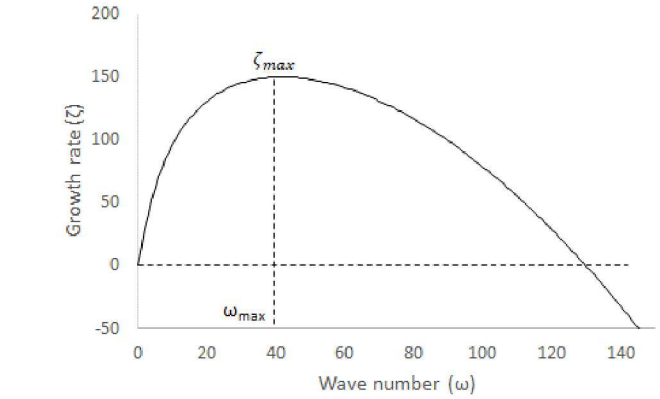

A

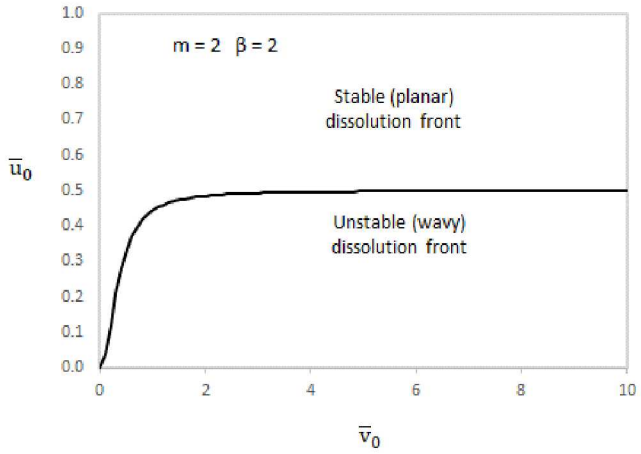

B

Figure 3.4. Linear stability analysis. A. Growth rate of a perturbation to a planar dissolution surface as a function of perturbation wave number ω (=2πL/wavelength). A positive growth rate of a perturbation implies that the perturbation would be amplified and the dissolution front then becomes unstable. The wave number ω_{max} with a maximum growth rate determines the wave length of an actual pattern formed. $\overline{u}_0 = 0.1$, $\overline{v}_0 = 8$ (ref. 21), $\gamma = 10^{-4}$ (see the discussion in the text), $\alpha_s = 0.05$, $\alpha_c = 0.33$, $\theta = 1$, $\eta = 2$, $\beta = 2$, and $m = 2$ (ref. 21). B. Behavior diagram delineating morphological instability in the parameter space of scaled silica and cation concentrations $\overline{u}_0$ and $\overline{v}_0$. A high cation concentration

combined with a low SiO_2(aq) concentration favors morphological instability. For simplicity, the concentrations outside the corrosion product layer are here assumed to be zero.

The behavior of $\zeta(\omega)$ is, to a large extent, controlled by two terms in the numerator of equation (3.16), Since, according to Equation (3.24), $\frac{\partial \overline{r}}{\partial \overline{u}}\Big|_{s=0} = (1+\beta \overline{v}^m)$ and is always negative, to make ζ positive, from Equation (3.23), it is required that

$$\frac{d\overline{r}}{ds}\Big|_{s=0} = \frac{\partial \overline{r}}{\partial \overline{v}}\Big|_{s=0}\frac{\partial \overline{v}}{\partial s}\Big|_{s=0} + \frac{\partial \overline{r}}{\partial \overline{u}}\Big|_{s=0}\frac{\partial \overline{u}}{\partial s}\Big|_{s=0}$$

$$= m\beta \overline{v}^{m-1}(1-\overline{u})\frac{\partial \overline{v}}{\partial s}\Big|_{s=0} - (1+\beta \overline{v}^m)\frac{\partial \overline{u}}{\partial s}\Big|_{s=0} < 0. \qquad (3.17)$$

This is a necessary condition for morphological instability of aqueous dissolution of a silicate material. In other words, a dissolution rate gradient at the front $\frac{d\overline{r}}{ds}\Big|_{s=0}$ is a driving force for morphological instability. A more negative gradient $\frac{d\overline{r}}{ds}\Big|_{s=0}$ would lead to a higher tendency for instability (larger ζ) and consequently a shorter wavelength for pattern formation (larger ω) (e.g., more compacted pitting spacing). Note that this negative rate gradient is solely contributed by a negative gradient of cation concentration, $\frac{\partial \overline{v}}{\partial s}\Big|_{s=0}$. In contrast, as shown in equation (3.17), the silica concentration gradient tends to stabilize a planar front (leads to negative ζ). For fixed concentrations of dissolved species outside the alteration zone, the necessary condition depends only on the concentration of the species at the front: $\frac{\partial \overline{u}}{\partial s}\Big|_{s=0} \approx u_1 - \overline{u}_0$ and $\frac{\partial \overline{v}}{\partial s}\Big|_{s=0} \approx v_1 - \overline{v}_0$. As shown in Fig. 3.4B, a high cation concentration combined with a low SiO_2(aq) concentration favors a morphological instability. As shown in our previous work (Wang et al., 2016), these concentrations may oscillate with time during material degradation, and so does the wavelength of the front. In constructing Figure 3.4B, due to the existence of dual time scales as discussed below, we assume that the steady state concentrations can be approximated linearly across the alteration zone (Figure 3.3).

Interactions of morphological instability with oscillatory dissolution: In scaling equations (3.2) through (3.13), we constrain a typical time scale (T) for morphological instability of a dissolution front such that a significant growth of a perturbation to the front would be observable [see equation (3.14) and Methods]. By a similar argument, to observe a significant variation in a dissolved concentration, from equations (3.19) through (3.20), the relevant time scale must be chosen to be ~ $2\epsilon T$ (= $2L/k$) (see details in Methods), which represents a typical time scale for repetitive banding in alteration products Since ϵ is small (10^{-4} to 10^{-2}) as discussed above, to simplify mathematical manipulations, as a first order approximation, the concentrations of dissolved silica and cations at a dissolution front, $\overline{u}_0$ and $\overline{v}_0$, in equations (3.19) and (3.20) can be treated as steady state variables in the analysis of morphological instability, i.e., $\epsilon \to 0$. As shown previously (Wang et al., 2016), these concentrations can oscillate with time, leading to repetitive bandings in alteration products as generally observed (Schalm and Anaf, 2016). Since the morphological instability depends on $\overline{u}_0$ and $\overline{v}_0$ as the concentrations oscillate at the dissolution front, the wavelength of morphological instability of the front would also oscillate.

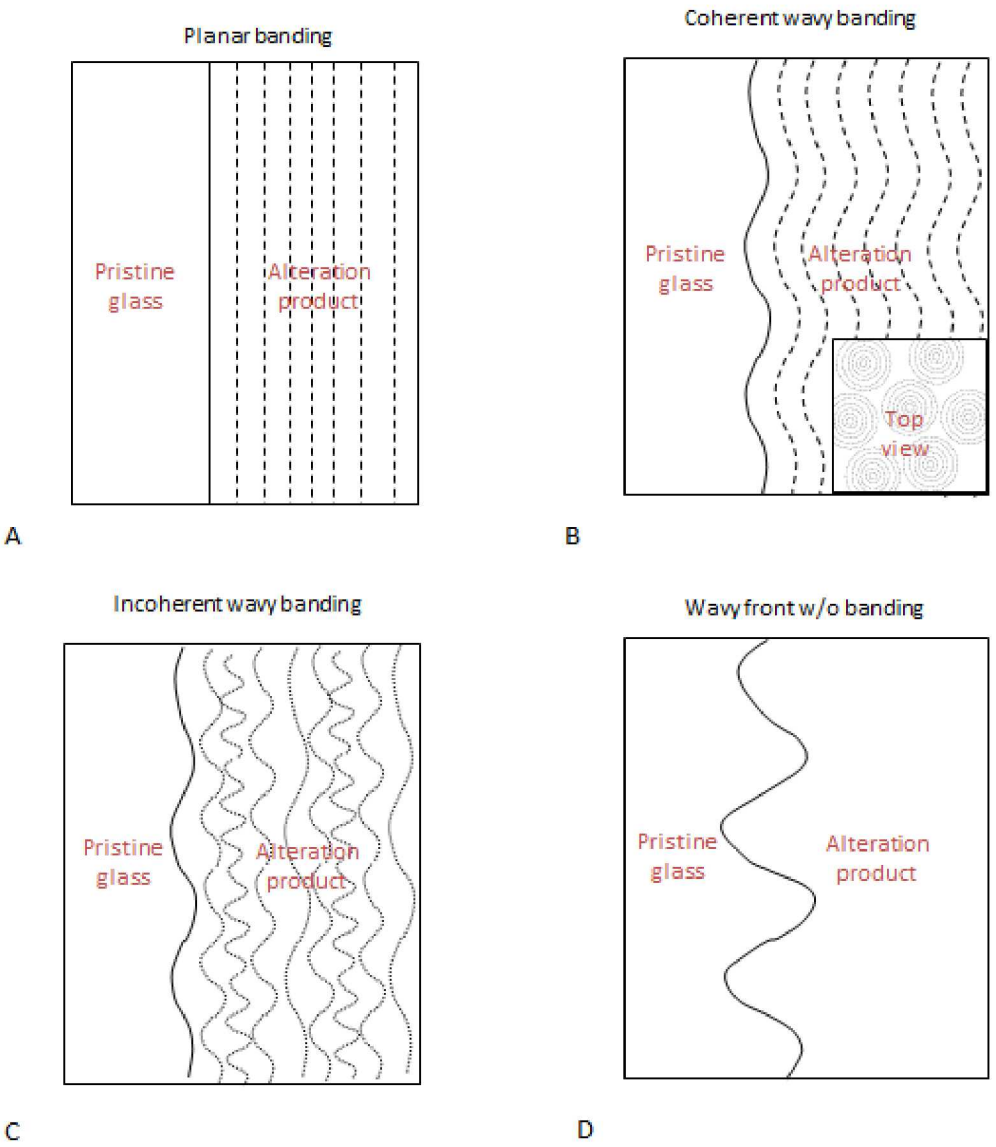

Figure 3.5. Interactions of morphological instability with oscillatory dissolution of silicate materials. A. Formation of coherent wavy bands in a case where the growth of morphological perturbations is much slower than dissolution front advancement or the aqueous species concentrations oscillate within a morphologically stable field. B. Formation of coherent wavy bands in a case where the growth rate of morphological perturbations is comparable with the rate of dissolution front advancement and the concentration oscillations excursion into a morphologically unstable field with narrowly ranged wavelengths. C. Formation of incoherent alteration bands in a case where the growth rate of morphological perturbations is comparable with the rate of dissolution front advancement and the concentration oscillations cross over a morphologically unstable field with a wide range of wavelengths. D. Formation of a pattern with no banding but a wavy dissolution front in a case where a dissolution front may be morphologically unstable but not oscillatory.

As mentioned earlier, in an actual system, a dissolution front is constantly subjected to environmental perturbations. The onset of morphological instability can start at any time once the conditions for the instability, Eq. (3.17), are met. A stagnant solution condition, a high cation content in glass and the formation of a lower permeability alteration layer would all promote morphological instability of a glass dissolution front by enhancing the negative cation concentration gradient at the front. Under certain conditions, the onset of morphological instability could happen at an early time, even at time zero probably, of a dissolution process. Whether a perturbation can develop into an observable wavy front depends the relative rates of perturbation growth and dissolution front advancement. Let's denote the maximum growth rate of perturbation by ζ_{max}, i.e., $\zeta_{max} = \zeta(\omega_{max})$. By trying different combinations of dissolved SiO_2 and cation concentrations ($\overline{u}_0$, $\overline{v}_0$) at a planar dissolution front, we found that ζ_{max} could vary up to ~150 (Fig. 3.4A). A typical time scale for perturbation growth is estimated more accurately to be $T/\zeta_{max} = T'/(2\zeta_{max}\epsilon)$, where T' is a typical time scale for oscillatory dissolution and banding [see Eq. (37) in Methods]. Given $\epsilon = 10^{-4} - 10^{-2}$, we postulate that the growth rate of a morphological perturbation could be small compared to the dissolution front advancement but, in some cases, it can become comparable with the later. For illustration, assume that the morphological instability started at time zero of the dissolution for the sample shown in Figure 3.1A. As the dissolution front advanced, the perturbation of morphological instability became amplified and developed into a wavy front as we see now in the figure. As shown in the figure, over 55 days, an alteration rim of ~ 660 μm thick was developed. The corrosion rate is thus estimated to be ~11 μm/day, which is high as compared to the initial rate of the international simple glass generally reported (~ 1.5 μm/day, Inagaki et al., 2013). This high rate could be attributed to a local accumulation of the cations released from glass dissolution as our model suggests. Given the amplitude of the wavy front (50 – 100 μm) (Fig. 3.1A), we estimate the growth rate of morphological instability to be approximately 1 μm/day, 10 times slower than the rate of dissolution front advancement, which seems consistent with our theoretical estimation.

Consequently, there are four possibilities for the interactions of morphological instability with oscillatory dissolution and therefore for pattern formations. In case 1, the growth of morphological perturbations is much slower than dissolution front advancement or the aqueous species concentrations oscillate within a morphologically stable field (Fig. 3.5A). In this case, only repetitive planar bandings are produced in the alteration zone. In case 2, the growth rate of morphological perturbations is comparable with the rate of dissolution front advancement and the concentration oscillations excursion into a morphologically unstable field with narrowly ranged wavelengths, resulting in a set of coherent wavy bands (Figs. 3.1B and 3.5B). On a view plane parallel to the dissolution front, these wavy bandings can be expressed as concentric growth rings (Dohmen et al., 2013, fig. 7b; Fig. 5B, insert). Obviously, the concentric bands formed as such would not follow a banding spacing law for typical Liesegang rings as observed (Schalm and Anaf, 2016). In case 3, the growth rate of morphological perturbations is comparable with the rate of dissolution front advancement and the concentration oscillations cross over a morphologically unstable field with a wide range of wavelengths, leading to a set of incoherent alteration bands (Fig. 3.5C). The structure within each band could be relatively messy or chaotic, due to a successive juxtaposition of incremental alteration layers with distinct wavelengths (Figs. 3.1C and 3.1D). Finally, since oscillatory dissolution occurs in a limited parameter space (Wang et al., 2016, fig. 4), in case 4, a dissolution front may be morphologically unstable but not oscillatory, which would lead to a pattern with no banding but a wavy dissolution front (Fig. 3.5D), as shown in Fig. 3.1A, if the growth rate of morphological perturbations is comparable with the rate of dissolution front advancement. Depending on the initial and boundary conditions imposed, material dissolution can shift from one regime to another as the dissolution proceeds. For example, as we have shown in our earlier work (Wang et al., 2016), at the beginning of the dissolution, no alteration zone is developed and the dissolution process is overwhelmed by diffusion, resulting in a plain alteration zone with no oscillations. As the alteration zone builds up, the dissolution rate becomes comparable with the diffusion rate, and oscillatory dissolution emerges (Wang et al., 2016, fig. 4A). Since, as mentioned earlier, morphological instability could happen at an early time of a dissolution process. As a result, we would see

a transition from a wavy dissolution front with no banding to a wavy front with bandings, as shown in Figures 3.1B. Since both solution chemistry and mineral precipitation rate vary at a dissolution front, the patterns formed in an alteration zone can be expressed as either chemical or structural contrasts (Dohmen et al., 2013; Schalm and Anaf, 2016; Geisler et al., 2010). Therefore, the self-accelerating mechanism we proposed can provide a systematical prediction of a whole suite of pattern formations observed in silicate material degradation (Dohmen et al., 2013; Silvestri et al., 2005; Schalm and Anaf, 2016; Bianco et al., 2004) (Fig. 3.1).

3.3 Discussions

In silicate glass dissolution experiments, a gap up to 50 μm wide was observed between an alteration zone and a neighboring pristine glass, which was interpreted as an indicator of a former atomically sharp reaction interface (Dohmen et al., 2013). The development of this gap could potentially affect the concentration gradients of dissolved species at the dissolution front. Let's consider the cation concentration gradient, the main driving force for the morphological instability of a silicate material dissolution front. Based on a mass-continuity argument (i.e., the flux remaining the same in the existence of a gap or no gap), we have:

$$\frac{\left(\frac{\partial \bar{v}}{\partial s}\Big|_{s=0}\right)_{gap}}{\left(\frac{\partial \bar{v}}{\partial s}\Big|_{s=0}\right)_{no\ gap}} = \frac{D_c(\phi)}{D_c^0} \approx \phi^2 \tag{3.18}$$

where D_c^0 is the diffusion coefficient of cations in bulk water, and ϕ is the porosity of the alteration products. It is assumed that the tortuosity of the alteration products to be ~ $1/\phi$ (Oelkers, 1996). Assuming $\phi = 0.1$, Equation (3.18) shows that the concentration gradient of cations at the front could be reduced by 100 times if a gap is present, implying that its presence would significantly enhance the stability of the front, consistent with experimental observations (Dohmen et al., 2013). Backscattered electron images show that such gaps were developed in the alteration of borosilicate glasses, and the repetitive alteration bands become less wavy from the outer rim of the alteration zone to the dissolution surface (Dohmen et al., 2013).

The work presented here highlights the importance of local solution chemistry in the alteration of geological materials (Ruiz-Agudo et al., 2016). Water at a reaction front is generally stagnant and its chemistry could significantly deviate from that of advective pore water. Using the chemistry of advective pore water to predict a weathering rate, as usually done currently, may significantly underestimate or overestimate the reaction rate. The fast carbon sequestration rate observed in the injection of CO_2 into a basaltic rock (Matter et al., 2016) may possibly be attributed to the accelerated silicate dissolution due to a local cation accumulation at a dissolution front. Furthermore, reactive surface area of a geological material is an important, but the least constrained, parameter for geochemical modeling. The morphological instability discussed above may add another level of complexity to the quantification of reactive surface area in actual geochemical systems. Due to the morphological instability, the reactive surface area may increase as the reaction proceeds. This is an important factor that needs to be considered in a long-term performance assessment of a silicate material as a waste form for nuclear waste disposal. Depending on experimental conditions, in principle, a local concentration variation could propagate through the alteration layer and therefore could be detected in the bulk solution outside the alteration layer, though the magnitude of the variation in the bulk solution could be much smaller than that at the dissolution front. As a matter of fact, temporal concentration oscillations were observed in the bulk solution in silicate mineral dissolution experiments (Falmon, 1996).

In addition, the proposed morphological instability may offer a sensible explanation for many other textural observations of material degradation in both natural and engineered systems. It is commonly observed that a chemical weathering front can deeply pit into a silicate mineral grain, such as a feldspar crystal, during

mineral alteration (Velbel, 1989; Anand et al., 1985). Similarly, a hemispherical-shape alteration front was observed deeply penetrating into a pristine glass domain (Silvestri et al., 2005). Such textures could be a manifestation of the proposed morphological instability – a localized concentration of cations released from an alteration reaction would further accelerate the reaction. Traditionally, pitting on a mineral surface has been attributed to the preferential dissolution on structural defects (Dove et al., 2005). A problem with this assumption is that the observed reaction front pitting and penetration are generally beyond a typical spatial correlation scale of mineral structural defects. It is particularly problematic for silicate glasses in which no long-range structural correlation exists but there are still μm-scale pits developed on a dissolution surface (Dohmen et al., 2013, fig.5). Therefore, there must be other mechanism in driving mineral dissolution and pitting. Our work suggests that structural defects may play a role as an initial perturbation to a dissolution front but a long-range pitting or a localized reaction front penetration is likely to be driven by the proposed morphological instability. Furthermore, it would be expected that a glass with a higher cation content is more likely to have pitting dissolution. In contrast, since release of borate would counter the pH rise by cations, a glass containing a borate component may stabilize a dissolution front, thus reducing the likelihood for pitting. Therefore, the advancement rate and the morphology of a dissolution front could be engineeringly controlled, if needed, by adjusting glass compositions.

As mentioned earlier, there are two schools of thought on the actual mechanism of silicate material degradation: the surface layer concept (Dran et al., 1986; Doremus, 1975; Petit et al., 1990) and the direct dissolution-precipitation concept (Putnis, 2015; Hellmann et al., 2015; Erui-Agudo et al., 2012; Geisler et al., 2015). The work presented here is not intended to make a judgement one vs. another on the two proposed concepts. As a matter of fact, our model seems general enough to apply to both situations. The point we want to make here is that the complex behaviors observed in silicate material degradation, including the occurrence of a sharp dissolution front or a leached surface layer, are likely to be the manifestations of a single unified mechanism under different circumstances. We have shown that the self-accelerating mechanism we have proposed can provide a consistent explanation for many, if not all, of the key features of the observed silicate material corrosion phenomena. We would also like to point out that the model analysis presented here, together with our earlier work (Wang et al., 2016), is intended to set up a theoretical framework for unraveling complex nonlinear dynamics of silicate material degradation. A full dynamics analysis of the system requires a numerical solution of equations (3.2) through (3.13), with a specified evolution of alteration layer thickness L, on two different time scales for banding and morphological instability. While a linear stability analysis presented here helps clarify the types of dissolution patterns that would form and the conditions for their formation, a full dynamics analysis will provide more detail information about a possible transition from one dissolution pattern to another in a specific dissolution experiment or process. The results of a full dynamics analysis of our model will be presented elsewhere.

3.4 Methods

Scaling: Using scaling factors introduced in equations (3.14), equations (3.2) through (3.13) can be cast into:

Within $f(y,\tau) < x < 1$:

$$\epsilon\theta \frac{\partial u}{\partial \tau} = \nabla^2 u \tag{3.19}$$

$$\epsilon\theta\sigma \frac{\partial v}{\partial \tau} = \nabla^2 v \tag{3.20}$$

At $x = f(y,\tau)$:

$$\alpha_s \theta r = -\vec{\nabla} u \cdot \vec{n} \tag{3.21}$$

$$\alpha_c \theta \eta r = -\vec{\nabla} v \cdot \vec{n} \tag{3.22}$$

$$r = (1 + \beta v^m)(1 + \gamma\kappa - u) \tag{3.23}$$

$$\overline{r} = (1 + \beta \overline{v}^m)(1 - \overline{u}) \tag{3.24}$$

$$\kappa = -\frac{\partial^2 f}{\partial y^2} \Big/ \left[1 + \left(\frac{\partial f}{\partial y}\right)^2\right]^{3/2} \tag{3.25}$$

$$\vec{n} = \left(1, -\frac{\partial f}{\partial y}\right)^T \Big/ \left[1 + \left(\frac{\partial f}{\partial y}\right)^2\right]^{1/2} \tag{3.26}$$

$$\frac{\partial f}{\partial \tau} = \overline{r} - r\left[1 + \left(\frac{\partial f}{\partial y}\right)^2\right]^{1/2} \tag{3.27}$$

At $x = 1$:

$$u = u_1 \qquad v = v_1. \tag{3.28}$$

Repetitive banding: Planar-front solution

For a planar dissolution front ($f = 0$), equations (3.19) through (3.28) are reduced to:

$$\epsilon\theta \frac{\partial \overline{u}}{\partial \tau} = \frac{\partial^2 \overline{u}}{\partial x^2} \tag{3.29}$$

$$\epsilon\theta\sigma \frac{\partial \overline{v}}{\partial \tau} = \frac{\partial^2 \overline{v}}{\partial x^2} \tag{3.30}$$

at $x = 0$:

$$\alpha_s \theta \overline{r} = -\frac{\partial \overline{u}}{\partial x} \tag{3.31}$$

$$\alpha_c \theta \eta \overline{r} = -\frac{\partial \overline{v}}{\partial x} \tag{3.32}$$

$$\overline{r} = (1 + \beta \overline{v}^m)(1 - \overline{u}) \tag{3.33}$$

at $x = 1$:

$$\overline{u} = u_1 \text{ and } \overline{v} = v_1. \tag{3.34}$$

where $\overline{u}$, $\overline{v}$ and $\overline{r}$ are the u, v, and r referred to the planar front. By integrating equations (3.29) and (3.30) over the alteration layer and assuming the concentrations of dissolved silica and cations can be approximated linearly within the alteration product layer ($0 \leq x \leq 1$) (ref. 31), we obtain:

$$\theta \frac{d\overline{u}_0}{d\tau'} = \alpha_s \theta (1 + \beta \overline{v}_0{}^m)(1 - \overline{u}_0) + u_1 - \overline{u}_0 \tag{3.35}$$

$$\theta\sigma\frac{d\bar{v}_0}{d\tau'} = \alpha_s\theta(1+\beta\bar{v}_0{}^m)(1-\bar{u}_0) + v_1 - \bar{v}_0 \tag{3.36}$$

where

$$\tau' = t/T' \text{ and } T' = 2\epsilon T = 2L/k \tag{3.37}$$

And $\bar{u}_0$ and $\bar{v}_0$ represent the $\bar{u}$ and $\bar{v}$ evaluated at the front. The new time scale (T') is chosen such that a significant variation in a dissolved concentration can be observed. As shown in Wang et al. (2016), equations (3.35) and (3.36) can have oscillatory solutions, which are postulated to be responsible for the formation of repetitive bands of alteration products. Therefore, T' is the time scale for material dissolution and banding.

Linearization:

Let $\epsilon \to 0$, and also make a coordinate transformation of $s = x - f(y,\tau)$. Equations (3.19) to (3.28) can then be linearized by introducing a perturbation around a steady state planar solution ($\bar{u}$, $\bar{v}$, $\bar{r}$) (Wang and Merino, 1995):

$$u = \bar{u} + \delta u \; v = \bar{v} + \delta v \; f = \delta f \qquad r = \bar{r} + \delta r \qquad \kappa = \delta\kappa \tag{3.38}$$

We obtain the following linearized equations:

Within $0 < s < 1$:

$$\frac{\partial^2\delta u}{\partial s^2} + \frac{\partial^2\delta u}{\partial y^2} - \frac{\partial\bar{u}}{\partial s}\frac{\partial^2\delta f}{\partial y^2} = 0 \tag{3.39}$$

$$\frac{\partial^2\delta v}{\partial s^2} + \frac{\partial^2\delta v}{\partial y^2} - \frac{\partial\bar{v}}{\partial s}\frac{\partial^2\delta f}{\partial y^2} = 0 \tag{3.40}$$

At $s = 0$:

$$\delta r = -\left(1+\beta\bar{v}_0^m\right)\left(\gamma\frac{\partial^2\delta f}{\partial y^2} + \delta u\right) + m\beta\bar{v}_0^{m-1}(1-\bar{u}_0)\delta v \tag{3.41}$$

$$\alpha_s\theta\delta r = -\frac{\partial\delta u}{\partial s} \tag{3.42}$$

$$\alpha_s\theta\eta\delta r = -\frac{\partial\delta v}{\partial s} \tag{3.43}$$

$$\frac{\partial\delta f}{\partial\tau} = -\delta r \tag{3.44}$$

At $s = 1$:

$$\delta u = \frac{\partial\bar{u}}{\partial s}\delta f \qquad \delta v = \frac{\partial\bar{v}}{\partial s}\delta f \tag{3.45}$$

where $\bar{u}_0$ and $\bar{v}_0$ are the steady state dissolved SiO_2 and cation concentrations at a planar dissolution front.

Here we do not solve the steady state concentrations directly for a planar front. As discussed above (see a detail treatment in Wang and Merino, 2995), due to the existence of dual time scales, the concentrations calculated from the earlier model for oscillatory dissolution (Wang et al., 2016) can be treated as the steady state concentrations for the morphological instability analysis. For simplicity, we further assume that the steady state concentrations can be approximated linearly across the alteration zone (Figure 3.3).

Dispersion equation:

Assume that the linearized equations have a solution in the form of:

$$\delta u = \hat{u}(s)e^{\zeta\tau}\cos(\omega y)$$

$$\delta v = \hat{v}(s)e^{\zeta\tau}\cos(\omega y)$$

$$\delta f = \hat{f}e^{\zeta\tau}\cos(\omega y)$$

$$\delta r = \hat{r}e^{\zeta\tau}\cos(\omega y) \tag{3.46}$$

where $\hat{u}(s)$, $\hat{v}(s)$, $\hat{f}$ and $\hat{r}$ are the infinitesimal amplitudes of perturbations δu, δv, δf, and δr and independent of y and τ. $\hat{f}$ and $\hat{r}$ are also independent of s. We now have:

Within $0 < s < 1$:

$$\frac{d^2\hat{u}}{ds^2} - \omega^2\hat{u} + \omega^2\frac{\partial\overline{u}}{\partial s}\hat{f} = 0 \tag{3.47}$$

$$\frac{d^2\hat{v}}{ds^2} - \omega^2\hat{v} + \omega^2\frac{\partial\overline{v}}{\partial s}\hat{f} = 0 \tag{3.48}$$

At $s = 0$:

$$\hat{r} = -\left(1+\beta\overline{v}_0^m\right)\left(-\gamma\omega^2\hat{f}+\hat{u}\right) + m\beta\overline{v}_0^{m-1}(1-\overline{u}_0)\hat{v} \tag{3.49}$$

$$\alpha_s\theta\hat{r} = -\frac{d\hat{u}}{ds} \tag{3.50}$$

$$\alpha_s\theta\eta\hat{r} = -\frac{d\hat{v}}{ds} \tag{3.51}$$

$$\zeta\hat{f} = -\hat{r} \tag{3.52}$$

At $s = 1$:

$$\hat{u} = \frac{\partial\overline{u}}{\partial s}\hat{f} \qquad \hat{v} = \frac{\partial\overline{v}}{\partial s}\hat{f} \tag{3.53}$$

Equations (3.47-3.48) have a solution in the form of:

$$\hat{u}(s) = d_{11}e^{\omega s} + d_{12}e^{-\omega s} + \frac{\partial\overline{u}}{\partial s}\hat{f} \tag{3.54}$$

$$\hat{v}(s) = d_{21}e^{\omega s} + d_{22}e^{-\omega s} + \frac{\partial\overline{v}}{\partial s}\hat{f} \tag{3.55}$$

where d_{ij} is a constant. Inserting equations (3.54-3.55) into the boundary conditions (3.49-3.53), we obtain a linear set of equations with respect to $\hat{u}(0)$, $\hat{v}(0)$ and $\hat{f}$:

$$\hat{u}(0) - \left[\frac{\alpha_s\theta\zeta\left(e^{2\omega}-1\right)}{\omega\left(e^{2\omega}+1\right)} + \left.\frac{\partial\overline{u}}{\partial s}\right|_{s=0}\right]\hat{f} = 0 \tag{3.56}$$

$$\hat{v}(0) - \left[\frac{\alpha_s\theta\zeta\left(e^{2\omega}-1\right)}{\omega\left(e^{2\omega}+1\right)} + \left.\frac{\partial\overline{v}}{\partial s}\right|_{s=0}\right]\hat{f} = 0 \tag{3.57}$$

$$\zeta\hat{f} - \left(1+\beta\overline{v}_0^m\right)\left(-\gamma\omega^2\hat{f}+\hat{u}\right) + m\beta\overline{v}_0^{m-1}\left(1-\overline{u}_0\right)\hat{v} = 0 \tag{3.58}$$

For equations (3.56-3.58) to have a nontrivial solution, the determinant of the coefficient matrix must be zero:

$$\begin{vmatrix} 1 & 0 & -\frac{\alpha_s\theta\zeta\left(e^{2\omega}-1\right)}{\omega\left(e^{2\omega}-1\right)} - \left.\frac{\partial\overline{u}}{\partial s}\right|_{s=0} \\ 0 & 1 & -\frac{\alpha_s\theta\zeta\left(e^{2\omega}-1\right)}{\omega\left(e^{2\omega}-1\right)} - \left.\frac{\partial\overline{v}}{\partial s}\right|_{s=0} \\ -\left(1+\beta\overline{v}_0^m\right) & m\beta\overline{v}_0^{m-1}\left(1-\overline{u}_0\right) & \zeta+\gamma\omega^2\left(1+\beta\overline{v}_0^m\right) \end{vmatrix} = 0 \tag{3.59}$$

From equation (59), we obtain:

$$\zeta = \frac{\omega^3\gamma\left.\frac{\partial\overline{r}}{\partial\overline{u}}\right|_{s=0} - \omega\left.\frac{d\overline{r}}{ds}\right|_{s=0}}{\omega + \alpha_c\theta\eta\left.\frac{e^{2\omega}-1}{e^{2\omega}+1}\frac{\partial\overline{r}}{\partial\overline{v}}\right|_{s=0} + \alpha_s\theta\left.\frac{e^{2\omega}-1}{e^{2\omega}+1}\frac{\partial\overline{r}}{\partial\overline{u}}\right|_{s=0}} \tag{3.60}$$

A planar front corresponds to $\omega = 0$. To observe a morphological instability, the wavelength of a wavy front must be smaller than the typical scale of a system, that is, $\frac{2\pi}{\omega} < 1$. Since $\omega > 2\pi$, $\frac{e^{2\omega}-1}{e^{2\omega}+1} \sim 1$, and we then obtain equation (3.16).

List of symbols:

A_w	Amplitude of a wavy front (cm)
C_{IEP}	Concentration of cations at the isoelectric point (IEP) (Figure 3.2) (mol/cm^3)
C_s, C_c	Concentrations of dissolved SiO_2 and cations (mol/cm^3)
C_s^e	Solubility of silica framework on a surface of curvature K (cm^{-1})
$C_s^e(\infty)$	Solubility of silica framework on a planar surface (Equation (3.7)] (mol/cm^3)
C_s^L, C_c^L	Concentrations of dissolved SiO_2 and cations outside an alteration zone (mol/cm^3)
$\overline{C}_c$, $\overline{C}_s$	Concentrations of dissolved SiO_2 and cations at a planar front (mol/cm^3)
D_s, D_c	Effective diffusion coefficients of dissolved SiO_2 and cations (cm^2/s)
D_c^0	Diffusion coefficient of cations in bulk water (cm^2/s)
E_s	Surface energy (J/cm^2)
F(Y,t)	Horizontal position of a dissolution front (cm)
f	Scaled horizontal position of a dissolution front [Equation (3.14)]
K	Curvature of a dissolution front (Equation (3.8)] (m^{-1})
k	Reaction rate constant of Reaction (3.1) (cm/s)
L	Thickness of an alteration zone (cm)

m	Reaction order with respect to cations [Equation (3.6)]
$\vec{n}$	Normal vector of a dissolution front pointing toward an alteration zone
R	Reaction rate (mol/cm^2/s)
r	Scaled reaction rate [Equation (3.14)]
$\overline{r}$	Scaled reaction rate evaluated at a planar dissolution front
$\overline{R}$	Reaction rate evaluated at a planar front (mol/cm^2/s)
R_g	Gas constant (J/mol/K)
s	Scaled horizontal coordinate of a dissolution front in a Lagrangian coordinate system
T	Typical time scale for morphological instability [Equation (3.14)] (s)
T'	Typical time scale for oscillatory dissolution and banding [Equation (3.37)] (s)
T_k	Absolute temperature (K)
t	Time (s)
u, v	Scaled concentrations of dissolved SiO_2 and cations [Equation (3.14)]
$\overline{u}$, $\overline{v}$	Scaled concentrations of dissolved SiO_2 and cations evaluated for a planar dissolution front case
$\overline{u}_0$, $\overline{v}_0$	Scaled concentrations of dissolved SiO_2 and cations evaluated at a planar dissolution front
u_1, v_1	Scaled concentrations of dissolved SiO_2 and cations outside an alteration zone (Equation (3.28)]
$\hat{u}$, $\hat{v}$, $\hat{f}$, $\hat{r}$	Amplitudes of perturbations δu, δv, δf and δr
v_m	Molar volume of silica
X, Y	Spatial coordinates (Figure 3.3) (cm)
x, y	Scaled spatial coordinates
α_s, α_c	Stoichiometric coefficients of dissolved SiO_2 and cations [Reaction (3.1)]
β	Constant characterizing the catalytic effect of cations [Equation (3.6)]
Γ	Surface tension of the interface between a pristine glass and a solution (Equation (3.8)] (cm)
γ	Scaled surface tension of [Equation (3.14)]
ζ	Growth rate of a perturbation to a planar dissolution front [Equation (3.16)]
ζ_{max}	Maximum growth rate of a perturbation to a planar dissolution front (Figure 3.4A)
η	Dimensionless parameter representing diffusional flux ratio between dissolved SiO_2 and cations [Equation (3.15)]
θ	Dimensionless parameter charactering relative importance between reaction and diffusion [Equation (3.15)]
κ	Scaled surface curvature [Equation (3.14)]
ρ	Molar density of a silicate material (Equation (3.12)] (g/mol)
τ	Scaled time for morphological instability [Equation (3.14)]
τ	Scale time for oscillatory dissolution [Equation (3.37)]
ω	Wave vector of a perturbation (2πL/wave length)
ϵ	Smallness parameter characterizing the disparity in molar density between solution and solid
δu, δv, δf, δr, $\delta\kappa$	Perturbations of u, v, f, r, and κ
ϕ	Porosity of alteration layer (Equation (3.18)]

3.5 References

Anand, R. R., Gilkes, R. J., Armitage, T. M., Hillyer, J. W. Feldspar weathering in lateritic saprolite. *Clays and Clay Minerals*, **33**, 31-43 (1985).

Berner, R. A., Kothavala, Z. GEOCARB III: A revised model of atmospheric CO_2 over Phanerozoic time. *Am. J. Sci.* **301**, 182-204 (2001).

Bianco, B. D., Bertoncello, R., Milanese, L., Barison, S. Glasses on the seabed: surface study of chemical corrosion in sunken Roman glasses. *J. Non-Crystalline Solids* **343**, 91-100 (2004).

Brady, P. V. The effect of silicate weathering on global temperature and atmospheric CO_2. *J. Geophysical Lett*. **96**, 18101-18106 (1991).

Cailleteau, C. et al. Insight into silicate-glass corrosion mechanisms. *Nature Materials* **7**, 978-983 (2008).

Dohmen, L. et al. Pattern formation in silicate glass corrosion zones. *Int. J. Appl. Glass Sci.* **4**, 357-370 (2013).

Domone, P., Illston, J. *Construction Materials* (Spon Press, New York, 2010).

Doremus, R. H. Interdiffusion of hydrogen and alkali ions in a glass surface. *J. Non-Crystalline Solids* **19**, 137-144 (1975).

Petit, J.-C. et al. Paccagnella, A. Hydrated-layer formation during dissolution of complex silicate glasses and minerals. *Geochim. Cosmochim. Acta* **54**, 1941-1955 (1990).

Dove, M. P., Han, N., De Yoreo, J. J. Mechanism of classical crystal growth theory explain quartz and silicate dissolution behavior. *PNAS* **102**, 15357-15362 (2005).

Dran, J.-C., Petit, J.-C., Brousse, C. Mechanism of aqueous dissolution of silicate glasses yield by fission tracks. *Nature* **319**, 485-487 (1986).

Eikenberg, J. *On the Problem of Silica Solubility at High pH*. Paul Scherrer Institut, PSI-Bericht Nr. 74 (1990).

Falmon, J. Oscillatory silicon and aluminum aqueous concentrations during experimental aluminosilicate weathering. *Geochim. Cosmochim. Acta* **60**, 2901-2907 (1996).

Geisler, T. et al. Aqueous corrosion of borosilicate glass under acidic conditions: A new corrosion mechanism. *J. Non-Crystalline Solids* **356**, 1458-1465 (2010).

Geisler, T. et al. The mechanism of borosilicate glass corrosion revisited. *Geochim. Cosmochim. Acta* **158**, 112-129 (2015).

Gin, S. et al. Dynamics of self-reorganization explains passivation of silicate glass. *Nature Communications* **9**, 2169 (2018).

Gin, S. et al. Origin and consequences of silicate glass passivation by surface layers. *Nature Communications* **6**, 6360 (2015).

Gin, S. Open scientific questions about nuclear glass corrosion. *Procedia Materials Sci.* **7**, 163-171 (2014).

Hellmann, R. et al. Nanometre-scale evidence for interfacial dissolution-reprecipitation control of silicate glass corrosion. *Nature Materials* **14**, 307-311 (2015)

Hin, T. S. *Engineering Materials for Biomedical Applications* (World Scientific Publishing Co, New Jersey, 2004).

Inagaki, Y., Kikunaga, T., Idemitsu, K., Arima, T. Initial dissolution rate of the international simple glass as a function of pH and temperature measured using microchannel flow-through test method. *Int. J. Appl. Glass Sci*. **4**, 317-327 (2013).

Kulprathipanja, S. (ed.) *Zeolites in Industrial Separation and Catalysis* (Wiley-VCH, Weinheim, 2010).

Matter, J. M. et al. Rapid carbon mineralization for permanent disposal of anthropogenic carbon dioxide emissions. *Science* 352, 1312-1414 (2016).

Matter, J. M., Kelemen, P. B. Permanent storage of carbon dioxide in geological reservoirs by mineral carbonation. *Nature Geoscience* **2**, 837-841 (2009).

Murata, H. *Handbook of Optical Fibers and Cables* (Marcel Dekker, New York, 1996).

Neeway, J. J., Ryan, J. V., Pierce, E. M., Qafoku, N. P., Freedman, V. L. *A Strategy to Conduct an Analysis of the Long-Term Performance of Low-Activity Waste Glass in a Shallow Subsurface Disposal System at Hanford*. Pacific Northwest National Laboratory, PNNL-23503 (2014).

Oelkers, E. H. Physical and chemical properties of rocks and fluids for chemical mass transport calculations. *Reviews in Mineralogy* **34**, 131-191 (1996).

Putnis, A. Sharpened interface. *Nature Materials* **14**, 261-261 (2015).

Rimstidt, J. D. Rate equations for sodium catalyzed quartz dissolution. *Geochim. Cosmochim. Acta* **167**, 195-204 (2015).

Rimsza, J. M., Jones, R. E., Criscenti, L. J. Surface structure and stability of partially hydroxylated silica surfaces. *Langmuir*, **22**, 3882-3891 (2017).

Rozalén, M. L. et al. Experimental study of the effect of pH on the kinetics of montmorillonite dissolution at 25 ºC. *Geochim. Cosmochim. Acta* **72**, 4224-4253 (2008).

Ruiz-Agudo, E., Putnis, C. V., Rodriquez-Navarro, C., Putnis, A. Mechanism of leached layer formation during chemical weathering of silicate minerals. *Geology* **40**, 947-950 (2012).

Ruiz-Agudo, E., Rodriquez-Navarro, C., Putnis, A. Control of silicate weathering by interface-coupled dissolution-precipitation processes at the mineral-solution interface. *Geology* **77**, 567-570 (2016).

Schalm, O., Anaf. W. Laminated altered layers in historical glass: Density variations of silica nanoparticle random packings as explanation for the observed lamellae. *J. Non-Crystalline Solids* **442**, 1-16 (2016).

Sekerka, R. F. Morphological instability. In: Hartman, P. editor, *Crystal Growth: An introduction* (North-Holland, Amsterdam, 1973), p. 403-443.

Silvestri, A., Molin, G., Salviulo, G. Archaeloogical glass alteration products in marine and land-based environments: morphological, chemical and microtextural characterization. *J. Non-Crystalline Solids* **351**, 1338-1349 (2005).

Skorina, T., Allanore, A. Aqueous alteration of potassium-bearing aluminosilicate minerals: from mechanism to processing. *Green Chem.* **17**, 2123-2136 (2015).

Strachan, D. M. et al. The characterization and testing of candidate immobilization forms for the disposal of plutonium. *Waste Management'98 Conf. Proc*. Tucson, AZ (1998).

Velbel, M. A. Weathering of hornblende to ferruginous products by a dissolution-reprecipitation

Wang, Y., Jove-Colon, C. F., Kuhlman, K. L. Nonlinear dynamics and instability of aqueous dissolution of silicate glasses and minerals. *Scientific Reports* **6**, 30256 (2016).

Wang, Y., Merino, E. Origin of fibrosity and banding in agates from flood basalts. *Am. J. Sci.* **295**, 49-77 (1995).

White, A. F., Brantley, S. L. The effect of time on the weathering of silicate minerals: why do weathering rates differ in the laboratory and field? *Chem. Geology* **2002**, 479-506 (2003).

Wolery, W. G., Tester, J. W., Grigsby, C. O. Quartz dissolution kinetics from 100-200 ºC as a function of pH and ionic strength. *AIChE J.* **42**, 3442-3457 (1996).

4. THERMODYNAMIC DATABASE DEVELOPMENT AND IDENTIFICATION OF ACTINIDE SEQUESTRATION IN CORROSION PRODUCTS

4.1 Introduction

This section summarizes research conducted at Lawrence Livermore National Laboratory (LLNL) within the Crystalline International Collaborations Activity. The activity is focused on our long-term commitment to engaging our partners in international nuclear waste repository research. This includes participation in the actinide sequestration in steel corrosion products, Nuclear Energy Agency (NEA) Thermochemical Database Project, thermodynamic database (TDB) collaborations, and surface complexation model international collaborations.

LLNL is supporting the overall objectives of the Disposal Research Crystalline International Collaborations R&D control account. The objective of this control account is to advance our understanding of long-term disposal of spent fuel in crystalline rocks (including both granitic and metamorphic rocks) and to develop necessary experimental and computational capabilities to evaluate various disposal concepts in such media. Specific tasks included in the FY18 effort include the following:

- Engagement with the NEA TDB project through the support of Dr. Atkins-Duffin as the SFWST representative for international thermodynamic database development effort. This effort ensures that US Geologic Disposal Safety Assessment (GDSA) model efforts are aligned with internationally accepted practices for repository performance assessment calculations.
- Collaboration with HZDR thermodynamic and sorption database development groups in support of the database needs of the SFWST program
- Thermodynamic database development in support of SFWST with particular focus on updating the thermodynamic database to be used for evaluating the mineralogic and geochemical evolution of near-field and far-field repository conditions.
- Investigating the role of steel corrosion on radionuclide sequestration and improved prediction of repository performance. This includes engaging with collaborators at the ESRF and SSRL synchrotron facilities to investigate actinide incorporation into oxide phases.

In FY18, LLNL continued their efforts in data collection and model development in support of the SFWST program. In particular, the research focused on identification, quantification, and parameterization of processes relevant for the evaluation of the performance of various repository scenarios under investigation by the SFWST program. Ongoing efforts funded in late FY18 under the Argillite Disposal, Argillite International Collaborations, and Crystalline Disposal work packages are not included in this summary. However, the scope associated with these efforts is reviewed under Ongoing FY18/FY19 Efforts at the end of this report.

Our particular interest in radionuclide sequestration by corrosion products stems from (1) the potential for this process to significantly inhibit radionuclide release during canister breaching and (2) from the absence of such processes in most repository performance assessments. Discussions with James Jerden (Argonne National Laboratory) suggest that a model of radionuclide incorporation can be added to the waste package cell of the GDSA model and may lead to a reduction in the source term of mobile radionuclides. Steel corrosion rates have been implemented within the spent fuel matrix degradation process model but have not yet been implemented into GDSA. Results from an experimental and modeling study of radionuclide partitioning into steel corrosion products will facilitate the incorporation of this process into the GDSA as the steel corrosion model is implemented.

LLNL evaluated this process from both an experimental and modeling perspective. Experimentally, LLNL has been in the process of developing methodologies to grow various iron oxides phases (goethite, hematite, magnetite) in the presence of radionuclides. We performed a small number of binary (RN-mineral) coprecipitation experiments to test radionuclide (Pu, Am, Np, and U) partitioning. Experiments are attempting to quantify coprecipitation partitioning and also examine the effects of aging and the potential iron oxide recrystallization effects associated with the presence of reduced iron (i.e. Fe(II)).

4.2. Nuclear Energy Agency Thermochemical Database Program

4.2.1 History of Project

The NEA Thermochemical Database Program was conceived of and initiated with the goal to: 1) make available a comprehensive, internally consistent, internationally recognized database of selected chemical elements; 2) meet the specialized modeling requirements for safety assessments of radioactive waste and, and; 3) prioritize the critical review of relevant data for inorganic compounds and complexes containing actinides. Data from other elements present in radioactive waste are also critically reviewed as well as compounds and complexes of the previously considered elements with selected organic ligands.

The objective of the Program is to produce a database that contains data for all the elements of interest in radioactive waste disposal systems; document why and how the data are selected; give recommendations based on original experimental data, rather than compilation and estimates; document the sources of experimental data; provide an internally consistent thermodynamic parameters, and treat solids and aqueous species of the elements of interest for nuclear storage performance assessment calculations.

The qualification of existing data is conducted using documented Guidelines which include several components. A Technical Review is conducted by subject matter experts who critically review experimentally-determined literature data; reanalyze the data as necessary; and select data for inclusion in the database. Upon completion of the Technical Review, a Peer Review is undertaken. A second, independent panel of reviewers ensure that the technical reviewers followed the review Guidelines. A Comment Resolution component ensures that the Technical Reviewers address the comments made by the Peer Reviewers. At this time the volume is readied for final publication.

4.2.2 History of Phases

Phase I of the NEA-TDB program was conducted between 1984 and 1998. Initial review volumes included Uranium, Americium, Technetium, Neptunium/Plutonium.

Phase II of the NEA-TDB program updated all the actinide volumes. The update is contained in a single volume. Added in this phase were Nickel, Selenium, Zirconium, and the compounds and complexes of the reviewed elements with selected organic ligands - EDTA, ISA, oxalate, and citrate. The Program also conducted a workshop, “The Use of Thermodynamics Databases in Performance Assessment.” The phase ran from 1998-2003.

Phase III of the NEA-TDB program saw the introduction of a second product, State-of-the-Art reports. The first such report covered solid solutions of interest to nuclear waste management. Thorium, Iron (part I), and Tin volumes were added to the published collection.

Phase IV of the NEA-TDB program, conducted from 2008-2014, started the second portion of the Iron review; review of Molydenum, and review of Auxiliary Data which includes species and compounds

necessary to describe aqueous chemistry of Aluminum and Silicon, data on inorganic species and compounds of elements such as Iodine, Boron, Magnesium, Calcium, Strontium, and Barium.

Phase V of the NEA-TDB program, the currently active phase, took on a second update to actinide and fission product volumes, and two State-of-the-Art reviews - Cement Minerals and High Ionic Strength Aqueous Systems. The design and development of a new TDB electronic database that is compatible with PHREEQC was undertaken.

The current status of the program and the associated reviews are:

- Iron, part 2 - The Peer Review is in process. Publication of the volume is anticipated at the end of 2018.
- Molybdenum - The Technical Review team required restructuring and reassignment of tasks. This was completed and the Peer Review draft is being compiled. The anticipated publication of this volume is early 2019 following the Peer Review and Comment Resolution processes.
- Auxiliary Compounds – The Peer Review draft is complete and process in its early stages. Following Comment Resolution, a publication date of early 2019 is planned.
- Second update of Actinides and Fission Products - The Peer Review of the sections on the individual elements are complete and the volume is in the Comment Resolution phase. Publication is anticipated by the end of 2018.
- State-of-the-Art report on Cement Materials - The Technical Review is in process with an expected completion date in mid- to late 2018. Expected publication is in 2019.
- State-of-the-Art report on High-Ionic Strength Solutions - The Technical Review is in process with an expected completion date in mid- to late 2018. Expected publication is in 2019.
- The new electronic database is complete and was made available to the public in June 2018.

Three workshops have been planned to increase awareness, particularly in students and early career staff, on topics of interest in modeling interactions of actinide and fission products with geochemical media. The workshops are being conducted at the ISSP-18 conference in July 2018 (Tours, France); Goldschmidt 2018 in August 2018 (Boston USA), and; The 256th American Chemical Society meeting in August 2018 (Boston USA).

4.2.3 Preparing for Phase VI

In April 2017 the NEA convened a meeting for interested parties to discuss options for the work plan in Phase VI. Attendees included not only representatives from Phase V members but also included other organizations with interests in actinides and fission product interactions with geologic media. Discussions focused on benefits of continuation of the Program, contents of future work scope, organizational issues, and funding options. Cindy Atkins-Duffin, Mavrik Zavarin, and Don Reed participated for the United States. They Program Management Board convened in November 2017 and took the decision to continue the Program.

Preparing the Program for a new Phase requires reviewing and editing the Framework Agreement. This document is the Agreement between the NEA and the various national programs participating in the Program. The NEA undertakes their projects in one of two formats - internally funded, directed, and executed or; membership funded, directed, and executed. In the past, the NEA-TDB Program has functioned as a hybrid of these two project types - the work scope was membership funded with the NEA providing a Program Coordinator. Management of the execution of the work was joint between the

Program Coordinator and the Executive Group. Entering Phase VI requires the TDB Program to restructure to comport with NEA By-Laws and function in one of the two governance models. In Phase VI, the Program Coordinator will be funded by the membership, significantly altering the amount of work that can be undertaken. It is anticipated the Agreement will be signed and enter into force in the near future. It is anticipated at this time that COVRA (Dutch nuclear waste processing and storage company) will join the Program as a paying member.

The work scope for Phase VI will include the following review volumes:

- Update of the Organic ligand review
- Lanthanides, and
- Weak Complexes
- State-of-the-Art report on High Temperature data.

The current plan is for Phase VI to enter into force in November 2018 when the next Program Management Board convenes.

4.3. Corrosion: Plutonium Interactions with Iron Minerals

For the long-term performance assessment of nuclear waste repositories, understanding the interactions of actinide ions with mineral surfaces is imperative. Iron (oxy)hydroxides are common soil minerals and are present in intermediate level radioactive waste (Marshall et al., 2014). In addition, they also form as corrosion products of steel which is a primary structural component of nuclear repositories and of waste canister materials (Music et al., 1993). Studies have shown that Pu(IV) has high sorption affinity for the goethite and hematite surface at circumneutral pH (Sanchez et al., 1985; Zhao et al., 2016; Romanchuk et al., 2011). At higher concentration, Pu(IV) colloids form on the goethite surface may undergo a lattice distortion, due to epitaxial growth, which leads to a stronger surface binding compared to other mineral phases, such as quartz (Powell et al., 2011). Gaining a detailed understanding of the interactions between iron oxide and plutonium is key in predicting the long-term stability and mobility of plutonium in the natural environment.

The hydrous ferric oxide, ferrihydrite (FH), is a common, poorly crystalline, metastable early product of both biotic and abiotic precipitation of iron, and is a precursor to other more crystalline iron oxides such as hematite (Fe_2O_3) and goethite (FeOOH). Ferrihydrite crystallizes to hematite or goethite depending upon solution conditions, pH, ionic strength and temperature (Schwertmann and Conell, 2000). The hematite and goethite formation process begins with ferrihydrite particle aggregation (Fischer and Schwertmann, 1975), followed by recrystallization within the aggregate via dissolution and reprecipitation processes that occur at the nanoscale (Combes et al., 1990). During this process, adsorbed plutonium has the potential to become incorporated into the structure of hematite or goethite. Co-precipitation (or structural incorporation) of co-contaminants into mineral structures most likely involves substitution of the cation site in the mineral or perhaps interstitial incorporation. Crystal chemical constraints that affect incorporation include: i) the cation coordination environment, ii) the cation charge and, iii) a charge balancing mechanism. It has been shown that goethite and hematite are able to accommodate various impurities into their structure including Si, Ti, Mn, Ni and U(VI) (Marshall et al., 2014; Liu et al., 2012). Coprecipitation of plutonium into stable mineral phases, such as iron (oxy)hydroxides, offers a pathway for sequestration with the potential for long term mobilization.

In FY17 we synthesized goethite (FeOOH) and hematite (Fe_2O_3) with varying amounts of plutonium (300, 1000 and 3000 ppm) from a poorly crystalline ferrihydrite (FH) precursor. The initial FH material was

obtained according to the following methodologies – note that the main difference within the two synthetic pathways is the timing of plutonium addition.

- *Method A* or *coprecipitation into FH*: 1 M $FeNO_3.9H_2O$ solution was mixed with Pu(IV), ferrihydrite was then formed by slow addition of 5 M KOH (for goethite) or 1 M KOH (for hematite);
- *Method B* or *sorption to FH method*: a KOH (5M or 1M) was slowly added to a 1M $FeNO_3.9H_2O$ solution to form ferrihydrite, Pu(IV) was then sorbed onto the ferrihydrite precipitate.

Data reported in FY 17 showed Pu strongly partitions in the ferrihydrite and goethite solids compared to hematite. In FY18 we focused our efforts in furthering our understanding of Pu-ferrihydrite/goethite interaction through spectroscopy and chemical characterization. The focus of this effort was to understand how the timing of Pu addition (coprecipitation -Method A- or sorption- Method B) to ferrihydrite as precursor to the more crystalline mineral goethite, affect the final form of plutonium associated with these minerals.

4.3.1 X-ray absorption spectroscopy

Samples FH-A-3000, FH-B 3000, GA-3000 and GB-3000 were selected for x-ray adsorption spectroscopy (XAS) analysis at the Stanford Synchrotron Radiation Light Source (SSRL). In general, the XANES (X-ray absorption near edge structure) region of the XAS spectra provides information on oxidation state changes in the samples based on comparisons to standard reference materials. The EXAFS (extended X-ray absorption fine structure) region is fit to determine the nearby neighbors and their distances from the plutonium site. The XANES region of the spectra confirmed that in all our samples, plutonium is present in the tetravalent oxidation state.

X-ray absorption spectroscopy of Ferrihydrite:

The EXAFS spectra of samples FH-A-3000 and FH-B-3000 are different, suggesting that plutonium may have different coordination environments in the samples (Figure 4.1). In FH-A-3000, plutonium is coordinated by six oxygen atoms at 2.29Å in the first coordination sphere (Table 4.1). The FH-B-3000 spectrum could be fit to the model structure of PuO_2, with four plutonium atoms at a distance of 3.82Å from each other and ~8 Pu-O distances at 2.3 Å (Table 4.2). This structural feature indicates that plutonium is likely present as a surface precipitate on sample FH-B-3000. The FH-A-3000 spectrum could not be fit with a PuO_2 model. These results suggest that the timing of Pu addition in the synthetic procedures (Method A or B) affects the final form of plutonium in the ferrihydrite structure. Importantly, more reduced phases of iron oxide are likely to form during cannister breaching and steel corrosion (e.g. magnetite) in a deep subsurface nuclear waste repository. Nevertheless, the ferrihydrite results clearly indicate that the association of Pu with corrosion products will depend on the timing of Pu release and corrosion product formation.

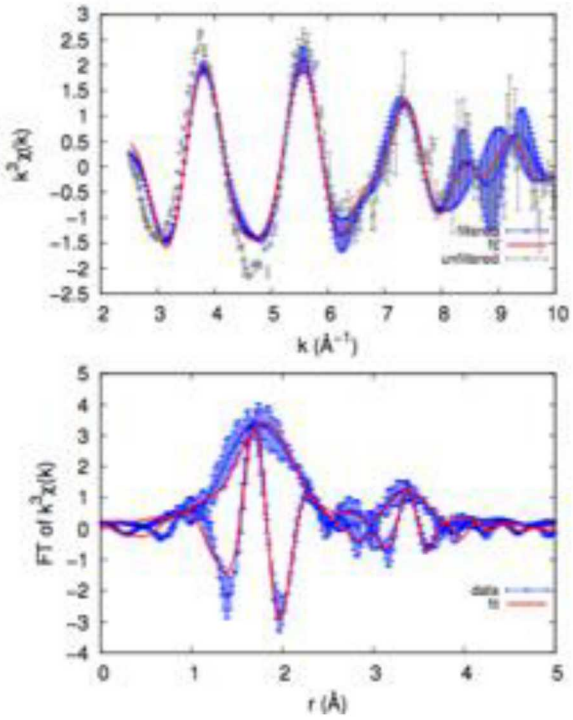

Figure 4.1. FH-A-3000 EXAFS spectra (top) and Fourier transform in R (Å) (bottom).

Table 4.1. Fit parameters for EXAFS spectrum of FH-A-3000.

	Sample **A2**		
	N	σ^2(Å^2)	R(Å)
Pu_O_2.3678.f10	5.5(*)	0.0176(3)	2.29(2)
Pu_O_3.7450.f10	3(2)	0.0037(2)	3.91(2)
ΔE_0		-11.9(14)	
S_0^2		1.000	
R(%)		14.82	

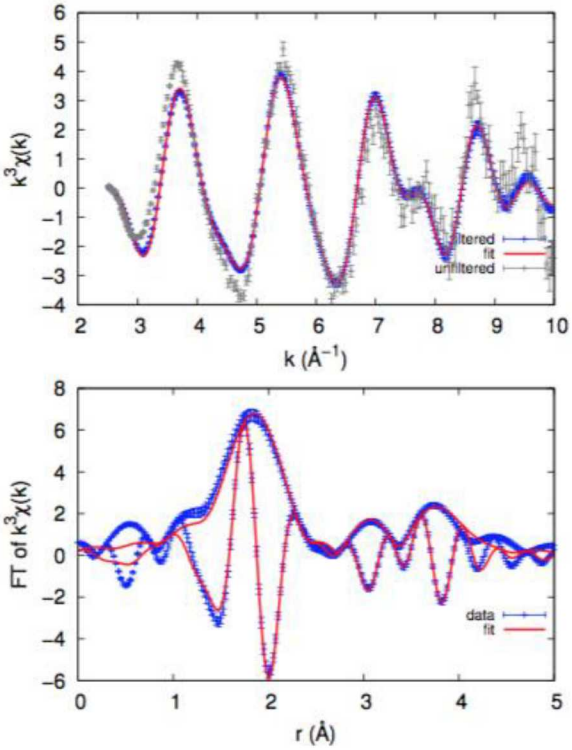

Figure 4.2. FH-B-3000 - EXAFS spectra (top) and Fourier transform R (Å) (bottom).

Table 4.2. Fit parameters for EXAFS spectrum of FH-B-3000.

	Sample **B2**		
	N	σ^2(Å^2)	R(Å)
Pu_O_2.3678.f10	7.7(9)	0.0113(1)	2.324(8)
Pu_Fe_3.4312.f10	3(3)	0.015(1)	3.36(2)
Pu_Pu_3.8666.f10	3(1)	0.0038(1)	3.82(2)
ΔE_0		-11.8(9)	
S_0^2		1.000	
R(%)		5.18	

X-ray absorption spectroscopy of Goethite

The precursor ferrihydrite material (FH-A-3000 and FH-B-3000) was aged hydrothermally (3 days at 70°C) to form goethite. The EXAFS spectra of samples GA-3000 and GB-3000 are also different. The GB-3000 spectrum could be fit to the model structure of PuO_2, with four plutonium atoms at a distance of 3.82Å (Table 4.3, Figure 4.4). This structural feature indicates that plutonium is likely present as a surface precipitate or inclusion in sample GB-3000. Presence of surface bound plutonium oxides (i.e. surface precipitates) was confirmed by TEM imaging (Figure 4.5). The GA-3000 spectrum could not be fit with a PuO_2 model. In GA-3000, plutonium is coordinated by eight oxygen atoms at 2.18 Å in the first

coordination sphere. These bond distances are slightly shorter than the Pu-O bond distances of G-B-3000, 2.31(1) Å (Table 4.4). The fitting of this data indicates one Pu-Fe distance at 3.5 Å and one Pu-Pu distance at 3.8 Å. These results suggest that in this sample, Pu may not be present as surface species. These results suggest that the timing of Pu addition to the ferrihydrite precursor (Method A or B) affects the final form of plutonium in the goethite structure.

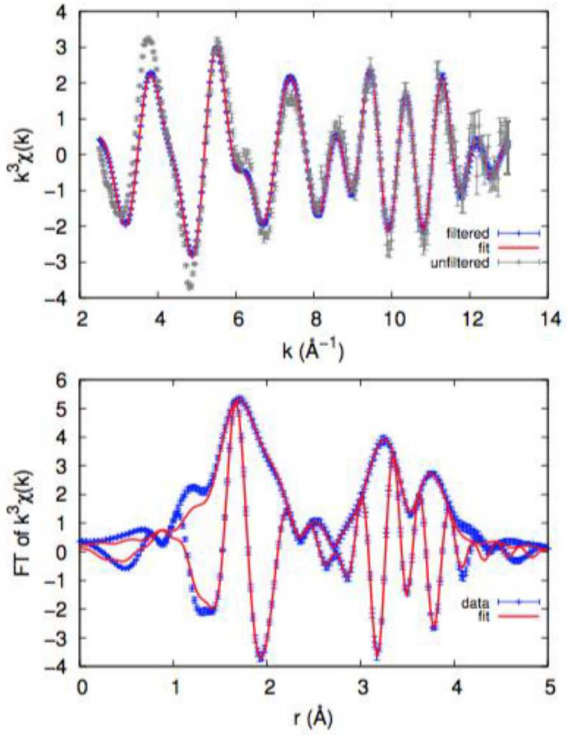

Figure 4.3. GA-3000- EXAFS spectra (top) and Fourier transform R (Å) (bottom).

Table 4.2. Fit parameters for EXAFS spectrum of GA-3000.

		009b1G	
	N	σ^2(Å^2)	R(Å)
Pu_O_2.3678.f10	2.5(1)	0.00311(2)	2.180(4)
Pu_O_2.3678.f10	2.42	0.00312	2.338(6)
Pu_Fe_3.4312.f10	1.1(3)	0.00025(1)	3.55(2)
Pu_O_3.7450.f10	2.5(7)	0.0001(5)	3.95(3)
Pu_Pu_3.8666.f10	1.5(10)	0.002(2)	3.799(8)
ΔE_0		-12.0(7)	
S_0^2		1.000	
R(%)		2.80	

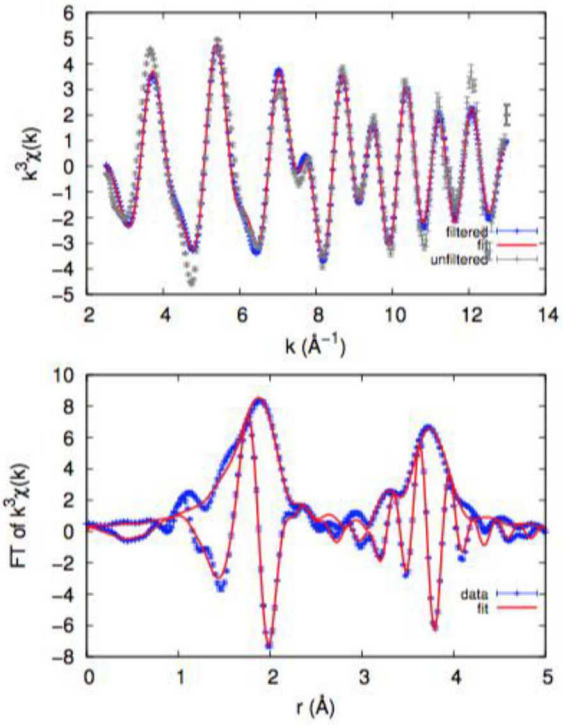

Figure 4.4. GB-3000 - EXAFS spectra (top) and Fourier transform R (Å) (bottom).

Table 4.3. Fit parameters for EXAFS spectrum of GB-3000.

	Sample B		
	N	σ^2(Å^2)	R(Å)
Pu_O_2.3678.f10	7.6(10)	0.01003(8)	2.321(8)
Pu_Pu_3.8666.f10	4.2(10)	0.0038(1)	3.807(5)
ΔE_0		-12.0(10)	
S_0^2		1.000	
R(%)		9.83	

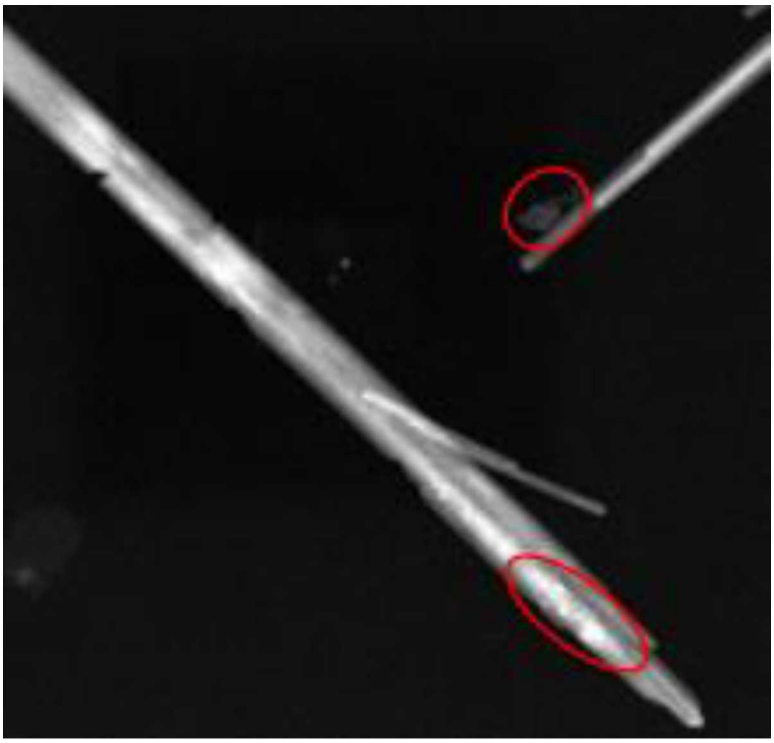

Figure 4.5. TEM image of GB-3000 (PuO_2 colloids circled in red).

4.3.2 Acid leaching of Fe and Pu from Goethite samples

Sample GA-3000 and GB-3000 were tested to determine the leaching behavior of Fe and Pu in HNO_3 (0.1-6M). Suspensions were equilibrated in the acid suspensions of different concentrations for 30 minutes prior to centrifugation. Fe measurements were conducted with ICP-MS (ppb-ppm) and UV-Vis (ppm). Pu concentration was determined by Liquid Scintillation Counting (LSC). Results reported in Figure 4.6 show that the concentrations of Fe leached from both goethite samples (GA-3000 and GB-3000) are similar (Figure 4.6). The leaching of Pu from these solids, however, shows that 2-3 times more Pu is leached from GB-3000 than from GA-3000 (Figure 4.7), suggesting that the association of Pu to GB-3000 may be different from GA-3000. Specifically, leaching of Pu from samples that include PuO_2 surface precipitates (Figure 4.5) is more favorable than when Pu is coprecipitated in the iron oxide phase.

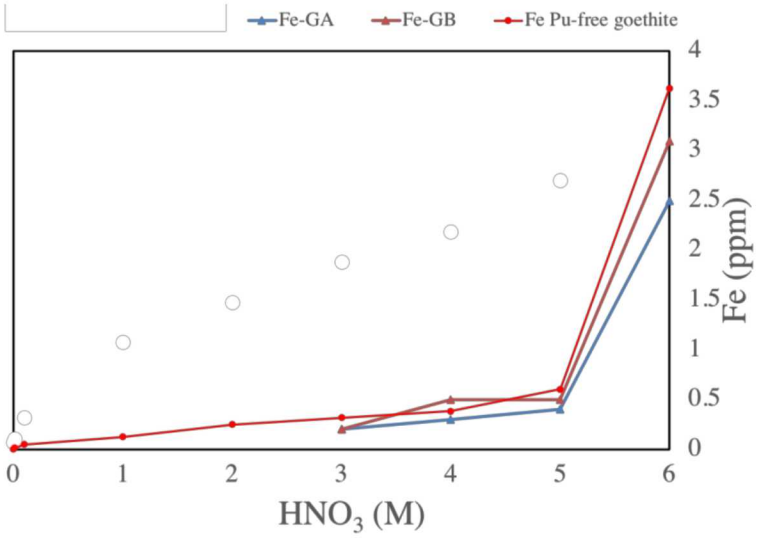

Figure 4.6. Leaching of Fe(ppm) from GA-3000 and GB-3000, measured by ICP-MS (red) and UV-Vis (orange and blue).

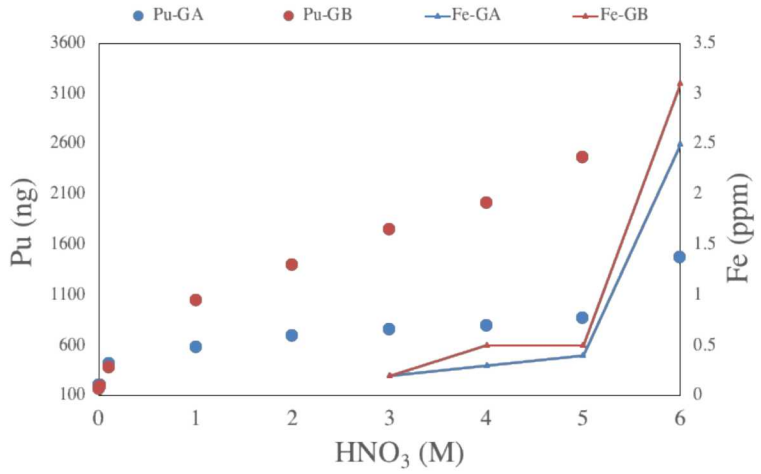

Figure 4.7. Leaching of Pu from GA-3000 (blue dots) and GB-3000 (red dots), and leaching of Fe(ppm) from GA-3000 (blue line) and GB-3000 (red line).

4.4. Thermodynamic Database Development

As part of our FY18 effort in thermodynamic database development, we prepared a draft report entitled "H2OI95: A Stand-Alone Fortran Code for Evaluating the IAPWS-95 Equation-of-State Model for Water" by T. Wolery. This report will be completed in early FY19 and released as a LLNL technical report. Below, we summarize the report which describes the calculation of the thermodynamic and thermochemical properties of water over a wide range of pressure relevant to SFWST.

H2OI95 is a stand-alone Fortran code for evaluating the IAPWS-95 equation-of-state model (Wagner and Pruss, 2002) for the thermodynamic properties of water. It further evaluates the corresponding thermochemical properties of water consistent with the CODATA recommendations (Cox et al., 1989). The IAPWS-95 model is based on a model equation for the dimensionless Helmholtz energy for which the primary variables are the inverse reduced temperature ($\tau=T_{cr}/T$) and reduced density ($\delta=\rho/\rho_{cr}$). Here T is the absolute temperature (K), ρ is density (kg/m^3), and the subscript "cr" refers to the critical point of water (647.096 K and 22.064 MPa pressure in this model, for which ρ_{cr} is 322 kg/m^3). The code solves four basic types of problems, distinguished by the specified inputs:

1, Temperature (K) and density (ρ kg/m^3) or reduced density (δ)
2. Temperature (K) and pressure (MPa).
3. Temperature (K) on the saturation (liquid-vapor equilibrium) curve
4. Pressure (MPa) on the saturation curve

Each type of problem is run using a corresponding input (text) file. All but the first type of problem require iteration. For example, to solve for desired temperature and pressure, the reduced density must be adjusted to give the desired pressure. Iteration is accomplished using the Newton-Raphson method, though the secant method is also used in solving the fourth type of problem.

H2OI95 has been used to conduct numerical studies of convergence and the problem of multiple numerical solutions, only some of which correspond to valid results. Obtaining valid results depends mainly on appropriate choice of starting values. The studies made as part of this work supplement those reported by Junglas (2008), which is unfortunately the only other known work addressing these numerical issues. The problem is illustrated by considering case of 500K (less than the critical temperature of 647.096K) and 25 MPa (somewhat greater than the critical pressure of 22.064 MPa). By varying the starting estimate for the density, three numerical solutions (each corresponding to a different density) were found. Partial results are summarized in Table 5, where κ is compressibility, w is speed of sound, S is absolute (thermochemical) entropy, and G is thermochemical Gibbs energy. The mid-density solution has a negative compressibility and no value for the speed of sound, as the calculated square of the speed of sound had a negative value. The mid density solution is non-physical and therefore invalid. It is just a numerical artifact. The low-density solution has a negative value for the absolute entropy. Therefore, it is also invalid. Only the high-density solution gives all physically meaningful results. This solution is valid. The density value matches that given by the steam tables of Wagner and Pruss (2002).

Table 4.5. Partial results of convergence studies for water at 500K and 25 MPa. Cells highlighted in orange contain unrealistic results.

Solution	ρ kg m^{-3}	κ MPa^{-1}	w m s^{-1}	S J kg^{-1} K^{-1}	G kJ mol^{-1}
High density	850.558202	$0.930558751 \times 10^{-6}$	$0.133010698 \times 10^{4}$	109.1009	-255.0398
Mid density	621.049863	$-0.487483957 \times 10^{-6}$	NC*	111.8598	-254.5668
Low density	331.832991	$0.275002785 \times 10^{-10}$	$0.338667401 \times 10^{6}$	-2.03222×10^{-6}	-4.80574×10^{4}

*Not calculated ($w^2 \leq 0$)

H2OI95 was used to calculate the pressure over a wide range of density at 500K. The results are shown in Figure 4.8. The pressure curve is extremely irregular, in places approaching near infinite negative and positive values. The curve appears broken because only a limited range of pressure is considered in the figure. Note that calculated pressures can be negative (hence unphysical). The red line marks the previously considered pressure of 25 MPa. Numerical solutions are where this intersects the curve of calculated pressure. Here points C, D, and E correspond to the previously found low, mid, and high-density solutions.

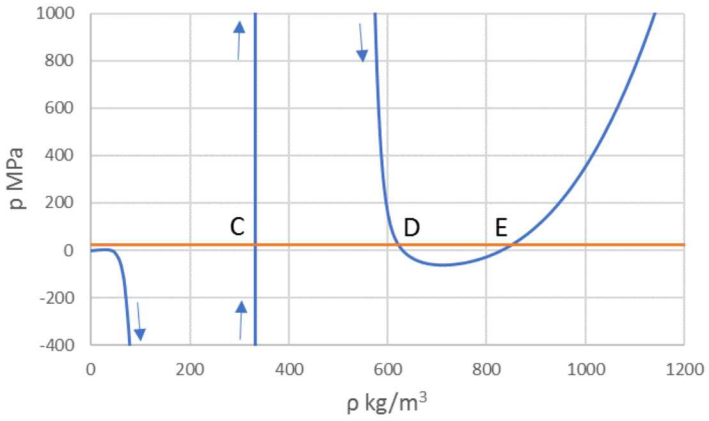

Figure 4.8. Pressure as a function of density (blue) at 500K. Arrows are shown to indicate curve direction moving outside the field of view. The red line marks a pressure of 25 MPa. For this pressure, C = low density solution, D = mid density solution, and E = high density solution.

For other temperatures and pressures, up to five numerical solutions have been observed. At most, only two solutions can be valid, in the case where the temperature and pressure lie on the saturation curve with one solution (with the lowest density) representing saturated vapor and the other (with the highest density) corresponding to saturated liquid.

The result obtained by the iteration process depends on the starting estimate for the density. Default values in H2OI95 are thought to lead to only physically meaningful solutions. It is noted that the IAPWS-95 model as documented by Wagner and Pruss (2002) does not address convergence studies and is silent on the topic of appropriate starting values for density when calculating water properties as a function of temperature and pressure.

With modification, H2OI95 can be used to support SUPCRT92 (Johnson et al., 1992) and similar codes that compute chemical thermodynamic properties of species and reactions over a wide range of temperature and pressure (273.16-1273K and 0-1000 MPa). The original SUPCRT92 uses a combination of two older equation of state models for water, that of Haar et al. (1984) for most of the range of temperature and pressure, and that of Levelt Sengers et al. (1984) near the critical point.

4.5 Planned FY18/FY19 Efforts

In late FY18, we received additional funding to support SFWST efforts within the Crystalline Disposal, Argillite Disposal, and Argillite Disposal International Collaborations work packages. These efforts will begin in FY18 with associated milestones that will be completed in mid-FY19. The efforts associated with these three work packages are outlined below. Support for NEA-TDB participation through the Crystalline International Collaborations work package will be minimally supported by the Argillite International Collaborations work package pending additional FY19 funding from the Crystalline International Collaborations work package.

FY18 carryover funding for this work package has focused on completion of experiments examining Pu incorporation into Fe(III) oxide phases (hydrous ferric oxide, goethite, and hematite). However, fuel matrix degradation models suggest that the near field is likely to be reducing at the time of canister breaching, steel corrosion, and radionuclide release. Thus, there is a need to evaluate Pu incorporation into reduced Fe-oxide phases (e.g. magnetite, green rust). The FY18/FY19 scope will identify synthesis methods for reduced Fe-oxide phases and perform Pu sorption and coprecipitation experiments to determine the fractionation of Pu into and onto these phases. Specifically, we will

- Quantify the rate of Pu incorporation to magnetite and green rust
- Characterize the nature and morphology of sorbed and coprecipitated Pu on these phases using Transmission Electron Microscopy
- Determine the oxidation state and near-neighbor environment of Pu associated with these phases to determine whether a direct cation substitution process controls Pu incorporation into these phases using synchrotron based X-ray Absorption Spectroscopy

Beamline access to the Stanford Synchrotron Radiation Light source (SSRL) was recently made available through our successful application for beamtime in FY17. Some of this effort may need to be carried past our planned milestone (12/3/18) depending on the availability and scheduling of beamtime at SSRL. The effort will be coordinated with the FMDM modeling and experimental work scope performed at Argonne National Laboratory.

4.6 Conclusions

Investigation into the molecular and crystallographic behavior of Pu associated with ferrihydrite and goethite iron oxide phases has led to the following conclusions regarding the potential for Pu sequestration in these solid phases as a result of canister corrosion:

- The timing of Pu release and ferrihydrite corrosion product formation can lead to differences in Pu association: formation of PuO_2 versus coprecipitated Pu
- Alteration of amorphous ferrihydrite to a more crystalline goethite phase will retain Pu association with the solid phase. However, the nature of Pu association will be affected by the characteristics of Pu associated with the precursor ferrihydrite.
- The molecular nature of Pu association with iron oxide phases affects the leaching behavior of Pu. EXAFS and TEM data confirm that in Pu association with goethite as a surface precipitate is more labile than the coprecipitate. This has implications to the longterm stability of Pu associated with corrosion products.

As stated earlier, it is likely that more reduced oxide phases (e.g. magnetite) will be favored over the ferrihydrite and goethite phases describe here. The incorporation of actinides into those more thermodynamically favorable phases (under deep nuclear waster repository conditions) is the subject of ongoing effort in FY18/FY19.

4.7 References

Cox J. D., Wagman D. D., and Medvedev V. A., eds. (1989) CODATA Key Values for Thermodynamics. CODATA Series on Thermodynamic Values. Hemisphere Publishing Corp., New York. 271 pp. ISBN 0-89116-758-7.

Haar L., Gallagher J. S., and Kell G. S. (1984) NBS/NRC Steam Tables. Hemisphere Publishing Corporation, Washington, DC. 320 pp. ISBN 0-89116-353-0.

Johnson J. W., Oelkers E. H., and Helgeson H. C. (1992) SUPCRT92: A software package for calculating the standard molal thermodynamic properties of minerals, gases, aqueous species, and reactions from 1 to 5000 bar and 0 to 1000°C. Comp. Geosci. 18, 899-947.

Junglas P. (2008) Implementing the IAPWS-95 standard in MATLAB. Preprint – ICPWS XV, Berlin, September 8–11, 2008.

Combes, J.M., A. Manceau, and G. Calas, *Formation Of Ferric Oxides From Aqueous-Solutions - A Polyhedral Approach By X-Ray Absorption-Spectroscopy .2. Hematite Formation From Ferric Gels.* Geochimica Et Cosmochimica Acta, 1990. 54(4): p. 1083-1091.

Cox J. D., Wagman D. D., and Medvedev V. A., eds. (1989) CODATA Key Values for Thermodynamics. CODATA Series on Thermodynamic Values. Hemisphere Publishing Corp., New York. 271 pp. ISBN 0-89116-758-7.

Fischer, W.R. and U. Schwertmann, *Formation of hematite from amorphous iron(iii)hydroxide.* Clays and Clay Minerals, 1975. 23(1): p. 33.

Levelt Sengers J. M. H., Kamgar-Parsi, B., Balfour F. W., and Sengers J. V. (1983) Thermodynamic properties of steam in the critical region. J. Phys. Chem. Ref. Data 12, 1-28.

Liu, J., et al., *General Strategy for Doping Impurities (Ge, Si, Mn, Sn, Ti) in Hematite Nanocrystals.* Journal of Physical Chemistry C, 2012. 116(8): p. 4986-4992.

Marshall, T.A., et al., *Incorporation of Uranium into Hematite during Crystallization from Ferrihydrite.* Environmental Science & Technology, 2014. 48(7): p. 3724-3731.

Music, S., M. Gotic, and S. Popovic, *X-Ray-Diffraction And Fourier-Transform Infrared-Analysis Of The Rust Formed By Corrosion Of Steel In Aqueous-Solutions.* Journal of Materials Science, 1993. 28(21): p. 5744-5752.

Powell, B.A., et al., *Stabilization of Plutonium Nano-Colloids by Epitaxial Distortion on Mineral Surfaces.* Environmental Science & Technology, 2011. 45(7): p. 2698-2703

Romanchuk, A.Y., S.N. Kalmykov, and R.A. Aliev, *Plutonium sorption onto hematite colloids at femto- and nanomolar concentrations.* Radiochimica Acta, 2011. 99(3): p. 137-144.

Sanchez, A.L., J.W. Murray, and T.H. Sibley, *The adsorption of plutonium-iv and plutonium-v on goethite.* Geochimica Et Cosmochimica Acta, 1985. 49(11): p. 2297-2307.

Schwertmann, U. and R.M. Cornell, *Iron oxides in the laboratory*, in *Iron Oxides in the Laboratory*. 2000, Wiley-VCH Verlag GmbH. p. i-xviii.

Wagner W. and Pruss A. (2002) The IAPWS formulation 1995 for the thermodynamic properties of ordinary water substance for general and scientific use. J. Phys. Chem. Ref. Data 31, 387-535.

Zhao, P.H., et al., *Plutonium(IV) and (V) Sorption to Goethite at Sub-Femtomolar to Micromolar Concentrations: Redox Transformations and Surface Precipitation.* Environmental Science & Technology, 2016. 50(13): p. 6948-6956.

5. EFFECT OF AGING ON CS SORPTION AND TRANSPORT IN ASSOCIATION WITH CLAY COLLOIDS

5.1 Introduction

Radionuclides including Cs have been released to the environment as a result of nuclear accidents, testing of nuclear weapons, and past accidental releases during processing of nuclear materials (Rani & Sasidhar, 2012). Radioactive cesium (^{137}Cs) is of special interest because it has been released at numerous sites in the U.S. and is known to transport effectively in the subsurface. Understanding the fate of ^{137}Cs is also important for repository science because it has a fission yield of 6.7% and is a hard gamma emitter with a 662 keV emission. ^{137}Cs has a half-life of ~ 30 years and is an important risk driver in nuclear repositories. The sorption and migration of Cs in the subsurface has been extensively researched (Bostick, 2002; Murota et al., 2016; Shenber & Eriksson, 1993; Zachara et al., 2002). Generally, past studies have found that cesium is reversibly adsorbed at the water/mineral interface and that clay minerals present in the soil control Cs sorption and transport. Sorption occurs at ion exchange sites at the edge of the clay layered structure and interlayer exchangeable sites. Several sorption models have been developed to describe Cs sorption behavior. In general, multisite models are required to describe the overall interaction of Cs with clay minerals. Two and three site models have been used to describe Cs sorption behavior. These models commonly describe the existence of low affinity sites and high affinity low abundance sorption sites. The abundant low affinity sites are referred to as the planar binding sites present at the surface of the mineral and the high affinity sites are referred to as frayed-edge sites (FES) (Steefel et al., 2003; Zachara et al., 2002). Examination of Cs association with clay colloids which can form stable colloidal suspension and transport effectively in the environment has also shown that a multi-site sorption model is necessary to represent Cs sorption. Missana et al. (2004) determined that the majority of Cs is sorbed to abundant planar sites on bentonite colloids, and a smaller fraction is sorbed more slowly and irreversibly to the less abundant frayed edge sites. Subsequent work is in agreement with this observation (Zhuang et al., 2003; De Koning et al., 2007).

Characterization of the kinetics and binding properties of the different sorption sites is important for the accurate description of Cs sorption and fate and transport. The characterization of the abundant low affinity sites is usually performed though batch and column studies carried out at elevated Cs concentration. However, the characterization of the high affinity sites is more challenging. Numerous, studies have reported the existence of slow sorption and irreversible desorption of Cs associated with the high affinity sites on clay. A subset of the high affinity sites sorbs and desorbs Cs extremely slowly making their characterization very challenging. In our previous effort, we focused on developing experimental approaches to interrogate these slow desorption sites. We reported on colloid-facilitated transport of ^{137}Cs associated with clay colloids through both granodiorite and fracture fill material which represent weakly sorbing geologic materials. A two-site model was necessary to explain the breakthrough of Cs through a granodiorite column (Wang, 2015). Our results showed that Cs adsorbed on bentonite colloids was not effectively transported through granodiorite and fracture fill material. We also did not see any evidence of very slow desorption kinetics or very strong sorption sites on colloids. Some of these observations are attributed to the relatively short equilibration time allowed for Cs to associate with the bentonite colloids which could have limited the association of cesium with the high affinity slow sorption sites. In this work we continued to develop our experimental approach and focused specifically on the interrogation of extremely slow and difficult to observe Cs sorption sites. More specifically, the focus of this work is to address the key issue: colloid-facilitated transport of Cs in association with irreversible binding site or sites with extremely slow desorption kinetics. Experiments were designed using a sequential injection approach and utilized a strong adsorbent as column fill material (analcime) to promote greater desorption from colloids. We also varied the equilibration time. The first experiment consisted of injecting Cs equilibrated

with clay colloids for only a few hours through a column packed with analcime to simulate conditions where only sorption sites with fast kinetics are occupied. The second experiment was performed with a colloidal suspension that was equilibrated for a longer time (after ~1200 hours of sorption). The breakthrough curves for the two experiments were analyzed using a multisite model. This work supports the Geologic Disposal Safety Assessment Framework (GDSA) model for assessing the performance of deep underground disposals for nuclear waste. This work developed experimental methods for the interrogation of slow desorption kinetics which are critical for studying the effect of material aging on radionuclides sorption and transport.

We have also started investigating the effect of hydrothermal treatment of clay colloids on radionuclides fate and transport. Increasing temperature is known to transform the clay minerals. Some of these transformations can lead to the formation of analcime and other minerals that can incorporate large amounts of Cs and other radionuclides (Cheshire et al., 2014). Hydrothermal treatment of clay colloids may also reduce the K_d of cesium sorption to clays, but if the Cs is sorbed prior to heating, the retention of Cs increases as a result of interlayer edge collapse (Cornell, 1993 and references therein). The electrokinetic properties of some of the new mineral phases could also have important implications for radionuclides transport in association with the newly formed phases.

5.2 Methods and Materials

Two types of experiments were conducted to examine the effect of aging on Cs transport in association with clay colloids. The first experiment consisted of a series of batch experiments performed to determine the effect of aging on Cs partitioning coefficients and to prepare colloidal suspension for the column transport experiments. The second set of experiments consisted of performing column flow experiment with repeated injection to characterize Cs desorption from the high affinity sites. The column experiments breakthrough results were treated numerically with a multisite model with variable desorption rate constants.

Batch Sorption Studies: Batch sorption studies were performed to determine the sorption capacity of analcime. A synthetic Chancellor water was used for all sorption and transport studies described in this report. The synthetic Chancellor water was prepared to match the chemistry of Chancellor Cavity water without radionuclides (Table 5.1). The solution was prepared by adding reagents grade salts of the different cations and anions (Fisher Scientific Analytical Grade) to deionized water (18 MΩ-cm). The pH was adjusted to 8.5 using 0.1 M HCl to match the Chancellor water pH. The ionic strength of the synthetic Chancellor water computed using Geochemist's Workbench is 0.0046 M.

Table 5.1. Recipe for synthetic Chancellor water from Reimus and Boukhalfa, 2014. ND: not determined.

Constituent	Recipe (mg/L)	Measured Concentration (mg/L)
Na^+	96	87
K^+	4.66	4.39
Ca^{2+}	1.12	1.08
Mg^{2+}	0.46	0.21
Cl^-	26.9	36.7
SO_4^{2-}	63.4	65.5
HCO_3^-/CO_3^{2-}	119-126	ND
SiO_2	115.3	30.4
pH	8.9	8.5

The analcime material used in the batch experiment and as a fill material for the column experiments was prepared from a large analcime crystal purchased from a private mineral collection ordered from Ebay. The single crystal was crushed and sieved to obtain grain sizes 75-200 um. The mineralogy and elemental composition are waiting to be determined by qXRD and XRF, respectively.

Four separate solutions of varying ^{137}Cs concentrations in background synthetic Chancellor water without colloids were added to 1.0 g of analcime in polyethylene test tubes in the combinations listed in Table 5.2.

Table 5.2. Experimental conditions for the batch experiment with analcime performed at varying solution to analcime ratios and different Cs ratios.

	Analcime (g)	Aqueous solution total volume in mL	Cs in M	^{137}Cs in cpm/mL
triplicate	1.0	14	$4.5x10^{-10}$	1120
triplicate	1.0	14	$2.3x10^{-10}$	569
triplicate	1.0	40	$4.5x10^{-10}$	1120
triplicate	1.0	40	$2.3x10^{-10}$	569

The radiotracer ^{137}Cs used in these experiments was ordered as a "low-carrier" source solution from Eckert and Ziegler Isotope Products, meaning that it was supposed to contain minimal nonradioactive Cs mixed in with the ^{137}Cs. The molar concentrations in Table 5.2 were calculated by assuming the low carrier ^{137}Cs solution contained 10% ^{137}Cs and 90% ^{133}Cs. The samples were equilibrated for four days under constant shaking at 50 RPM. Following the equilibration time, the samples were filtered through 0.02 µm filters to separate the solid analcime material from the aqueous solution. Three aliquots from each batch were counted by liquid scintillation to determine the activity remaining in solution. All samples were run in triplicate. The concentration of Cs adsorbed on analcime was calculated as the difference between the activity added to the batch samples and the activity remaining in solution.

A second batch sorption experiment was performed to examine ^{137}Cs sorption to FEBEX colloids and the effect of aging on the partitioning coefficient. Previous experiments investigating the colloid-facilitated transport of ^{137}Cs by FEBEX bentonite colloids (Dittrich and Reimus, 2015) did not use a low-carrier ^{137}Cs source, and it was estimated that the ^{137}Cs in those experiments was less than 0.1% of the total Cs. Although we were unable to verify the ratio of ^{137}Cs to total Cs in the current experiments, discussions with Eckert and Ziegler representatives indicated that the ratio should have been no less than about 0.1, or 10%. Thus, for the same concentration of ^{137}Cs in the current experiments, the concentration of total Cs was at least 100 times less than in the experiments of Dittrich and Reimus (2015). This difference is significant because it allowed us to interrogate colloid-facilitated ^{137}Cs transport under conditions in which far fewer sorption sites on the colloids were occupied by Cs, which, in principle, should result in preferential interrogation of stronger sorption sites. The experiment was conducted by adding a spike of the low carrier ^{137}Cs (1164 cpm/mL) radiotracer to a colloidal suspension of FEBEX colloids containing 100 mg/L of colloids prepared in synthetic Chancellor water. Aliquots were taken in triplicate over 1200 hours, filtered through 0.02 µm, and analyzed for ^{137}Cs. The filters were checked for ^{137}Cs sorption and found to not sorb any measurable amounts of ^{137}Cs. The FEBEX colloids were prepared by the method described in our previous report (Dittrich & Reimus, 2015). Briefly a block of FEBEX material from the Grimsel Site in Switzerland was crushed and sieved to obtain grain sizes less than 75 µm. The mineralogy of the FEBEX material was determined previously and is presented in Table 5.3.

Table 5.3. Quantitative X-ray diffraction interpretation (wt. %) of FEBEX bentonite (Dittrich & Reimus, 2015).

Mineral	Content in Wt. %
Quartz	2 ± 1
Plagioclase (Na, Ca)	3 ± 1
Cristobalite	2 ± 1
Feldspars	Trace
Smectite	92 ± 3
Calcite	1 ± 0.5

50 g of the sieved material was suspended in 1.0 L of DI water for colloid preparation according to Dittrich & Reimus (2015). The suspension was equilibrated for 24 hours to allow sodium saturation. The process was repeated several times to allow for complete exchange of the Na. The solution was decanted and replaced with synthetic Chancellor water. This suspension was sonicated, shaken, centrifuged, decanted, and replaced with fresh synthetic Chancellor water. This process was repeated until the conductivity of the solution matched that of the synthetic Chancellor water (463 µS/cm). Eight batches of ~ 30 mL of FEBEX solution were prepared in this way. Each batch was then diluted with 1 L of synthetic Chancellor water and transferred to a 1 L graduated cylinder and allowed to settle for approximately 2 weeks. The upper 700 mL of the suspension was then removed by syringe. The concentration of the suspended colloids determined by drying aliquots (~25 mL) of the solution on a watch glass was ~300 mg/L.

A third sorption experiment was performed by equilibrating ^{137}Cs simultaneously with analcime and *FEBEX* colloids. The experiment was conducted by adding ^{137}Cs-spiked FEBEX colloid solution to analcime. The following combinations of liquid to solid ratios were prepared (Table 2-4).

Table 5.4. Experimental conditions for the batch experiment with analcime and FEBEX colloids at varying solution to analcime ratios and different Cs ratios.

	Analcime in g	Liquid *FEBEX* colloids mL	Cs in M	^{137}Cs in cpm/mL
triplicate	0.1	4.0	4.6×10^{-10}	1164
triplicate	0.2	2.8	4.6×10^{-10}	1164

Triplicate solutions were prepared for each condition. A control series was also prepared without analcime. The batch samples were incubated for 4 days under constant shaking. Aliquots were filtered through a 0.02 µm filter to separate the liquid for the solids and colloids and counted by liquid scintillation to determine the amount of ^{137}Cs that remained in solution.

A fourth batch experiment was conducted to determine the cation exchange capacity of the analcime. Three 2-g samples of analcime were reacted with 20 mL of a 0.1 M CsCl solution in 50 mL polyethylene test tubes. Samples were left on a shaker table and 2 mL aliquots were sampled and filtered after 1, 2, and 7 days. Samples were analyzed for major cations and anions and Cs.

Column Transport Studies: Our previous work tested the stability of Cs bound to colloids transporting through a column filled with Grimsel granodiorite. Granodiorite proved to have a very low affinity for Cs. To contrast with the granodiorite work, this effort examined the transport of Cs bound to clay colloids transporting through columns filled with analcime. Two series of experiments with repeat injections were

performed and a third column experiment is currently running. The repeat injection approach was described previously (Dittrich & Reimus, 2015; summarized in Figure 5.1). Briefly, Teflon™ tubes of 0.8 cm diameter were cut to ~10 cm (Table 5.5). The columns were packed with ~10 g analcime, and glass wool was packed at both ends to prevent sediment erosion. The inlet column was connected with PEEK tubing to a syringe pump (KD Scientific 60 cc syringe), and the outlet of the column was connected with PEEK tubing to a fraction collector. The columns were saturated with the synthetic Chancellor water. Saturation was achieved by alternating a vacuum atmosphere and an atmosphere of CO_2 prior to flushing the columns with synthetic Chancellor water (Table 5.1). For all columns, the flow rate was set to 0.5 mL/hr. Samples were collected over a 6-hour interval, except for the latter 2 column experiments which collected sample every hour for the first 24 hours prior to the 6-hour collection. For the first two sets of column experiments, the FEBEX colloid solution was spiked with the low carrier ^{137}Cs stock solution. The concentration of the injected solution was prepared to be 4.8 x10^{-10} M to ensure ^{137}Cs would be low enough to theoretically sorb entirely to the strong sites on the colloids (Missana et al., 2004). The solution was also spiked with either iodide or tritiated water (^{3}HHO) to achieve concentrations of 25 ppm or 27,460 cpm/ml, respectively, which served as inert tracers. This aliquot was injected through a column filled with analcime and the eluent fractions were measured for ^{137}Cs, ^{3}HHO or iodide, and colloid concentration. The eluted fractions with a concentration of colloids approaching the injected concentration were combined and injected through a second fresh column filled with the same batch of analcime (Figure 5.1). The sequential injection was designed to test if the eluted Cs associated with the colloids was more strongly bound to colloids after the weakly sorbed ^{137}Cs was stripped by the analcime. The first two sets of experiments were run identically, except for the aging time of the ^{137}Cs spiked colloid solution. The first set of experiments injected the spiked colloid solution within a few hours of spiking the colloid solution with ^{137}Cs, whereas the second set of experiments injected the spiked solution ~ 2 months after the colloids were spiked with ^{137}Cs. The variability in K_d values for ^{137}Cs sorption to colloids as a function of aging was quantified by batch experiments in order to compare the 2 sets of column experiments. A third column experiment was run by injecting Chancellor Cavity water (collected from the Nevada Test Site; Reimus & Boukhalfa, 2014) through a mini column filled with analcime. The third column experiment is identical to the experiment reported in our previous report with the exception of using analcime as a column fill material as opposed to granodiorite. The choice of analcime was motivated by the higher affinity of analcime for Cs sorption compared to granodiorite and might allow us to interrogate more effectively the high affinity sorption sites on the colloids which were not fully characterized in our previous report.

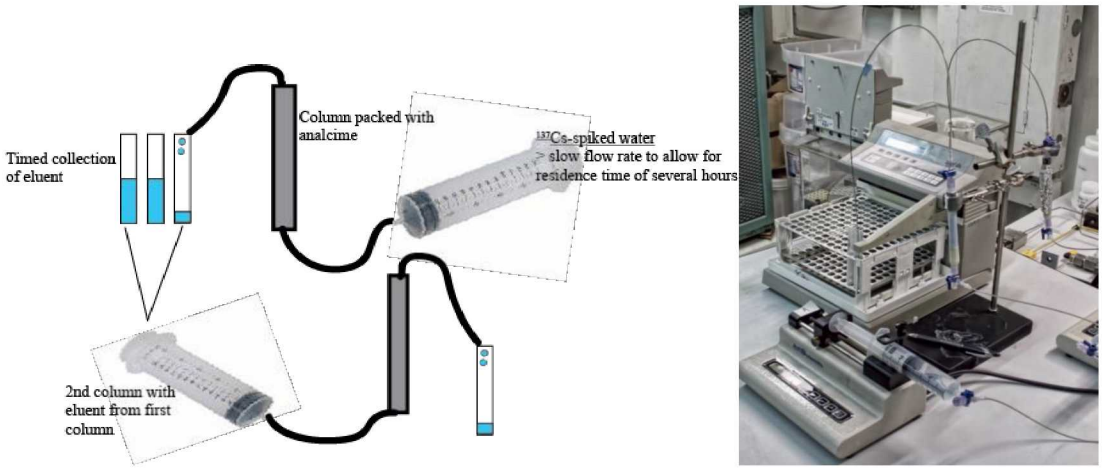

Figure 5.1. Schematic representation of the repeat injection approach and image of laboratory setup.

Table 5.5. Summary of the column parameters for the three analcime columns used in the current study. Samples A1 and A2 are analcime columns run sequentially using the ^{137}Cs spiked colloid solution with a few hours of equilibration (no aging), C1 and C2 samples are analcime columns run sequentially with the aged ^{137}Cs spiked colloid solution, and C5 is the analcime column run with Chancellor water.

Column ID	Analcime Mass (g)	Pore volume (mL)	Column Length (cm)	Column Inner Diameter (cm)	Injection Volume (mL)	Cs concentration in M	Injection Conc. ^{137}Cs (cpm/mL)
A1	8.97	3.74	10.8	0.8	97	4.1×10^{-10}	1035
A2	9.62	3.95	11.3	0.8	66 (eluted samples #3-31 from A1)	7.6×10^{-12}	36
C1	9.55	3.53	11.4	0.8	300	6.5×10^{-10}	1622
C2	9.48	3.93	11.4	0.8	157 (eluted samples #11-76 from C1)	$1.9\times^{-11}$	47
C5	9.20	3.86	10.9	0.8	ongoing	1.1×10^{-11}	27

Analytical Techniques: Samples were measured for ^{137}Cs and ^{3}HHO using liquid scintillation counting. Aliquots of 0.2 mL of the sample were pipetted into 20 mL plastic liquid scintillation vials and combined with 3.8 mL DI and 16 mL Ultima Gold AB scintillation cocktail. Samples were analyzed on a Perkin-Elmer Tri-Carb Model 2500 for 5-hour counts per sample for ultra-low-level beta and alpha decay counting. ^{137}Cs counts were taken from 15-500 kev, and tritium counts were taken from 0-15 kev. The I^- tracer was measured using an Orion™ electrode calibrated with standards made from NaI salts in DI water.

Colloid concentrations were determined by a Hach® 2100N turbidimeter as described previously. We also developed a new spectrophotometric method to measure very low colloid concentrations. The new method

employs a blue filter added to an Agilent 8453 UV-vis Spectrophotometer. Absorbances are averaged every 25 nm between 320 and 920 nm. The absorbance value at 700 nm is then subtracted as background from the absorbance at 400 nm. Standards were prepared from a serial dilution of the synthetic colloid solution or the Chancellor water. This method proved to be as accurate as the turbidimeter method (Figure 2-2) and requires less sample (<0.2 mL).

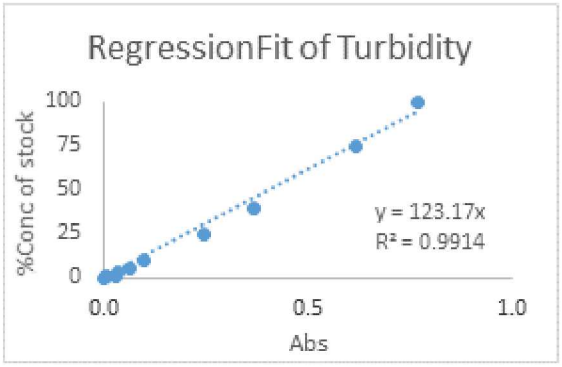

Figure 5.2. Calibration of spectrophotometry method for determination of colloid concentration.

Non-rad samples from the batch experiments were measured for major cations and anions using inductively couple plasma optical emission spectrometry (ICP-OES) and ion chromatography (IC).

SEM analyses were performed on colloid samples from both the upper 700 mL and lower 300 mL of the settling colloid suspension processed at ambient temperature. SEM analysis was also performed on the upper 700 mL and lower 300 mL of the settling colloid suspension of the bentonite colloids treated hydrothermally. The colloid samples were collected on 0.22 µm polycarbonate filters using a vacuum filtration system. The solids were washed several times with DI to eliminate any dissolved salts and dried at 65ºC under vacuum for ~2 hours. The solids were dispersed on a SEM carbon mount and gold coated (5 nm thickness) prior to analysis by scanning electron microscopy (SEM) on an FEI™ Inspect F SEM equipped with Energy dispersive X-ray spectroscopy EDS for elemental analysis. Imaging was performed using 5-20 kV accelerating voltage and a 3.0 spot size.

Zeta potential of bentonite colloidal suspensions was measured by a Malvern Zetasizer Nano. Zeta potential measurements were performed on both sonicated and un-sonicated suspensions. Sonication was performed on the entire colloidal stock solution (25 mL) for 15 min. A small aliquot was transferred to the electrophoresis cell and allowed to stabilize at ambient temperature (23.5 ºC) for a few minutes before the run. The measurements were conducted at 22 ºC. For each sample, readings were performed by averaging 3 independent runs of 100 measurements. The concentration of the colloidal suspensions had turbidity of less than 0.01 OD.

Model Description and Column Data Analysis: Similar to the column experiments with granodiorite-filled columns, the column experiments with analcime fill were interpreted using the colloid-facilitated transport models described in (Reimus, 2017; Reimus et al., 2017). The model employed the following equations:

Mobile Colloid Transport in Fractures:

$$\frac{\partial C_c}{\partial t} + div(v_c C_c - D_c \nabla C_c) + k_{filt} C_c = 0 \quad (5.1)$$

Colloids Filtered onto Immobile Surfaces in Column:

$$\frac{\partial S_c}{\partial t} = k_{filt} C_c \quad (5.2)$$

Mobile Solute in Column:

Advective and Dispersive Transport: $\frac{\partial C_a}{\partial t} + div(v_a C_a - D_a \nabla C_a) =$

Reactions with Immobile Surfaces (1 sorption site): $-k_{as} \frac{\rho_B}{\emptyset} C_a \left(1 - \frac{S_a}{S_{a,max}}\right) + k_{sa} \frac{\rho_B}{\emptyset} S_a +$

Reactions with Mobile Colloids (2 sites): $\sum_{i=1}^{2} \left[-k_{ac,i} C_a C_c \left(1 - \frac{C_{ac,i} C_c}{C_{ac,max,i} C_c}\right) + k_{ca,i} C_{ac,i} C_c\right] +$

Reaction with Immobile Colloids (2 sites): $\sum_{i=1}^{2} \left[-k_{ac,i} C_a S_c \left(1 - \frac{C_{ac,i} S_c}{C_{ac,max,i} S_c}\right) + k_{ca,i} C_{ac,i} S_c\right]$ (5-3)

Solute Adsorbed onto Immobile Surfaces in Column:

$$\frac{\partial S_a}{\partial t} = k_{as} C_a \left(1 - \frac{S_a}{S_{a,max}}\right) - k_{sa} S_a + \sum_{i=1}^{2} \left[-k_{ac,i} C_a S_c \left(1 - \frac{C_{ac,i} S_c}{C_{ac,max,i} S_c}\right) + k_{ca,i} C_{ac,i} S_c\right] \quad (5\text{-}3)$$

Solute Adsorbed onto Mobile Colloids in Fractures (2 equations; i = 1, 2):

$$\frac{\partial C_{ac,i} C_c}{\partial t} + div\left(v_a C_{ac,i} C_c - D_c \nabla C_{ac,i} C_c\right) = k_{ac,i} C_{ac,i} C_c \left(1 - \frac{C_{ac,i} C_c}{C_{ac,max,i} C_c}\right) - k_{ca,i} C_{ac,i} C_c - k_{filt} C_{ac,i} C_c \quad (5\text{-}4)$$

where, C_c = concentration of colloids in mobile phase, g/cm^3
C_a = solution concentration of solute in mobile phase, g/cm^3
S_a = adsorbed concentration of solute on granodiorite, g/g
S_c = filtered concentration of colloids on immobile phase, g/cm^3 of solution
$C_{ac,i}$ = concentration of solute sorbed to colloid site i, g/g colloid
$S_{a,max}$ = maximum adsorbed concentration of solute on granodiorite, g/g
$C_{ac,max,i}$ = maximum concentration of solute sorbed to colloid site i, g/g colloid
v_c = advective velocity of colloids in column, cm/hr
v_a = advective velocity of solutes in column, cm/hr
D_a = solute dispersion coefficient in column, cm^2/hr
D_c = colloid dispersion coefficient in column, cm^2/hr
ρ_B = effective bulk density within granodiorite, g/cm^3
$\emptyset$ = porosity within granodiorite
k_{filt} = filtration rate constant for colloids (assumed irreversible), 1/hr
k_{as} = rate constant for sorption of solute onto granodiorite, cm^3/g-hr
k_{sa} = rate constant for desorption of solute from granodiorite, 1/hr

$k_{ac,i}$ = rate constant for sorption of solute onto colloid site *i*, cm^3/g-hr
$k_{ca,i}$ = rate constant for desorption of solute from colloid site *i*, 1/hr

5.3 Results

Batch Sorption

The batch experiments were conducted to develop a better understanding of how very low levels of Cs and changes in the both the concentration of Cs and liquid to solid ratios influence the sorption of Cs to the colloids. Table 5.6 shows the results of the batch sorption experiments with dissolved ^{137}Cs and analcime.

Partitioning coefficient (K_d) values range from 293 mL/g to 486 mL/g and all samples show > 90 % adsorption (Table 2-6). The K_d values were calculated as:

$$Kd = \frac{C_0 - C_t}{C_t} \cdot \frac{sample\ volume}{sediment\ weight}\ \text{mL g}^{-1}$$

in which C0 is the intial 137Cs concentration and Ct is the concentration at the end of the experiment (Erdem et al., 2014; Murali and Mathur, 2002). The percent adsorption is calculated as (Erdem et al., 2004):

$$\%A = 100 \cdot Kd/(Kd + \left(\frac{solution\ volume}{sediment\ weight}\right))$$

Table 5.6. Sorption constants and percent adsorption. Analcime amount was fixed to 1.0 g in all samples.

Sample volume (mL)	Starting Cs concentration in M	K_d in mL/g	% Cs Adsorbed
40	$4.5x10^{-10}$	486 ± 37	92 ± 0.5
40	$2.3x10^{-10}$	474 ± 99	92 ± 1.6
14	$4.5x10^{-10}$	398 ± 20	97 ± 0.2
14	$2.3x10^{-10}$	293 ± 38	96 ± 0.5

This experiment demonstrates the strong sorption of analcime for dissolved Cs. Therefore, we assume that all ^{137}Cs eluting through the column is associated with colloids, and all dissolved ^{137}Cs is sorbed by the analcime. The cation exchange capacity of analcime used in the batch was calculated as 18 meq/kg. This value is much lower than previously reported cation exchange capacity of analcime, which was several hundred meq/kg (Allard et al., 1983; Ames, Jr., 1966).

The second batch experiment performed to examine the effect of aging on Cs sorption to FEBEX colloids yielded results that are in agreement with the literature. The results of the batch sorption experiment are shown in Figure 5.3. The loss of dissolved ^{137}Cs through time demonstrates the progressive uptake of ^{137}Cs by the FEBEX colloids. The K_d value after 2 hours is 12876 and fluctuates by a value of 4072 over the following ~340 hours. With 58-64 % of the ^{137}Cs being adsorbed to the colloids. By the final sampling time

at 1200 hours, however, the K_d increased to 27803, with about 75% of the ^{137}Cs being adsorbed to the colloids. In contrast, in the experiments of Dittrich & Reimus (2015), which involved much higher total Cs concentrations because of the abundance of nonradioactive Cs in the ^{137}Cs source, only about 25% of the ^{137}Cs was adsorbed to the colloids.

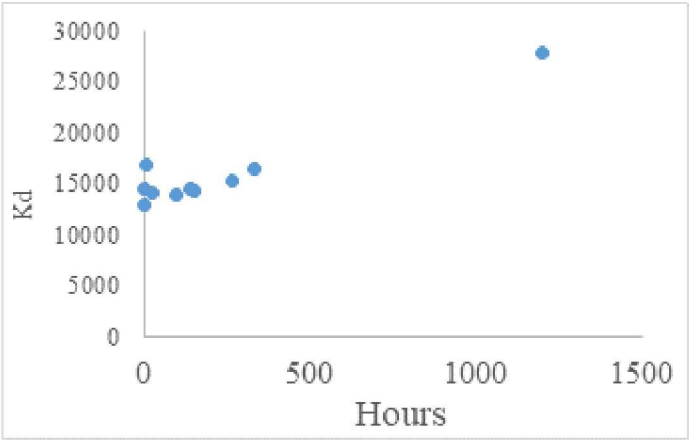

Figure 5.3. Results from batch sorption experiment, showing the increase of the partitioning coefficient as a function of time.

The data presented in Figure 5.3 can be interpreted by the presence of two sorption processes with different reaction kinetics. The first process is fairly fast and is complete within a few hours and a second process that is much slower. The batch data were modeled with a two-site model that assumes the presence of two populations of Cs sorption sites with different sorption kinetics. In all modeling calculations the total Cs concentration was assumed to be 10 times greater than the measured ^{137}Cs activity, with the initial total Cs concentration assumed to be 4×10^{-10} M Cs (based on a measured ^{137}Cs concentration of about 4.5×10^{-11} M). The experimental data and model interpretation are shown in Figure 5.4. The figure shows the results of modeling the fraction of ^{137}Cs adsorbed to the colloids as a function of time in the bentonite-only batch experiment. A two-site sorption model on the colloids was used to match the data, as a single-site model failed to simultaneously explain the very rapid sorption of about 58% of the ^{137}Cs followed by the very slow sorption of the remaining 15% or so of the ^{137}Cs that was sorbed by the end of the experiment. The sorption parameters used to match the data are listed in Table 5.7. The parameter that is most tightly constrained by the data set is the adsorption rate constant for the second site, as this rate constant dictates the rate of increase of the fraction sorbed after the initial rapid sorption. The rapid initial sorption is modeled as a rapid equilibration between the first sorption site and the solution. The sorption site density for the second site is also relatively well constrained by the data set. The desorption rate constant for the second site is not well constrained, but it cannot be greater than about 0.0005 hr^{-1} because if it is greater than this, the fraction adsorbed after 1200 hours is underpredicted (even if the sorption site density of the second site is increased significantly). Figure 5.4 also shows the fraction of total adsorbed ^{137}Cs that is predicted by the model to be adsorbed to the stronger sorption site over time.

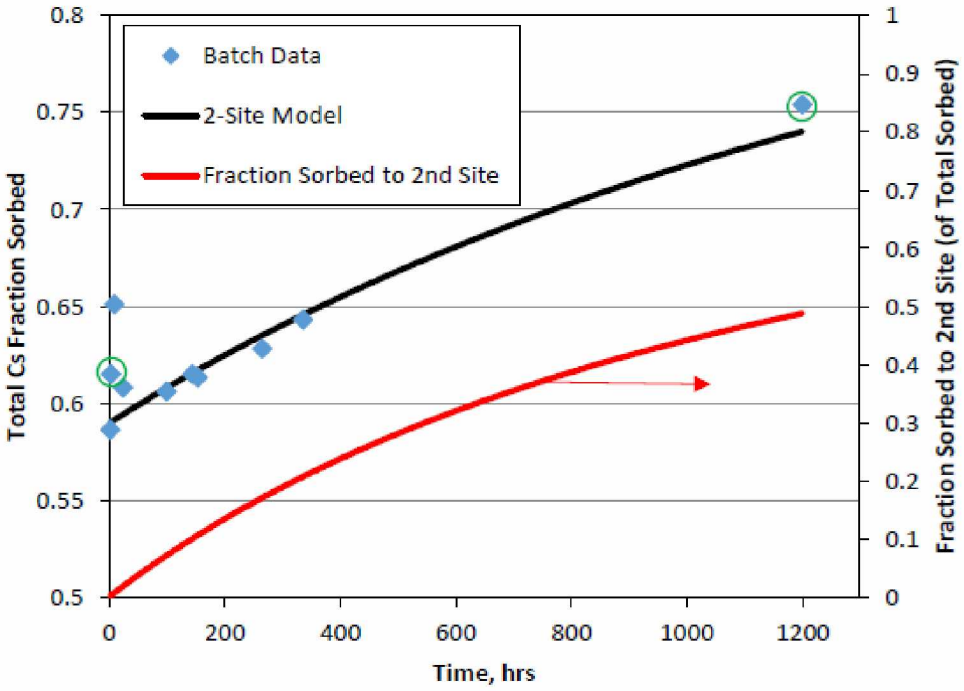

Figure 5.4. Fraction ^{137}Cs sorbed to bentonite colloids in batch experiment and matched by a two-sorption-site model. Red curve is the fraction of total adsorbed Cs that is predicted by the model to be sorbed to the second (stronger) sorption site (right axis). Green circles indicate the data points associated with the start of the first and second set of column experiments.

Table 5.7. Model parameters used to match the batch experiment data of Figure 5.4.

Parameter	Value
$k_{ac,1}$ (Site 1 sorption rate constant), ml/g-hr	15,000
$k_{ca,1}$ (Site 1 desorption rate constant), hr^{-1}	1.1
$C_{ac,max,1}$ (Site 1 sorption site density), mol/g	5×10^{-8}
$k_{ac,2}$ (Site 2 sorption rate constant), ml/g-hr	10
$k_{ca,2}$ (Site 2 desorption rate constant), hr^{-1}	0.0001
$C_{ac,max,2}$ (Site 2 sorption site density), mol/g	7×10^{-9}

Note that the ratio of the sorption to desorption rate constant corresponds to a K_d value (ml/g).

The results of the third sorption experiment involving the sorption of ^{137}Cs onto the bentonite colloids in the presence and absence of analcime are shown in Table 5.8. The fraction bound to analcime dominates the partitioning of ^{137}Cs, although the uptake is less than in the experiments without colloids (first batch experiment with analcime). As expected, the higher solution:solid ratio (40 vs 14) results in less uptake by the analcime, and most (~80%) of the total aqueous (dissolved and colloidal) ^{137}Cs is bound to the colloids, especially in the presence of analcime. This observation supports the assumption that in the presence of analcime, all dissolved ^{137}Cs should sorb to the analcime.

Table 5.8. Results from batch sorption of ^{137}Cs bound to colloids with analcime after 96 hours and 252 hours. K_d Analcime relates the fraction of Cs on analcime to Cs in the dissolved phase and K_d Colloids relates the fraction of Cs on colloids to the Cs in the dissolved phase.

Sample-96 hours	Fraction Colloids	Fraction Analcime	Fraction Solute	K_d Analcime	K_d Colloids
0.1 g: 4 mL	0.23	0.71	0.06	442	32281
0.2 g: 2.8 mL	0.12	0.86	0.02	582	52987
No analcime	0.64	-	0.36	-	15964
252 hours					
0.1 g: 4 mL	0.20	0.74	0.06	503	30481
0.2 g: 2.8 mL	0.13	0.86	0.02	714	68588
No analcime	0.66		0.34		17780

Column Experiments

The breakthrough curves of ^{137}Cs, conservative tracer I^-, and colloids injected through the first set of analcime filled columns are shown in Figure 5.5. This experiment was designed to test the transport of Cs in association with colloids at the early stages of the equilibration of Cs with the colloids. The first green circle at about just a few hours in Figure 5.4 indicates the state of the Cs equilibrium associated with the start of the first column experiments. The colloid concentration and conservative tracer indicate that the breakthrough occurs rapidly through the first column. The concentration of the colloids and tracer reach the injection solution rapidly. The ^{137}Cs concentrations, however reach a maximum value of only 4.5% of the initial concentration injected (Figure 5.5). This value is less than the fraction recovered from the batch experiments (Table 5.8), but the solution to solid ratio is much less in the column experiments than in the batch experiments.

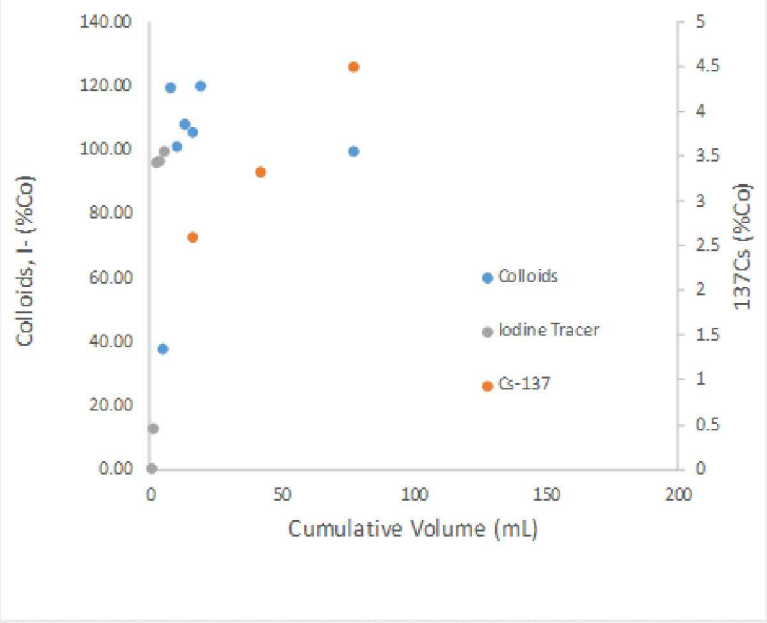

Figure 5.5. Breakthrough curves of ^{137}Cs, colloids, and conservative tracer I^- from the injection of Cs equilibrated with FEBEX colloids from ~4 hours.

The breakthrough of the sequential experiment performed by injecting the elutions collected from the first column into a new column is shown in Figure 5.6. The ^{137}Cs concentration of the combined eluent through the first column was only ~36 cpm/mL (Table 5.5), and when this fraction was injected into a second analcime column (Figure 5.6), no ^{137}Cs was recovered. Model interpretations for the first set of columns was not performed because of the low levels of Cs recovered in the first column and the complete stripping of Cs from colloids in the second column.

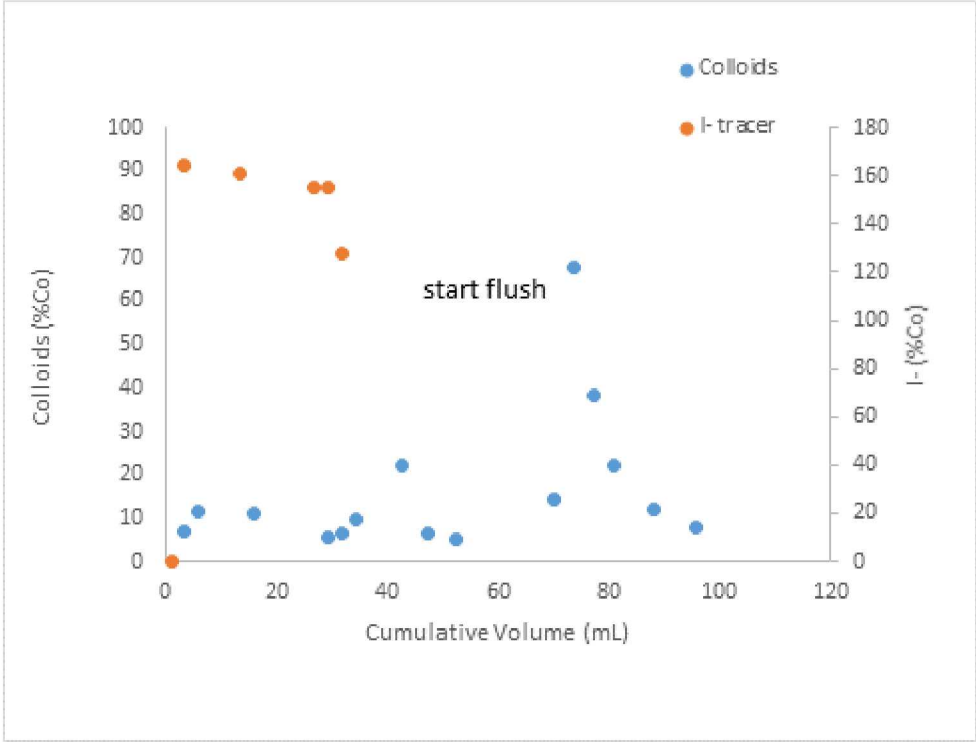

Figure 5.6. Breakthrough curves of ^{137}Cs, colloids, and conservative tracer I^- from the sequential injection of the solution eluted from the first column (Figure 5. 5) into a second column.

Note that only ~10% of the colloids were recovered from the second column, indicating significant filtration of the colloids by the analcime column. It is not clear why the colloids were strongly filtered through the second column. We hypothesize that it was because some of the Na that initially occupied cation exchange sites on the bentonite colloids exchanged with Ca from the analcime during the first column experiment and destabilized the colloid suspension causing grater filtration. We also hypothesized that some of the filtration could be due to a change of the colloid properties including size distribution and surface charge. This is possible if the analcime releases colloids to the solution and alters the nature of the colloidal suspension. To check this hypothesis, we performed the characterization of the size distribution of the colloidal suspension before injection into the analcime column and after elution from the column. Zeta potential and size distribution measurements were performed on the colloid stock solutions injected through the column (top 700 mL) and the colloidal fractions collected from the outlet of column. The data in Figure 5.7 show a plot of the size distribution of the colloidal suspension injected through the column. Sonication for 15 min did not affect the size distribution.

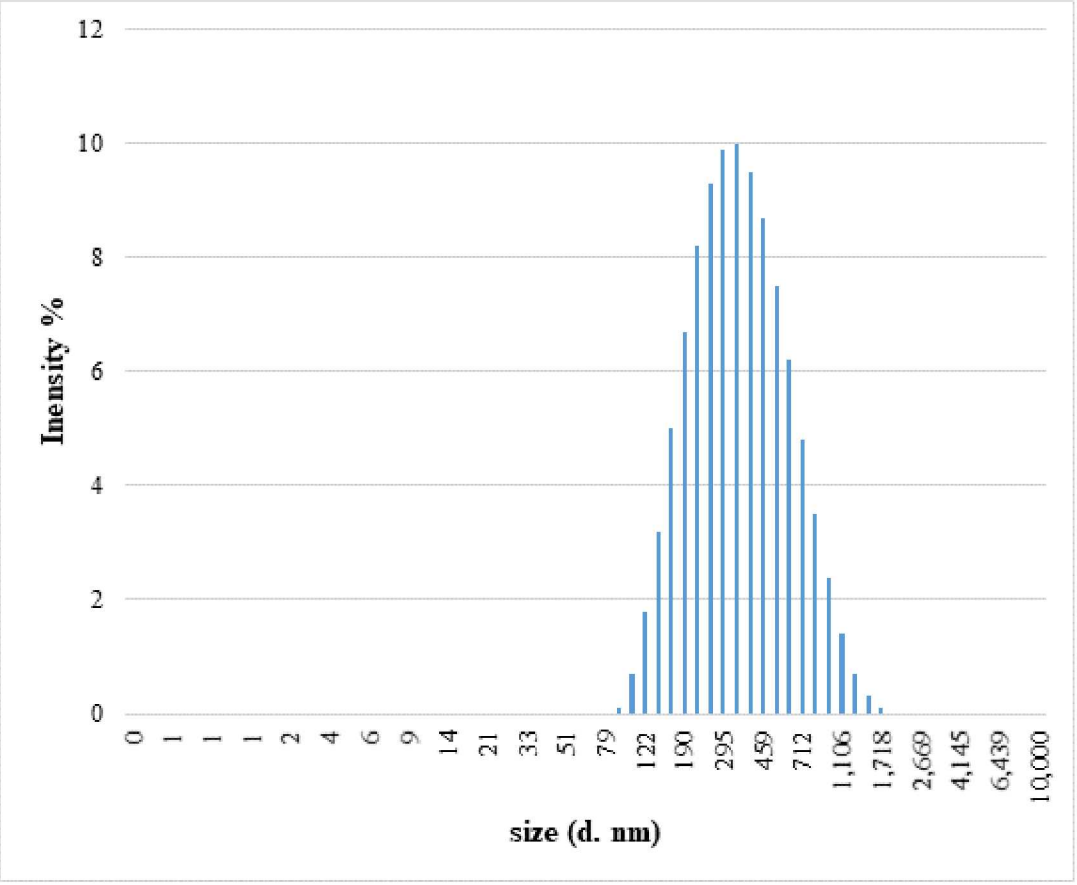

Figure 5.7. Size distribution of the bentonite colloids injected through the column. Colloids in the top 700 mL.

The colloidal suspension registered a broad distribution of sizes ranging from 100 to 1700 nm and remained stable. The suspension was stable with no visible settling. The colloidal suspension exhibited a strong negative zeta potential at pH of ~ 8. The average zeta potential of 100 measurements recorded three times for the un-sonicated suspensions is -27.3 ± 3 mV. The average zeta potential for the sonicated solution was slightly more negative ζ= -35.4 ± 3 mV. The negative zeta potential recorded is what would be expected for the silicate/colloids at neutral pH and is in agreement with the values reported in the literature (Stenger et al., 2005; Swartzen-Allen & Matijević, 1974). The slight shift toward more negative values with sonication is also in agreement with previous investigation (Mekhamer, 2010) and is indicative of the strong repulsion between particles. The high negative zeta potentials are also an indication of the stability of colloidal suspensions prepared.

The size distribution of the colloids contained in the fractions exiting the column was very similar to the size distribution in the suspension injected through the column. We did not record any visible size distribution changes or reduction in the colloid counts. The average zeta potential at pH ~8 of the colloidal fractions that transported through the column un-sonicated ζ= -23.0 ± 3 mV and ζ= -35.4 ± 3 mV is very similar to that of the injected suspensions. The data indicate that the colloidal suspension that transported through the column did not change to any degree that would explain the significant filtration observed during the sequential injection into a second column.

The results of the second column experiment designed to test the transport of Cs in association with colloids after a longer equilibration time are shown in Figure 5.8. Modeling of the breakthrough results is also presented in Figures 5.8. The second green circle at about 1200 hours in Figure 5.4 indicates the state of the Cs equilibrium associated with the start of the second column experiments. The fraction of total adsorbed ^{137}Cs that is predicted by the model to be adsorbed to the stronger sorption site over time is also shown in Figure 5.4. It is apparent that more than twice as much ^{137}Cs is predicted to be adsorbed to the stronger site at the time the second set of column experiments was initiated relative to the first set of experiments, which may explain why no ^{137}Cs was detected in the eluents from the second column in the first set of column experiments, whereas more Cs is eluted in the second column of the second series of column experiments. The breakthrough curves show that the colloids and conservative tracer reach saturation very rapidly. Cs also breaks through very rapidly and its breakthrough profile matches the breakthrough of the colloids and conservative tracer. The maximum fraction of Cs eluted from the column increased from 1.7% to 2.7% towards the later stages of the injection. Note that there is some apparent loss of colloids due to filtration.

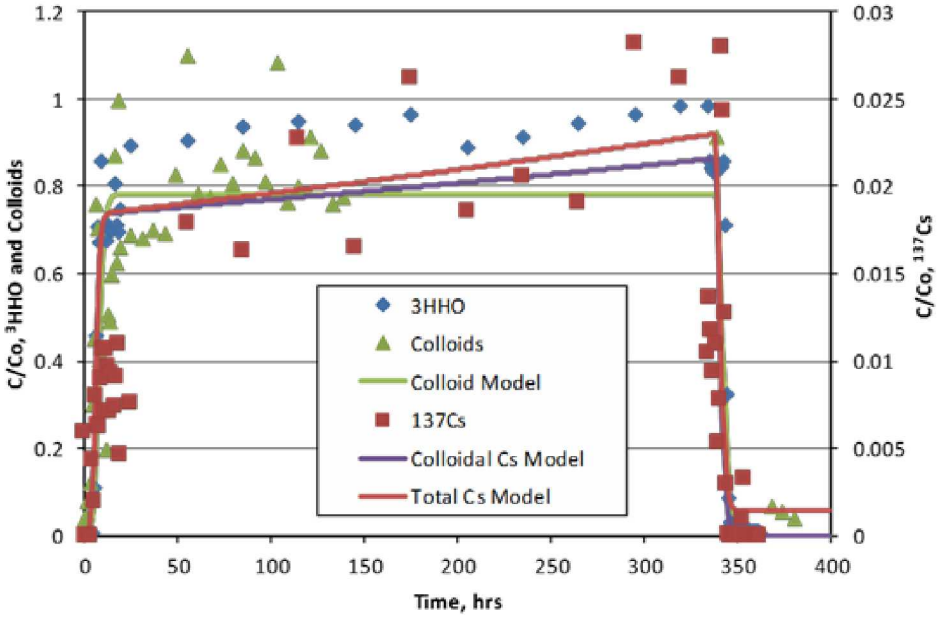

Figure 5.8. Observed and modeled breakthrough curves of ^{3}HHO, bentonite colloids and ^{137}Cs in first column experiment, expressed as normalized concentrations (C_o = injection concentration). Note that ^{137}Cs concentrations are referenced to right vertical axis. The ^{137}Cs desorption rate constant for the second colloid sorption site was increased to 0.4 hr^{-1} to match the ^{137}Cs data, but all other parameters were the same as in Table 5.7.

Model interpretations of column experiment assumed a cesium concentration of the computed starting concentration of 4 x 10^{-10} M Cs (the actual measured concentration is 6.5x10^{-10}). The model interpretation assumed a two-site sorption model on the colloids. The model assumes a rapid initial sorption with rapidly established equilibrium and a second slower sorption process. When the sorption parameters of Table 5.7 were used to model the first column of the second set of column experiments, the fraction of ^{137}Cs recovered from the column was over predicted by nearly an order of magnitude. This result was not surprising given that the amount of ^{137}Cs remaining adsorbed to the bentonite colloids after contact with the analcime in the

competitive batch experiments was much less than would have been predicted using the parameters of Table 5.7 (especially considering the large fraction of ^{137}Cs adsorbed to the second site when the competitive experiments started). It was found that to obtain a reasonable match to the ^{137}Cs breakthrough curve in the first column experiment, it was necessary to increase the desorption rate constant of the second sorption site on the colloids to 0.4 hr^{-1} (i.e., an increase of more than 3 orders of magnitude). All other sorption parameters were assumed to be the same as those in Table 5.7. The resulting match to the column data is shown in Figure 5.8. Note that ^{137}Cs adsorption onto the analcime in the column was assumed to be rapid and reversible, with an effective K_d value of 500 ml/g, approximately the K_d value observed in the competitive batch sorption experiments (Table 5.6). Also, an irreversible colloid filtration rate constant of 0.031 hr^{-1} was used to account for the incomplete recovery of the colloids (with any ^{137}Cs adsorbed to the colloids being likewise filtered, but free to desorb from the filtered colloids).

The results and modeling of the sequential injection in the second series of column experiments are shown in Figure 5.9.

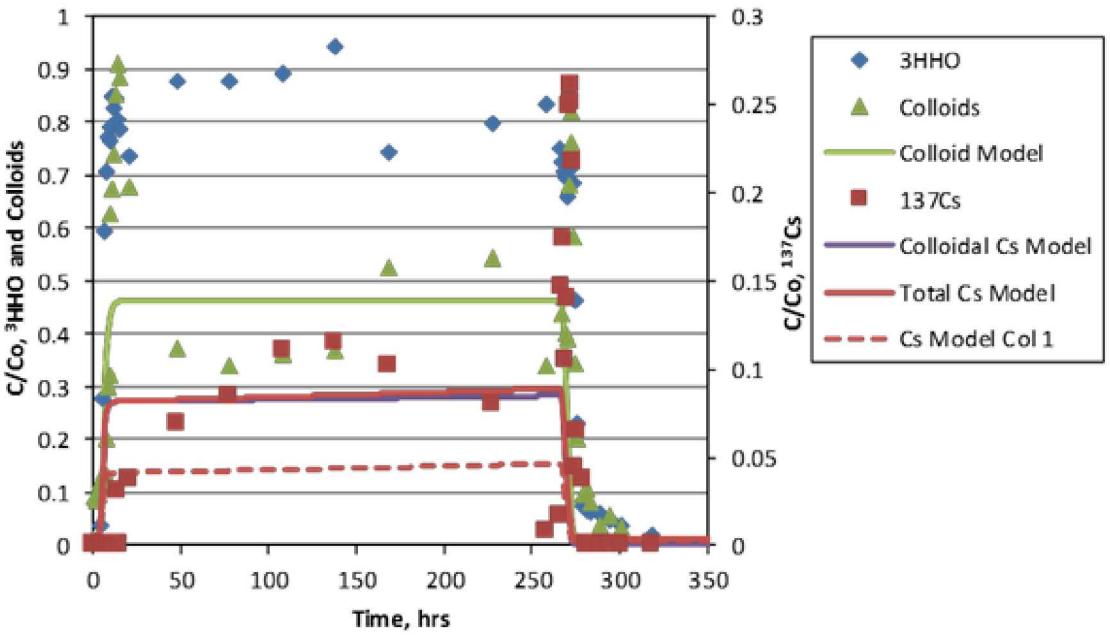

Figure 5.9. Observed and modeled breakthrough curves of ^{3}HHO, bentonite colloids and ^{137}Cs in second column experiment, expressed as normalized concentrations. The ^{137}Cs desorption rate constant for the second colloid sorption site was decreased from 0.4 hr^{-1} (from the first column experiment) to 0.27 hr^{-1} to match the ^{137}Cs data. Dashed line shows ^{137}Cs model predictions using desorption rate constant from first column experiment. All other sorption parameters were the same as in Table 5.7.

Significant scatter of the colloids is observed during the initial and late stages of the injection and is attributed to a series of restarts of the injection pump. Note also a significant loss of colloids relative to the injection solution. Cs is also removed but at much lower rate than in the previous injection. Before modeling the sequential injection results, the ^{137}Cs that was predicted to be in the solution phase in the eluent from the first column was allowed to re-equilibrate (in the model) with the first sorption site on the colloids, but the ^{137}Cs predicted to be adsorbed to the second colloid site was not re-equilibrated. The second site was

not re-equilibrated because after the solution exited the first column, it was assumed that the desorption rate from the second site reverted back to the low value deduced from the bentonite-only batch experiment (0.0001 hr^{-1}), which was much too low for any appreciable desorption to occur in the 2 weeks between the two column experiments. When the second column was modeled using the same sorption parameters as the first column (albeit with a much lower overall ^{137}Cs concentrations), the model underpredicted the amount of ^{137}Cs recovered by about a factor of 2. The desorption rate constant for the second site had to be reduced from 0.4 hr^{-1} to 0.27 hr^{-1} to achieve a good match to the data, as shown in Figure 5.9.

Note that in this case, the irreversible colloid filtration rate constant was increased from 0.031 hr^{-1} to 0.115 hr^{-1} to account for the significantly lower recovery of colloids in the second column compared to the first column. It is unclear why there was more colloid filtration in the second column relative to the first. This was also observed in the first series of columns and is attributed to the Na exchange from the colloids with Ca from the analcime during the first column which destabilizes the colloidal suspension. Ca-exchanged bentonite is known to be much less stable as colloids than Na-exchanged bentonite (Birgersson et al., 2009), and these less stable colloids would be much more likely to be filtered. The model parameters used for the model curves of Figures 5.8 and 5.9 that are not already listed in Table 5.7 are listed in Table 5.9.

Table 5.9. Model parameters used for the model curves shown in Figures 5.8 and 5.9.

Parameter	Column 1	Column 2
Mean residence time, hr	8	7
Peclet number (length/dispersivity in column)	24	20
Column porosity	0.5	0.5
K_d value for ^{137}Cs on analcime (ml/g)	500	500
k_{filt} (Colloid filtration rate constant), hr^{-1}	0.031	0.115
$k_{ca,2}$ (Site 2 desorption rate constant), hr^{-1}	0.4	0.27
Initial fraction ^{137}Cs sorbed to colloid site 2	0.365	0.87

Note: Refer to Table 5.7 for all parameters not listed in this table.

5.4 Discussion

The column experiments, and also the competitive batch sorption experiments, showed that the analcime was very effective at "stripping" ^{137}Cs off the bentonite colloids and thus revealing sorption reversibility that was not otherwise apparent from the bentonite-only batch experiments. We believe that we interrogated stronger ^{137}Cs sorption sites on the bentonite colloids than in the experiments of Dittrich & Reimus (2015) because of the much lower overall Cs concentrations in the current experiments due to the use of the "low-carrier" ^{137}Cs source. This was reflected in the higher overall partitioning of ^{137}Cs to the bentonite colloids in the current batch experiments (about 75% sorbed after 1200 hours) relative to the batch experiments of Dittrich and Reimus (about 25% sorbed). It was also reflected in the sorption parameters of the "weaker" of the two sorption sites on the colloids in the two sets of experiments, with Dittrich and Reimus (2015) reporting a K_d value for the weaker site that was more than a factor of 4 less than the K_d value of the weaker site in the current experiments. The "aging" effect observed in the bentonite-only batch experiments of this study indicate that the sorption rate onto the second "stronger" colloid sorption site is very slow compared to the rate onto the first site. An aging effect was not observed in the experiments of Dittrich and Reimus (2015), presumably because their observed ^{137}Cs partitioning was dominated by high- abundance weak sites that swamped any ability to observe the effects of the stronger sites.

The increased apparent K_d values of the ^{137}Cs on the bentonite colloids in the competitive batch experiments with increasing ratios of analcime to bentonite (Table 5.6) is taken to reflect a greater influence of the stronger sorption sites on the colloids as the amount of ^{137}Cs on the colloids decreases. The ^{137}Cs transport behavior in the two column experiments also reflects this. The fact that the desorption rate constant for the second colloid sorption site had to be decreased slightly from the first column to the second column to match the observed breakthrough curves suggests that as more ^{137}Cs is stripped off the colloids, the remaining ^{137}Cs is associated with ever-stronger sites. The implication of having to change the desorption rate constant of the second site to match both sets of column data is not that the desorption rate from the second site changed in the second column, but rather that there are actually more than two types of sites on the colloids, with each successive site being stronger but less abundant. Although no attempt was made to model the column data with three colloid sorption sites, we are confident that a three-site model could fit both column data sets and the bentonite-only batch experiments with a single set of sorption parameters. However, we also believe that if a third column experiment were conducted using the eluent from the second column as the injection solution, it is likely that a fourth sorption site would be needed because the apparent ^{137}Cs desorption rate from the strongest site on the colloids would decrease further still. In reality, there may be a large number of sorption sites with different site strengths on colloids that would only be revealed by conducting ever more sequential experiments. A third column experiment was not attempted here because ^{137}Cs concentrations, as measured by liquid scintillation counting, were already approaching background levels in the eluent from the second column, and it was also anticipated that more colloid filtration would be observed in a third column. In hindsight, a flow interruption during the second column experiment may have provided interrogation of stronger sorption sites on the colloids.

While we did not carry out experiments to interrogate the very strongest ^{137}Cs sorption sites on the bentonite colloids, or answer the question of whether there is some ^{137}Cs that is effectively irreversibly-adsorbed to the colloids, we believe that we successfully demonstrated a method that could effectively address these issues given enough time and sensitive enough analytical measurements. The sequential injections of colloid-borne radionuclide solutions through successive columns packed with a material that has a high affinity for the radionuclide was shown to accelerate the process of desorption from colloids. Even if the column packing material does not represent a geologic material expected to be abundant downgradient of a repository, our hypothesis is that any radionuclide mass fraction that can be effectively stripped from colloids over the short time and distance scales of a laboratory experiment is unlikely to be transported over long distances and times from a repository. However, additional research is needed to determine how best to translate the results of laboratory experiments such as these to transport predictions over long time and distance scales. We also showed an apparent aging effect in the case of ^{137}Cs sorption to bentonite colloids, where the longer the ^{137}Cs was in contact with the bentonite, the more strongly some of ^{137}Cs seemed to be adsorbed to the colloids (or perhaps the greater the fraction of strongly-sorbed ^{137}Cs). As with our previous efforts for the Spent Fuel and Waste Systems Technology program, the methods demonstrated here are considered to be of greater value than the actual results obtained. The methods should prove useful for the parameterization of colloid-facilitated transport models in repository performance assessments, particularly after design-specific and site-specific information becomes available to allow the experiments to be tailored to address specific issues.

5.5 References

Allard, B., Karlsson, M., Tullborg, E., & Larson, S. Å., 1983. Ion exchange capacities and surface areas of some major components and common fracture filling materials of igneous rocks. Svensk Kaernbraenslefoersoerjning AB (No. SKBF-KBS-TR--83-64). Retrieved from https://inis.iaea.org/collection/NCLCollectionStore/_Public/15/034/15034310.pdf.

Ames, Jr., L. L., 1966. Mineralogical notes. The American Mineralogist, 51, 903–909. https://doi.org/10.1080/11035891609444411.

Birgersson, M., Börgesson, L., Hedström, M., Karnland, O., & Nilsson, U., 2009. Svensk Kärnbränslehantering AB Bentonite erosion Final report Bentonite erosion-Final report. Swedish Nuclear Fuel and Waste Management Co. (Vol. SKB-TR-09-). Retrieved from www.skb.se.

Bostick, B. C., Murthy A., Vairavamurthy, K. G., Karthikeyan, and Chorover, J. 2002. Cesium Adsorption on Clay Minerals: An EXAFS Spectroscopic Investigation. Environ. Sci. Technol, 36, 2670–2676. https://doi.org/10.1021/es0156892

Cheshire, M. C., Caporuscio, F. A., Rearick, M. S., Jové-Colón, C., & McCarney, M. K., 2014. Bentonite evolution at elevated pressures and temperatures: An experimental study for generic nuclear repository designs. American Mineralogist, 99(8–9), 1662–1675. https://doi.org/10.2138/am.2014.4673.

Cornell, R. M., 1993. Adsorption of cesium on clay minerals. Journal of Radioanalytical and Nuclear Chemistry, 171(2), 483–500.

De Koning, A., Konoplev, A. V, & Comans, R. N. J., 2007. Measuring the specific caesium sorption capacity of soils, sediments and clay minerals. Applied Geochemistry, 22, 219–229. https://doi.org/10.1016/j.apgeochem.2006.07.013.

Dittrich, T. M., & Reimus, P. W., 2015. Colloid-Facilitated Transport of ^{137}Cs in Fracture-Fill Material: Experiments and Modeling. LA-UR-15-28482. Los Alamos National Laboratory.

Dittrich, T. M., Reimus, P. W., & Ware, S. D., 2015. Mini-columns for Conducting Breakthrough Experiments: Design and Construction. LA-UR-15-24392.

Erdem, E., Karapinar, N., & Donat, R., 2004. The removal of heavy metal cations by natural zeolites. Journal of Colloid and Interface Science, 280(2), 309–314. https://doi.org/10.1016/j.jcis.2004.08.028.

Mekhamer, W. K., 2010. The colloidal stability of raw bentonite deformed mechanically by ultrasound. Journal of Saudi Chemical Society, 14, 301–306. https://doi.org/10.1016/j.jscs.2010.04.013.

Missana, T., García-Gutiérrez, M., & Alonso, Ú., 2004. Kinetics and irreversibility of cesium and uranium sorption onto bentonite colloids in a deep granitic environment. Applied Clay Science, 26(1–4), 137– 150. https://doi.org/10.1016/j.clay.2003.09.008.

Murali, M. S., & Mathur, J. N., 2002. Sorption characteristics of Am(III), Sr(II) and Cs(I) on bentonite and granite. Journal of Radioanalytical and Nuclear Chemistry (Vol. 254). Retrieved from https://link.springer.com/content/pdf/10.1023%2FA%3A1020858001845.pdf

Murota, K., Saito, T., & Tanaka, S., 2016. Desorption kinetics of cesium from Fukushima soils. Journal of Environmental Radioactivity, 153, 134–140. https://doi.org/10.1016/j.jenvrad.2015.12.013

Rani, R. D., & Sasidhar, P., 2012. Sorption of Cesium on Clay Colloids: Kinetic and Thermodynamic Studies. Aquatic Geochemistry, 18(4), 281–296. https://doi.org/10.1007/s10498-012-9163-6

Reimus, P. W., 2017. Mathematical Basis and Test Cases for Colloid-Facilitated Radionuclide Transport Modeling in GDSA-PFLOTRAN Intended for. Los Alamos National Laboratory, LA-UR-26560. Retrieved from https://permalink.lanl.gov/object/tr?what=info:lanl-repo/lareport/LA-UR-17-26560

Reimus, P. W., & Boukhalfa, H., 2014. Chancellor Water Colloids : Characterization and Radionuclide Associated Transport. Los Alamos National Laboratory (LA-UR-14-27538).

Reimus, P. W., Zavarin, M., & Wang, Y., 2017. Colloid-Facilitated Radionuclide Transport: Current State of Knowledge from a Nuclear Waste Repository Risk Assessment Perspective. Los Alamos National Laboratory (LA-UR-16-26638). Retrieved from https://permalink.lanl.gov/object/tr?what=info:lanl- repo/lareport/LA-UR-16-26638.

Shenber, M. A., & Eriksson, Å., 1993. Sorption behaviour of caesium in various soils. Journal of Environmental Radioactivity, 19(1), 41–51. https://doi.org/10.1016/0265-931X(93)90057-E.

Steefel, C. I., Carroll, S., Zhao, P., & Roberts, S., 2003. Cesium migration in Hanford sediment: a multisite cation exchange model based on laboratory transport experiments. Journal of Contaminant Hydrology, 67, 219–246. https://doi.org/10.1016/S0169-7722(03)00033-0.

Stenger, F., Mende, S., Schwedes, J., & Peukert, W., 2005. Nanomilling in stirred media mills. Chemical Engineering Science, 60, 4557–4565. https://doi.org/10.1016/j.ces.2005.02.057.

Swartzen-Allen, S. L., & Matijević, E., 1974. Surface and Colloid Chemistry of Clays. Chemical Reviews, 74(3), 385–400. Retrieved from https://pubs.acs.org/sharingguidelines.

Wang, Y., 2015. Used Fuel Disposal in Crystalline Rocks. FY15 Progress Report. Sandia National Laboratories. FCRD-UFD-2015-000125. https://doi.org/10.2172/1229704.

Zachara, J. M., Smith, S. C., Liu, C., McKinley, J. P., Serne, R. J., & Gassman, P. L., 2002. Sorption of Cs+ to micaceous subsurface sediments from the Hanford site, USA. Geochimica et Cosmochimica Acta, 66(2), 193–211. https://doi.org/10.1016/S0016-7037(01)00759-1.

Zhuang, J., Flury, M., & Jin, Y., 2003. Colloid-Facilitated Cs Transport through Water-Saturated Hanford Sediment and Ottawa Sand. Environmental Science and Technology, 37(21), 4905–4911. https://doi.org/10.1021/es0264504.

6. MICRO FRACTURE FLOW SIMULATION USING DISCRETE FRACTURE NETWORK MODEL

6.1 Introduction

Long Term Sorption Diffusion Experiments (LTDE) have been conducted in Sweden and focused on tracer transport in the stagnant pore water of the rock matrix. In the in-situ experiment, a cocktail of both sorbing and non-sorbing tracers was allowed to contact a natural fracture surface, as well as the unaltered rock matrix, for a time period of 200 days (Lofgen et al. 2015).

Analyzing the shape of the tracer penetration profiles observed in the experiment and comparing it to the predicted general shape of a 1D diffusion model, vastly different behavior was observed for the natural fracture surfaces and for the unaltered rock matrix. Figure 6.1 shows the measured experimental shapes of Cs penetration profile (symbols) and modeled penetration profile (dashed line). In order to understand the differences in the behavior, certain features of the samples and processes that are not included in the modeling should be considered (Lofgen et al. 2015; Widestrand et al. 2010).

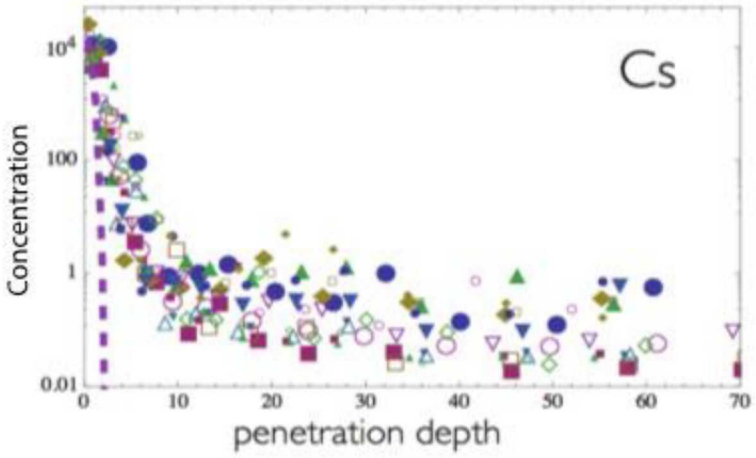

Figure 6.1. The measured experimental shapes of Cs penetration profile (symbols) do not satisfy modeled penetration profile (dashed line).

Our study focuses on understanding how micro fractures, which provide faster transport paths, affect the penetration profile. The micro fractures were observed in different slices of the sample core. Several slices of the individual cores had micro fractures that were fresh and consequently they were likely newly formed, i.e. induced by drilling or stress release (Nilsson K. et al. 2010, p. 38). The surface of micro fractures forms an external damage layer of the sample. The existence of micro structure may change an interpretation of the obtained experimental results and suggests including advective term into a modeling approach, where micro fractures play a leading role in tracer movement through the sample.

A Discrete Fracture Network (DFN) model is used to investigate the contribution of advective transport into the penetration profile of tracer, as well as diffusion through fracture surface. Recently developed at Los Alamos National Laboratory, dfnWorks (Hyman et al., 2015a), is a parallelized computational suite based on the DFN modeling approach. It has been successfully applied for multiple subsurface flow and

transport applications (Hadgu, et al., 2017; Hyman et al., 2016a; Karra et al., 2018; Mudunuru et al., 2017). We have applied dfnWorks to the problems associated with contaminant transport in nuclear waste repositories (Hyman et al., 2015b) and natural gas production from fractured reservoirs (Karra et al., 2015; Hyman et al., 2016b). Here, dfnWorks is applied to micro fracture modeling for the first time.

In the DFN modelling approach, the transport through fracture networks, where fractures are planar polygons that intersect each other in a 3D simulation domain, is usually used to simulate advection through fractured rock. Diffusion into the matrix is usually ignored in the DFN approach. The Time Domain Random Walk (TDRW) technique is implemented into existent Lagrangian particle tracking code in order to include diffusion between fractures surface and the rock matrix. The TDRW particle tracking is simulated in micro fractured DFN and the obtained penetration profile of the particles is compared to LTDE results (Fig. 6.1).

6.2 Methodology

6.2.1 dfnWorks: DFN Modeling Suite

The DFN approach represents individual fractures as two-dimensional planar objects, placed in a three-dimensional domain, intersecting each other and forming fracture networks. Fractures are generated according to fracture network characteristics extracted from site-specific geological observations. The dfnWorks suite can be used to generate fractures at scales ranging from millimeters to kilometers. Each fracture in the network is assigned a shape, location, aperture, and orientation on the basis of geological evidence and observation. The individual fractures are generated using Feature Rejection Algorithm for Meshing (FRAM) (Hyman et al., 2014), which guarantees that the DFN does not have any small features, such as, length of intersections between fractures and distance between lines of intersection of a fracture, smaller than a user-defined minimum length scale. This restriction provides a firm lower bound on the required mesh resolution, and special care is taken so that prescribed geological statistics are not affected by this restriction. The final DFN mesh is a conforming Delaunay triangulation, which provides a framework for control volume flow solutions that obey mass conservation law and prevent non-physical sources, sinks or stagnation points. The mesh of intersecting fractures is coincident along fracture intersection lines, where control volumes are split into four pieces, and the transport velocity is reconstructed independently on each piece, representing flow direction on fracture intersection explicitly. This method supports Lagrangian particle tracking modeling (Makedonska et al., 2015; Makedonska et al., 2016).

In the current work dfnWorks is used for micro fractures simulations for a first time. The developed capability to vary fracture intensity in horizontal layers in the simulation domain is applied to model different scenarios of micro structure in the experimental sample. There are two leading hypothesis of microstructure presence: 1) the sample has microfractures originally, before it was extracted; 2) the source of microfractures is a surface deformation of the sample, caused by extraction or drilling process. Both hypotheses are considered in our numerical experiments.

6.2.2 Input DFN Parameters

DFNs in the numerical experiments are generated according to Äspö characteristics for the fracture data, with slight modifications for micro-structure modeling:

- Domain size is 5 cm x 5 cm x 5 cm; total volume 125 cm^3.
- All fracture sizes follow Power Law distribution, where smallest fracture length is 1 mm and longest fracture length is 1 cm. The fracture shape is square.

- All fractures in the DFN are connected and provide connected path through fractures for transport.

The DFN input parameters used in DFN generation in the numerical experiments are shown in Table 6.1.

Table 6.1. Input parameters for DFN generation.

Set	Trend	Plunge	Kappa	R_{Min}	R_{Max}	Alpha	P_{32}
1	280	20	10	0.0005	0.005	2.6	650
2	20	10	15	0.0005	0.005	2.6	900
3	120	50	10	0.0005	0.005	2.6	500

A DFN realization, generated based on parameters presented in Table 6.1 is shown on Figure 6.2. Every fracture is indicated by its own color. Fractures represented as two-dimensional polygons, which are located in the three-dimensional domain and intersect each other forming one big cluster of the fracture network. Initially, fractures are generated and placed randomly into the domain, and then a connectivity check is performed and all the isolated fractures or isolated clusters are removed. This way, the remaining fracture network guarantees a connected path for transport from the in-flow boundary face to out-flow boundary face.

In our simulations we assume that the top boundary of the simulation domain is the surface of the sample and the injected tracer starts to penetrate from the surface to the core of the sample. The top boundary of the simulation domain is an in-flow boundary and represents the surface. The core, center of the sample, is represented by the bottom face of the domain, out-flow boundary. All remaining faces of the domain are no-flow boundaries.

6.2.3 Numerical Experiments

Three different DFN configurations are considered, where each of them represents one of suggested microstructure configurations:

1. Microfractures are present in the sample originally, no additional deformation at surface (Figure 6. 2).
2. Microfractures are present in the sample originally and the sample was deformed at a surface (Figure 6.3).
3. There are no original microfractures in the sample, but significant deformation at the surface (Figure 6.4).

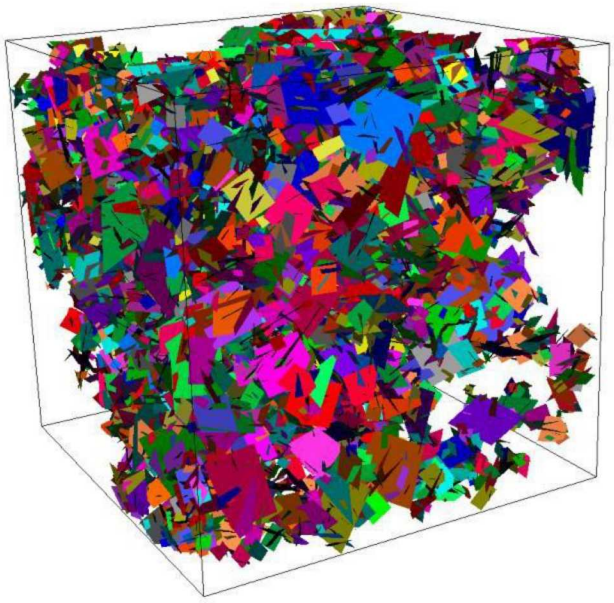

Figure 6.2. First numerical experiment: DFN realization where microfracture intensity is applied uniformly along the sample, assuming presence of original microfractures in the sample. Colors represent fractures.

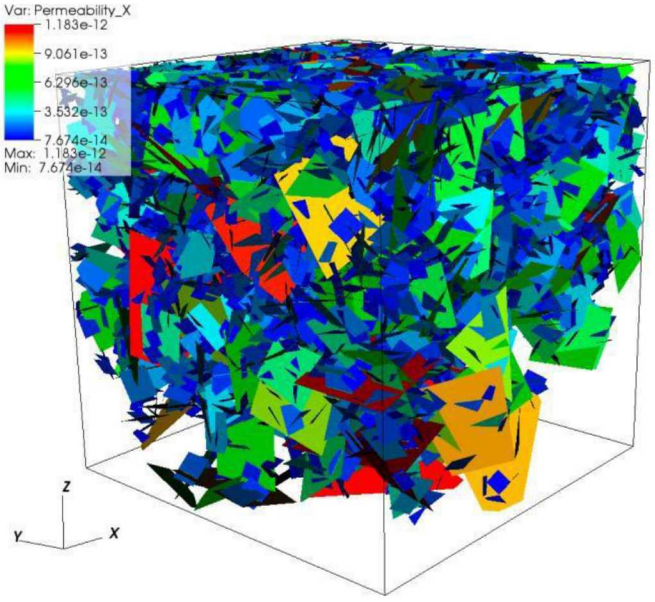

Figure 6.3. Second numerical experiment: DFN realization where microfractures are placed at surface with higher intensity; the microfracture intensity slowly decreases from surface to core, assuming both, original

presence of microfractures and sample deformation at surface. Colors show the fracture permeability profile.

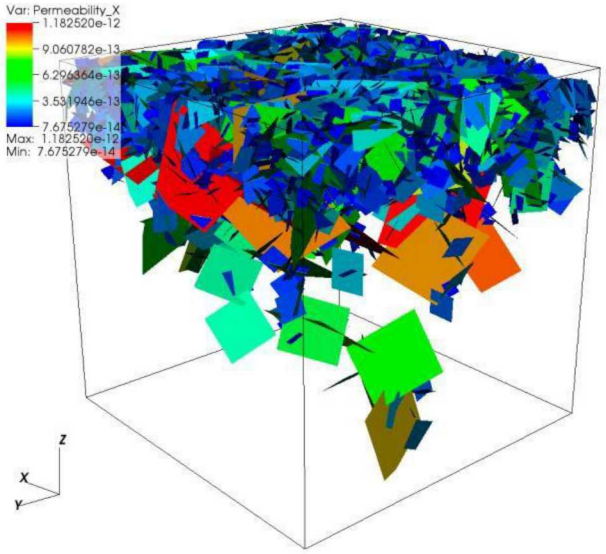

Figure 6.4. Third numerical experiment: DFN realization where microfractures are placed at surface with high intensity; the microfracture intensity rapidly decreases from surface to core, assuming no original presence of microfractures and sample deformation at surface. Colors show fracture permeability profile.

The DFN parameters (Table 1-1), such as fractures size distribution and fracture orientations, are the same in each numerical experiment. The difference is in fracture network intensity, P32, which is equal to the total surface area of fractures over volume of the simulation domain. In the first DFN configuration, numerical experiment 1, where we assume an original presence of microfractures, the fracture network intensity applies to entire simulation domain uniformly. The DFN configurations in the second and third numerical experiments has different intensity along vertical direction, assuming high intensity at the surface (top boundary of the simulation domain), where the sample was deformed, and lower intensity as we move further from surface and getting closer to the sample core (bottom boundary face). Table 6.2 shows the used intensity values. There are 5 horizontal layers in vertical direction; thickness of each layer is 1 cm.

Table 6.2. DFN intensity, P_{32}, in generated microfracture configurations

	Fracture Set 1	Fracture Set 2	Fracture Set 3
Numerical Exp. 1			
	650	900	500
Numerical Exp. 2			
Layer 1 (top, surface)	650	900	500
Layer 2	550	800	400

Layer 3	450	700	300
Layer 4	350	600	200
Layer 5 (bottom, core)	250	500	100
Numerical Exp. 3			
Layer 1 (top, surface)	650	900	500
Layer 2	325	450	250
Layer 3	220	300	180
Layer 4	160	225	125
Layer 5 (bottom, core)	150	200	110

6.2.4 Flow Solution

A massively parallel multi-physics solver PFLOTRAN (Lichtner et al., 2015 a&b) is used to obtain steady state pressure solution for fully saturated flow in all three numerical experiments described above in Section 6.2.3. The LTDE injects a tracer at a surface of a sample and measures a penetration profile from surface to the core. The same technique is used in our numerical modeling: we apply in-flow boundary conditions at a top face of the simulation domain, out-flow boundaries are defined at the bottom face, and all remaining boundary faces are no-flow conditions.

Lagrangian transport modeling in DFN simulation tools assumes that transport is driven mainly by advection. In order to compare numerical modeling with LTDE results, which is focused on diffusion processes, the advection term should be eliminated as much as possible, and the pressure difference between in-flow and out-flow boundaries should be as small as possible. In the presented numerical simulations applied pressure difference is 1 Pa, what allows simulating transport with low influence of advection. There is no gravity included in the current simulations.

6.2.5 Transport Modeling

The steady state pressure solution provides Darcy velocities of the flow on every computational cell of the DFN mesh. Lagrangian approach is used to simulate advective transport on particle tracking method on DFN (Makedonska et al, 2015). About 1.2×10^5 particles are seed onto fracture edges at in-flow boundary face. Particles are placed in equidistance between each other; there is 2×10^{-6} m distance between particles in their initial positions. Figure 6.5 shows 1000 trajectories shown mainly for visualization, which is ~0.8% of total number of released particles, obtained in the first numerical experiment, where fracture intensity is homogeneous along the sample.

In order to compare with tracer penetration profile of LTDE, we need to plot the penetration profile of particle tracking. For this purpose, the horizontal control planes, perpendicular to flow direction, are simulated: the travel time and positions of particles are captured at every control plane (Figure 6.6). There are 100 control planes in the current simulations, 5×10^{-4} m distance between planes.

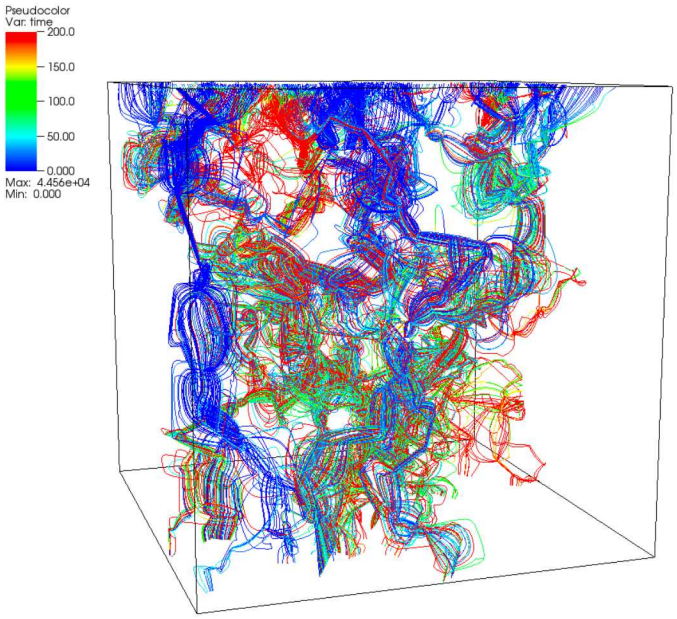

Figure 6.5. 1000 particle trajectories moving from top to bottom boundaries through micro fractures. Colors show the travel time of particles.

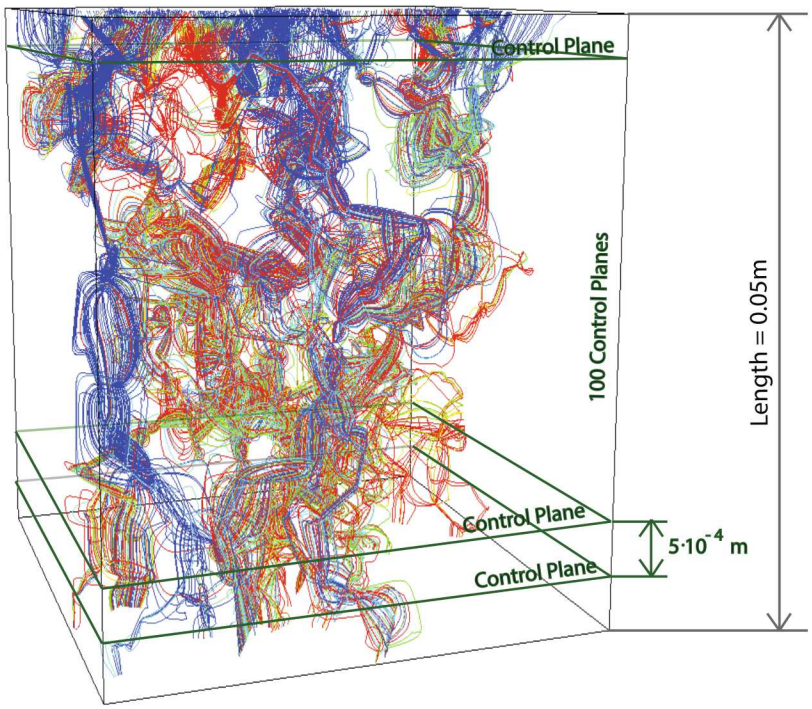

Figure 6.6. Schematic representation of control planes setup along the flow direction.

6.2.6 Time Domain Random Walk (TDRW) Approach

Time Domain Random Walk approach is implemented and used in the particle tracking modeling in micro fracture DFN. The particle travel time, T, the time that particle spends in one fracture, is calculated as a sum of two terms: 1) advective time, the time that particles spends moving in fracture with fracture flow, and 2) the time that particle spends due to diffusion process at fracture surface – matrix interaction.

$$T = T_{adv} + \left[\frac{aT_{adv}}{erfc^{-1}(r)}\right]^2, where\ a = \frac{\varphi\sqrt{D_e}}{b} \quad (6.1)$$

T_{adv} is calculated at every time step using Darcy velocities at cell centers (for details in method see Makedonska et al. 2015). The diffusion term is calculated at every fracture intersection and uses calculated T_{adv}. In equation 1, ϕ is a matrix porosity, D_e is a matrix diffusivity, m^2/s, b is a fracture aperture, m, and r is a random number from uniform distribution, *(0,1), r* is a parameter in inverse complementary error function, $erfc^{-1}$.

We use 0.25 fracture porosity and 0.001 (0.1%) of matrix porosity. Fracture aperture is calculated as function of fracture size and varies between 1.0×10^{-6} m and 3.4×10^{-6} m in DFN, and fracture permeability, calculated using cubic law, varies between 1.2×10^{-13} and 9.5×10^{-13} m^2. In each DFN configuration we consider 7 different diffusion coefficients of rock matrix, D_e, from 10^{-11} to 10^{-2} m^2/s.

Figure 6.7 shows a CCDF distribution of travel time obtained in the first numerical experiment. The plot shows two examples of TDRW with diffusion coefficients $4*10^{-11}$ m^2/s and $4*10^{-8}$ m^2/s. The results of TDRW are compared to travel time distribution of particle tracking numerical simulation where particles are driven by advection only. Particles are weighted by the input flow flux at the inflow boundary face of the simulation domain. The curve of travel time of advective transport is very close to TDRW curve with low diffusion coefficient. The contribution of diffusion process to particles travel time is plotted in Figure 6.8. Low matrix diffusivity decreases chances of particles to get into matrix through fracture surface, so most of particles are still driven mainly by advection. High diffusion coefficient slows the particles through domain and increases a chance to be absorbed into matrix through fracture surface – matrix interaction.

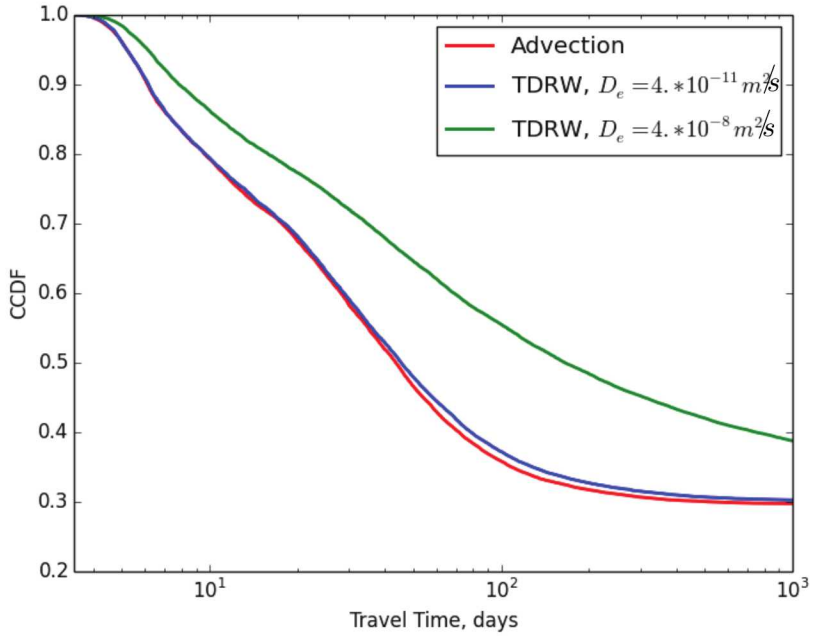

Figure 6.7. First numerical experiment. Two examples of CCDF of total travel of 1.2 x 10^5 particles participated in TDRW simulations are compared to CCDF of travel time in particle simulations, where transport is driven by advection only.

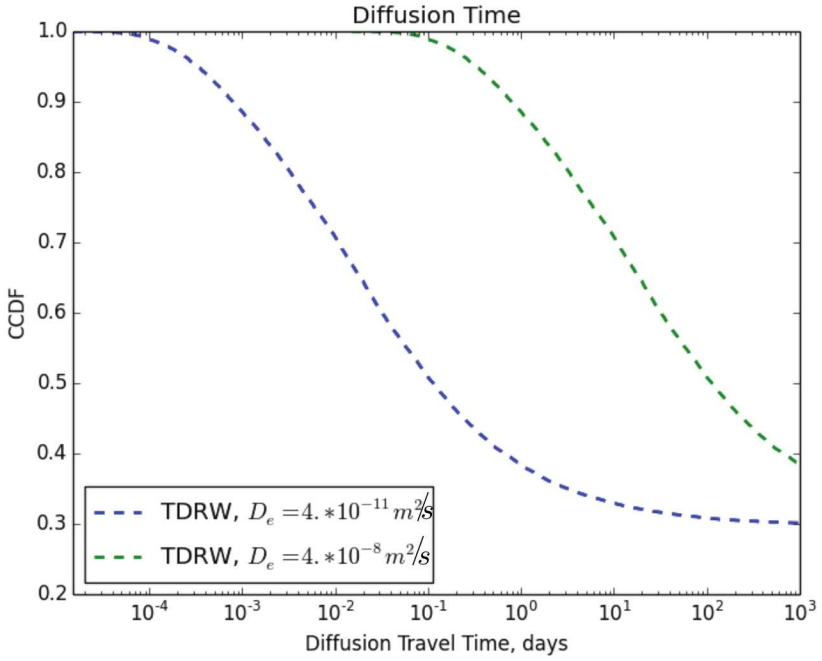

Figure 6.8. First numerical experiment. Two examples of CCDF of diffusion time of 1.2 x 10^5 particles participated in TDRW simulations.

6.3 Results

Figure 6.9 shows examples of particle trajectories in performed numerical experiments. All DFN configurations have high microfracture intensity at the top boundary, at the surface of the sample. Particles are initially distributed at the top face evenly. As the fracture intensity decreases in vertical direction from top to bottom in second and third DFN configuration, the clear channeling is observed. In the second experiment (the middle plot in Figure 6.9) particles choose preferable paths, while in the third configuration (right panel in Figure 6.9) the only path is available and particles are moving through it to the out-flow boundary.

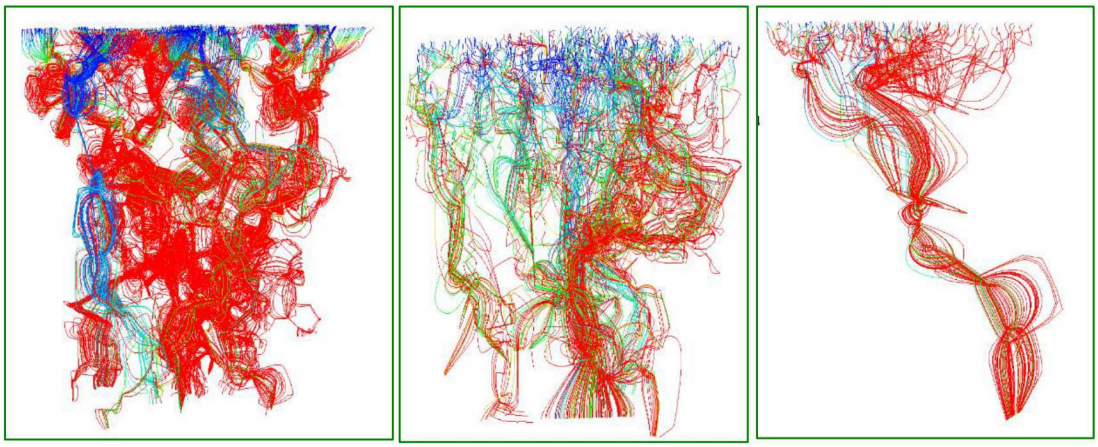

Figure 6.9. Examples of particles trajectories in three DFN configurations. As DFN intensity gets smaller (from left to right, for first, second and third numerical experiment) the clear channeling is observed for transport moving from top to bottom. The trajectories are colored by the travel time, slow trajectories are at blue colors.

The control planes technique, described above, is used to plot the particles penetration profile (Figures 6.10, 6.11, 6.12) in all three numerical experiments. The penetration profile is shown for 7 independent particle tracking simulations, where in each simulation diffusion coefficient is varied from low (10^{-11} m^2/s) to very high (10^{-2} m^2/s) value. In case of a high diffusion coefficient the advective term is almost eliminated and the particles are mostly driven by diffusion process. In Figures 6.10, 6.11, 6.12 black circles show the penetration profile with highest diffusion coefficient. The behavior is similar to those obtained before using 1D diffusion simulation and shown by pink dashed line in the plot with an experimental penetration data, Figure 6.1. As we decrease the diffusion coefficient, the advection term becomes more noticeable. In case of a lowest considered diffusion coefficient, the transport is driven mainly by advection (see Figure 6.7). As a result of advection, the penetration profile behavior is changing from a straight line (black circles) to a curve with a horizontal tail, which is similar to behavior of experimental penetration profile.

The penetration profile shows similar results in all three considered DFN configurations. In third numerical experiment, where no original micro fractures assumed, but only deformation at a surface, the penetration profile curve developed a horizontal tail at lower diffusion coefficient (10^{-6} m^2/s) than in those configurations where micro fractures are present originally.

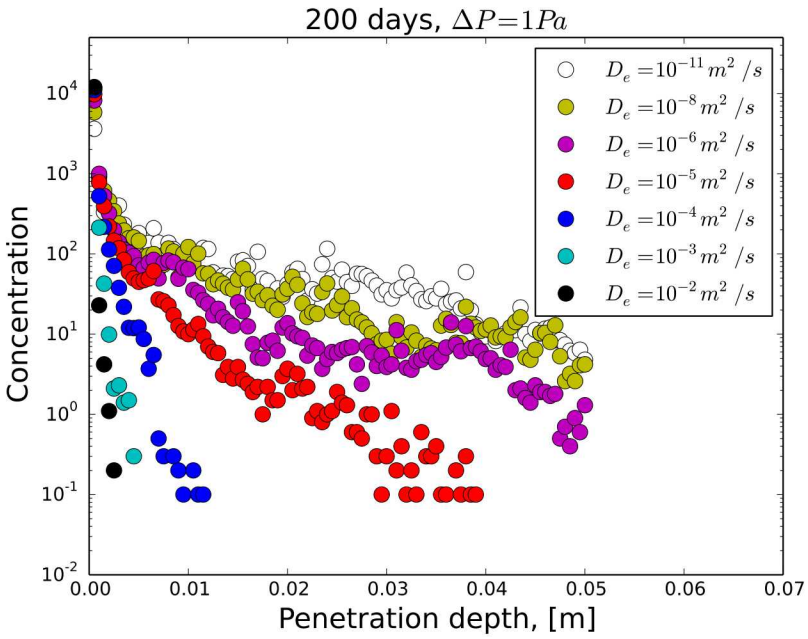

Figure 6.10. Penetration profile of particles in the First numerical experiment, where the microfractures intensity is distributed evenly in the sample.

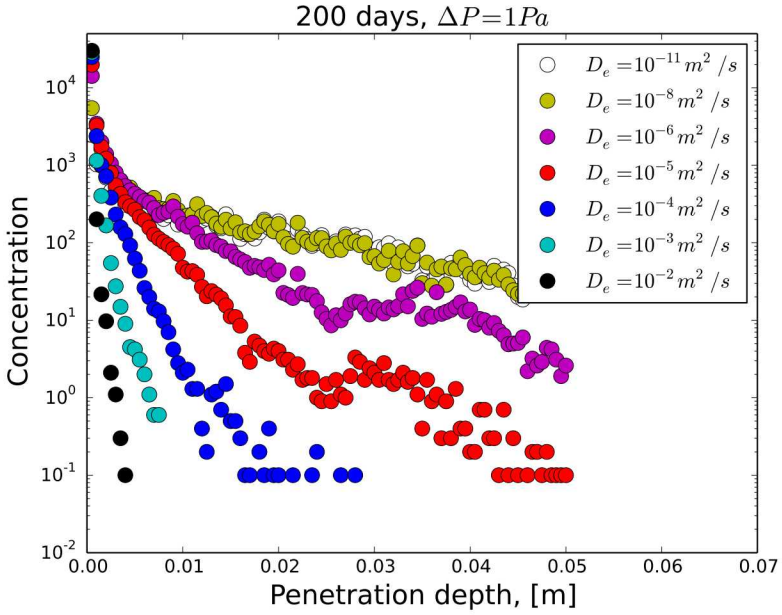

Figure 6.11. Penetration profile of particles in the Second numerical experiment, where the highest microfractures intensity is on a surface of the sample.

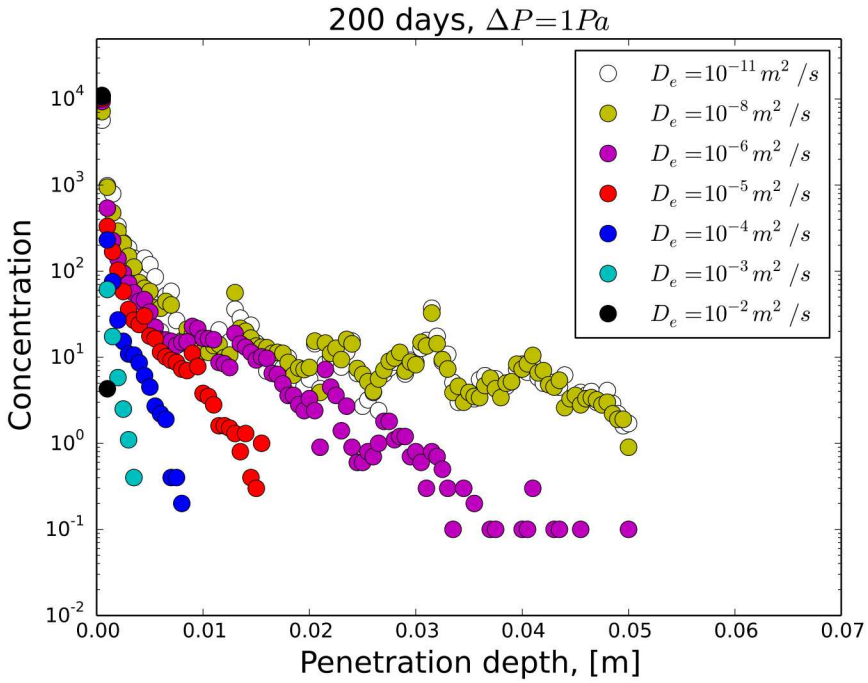

Figure 6.12. Penetration profile of particles in the Third numerical experiment, where the microfractures are present and intense on a surface of a sample.

Figure 6.13 shows a comparison of the simulated penetration profile with the experiment. From each numerical experiment we chose the results of particle tracking simulations with diffusion coefficient, which showed the closest behavior to experiment. The experimental penetration profile has a rapid drop in concentration at penetration depth ~10 cm, while numerical results have a slower decline in particle concentration. However, the developed horizontal tail of penetration profile corresponds to advective transport, proving that microfractures are present at the sample and most of the tracer are driven by both processes, advection and diffusion.

Figures 6.14, 6.15, 6.16 show the penetration profile of particles with chosen diffusion coefficient (chosen for comparison with an experimental data, Figure 6.13) at 50, 100 and 200 days after injection for all three numerical experiments. With increase in time after injection, better horizontal tail of penetration profile is developed, indicating that the slow motion of particles through microfractures and their ability to penetrate deeply into sample core.

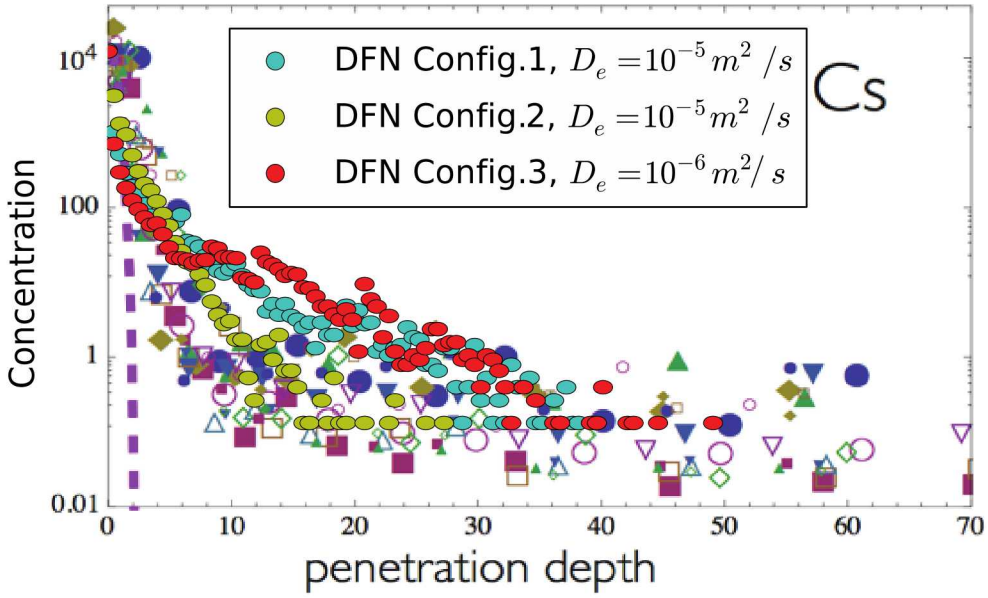

Figure 6.13. Penetration profile of experimental data is compared with simulation penetration profile for three considered DFN configurations.

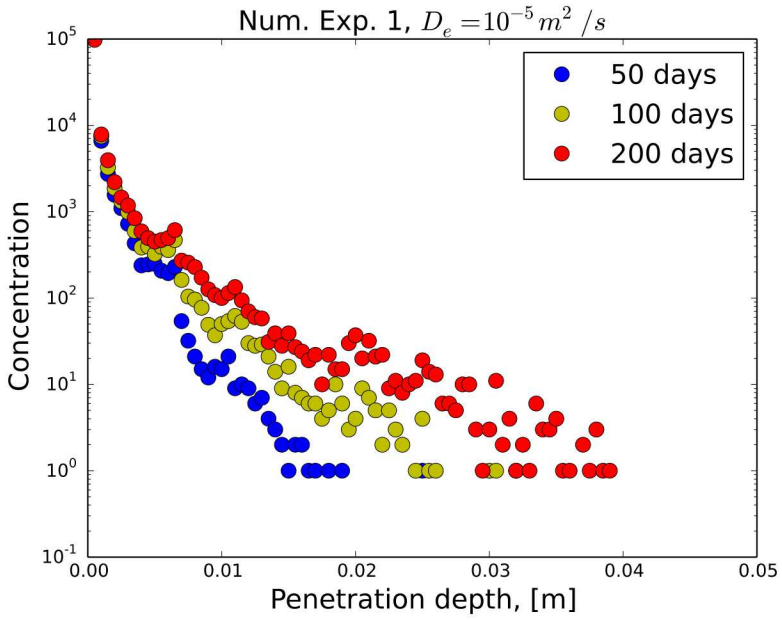

Figure 6.14. First numerical experiment. Penetration profile of particles at 50, 100 and 200 days after injection.

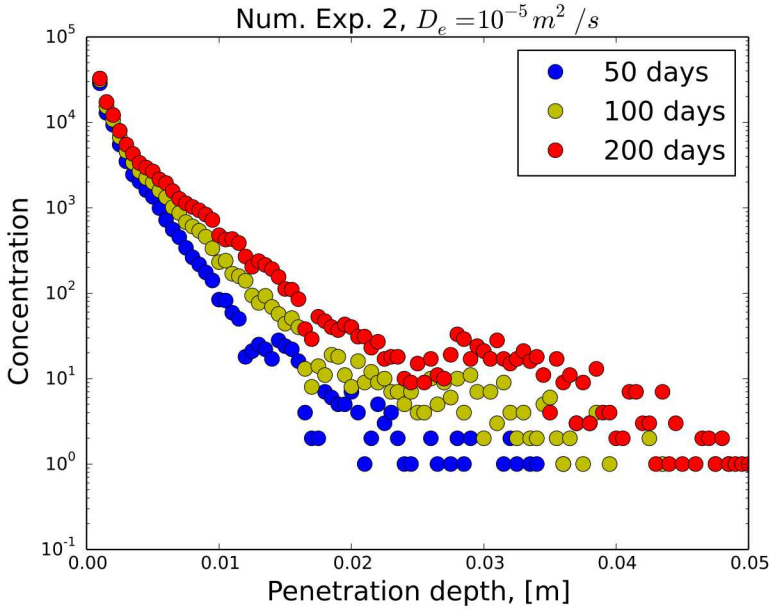

Figure 6.15. Second numerical experiment. Penetration profile of particles at 50, 100 and 200 days after injection.

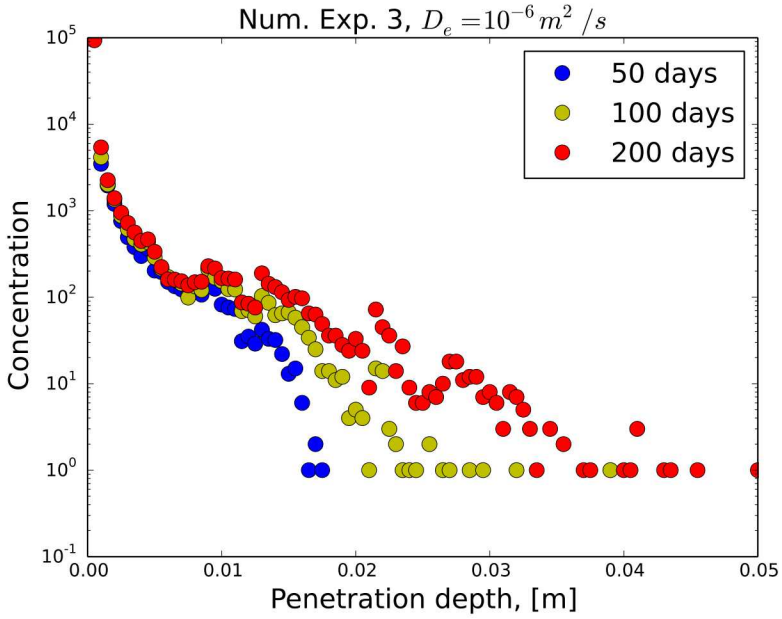

Figure 6.16. Third numerical experiment. Penetration profile of particles at 50, 100 and 200 days after injection.

6.4 Conclusion

The Discrete Fracture Network model is applied to generate different configurations of microstructure with following simulations of flow and transport. Time Domain Random Work approach is used to model particles tracking through microfractures, where particles are driven by advection and diffusion processes. The simulated penetration profile shows similar behavior with experimental data.

Three numerical experiments with different microstructure configurations are performed. The following hypothesis of microfractures appearance in the experimental sample are considered:

- Sample is originally microfractured. DFN configuration with high fracture intensity in the whole sample.
- Sample is originally microfractured but also deformed at a surface. DFN configuration with a high fracture intensity at a top boundary. P32 slightly decreases in vertical direction.
- Sample has no original microfractures but deformed at a surface. DFN configuration with a high fracture intensity at a surface. P32 dramatically decreases in vertical direction.

There is no clear dependence on DFN configuration is observed on particles penetration profile. High range of diffusion coefficients is considered in particle tracking simulations using TDRW approach. Increasing diffusion coefficient helps to eliminate advection term. Penetration profile of particles simulated with $De=10^{-2}$ m^2/s is similar to 1D diffusion simulations, performed as prediction of the experimental results. Decreasing diffusion coefficient allows emphasizing advective transport, what helps to develop a horizontal tail in the particles penetration profile. The similar behavior of simulated results with experimental data is observed at $De=10^{-5}$ m^2/s. The diffusion coefficient in the current simulations corresponds to ability of particles to diffuse into matrix through fracture surface.
The following conclusions can be made:

1. The existence of micro fractures in the sample and their leading role in tracer movement through sample cannot be neglected in simulation procedure.
2. The tracer is driven by advection as well as by diffusion in the LTDE.

6.5 References

Hadgu, T., Karra, S., Kalinina, E., Makedonska, N., Hyman, J.D., Klise, K., Viswanathan, H.S. and Wang, Y., 2017. A comparative study of discrete fracture network and equivalent continuum models for simulating flow and transport in the far field of a hypothetical nuclear waste repository in crystalline host rock. Journal of Hydrology, 553, 59-70.

Hyman, J. D., Gable, C. W., Painter, S. L., and Makedonska, N., 2014. Conforming Delaunay triangulation of stochastically generated threedimensional discrete fracture networks: A feature rejection algorithm for meshing strategy, SIAM J. Sci. Comput., 36:4, A1871–A1894.

Hyman, J. D., Karra, S., Makedonska, N., Gable, C. W., Painter, S. L., and Viswanathan, H. S., 2015a. dfnWorks: A discrete fracture network framework for modeling subsurface flow and transport. Comput. Geosci., 84: 10–19.

Hyman, J. D., Painter, S. L., Viswanathan, H., Makedonska, N., and Karra, S., 2015b. Influence of injection mode on transport properties in kilometer-scale three-dimensional discrete fracture networks. Water Resources Research, 51:9, 7289-7308.

Hyman, J.D., Jiménez-Martínez, J., Viswanathan, H.S., Carey, J.W., Porter, M.L., Rougier, E., Karra, S., Kang, Q., Frash, L., Chen, L., Lei, Z., O'Malley, D., and Makedonska, N., 2016a. Understanding hydraulic fracturing: a multi-scale problem. Phil. Trans. R. Soc. A, 374:2078, 20150426.

Hyman, J.D., Aldrich, G., Viswanathan, H.S., Makedonska, N., and Karra, S., 2016b. Fracture size and transmissivity correlations: Implications for transport simulations in sparse three-dimensional discrete fracture networks following a truncated power law distribution of fracture size. Water Resources Research, 52, 6472-6489.

Karra, S., Makedonska, N., Viswanathan, H. S., Painter, S. L., and Hyman, J. D., 2015. Effect of advective flow in fractures and matrix diffusion on natural gas production. Water Resources Research, 51:10, 8646-8657.

Lichtner P., Hammond G., Lu C., Karra S., Bisht G., Mills R., Kumar J., Andre B., 2015a. PFLOTRAN: a massively parallel flow and reactive transport model for surface and subsurface processes, Los Alamos National Laboratory Technical Report No: LA-UR-15-20403, Los Alamos National Laboratory, Los Alamos, NM.

Lichtner P. C., Hammond G. E., Lu C., Karra S., Bisht G., Andre B., Mills R. T., and Kumar J., 2015b. PFLOTRAN user manual: A massively parallel reactive flow and transport model for describing surface and subsurface processes, Technical report, Los Alamos National Laboratory.

Lofgen M., Nilsson K., Lanyon G. W., 2015. Task 9: Increasing the realism in solute transport modeling – Modelling the field experiments of REPRO and LTDE-SD. Task description.

Los Alamos Grid Toolbox, LaGriT, Los Alamos National Laboratory, ⟨ http:// lagrit.lanl.gov⟩ , 2018.

Makedonska N., Painter, S. L., Bui, Q. M., Gable, C. W., and Karra, S., 2015. Particle tracking approach for transport in three-dimensional discrete fracture networks. Computational Geosciences, 19(5), pp. 1123-1137.

Makedonska, N., Hyman, J. D., Karra, S., Painter, S. L., Gable, C. W., and Viswanathan, H. S., 2016. Evaluating the effect of internal aperture variability on transport in kilometer scale discrete fracture networks. Advances in Water Resources. 94, 486-497.

Nilsson K., Byegård J., Selnert E., Widestrand H., Höglund S., Gustafsson E., 2010. Long Term Sorption Diffusion Experiment (LTDE-SD). Results from rock sample analyses and modelling. SKB R-10-68, Geosigma AB.

Widestrand H., Byegård J., Selnert E., Skålberg M., Höglund S., Gustafsson E., 2010. Supporting laboratory program – Sorption diffusion experiments and rock material characterization. With supplement of adsorption studies on intact rock samples from the Forsmark and Laxemar site. SKB R-10-66, Geosigma AB.

7. FLUID FLOW AND TRANSPORT MODELING OF MIZUNAMI SITE

7.1 Introduction

Through the Development of Coupled Models and their Validation against Experiments (DECOVALEX-2019) project, we have obtained a comprehensive set of hydrologic and chemical data from a research tunnel at the Japan Atomic Energy Agency (JAEA) Mizunami Underground Research Laboratory (MIU). In this section, we show how to develop a general workflow or methodology to synthesize these data into a flow and transport model. This work was carried out for Task C of DECOVALEX 2019 - Groundwater Recovery Experiment in Tunnel (GREET). The data obtained from the experiments in a research tunnel located at 500 m depth, at the MIU. The main aim of GREET is to understand the hydrological-mechanical-chemical environment in the vicinity of the research laboratory. One of the objectives of Task C, Step 1, is to establish modeling methods and tools for analysis of excavation of the tunnel. Fracture data analysis and flow-transport modeling analysis were carried out at Sandia National Laboratories as part of Task C, Step 1. The fracture data analysis utilized fracture data collected in the research tunnel and monitoring borehole 12MI33. A discrete fracture model was developed based on fracture orientation, size and intensity derived from the fracture data analysis. The discrete model was upscaled to an effective continuum model to be used in flow and transport simulations. The modeling analysis also used project data to construct a simulation model to predict inflow into the inclined drift and the Closure Test Drift (CTD) during excavation. The modeling analysis also predicts pressure and chloride concentration histories at observation points. The work documented in this section is a continuation of DECOVALEX 19, Task C analysis reported in the 2017 Crystalline Work Package progress report (Wang et al., 2017). The work presented in the 2017 report was on Task C, Step 1, which included fracture data analysis and preliminary modeling. In FY18 Sandia National Laboratories participated in Step2a and Step2b of Task C.

The GREET project involves experiments in a research tunnel located at 500 m depth, at the Mizunami Underground Research Laboratory (MIU) (Figure 7.1). One of the objectives of Task C is to establish modeling methods and tools for analysis of excavation of the tunnel. So far Step 1 and Step 2 have been carried out to support the objectives. In Step2a the fracture characterization analysis and flow and transport modeling work continued from that of Step 1. As also reported in Wang et al. (2017) the fracture analysis was based on data collected in the research tunnel and monitoring borehole 12MI33 (Figure 7.2). A discrete fracture model was developed based on fracture orientation, size and intensity derived from the fracture data analysis. The discrete model was upscaled to an effective continuum model to be used in flow and transport simulations. The modeling analysis also used project data to construct a simulation model to predict inflow into the inclined drift and the CTD during excavation. The modeling analysis also predicts pressure and chloride concentration histories at observation points. In Step 2b a preliminary modeling analysis was carried out to simulate filling of the CTD and pressure recovery in the rock. The fracture characterization work and modeling analysis for Step 2a are described in Section 7.2. The preliminary modeling analysis for Step 2b is described in Section 7.3. A short summary is provided in Section 7.4.

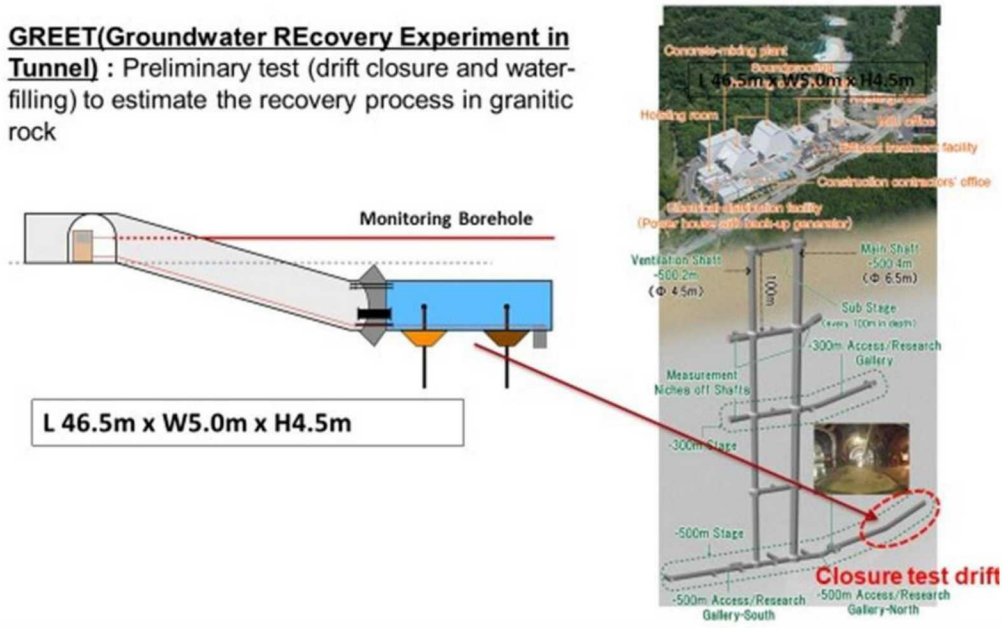

Figure 7.1. Location and layout of the Mizunami Underground Research Laboratory.

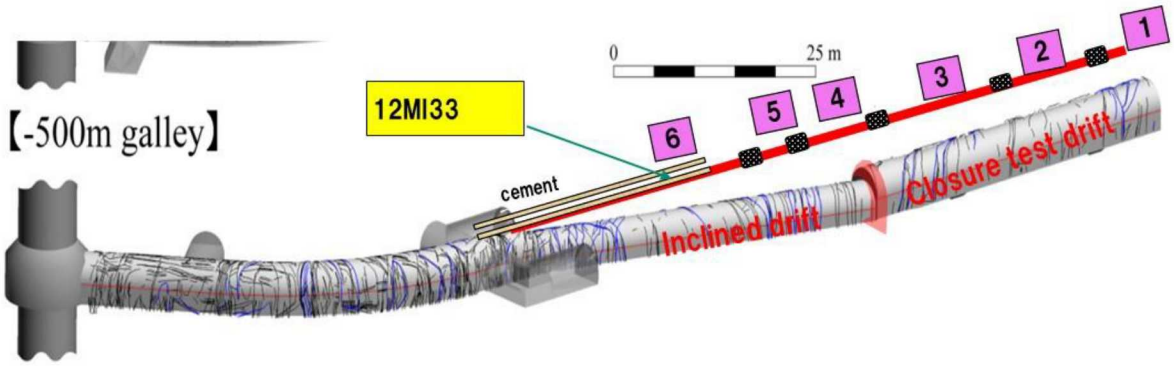

Figure 7.2. Schematic diagram showing the modeled part of the tunnel and monitoring well 12MI33 with monitoring sections.

7.2 DECOVALEX2019 Task C Step 2a Modeling Analysis

7.2.1 Model Setup

Task C, Step 2a, is a continuation of the modeling analysis that was developed using the GREET project data to predict inflow into the inclined drift and the CTD during excavation. In the current work a larger domain is used. Statistical analysis was also added to quantify uncertainty in the model results. As documented in Wang et al. (2017) the project provided data of tunnel excavation progress was used for the modeling analysis to predict inflow. Figure 7.3 is a plot of the excavation progress obtained from the project in terms of days since excavation began. Time zero in the figure refers to 4/6/2013 in the project data. Time 173 days refers to the completion of excavation of the CTD on or around 9/25/2013.

Simulations were conducted with PFLOTRAN, an open source, state-of-the-art massively parallel subsurface flow and reactive transport code (Hammond et al., 2014) in a high-performance computing environment. The excavation progress was modeled by progressively removing material assigned as the host rock. This is equivalent to increasing the grid blocks representing the tunnel. A schematic diagram of the process is shown in Figure 7.4. In order to get a better representation of the excavation progress a small portion of rock material was removed at a time. Thus, the material removal was in 2 m increments for a total of 103 m (i.e. 57 m of the Inclined Drift and 46 m of the CTD). This resulted in 52 PFLOTRAN runs applying the pressure and chloride concentration boundary conditions assigned for the excavated area. The modeling was carried out with output of each PFLOTRAN run used as input for the next run until the complete excavation of the tunnel parts. To automate the simulation process, the Sandia developed optimization code DAKOTA (Adam, et al., 2017) was used as a driver to PFLOTRAN. A schematic diagram of the process in shown in Figure 7.5. DAKOTA also provides statistical analysis of the process, which will be used in future simulations.

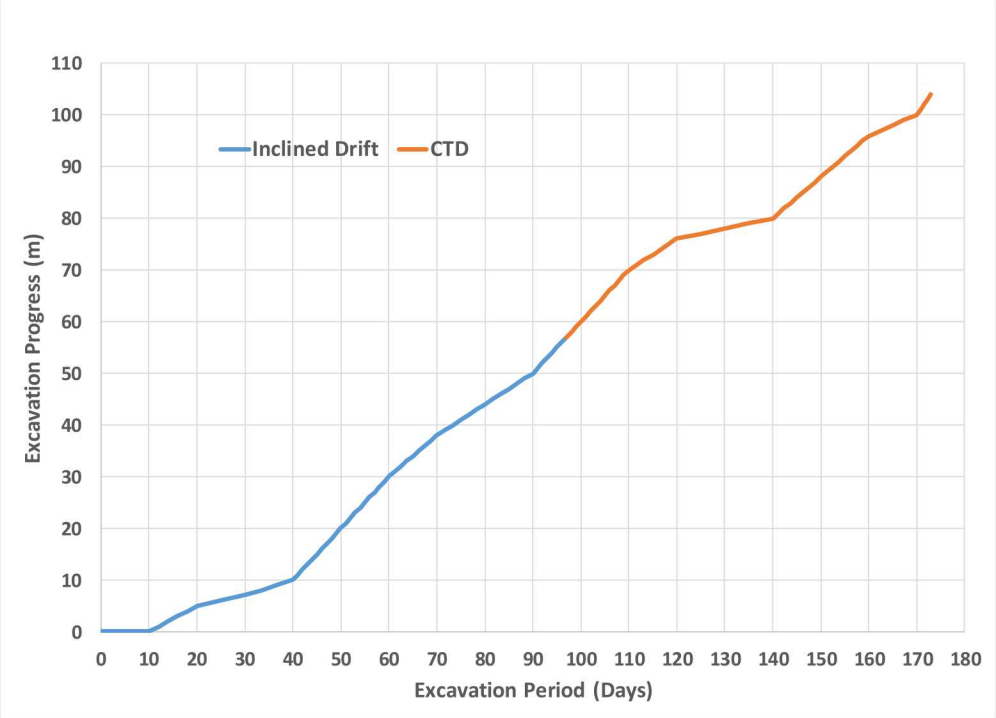

Figure 7.3. Data of excavation progress

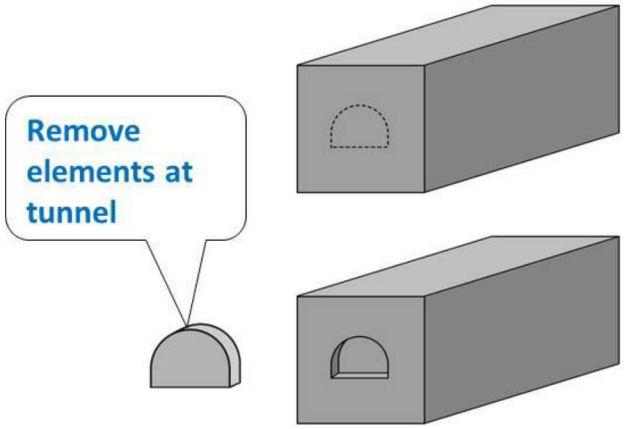

Figure 7.4. Schematic diagram showing simulation approach.

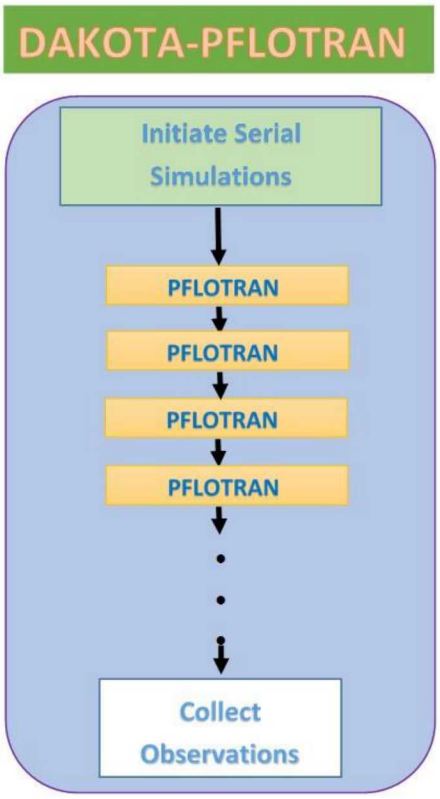

Figure 7.5. Schematic diagram for DAKOTA-PFLOTRAN coupling

7.2.2 Step 2a inflow modeling and results

In previous analyses simulations were carried out for a fracture model using a Visualization Area domain, which is a CTD-scale domain recommended by the project (Wang et al., 2017). In that setup one side of the CTD-scale domain coincides with the inlet of the inclined drift. In this study the domain was enlarged to reduce boundary effects. The new domain is 200 m x 300 m x 200 m, with cell size of 2 m x 2m x 2m, resulting in a mesh size of 1,500,000 grid blocks. The cell size was increased to keep the same number of grid blocks as before. In this setup the inlet to the inclined drift is away from the domain side boundaries, and the tunnel is situated near the middle of the domain.

Fracture characterization for the new domain and mesh was conducted using the method detailed in Wang et al. (2017). Figure 7.6 represents the DFN method with the tunnel and location of fracture trace data. The figure shows the CTD-scale domain and the new enlarged domain. For this study 10 DFN realizations were generated to provide a measure of uncertainty. Figures 7.7 and 7.8 show DFN permeability and aperture for one of the realizations, respectively. The DFN permeability and porosity results for the 10 realizations were upscaled to continuum mesh for use in flow and transport simulations. Figures 7.9 and 7.10 show the upscaled permeability and porosity fields for the same realization.

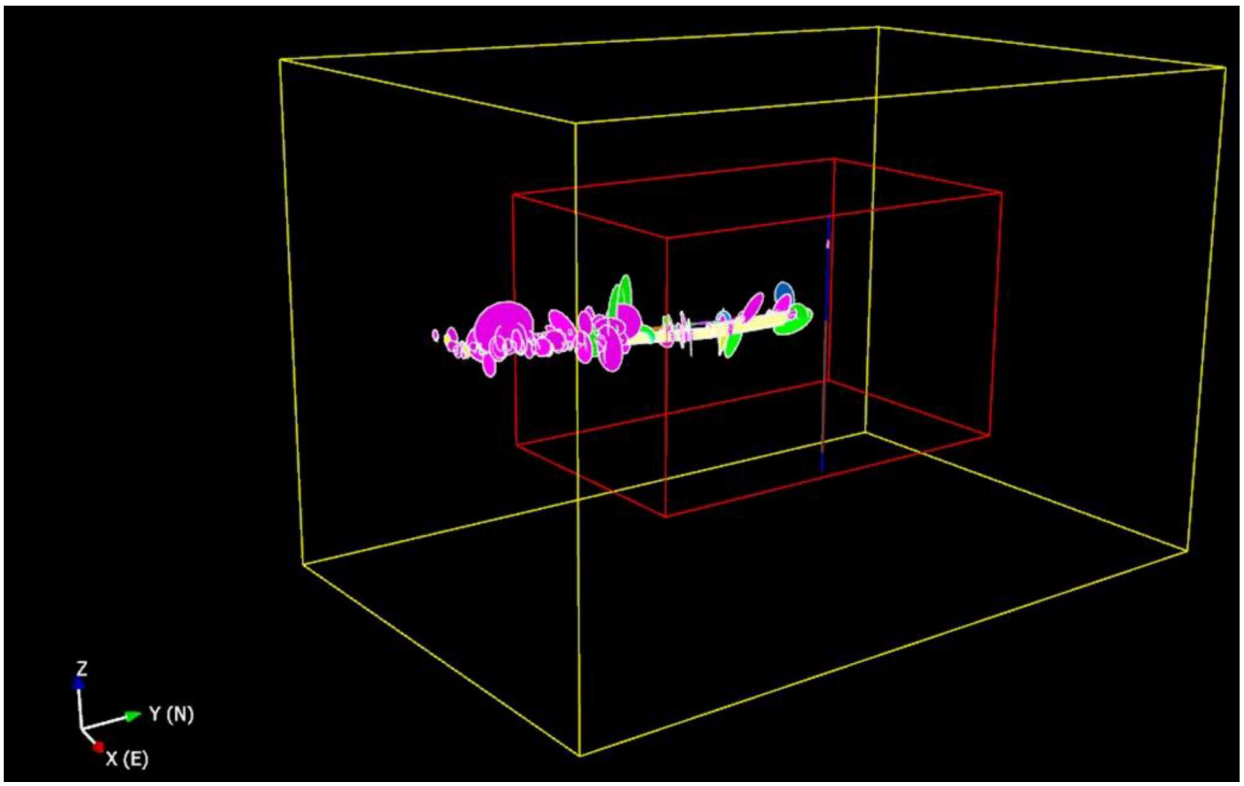

Figure 7.6. Representation of enlarged domain with mapping of fracture traces

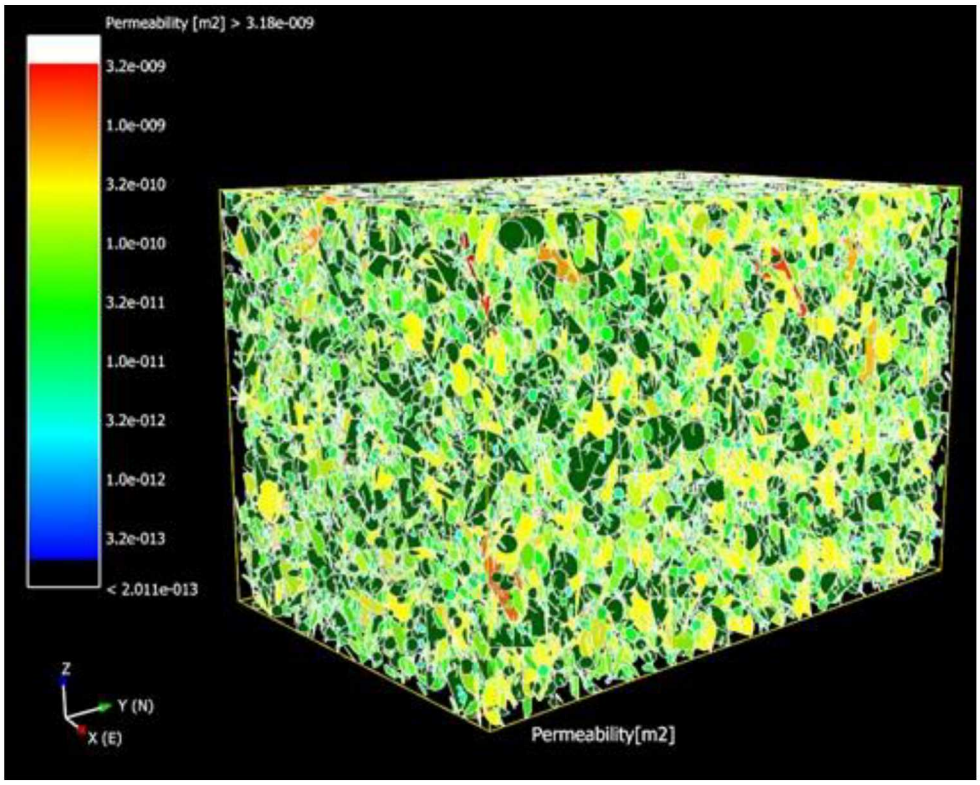

Figure 7.7. DFN permeability field for Realization 2

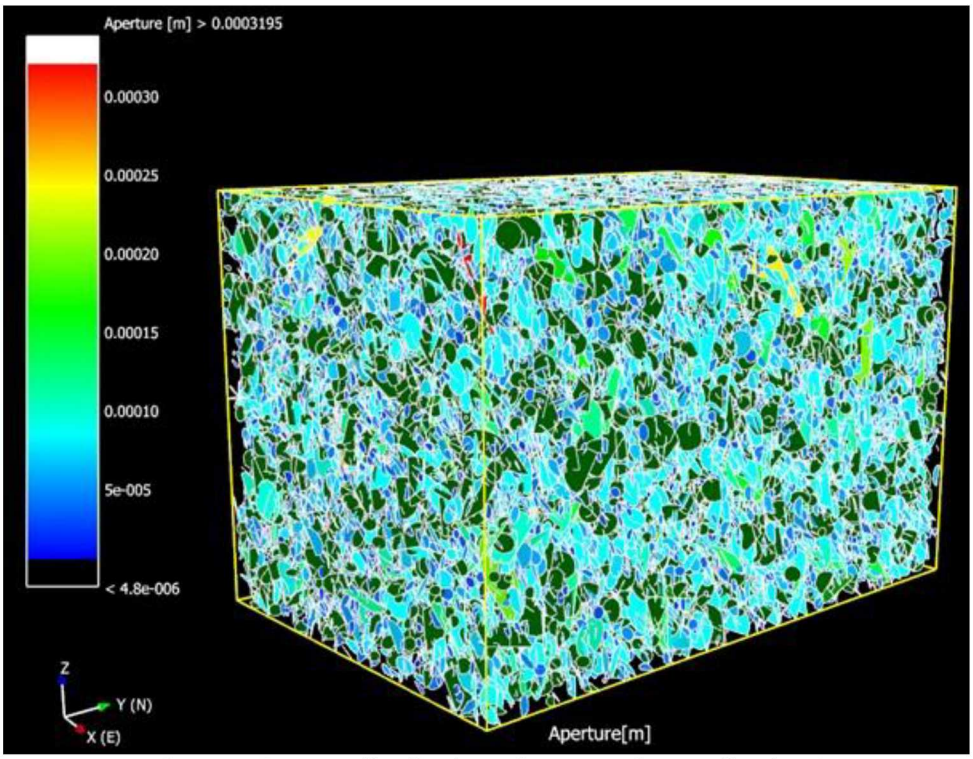

Figure 7.8. DFN distribution of aperture for Realization 2

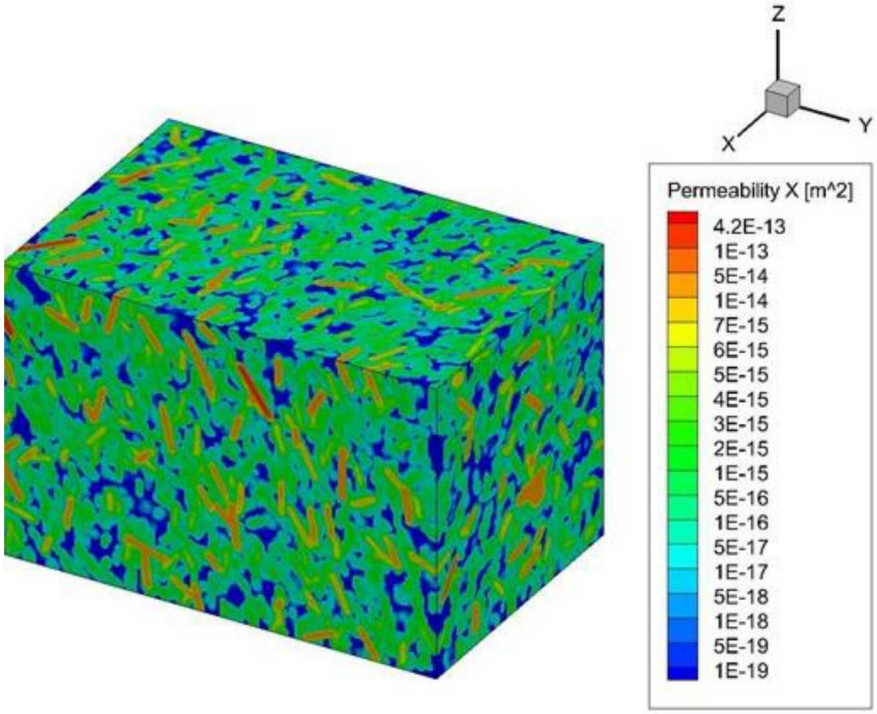

Figure 7.9. Upscaled permeability field for Realization 2

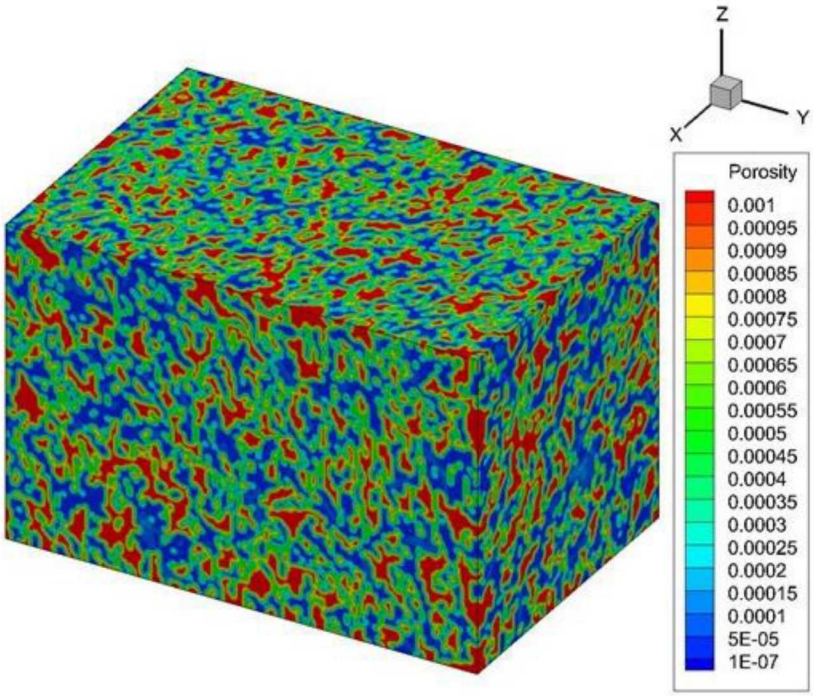

Figure 7.10. Upscaled porosity field for Realization 2

PFLOTRAN simulations were conducted using the method described above. An initial Condition run was made with the new mesh to set hydrostatic pressure and chloride concentration gradient. As previously done specified pressure and chloride boundary conditions were applied to the top, bottom and side domain boundaries. Figure 9.11 shows the new mesh and location of the include drift and CTD tunnel components. Figure 9.12 shows the steady state hydrostatic pressure used for Realization 2. Flow and transport simulations were then conducted as excavation progressed, applying constant atmospheric pressure boundary conditions at the tunnel walls to the excavated portion of the tunnel. The simulations ran for the duration of the excavation. The output of the 10 realizations provided inflow rate and pressure predictions at observation points. Figures 9.13 to 9.16 show distribution of pressure at the end of the simulation time for Realization 2. Figure 9.13 shows a vertical slice (x-axis) at the tunnel level. Figures 9.14 and 9.15 show vertical slices (y-axis) at levels of the inclined drift and the CTD, respectively. Figure 9.16 shows a horizontal slice (z-axis) at the tunnel level. Figure 9.17 shows predictions of inflow for the 10 realizations together with experimental data points. The figure shows a better prediction of inflow for the inclined drift than the total inflow (inclined drift + CTD). Future simulations could improve the predictions when additional fracture data are incorporated in the fracture characterization method.

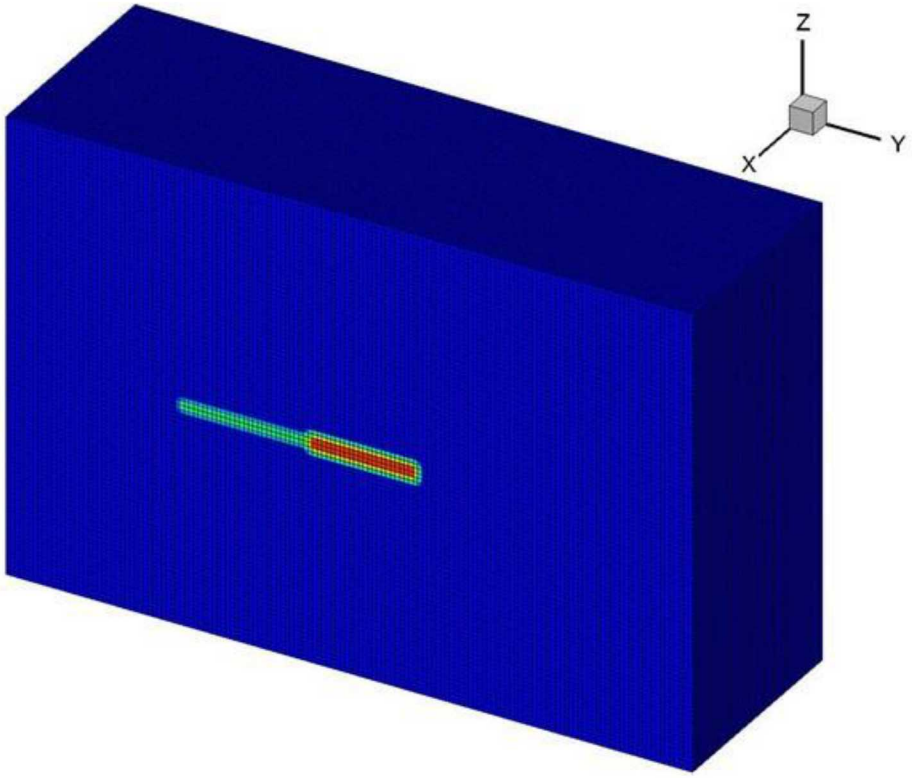

Figure 9.11. Location of Inclined Drift and CTD

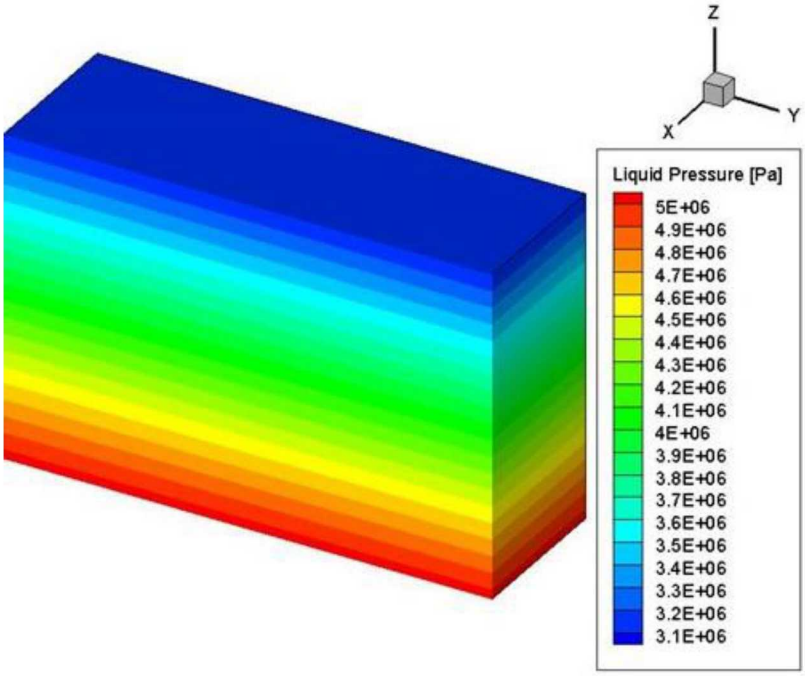

Figure 7.12. Step2a: Steady State Pressure Distribution for Realization 2

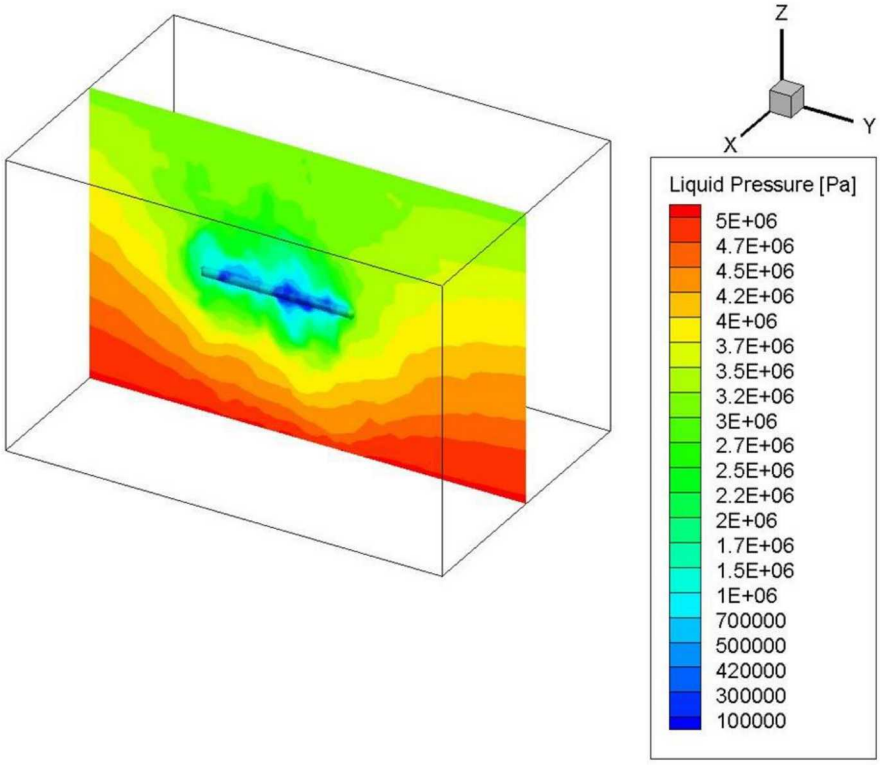

Figure 7.13. Step2a: Predicted pressure distribution at end of excavation time for Realization 2 (173 days simulation time). The figure shows a vertical slice (x-axis) at the tunnel level.

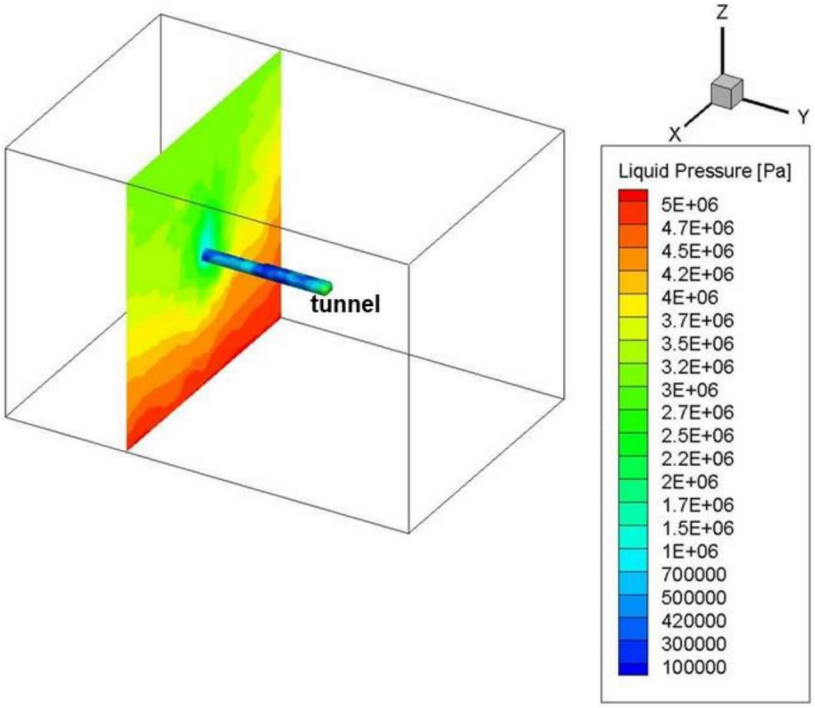

Figure 7.14. Step2a: Predicted pressure distribution at end of excavation time for Realization 2 (173 days simulation time). The figure shows a vertical slice (y-axis) at the level of the inclined drift.

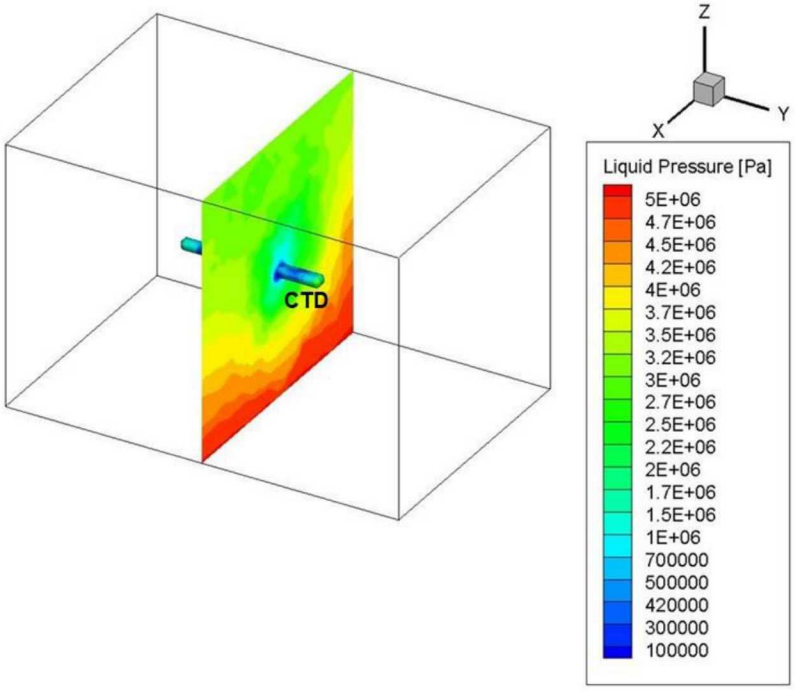

Figure 7.15. Step2a: Predicted pressure distribution at end of excavation time for Realization 2 (173 days simulation time). The figure shows a vertical slice (y-axis) at the level of the CTD.

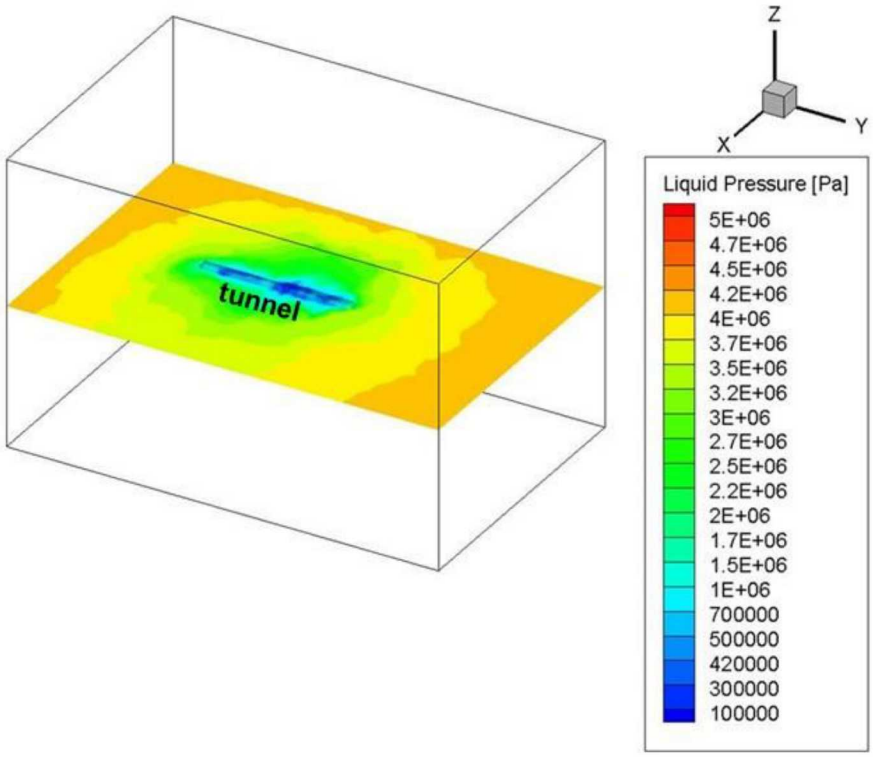

Figure 7.16. Step2a: Predicted pressure distribution at end of excavation time for Realization 2 (173 days simulation time). The figure shows a horizontal slice (z-axis) at the tunnel level.

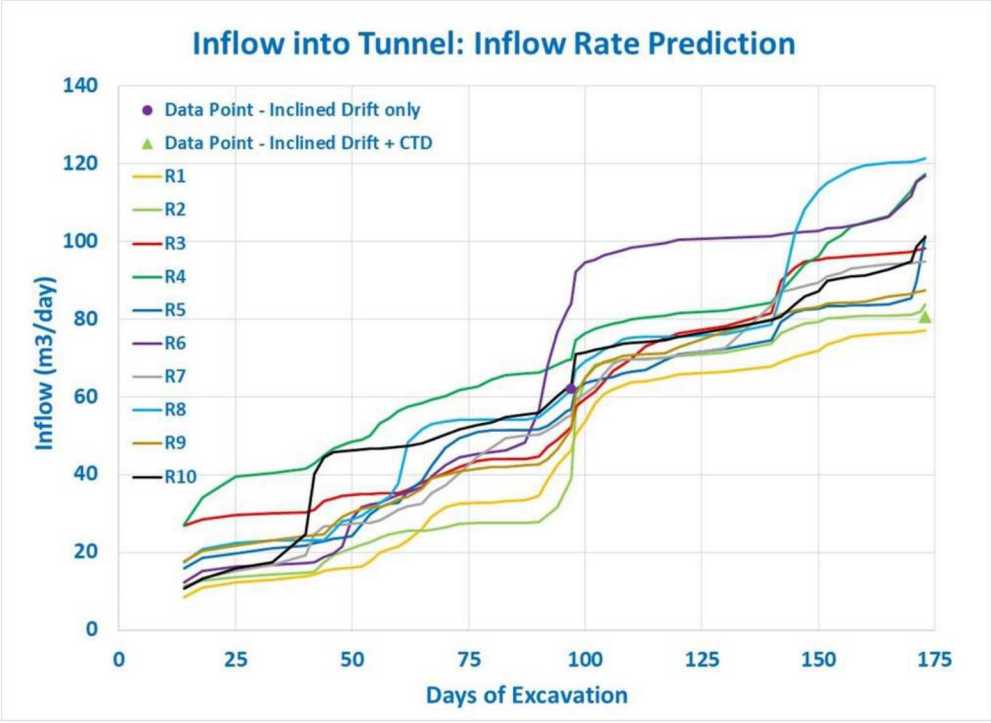

Figure 7.17. Step2a: Inflow prediction for 10 realizations

7.3 DECOVALEX2019 Task C Step 2b Preliminary Flow Modeling Analysis

The GREET project conducted further flow, transport and chemical tests after the excavation of the Inclined drift and the CTD. The experiments include applying of a concrete plug to isolate the CTD, filling it with water and observing hydraulic and chemical recovery following the excavation of the tunnel. The time line shown below indicates durations of major tests starting from the excavation of the tunnel.

- Incline drift and CTD excavation: 4/20/2013 to 10/14/2013
- Construction of impervious plug: 11/3/2014 to 6/2/2015
- First water-filling test (plug performance test): 8/24/2015 to 10/5/2015
- Injection of water to CTD at 500 m: 1/8/2016 to 1/25/2016
- CTD full of water: 1/25/2016 to 9/5/2017

The DECOVALEX19, Task C, Step 2b is designed to simulate the filling of water of the CTD and associated hydraulic and chemical recovery. In this section preliminary blind flow simulations of the filling and post-filling of the CTD conducted at Sandia National Laboratories are presented.

For the flow simulations the domain and mesh described in Section 7.2 were used. Permeability and porosity fields of Realization 2 were applied and the PFLOTRAN numerical code was used. Initial conditions were obtained by running the model using experimental initial condition data described below.

- Initial pressure at CTD: 1 atm.
- Initial pressure data at observation points in Borehole 12MI33:
    - P1 = 3.822 MPa
    - P2 = 1.286 MPa
    - P3 = 1.76 MPa
    - P4 = 3.48 MPa
    - P5 = 3.79 MPa
    - P6 = 3.357 MPa

Note that the experimental data also include data from Borehole 13MI38. We have not used the data because the borehole has not been included in our fracture, flow and non-reactive transport models. Future simulations will incorporate fracture data from the borehole, and flow and transport experiments.

The initial condition was obtained by setting the pressure values for the observation points. The flow model was then run to one year (Starting Jan. 7/2016) using steady state as initial condition. Various approaches were utilized to match the measured data. Better results were obtained applying 0.0 flux boundary condition at all CTD walls. For the simulation pressure at the inclined drift was held at 1 atmosphere because it was kept open. The results of the simulation are shown in Figures 7.18 to 7.25. Figure 7.18 shows pressure distribution at the end of the simulation time (358 days). Pressures in the CTD and the rock have recovered due to the filling if the CTD. The pressure distribution also reflects the pressure gradient towards the inclined drift, which is at 1 atmosphere boundary condition. Figures 7.19 and 7.20 show pressure distributions at the levels of the inclined drift and the CTD, respectively. There is larger pressure recovery around the CTD. Figure 7.21 shows pressure distribution at a horizontal slice (z-axis) at the tunnel level, again showing pressure recovery at the CTD and surroundings.

Figure 7.22 and 7.24 show blind predictions of pressure history due to CTD water filling and post-filling pressure recovery. Figure 7.22 shows plots of experimental and predicted pressure history in the CTD. The results show over prediction of the pressure in the CTD. JAEA project data shows that the concrete plug isolating the CTD did not function properly and that there was some leakage. Thus, the over prediction

could be attributed to the water leakage. Future simulations will include leakage from the CTD. Figure 7.23 shows pressure predictions at the observation points in Borehole 12MI33 together with the corresponding experimental data. There are differences between the blind predictions and the experimental data. As with the CTD, the pressure predictions would need to include the water leakage from the CTD.

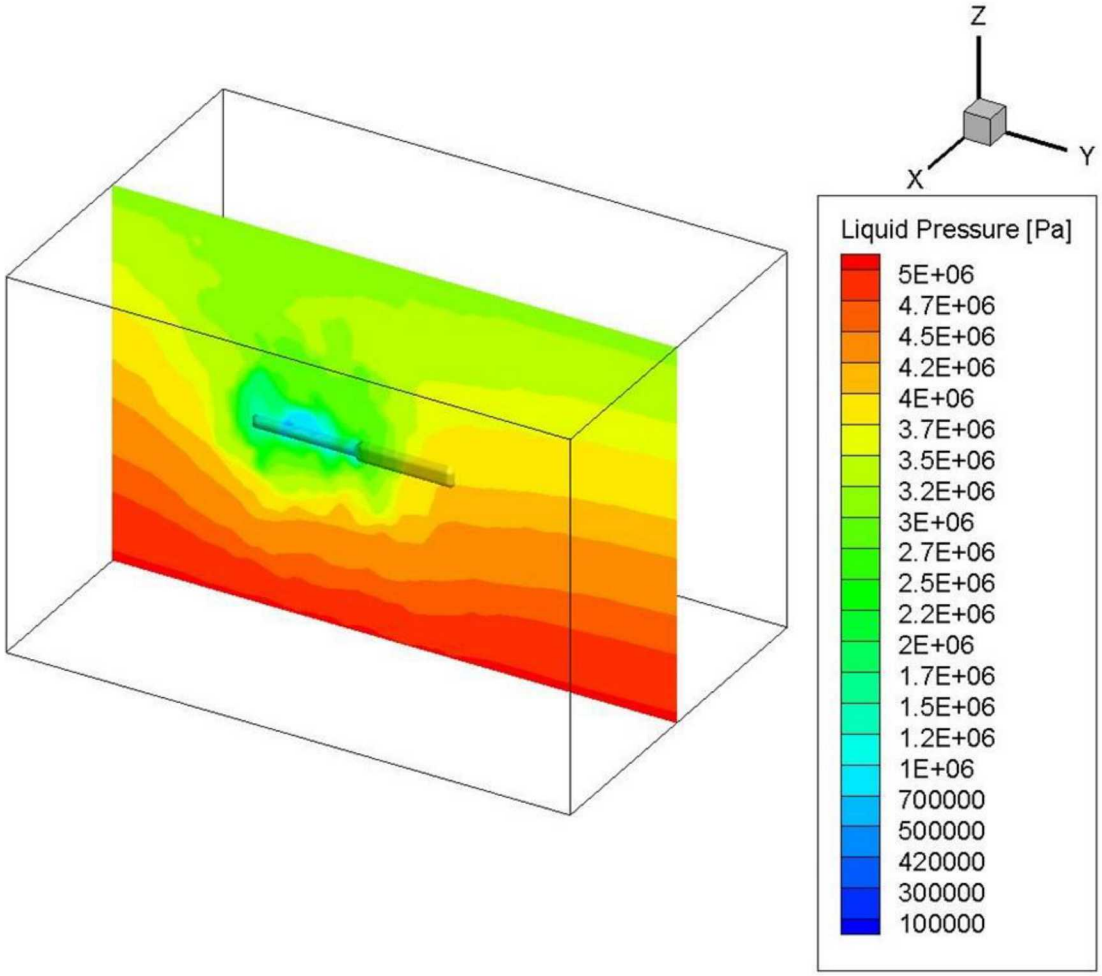

Figure 7.18. Step2b: Predicted pressure distribution at end of simulation time for Realization 2 (358 days). The figure shows a vertical slice (x-axis) at the tunnel level.

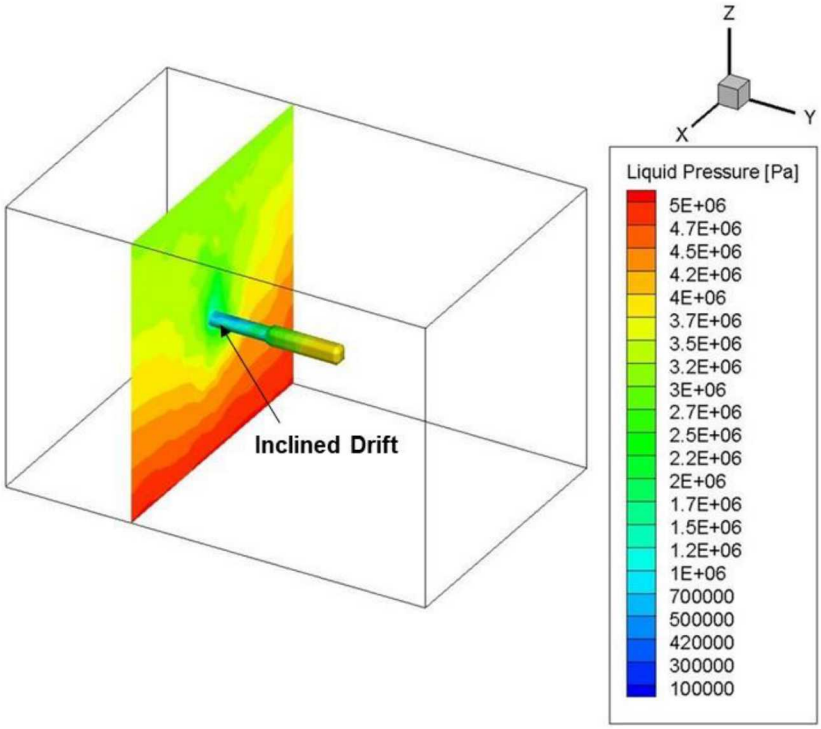

Figure 7.19. Step2b: Pressure Distribution at end of simulation time for Realization 2 (358 days). The figure shows a vertical slice (y-axis) at the level of the inclined drift.

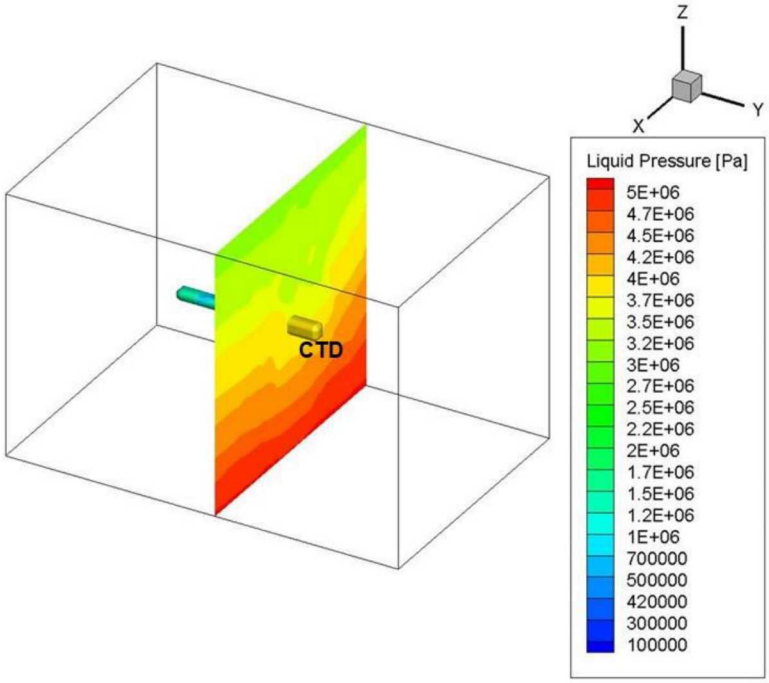

Figure 7.20. Step2b: Pressure Distribution at end of simulation time for Realization 2 (358 days). The figure shows a vertical slice (y-axis) at the level of the CTD.

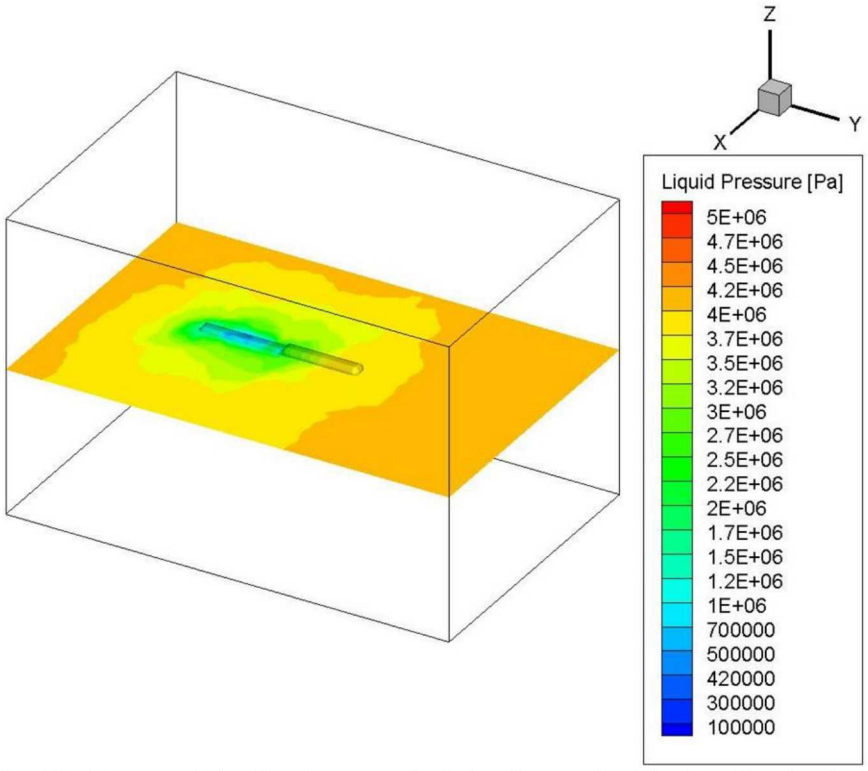

Figure 7.21. Step2b: Pressure Distribution at end of simulation time for Realization 2 (358 days). The figure shows a horizontal slice (z-axis) at the level of the tunnel.

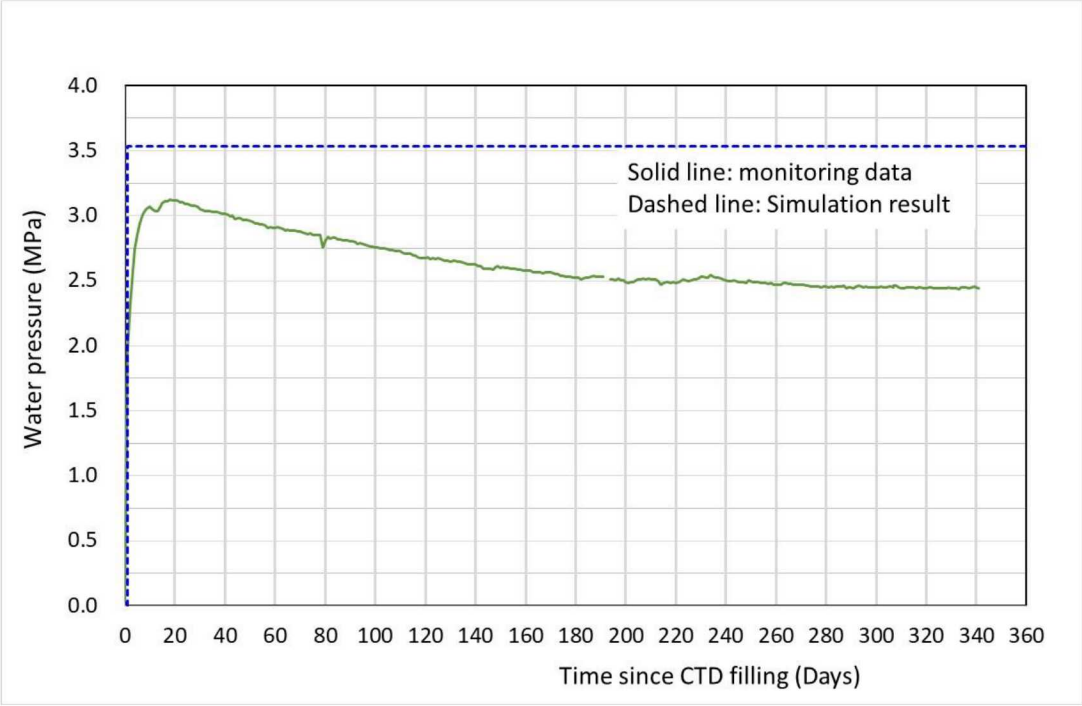

Figure 7.22 Step2b: Preliminary predicted pressure history at CTD (time since CTD filling)

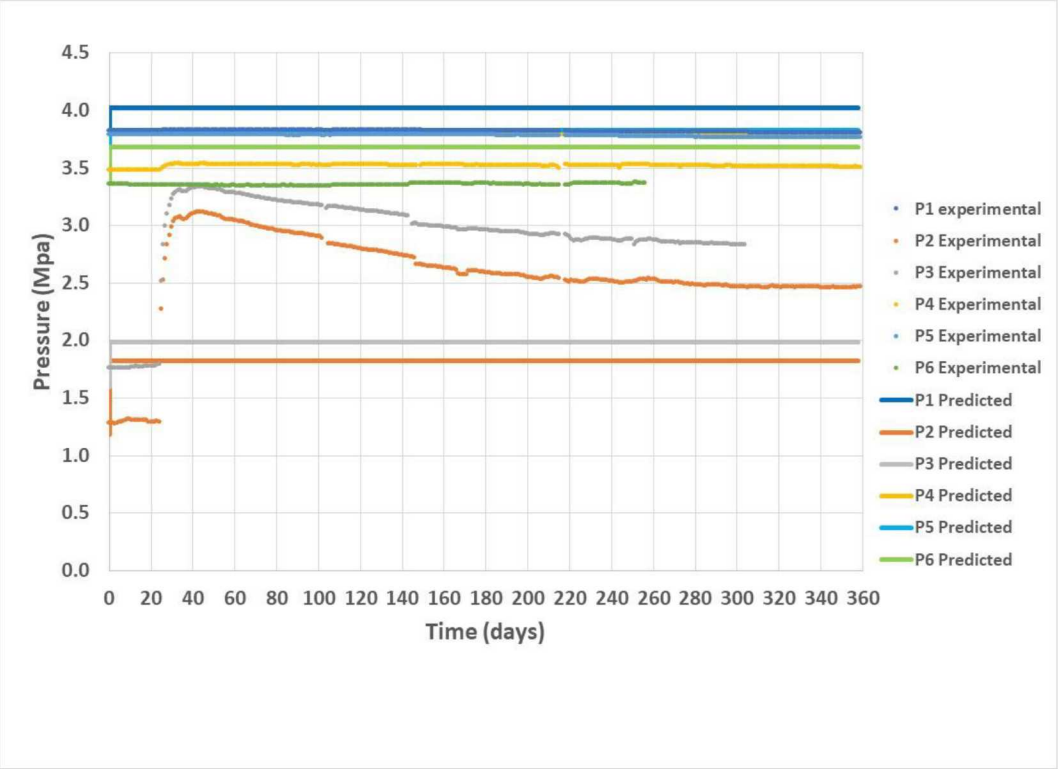

Figure 7.23. Step2b: Preliminary predicted pressure history at observation points on Borehole 12MI33

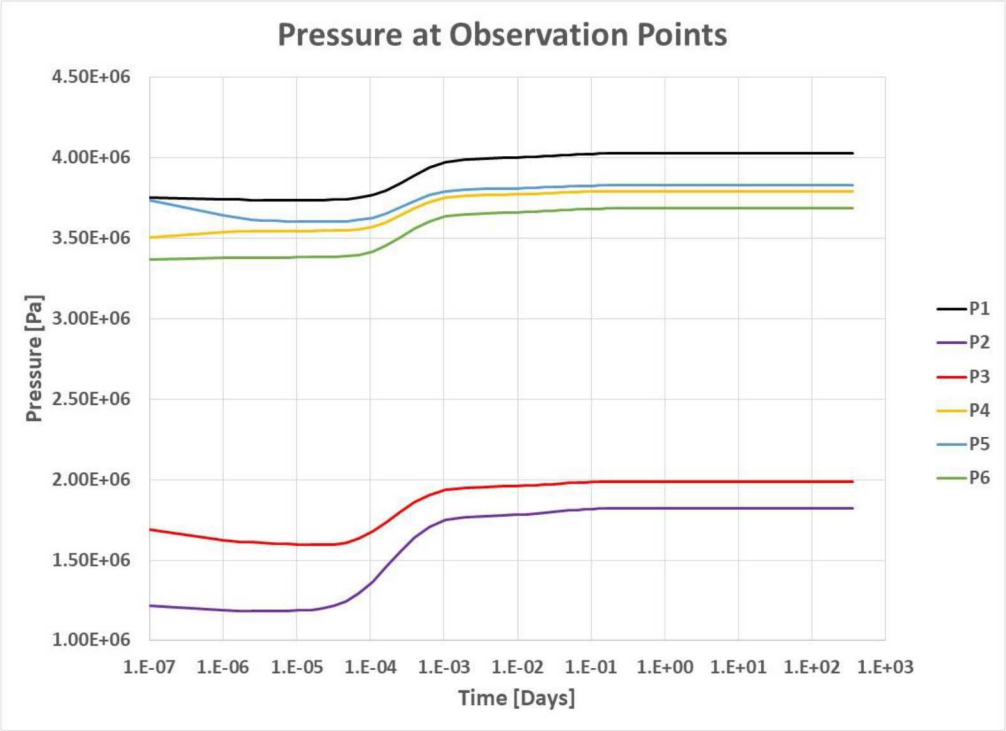

Figure 7.24. Step2b: Preliminary predicted pressure history at observation points on Borehole 12MI33

7.4 Summary of Task C Step 2a and Step 2b Modeling Work

Modeling analyses were conducted at Sandia National Laboratories on DECOVALEX19, Task C, Step 2a and Step 2b. For Step 2b, the analysis was based on a larger domain to reduce boundary effects. The analysis also included fracture characterization using the new domain. The fracture model produced 10 DFN realizations which were upscaled to a continuum mesh for use in flow and transport. Boundary and initial conditions specified by the project were applied to flow and transport simulations for Step 2b. Project experimental data of excavation progress were also used. The simulation method previously developed to simulate excavation progress by continuously removing material from the excavated area was utilized. The DAKOTA statistical analysis and optimization code and the PFLOTRAN numerical flow and transport code were used. Predictions of inflow into the inclined drift for the 10 realizations are reasonable when compared with the experimental data. Inflow of the combined inclined drift and CTD were largely overpredicted. The simulations provided statistical data with uncertainty range. Future simulations will attempt to improve the predictions by using additional fracture data from Borehole 13MI38.

Step 2b preliminary flow modeling was also conducted to simulate water filling of the plugged CTD and pressure recovery. The excavation process resulted in pressure drawdown in the vicinity of the experimental area. An experiment was conducted with the aim of pressure recovery by closing the CTD using a concrete plug and water filling. Preliminary blind simulations were carried out using project data with initial conditions at the CTD and 6 observation points in Borehole 12MI33. For the simulations upscaled permeability and porosity fields for Realization 2 were used. The simulation results were compared with project experimental data. The pressure predictions at the CTD and the observation points did not match the experimental data. However, the modeling exercise produced a method that will be used for future simulations. The experimental data includes leakage of water from the CTD due to plug failure. This information was not included in the modeling analysis. Further modeling will incorporate the leakage.

7.5 References

Adams, B. M. et al. (2017). Dakota, A Multilevel Parallel Object-Oriented Framework for Design Optimization, Parameter Estimation, Uncertainty Quantification, and Sensitivity Analysis: Version 6.6 User's Manual. SAND2014-4633. Updated May 9, 2017.

Hammond, G. E., Lichtner, P. C., and Mills, R. T., *Evaluating the Performance of Parallel Subsurface Simulators: An Illustrative Example with PFLOTRAN*, Water Resources Research, 50, doi:10.1002/2012WR013483 (2014).

Wang, Y., T. Hadgu, E. A. Kalinina, J. Jerden, V. K. Gattu, W. Ebert, H. Viswanathan, J. Hyman, S. Karra, N., Knapp, N. Makedonska, P. Reimus, K. Telfeyan, P. M. Fox, P. S. Nico, M. Zavarin, E. Balboni, and C. Atkins-Duffin: Evaluation of Spent Fuel Disposition in Crystalline Rocks: FY17 Progress Report, Spent Fuel and waste Disposition, SFWD-SFWST-2017-000007, September, 2017.

8. MULTI-SCALE CHARACTERIZATION OF CRYSTALLINE ROCKS FOR NUCLEAR WASTE DISPOSAL

8.1 Introduction

Lawrence Berkeley National Laboratory's (LBNL) research contributions to the nuclear waste disposal project crystalline rock in FY18 consist of a broad scope of activities, building upon relevant work conducted in previous years relating to deep borehole disposal in crystalline rock. These research activities provide important insights to understanding and predicting flow and transport processes that could occur in low permeability crystalline rocks, where fractures might serve as the main conduits for fluid flow and radionuclide transport.

Section 8.2 provides an introduction to a new R&D activity aimed at simulation of pore-scale gas bubble migration. Gas production could occur from metal corrosion, radiolysis of trapped water, or from microbial activities. The generation of gas bubbles could impact the migration of radionuclides in the subsurface or cause rock fracturing and the creation of new flow paths. The preliminary modeling work investigates the migration of gas bubbles within different simulated pore structures to evaluate the behavior of bubbles and their potential impact of radionuclide migration.

Section 8.3 presents the results of laboratory and modeling studies to evaluate the nature of the excavation damage zone (EDZ), which would be an important feature of a mined crystalline repository. One of the challenges of conducting laboratory experiments is to ascertain that the results can be scaled to field scale geometries. A series of laboratory experiments were conducted in FY18 on granite slabs with a special geometry to replicate the stresses and rock deformation responses that would be present in larger circular excavations – the formation of microcracks was monitored using seismic techniques. Permeability measurements were conducted on the damaged samples to evaluate the impact that the damage zone had on fluid flow properties. Preliminary work was also conducted using rigid body spring network modeling to begin to numerically simulate these experiments.

Sections 8.4 and 8.5 of the report describe our work with members of the science team of the "Collisional Orogeny in the Scandinavian Caledonides" (COSC) project, which drilled and characterized a 2.5 km borehole COSC-1 in central Sweden, to obtain key scientific insights on the flow characteristics of crystalline basement rocks. In particular, Section 8.4 examined the hydraulic properties of crystalline rock cores from the COSC-1 well determined using a unique laboratory-scale apparatus, developed at LBNL. This apparatus was used to measure multi-directional transmissivity to assess fracture anisotropy under confining stress conditions. These fractured core samples were spatially correlated with fluid flow zones in the COSC-1 well, which were identified by flowing fluid electrical conductivity (FFEC) logs. Section 8.5 examines the relation between conductive zones in the COSC-1 borehole determined using flowing fluid electrical conductivity logging with fractures that were mapped from acoustic borehole image logs and core sample descriptions. Two main types of fractures have been observed: a steeply dipping fracture set that is associated with the current stress regime, and more shallowly dipping fractures that parallel the rock foliation. It appears that most of the flow zones are associated with foliation-parallel fractures.

8.2 Simulation Pore-Scale Gas Bubble Migration

8.2.1 Introduction

Gas production in geologic nuclear waste disposal systems has been identified as one of the processes that can affect the long-term performance and safety of these systems (Birkholzer et al., 2012; Claret et al., 2018; Tsang et al., 2015). Three main mechanisms are responsible for gas production in nuclear waste disposal systems. Corrosion of metals in canisters, which is considered as the primary gas source, typically involves iron oxidation and hydrogen gas (H_2) production (Xu et al., 2008). Radiolysis of trapped water due to radiation emitted by the spent fuel can also produce hydrogen gas and oxygen gas (O_2) (Christensen and Sunder, 2000). In addition, activities of subsurface microorganisms, which have been reported for crystalline rock at depth (Pedersen, 1999), can lead to the production of an ensemble of gases including carbon dioxide, hydrogen, methane, and hydrogen sulfide (Pedersen, 1996; 1999). Gas bubbles may form and sometimes continuous gas flow may be created as a result of local accumulation of the produced gases. Understanding the migration of gas bubbles, and the gas-liquid interface, is generally important for the evaluation and assessment of waste disposal sites. First, radionuclides and microorganisms may be preferentially sorbed on the gas-water interface, and the gas velocity is expected to control the migration of these radionuclides (Wan and Wilson, 1994). While continuous flow of gas may enhance transport of radionuclides, gas bubbles trapped in the rock formation can lead to the immobilization of radionuclides. Second, gas migration into regions where there is substantial pressure build-up can induce damage or cause fracturing, and thus create new flow paths (Kim et al., 2011).

The migration of gas bubbles in porous media is controlled by the interplay between the surface tension, inertial, viscous and buoyancy forces (Cihan and Corapcioglu, 2008). Gas bubble migration is affected by not only the liquid and gas properties (e.g., density and viscosity), but also by the pore structure, which control the curvature of the gas-liquid interface, and thus the surface tension force. For example, as gas bubbles enter or exit a pore-throat, the deformation of the bubbles can cause large changes in the surface tension force. The well-known Haines jump is one example that highlights the impact of the pore- structure on two-phase flow (Berg et al., 2013; Armstrong et al., 2015). When the interface exits the pore- throat, capillary pressure drops and the interfacial velocity increases as a result of elastic energy being converted to kinetic energy. The interfacial velocity then decreases as the kinetic energy dissipates. Bubble breakups or snap-offs in pore throats and coalescence have also been observed (Berg et al., 2013, Roman et al., 2017). Enhancing our understanding of the gas bubble migration at a pore scale is important because we need to study the effects of chemical reactions of radionuclides or microbial activities and fracturing events that occur at a micro-scale. It is also important because these pore-scale processes can propagate through larger scales and affect macroscopic flow and pressure behaviors (Berg et al., 2013; Armstrong et al., 2015). For example, in the experiment by Berg et al. (2013), the pressure drop measured across a 10 mm core showed variations on the temporal scale of dozens of seconds. The pressure variations were attributed to pore-scale Haines jump that was confirmed by real-time 3D imaging (Berg et al., 2013).

The overall objectives of this study are (a) to investigate the impact of pore structures and macroscopic pressure gradient on gas bubble and interfacial migration velocity and local transient pressure variations, and (b) to evaluate the dynamics of gas bubble formation and consumption coupled with reactions, and to evaluate possible mechanical responses, and radionuclides migration at a larger field scale. This chapter reports the results of preliminary investigations, and focuses on the morphological analysis and model verification, which are followed by an outline of future research.

8.2.2 Modeling Approach

To investigate the impact of pore structures on gas bubble migration, we selected the traditional mesh-based Computational Fluid Dynamics (CFD) approach, which numerically solves the Navier-Stokes equation. Compared to the Lattice Boltzmann method, CFD has the advantages of being computationally efficient and able to handle systems with large density and viscosity contrasts (e.g. water-gas systems). It also avoids the use of idealized geometries and effective properties in pores and throats as in pore network modeling (Meakin and Tartakovsky, 2009; Blunt et al., 2013; Bultreys et al., 2016).

An open source software package, OpenFOAM (Open Field Operation and Manipulation) (Jasak, 2009), was used for the simulations. It is a C++ toolbox that includes a collection of numerical solvers and pre/post-processing utilities, which can be used to solve of a multitude of physical problems in areas including fluid dynamics and continuum mechanics.

InterFoam, a transient solver for two incompressible isothermal immiscible fluids, was selected for the simulations. It is widely used for two-phase flow simulations and has been reported to be applicable for a wide range of conditions (Deshpande et al., 2012; Adrian et al., 2016). InterFoam implements a modified version of the volume of fluid (VOF) method, inheriting features such as mass conservation from the VOF method and reducing numerical smearing of the interface.

In general, the VOF approach treats the two phases as an effective single phase by solving the continuity and momentum equations given by

$$\nabla \cdot \boldsymbol{U} = 0 \tag{8.1}$$

$$\frac{\partial(\rho \mathbf{U})}{\partial t} + \nabla \cdot (\rho \mathbf{U}\mathbf{U}) = -\nabla p + \mu[\nabla \mathbf{U} + (\nabla \mathbf{U})^T] + \mathbf{F} \tag{8.2}$$

where **F** is the body force, e.g., surface tension force, and $\boldsymbol{U}$, ρ and μ are weighted averages between the two phases, determined based on the volume fraction of the two phases:

$$\boldsymbol{U} = \alpha \boldsymbol{U_w} + (1-\alpha)\boldsymbol{U_{nw}} \tag{8.3a}$$

$$\rho = \alpha \rho_w + (1-\alpha)\rho_{nw} \tag{8.3b}$$

$$\mu = \alpha \mu_w + (1-\alpha)\mu_{nw} \tag{8.3c}$$

where α is the volume fraction of the wetting phase, and the subscripts *w* and *nw* denote the wetting and non-wetting phases, respectively.

An additional equation is introduced for the transport of α

$$\frac{\partial \alpha}{\partial t} + \nabla \cdot (\alpha \mathbf{U}) = 0 \tag{8.4}$$

The modified VOF method requires first writing the transport equations for both phases separately, as it would be the case for the Euler-Euler approach, and combines them into the following equation given by

$$\frac{\partial \alpha}{\partial t} + \nabla \cdot (\alpha \mathbf{U}) + \nabla \cdot (\alpha(1-\alpha)\mathbf{U_r}) = 0 \tag{8.5}$$

where $\mathbf{U_r}$ is the compression velocity defined as the velocity difference between the wetting and non-wetting phases, and the additional term in Equation (8.5) ensures a sharp interface.

8.2.3 Model Verification

Two test cases were simulated to validate the modeling approach under conditions that are most relevant to nuclear waste disposal systems, which are described below.

Young-Laplacian Equation for a Spherical bubble

In this case, a single static spherical gas bubble was placed in a cube of water as illustrated in Figure 8.1(a). 3D simulations were performed for a range of gas bubble radii (R) between 5 and 500 µm. The dimension of the cube is ten times of the radius of gas bubble, i.e. 50 to 5,000 µm, which is assumed to minimize the wall effect. The mesh for each simulation was generated such that the bubble diameter was represented by 20 grid cells. The simulations were performed to evaluate the pressure field for the gas bubble and the surrounding water with no flow boundary conditions. The simulated pressure difference (dP) between the interior of the gas bubble and the surrounding water was compared with the theoretical prediction using the Young-Laplace law (Equation (8.6))

$$dP = 2\sigma/R \tag{8.6}$$

where R is the bubble radius, and σ is the surface tension. Properties of the water and air phases and the surface tension used in the simulations are summarized in Table 8.1.

Table 8.1. Density and kinematic viscosity of water and air, surface tension and contact angle used in the numerical simulations.

Property	Value
Water density	1000 kg/m^3
Water kinematic viscosity	1.0e-6 m/s^2
Air density	1.2 kg/m^3
Air kinematic viscosity	1.5e-5 m/s^2
Surface tension	0.072 N/m
Contact angle (for water and gas on PDMS)	45°

Figure 8.1(b) plots the pressure difference against the radius of the gas bubble. The simulation results are in good agreement with the analytical solution of the Young-Laplace equation. However, over time, the bubble center deviates from the center of the computational domain. This unexpected bubble motion is more evident for bubbles with small radii.

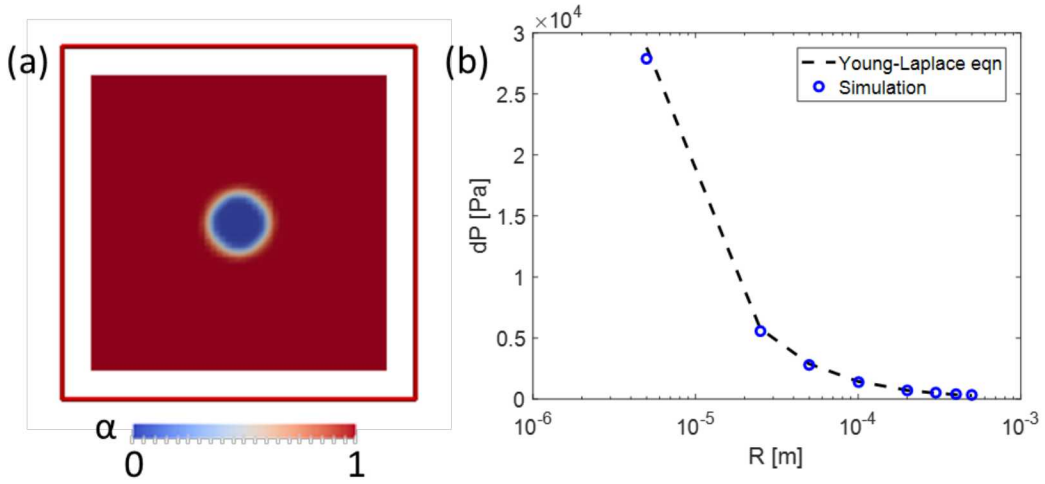

Figure 8.1. (a) A cross-section of the computational domain with the gas bubble in the center. (b) Pressure difference between the gas bubble and its surrounding water in relation to the radius of the gas bubble. The dashed line is the results from the Young-Laplace equation, and the blue circles are simulation results from interFoam.

Two-Phase Flow in a Rough Channel

In the second test case, the migration of a water-air interface in a rough channel was simulated and compared with previous experimental observations (Chang et al., 2017). Chang et al. (2017) described the results of microfluidic experiments performed using rough fracture sections, where water was displaced by air at a flow rate of 0.1 ml/hr, which divided by the average aperture and depth of the fracture gives an average velocity v=208 µm/s. The capillary number ($Ca = \mu_w v/\sigma$) of the experiments was on the order of 1e-7, which is representative of the low capillary number conditions typically encountered in the subsurface. *In situ* images were taken to track the water-air interface and to quantify the migration velocity of the interface. A subsection of the rough-fracture reported in the paper was used to reconstruct the geometry (Figure 8.2). The average width of the channel is 2.2 mm and the length of the subsection is 6 mm. The 2D mesh used for the numerical simulations was generated using the OpenFOAM utility *snappyHexMesh*, with an average grid cell size of 24 µm.

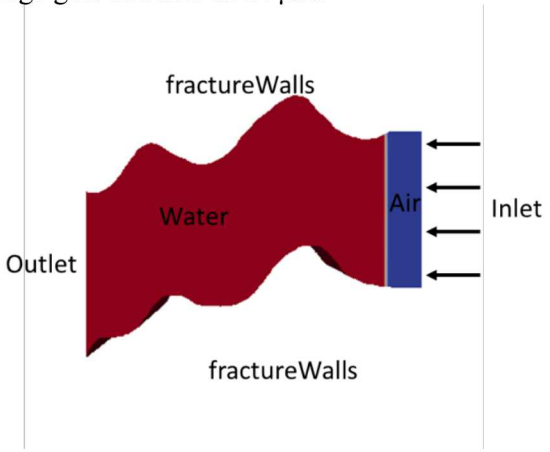

Figure 8.2. Schematic of the computational domain, initial volumes of air and water fractions, and boundary conditions.

Properties of the water and air phases and the surface tension used in the simulations were the same as in the first test (see Table 8.1). The contact angle was 45° as reported in the experimental study. Boundary conditions of the rough fracture simulations and the information of the solvers used in all simulations are summarized in Tables 2 and 3, respectively. The time step was constrained by the Courant number of the average flow and the Courant number of the interface. The values of the two Courant numbers were set to 0.1. Default numerical schemes were used, except for the divergence term of velocity. It was set to *Gauss linearUpwindV cellLimited Gauss linear 1*, i.e., a linear upwind scheme was used to interpolate the face values using a cell limiter in the direction of greatest changes, to increase stability of the solution.

Table 8.2. Boundary conditions used for the rough fracture simulations

Boundary Condition	Velocity [m/s]	Pressure [Pa]	Volume fraction of water
Inlet	Uniform fixed value	Zero Gradient	Zero
Outlet	Zero Gradient	Uniform fixed value	Zero Gradient
Fracture Walls	No Slip	Fixed Flux Pressure	Constant contact angle

Table 8.3. Solver information

Boundary Condition	p_corr (pressure correction)	p_rgh (dynamic pressure)	U (laminar velocity)
Solver	PCG (preconditioned conjugate gradient)	PCG (preconditioned conjugate gradient)	PBiCG (preconditioned bi-conjugate gradient,)
Preconditioner	DIC (diagonal incomplete-Cholesky, symmetric)	DIC (diagonal incomplete-Cholesky, symmetric)	DILU (diagonal incomplete-LU, asymmetric)
Tolerance	1e-10	1e-7	1e-6
Relative tolerance	0	0.05	0

The snapshots of water volume fraction in the rough channel shown in Figure 8.3 illustrate the results of simulations of the dynamic water displacement by air. Using the modified VOF method, the water-air interface is only slightly smeared. The interfacial velocity shows a positive correlation with the local aperture—the velocity is higher when the air-water interface is at places where apertures are larger (e.g., at times 3 s and 4 s), which is consistent with the experimental observations.

However, the predicted interfacial velocity is substantially (up to five times) larger than the experimental observations. Although the inlet boundary condition used in the simulation is different from the actual flow conditions at that location during the experiment, because the inflow is expected to be affected by upstream channel geometry and flow processes in the experiments, and it is unlikely that the changes in boundary conditions and refining the mesh size would explain such a large discrepancy.

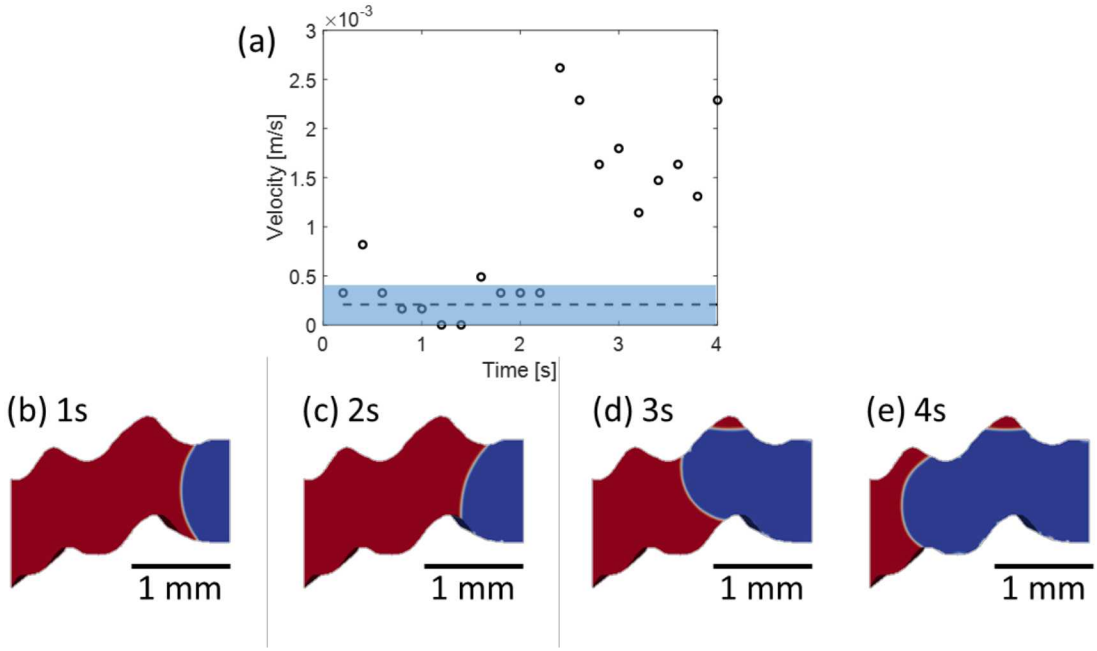

Figure 8.2. (a) Interfacial velocity from the results of numerical simulations, and (b)-(e) snapshots of the water-air interface predicted by the simulation. The blue band in (a) illustrates the variation of the gas phase volume observed in the experiment.

Discussions

Both test cases highlighted the challenges of simulating two-phase flow systems dominated by capillary forces by means of the code interFoam. This can be explained by the presence of spurious currents at the air-water interface, which may be attributed to the imbalance of local forces, as the surface tension body force is represented using the continuous surface force method, and the inaccuracy of the local curvature estimated from the reconstructed interface (Deshpande et al., 2012; Hoang et al., 2012; Raeini et al., 2012; Nieves-Remacha et al., 2015). Several methods have been proposed to reduce the spurious currents, including (i) smoothing or filtering (Hoang et al., 2012; Raeini et al., 2012), (2) sharpening the interface by modifying the interfacial tension force model (Raeini et al., 2012), and (3) combining VOF with or using interface tracking method such as the level set method (Abu-Al-Saud et al., 2017). However, balancing the need of accurate interface representation, mass conservation, minimizing spurious currents and handling large density ratios are still challenging (Deshpande et al., 2012).

8.2.4 Pore Scale Characterization for Simulations in Actual Pore Structures

In order to examine the impact of pore structures on gas bubble migration, high-resolution characterization and quantification of pore structures are required. In this subsection, two types of rocks representing two drastically different types of pore geometries were analyzed: (a) a compacted clay material (Illite du Puy from Gaboreau et al., 2016), which has generally smaller pores and flatter pore geometry, and (b) a carbonate rock that has larger pores and a more granular structure.

The pore structures are to be used to generate computational meshes for direct numerical simulations in actual pore structures. The analyses also provide morphological information (e.g. pore/pore throat ratio,

pore and pore throat shape factor) to constrain the generation of idealized pore and pore-throat geometry for numerical experiments of gas bubble migration, which can provide valuable information for upscaling. The 3D data set of the clay material was collected using FIB-SEM (Focus Ion Beam Scanning Electron Microscopy) and has a voxel size of 5 × 5 × 5 nm (Gaboreau et al., 2016). A subsection of the 3D data set (150 × 150 × 180) was analyzed using iMorph (http://www.imorph.fr/). The size of pore and pore throats were calculated from local aperture diameter, which was determined by the maximal ball diameter accommodated by the void space. The ratios between the half axis length of the equivalent ellipsoid provided measures of the aspect ratio of the pores and pore throats. The 3D volume of the carbonate rock was reconstructed from computed tomography images with a resolution of 16 µm. A sub-volume of 350 × 350 × 150 voxels was analyzed using the same approach.

Figure 8.4(a) shows the 3D rendering of the clay volume with a porosity of ~30%. The pore bodies are well connected (Figure 8.4(b)), with an average diameter of 81 nm and a standard deviation of 21 nm. The pore throats show obvious flattened geometry (Figure 8.4(c)), with the size of 19±8 nm. The pore size and pore throat size distributions are also shown in Figure 8.4(d). Figures 8.4(e,f) depict the aspects ratios of the pores based on the conceptual model of the equivalent ellipsoid, shown in Figure 8.4(g). The ratio between the lengths of different axes (a/b and b/c) varies mostly between 1 and 2. Approximately 3% and 9% of the pores have the a/b and b/c ratios larger than two, respectively. More than 40% of pores have the b/c ratio larger than 1.5.

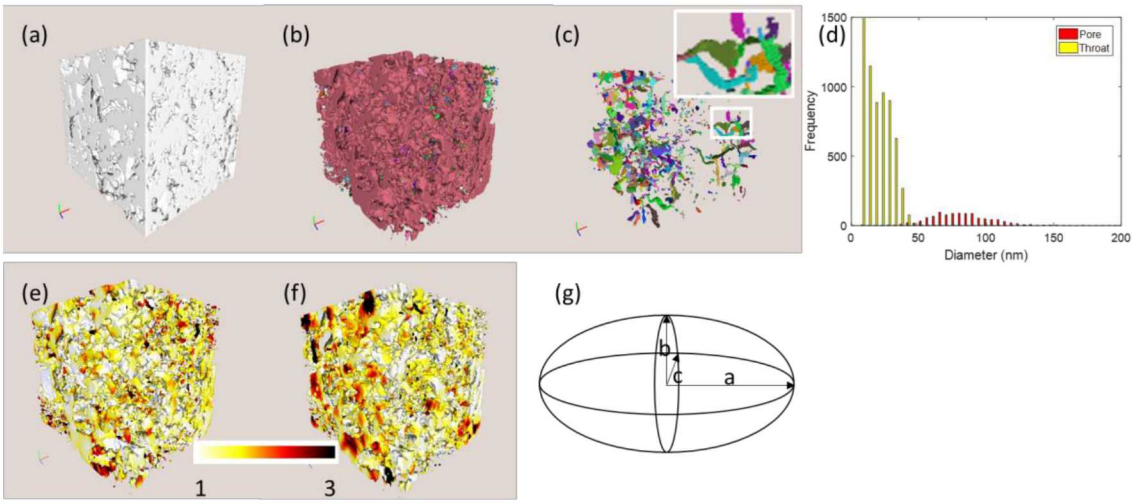

Figure 8.3. (a) 3D volume, (b) connected pore components, and (c) pore throats in the clay volume. (d) Distributions of pore and pore throat size. (e) Ratio a/b and (f) ratio b/c of equivalent ellipsoid. (g) Illustration of the equivalent ellipsoid.

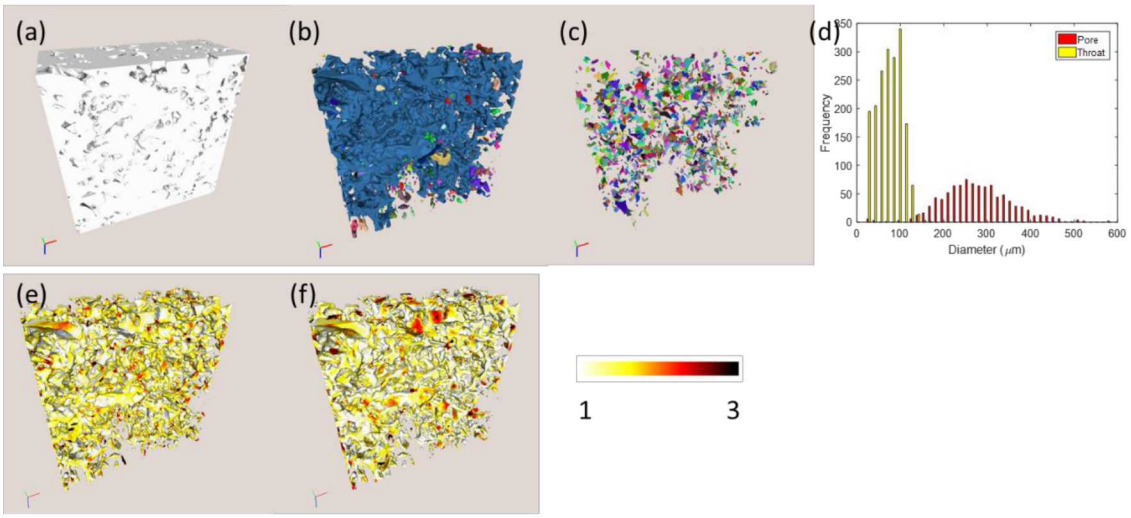

Figure 8.4. (a) 3D volume, (b) connected pore components, and (c) pore throats in the carbonate volume. (d) Distributions of pore and pore throat size. (e) Ratio a/b and (f) ratio b/c of the equivalent ellipsoid.

The carbonate (with porosity of 18%) has larger pores and pore-throats (Figures 2-5(b,c,d)). The pore sizes and pore throats are 281±78 µm and 74±29 µm, respectively. However, the ratio between pore and pore throat (3.6) is comparable to that of the clay sample (3.9). The pore geometry is also more rounded as indicated by the lighter color on Figures 2-5(e,f). Less than 2% and 3% of the void space has a/b and b/c ratio larger than two.

8.2.5 Future Work

In the upcoming fiscal year, three tasks will be performed. First, the modeling approach will be modified to ensure accurate simulation of low capillary number conditions typical for the nuclear waste disposal systems. In particular, two methods will be evaluated – the semi-sharp surface model (Raeini et al., 2012) and the coupling with level-set method (Abu-Al-Saud et al., 2017). Second, pore and pore throat geometries extracted from real rock images presented here will be compared with characteristics of the pore structures of crystalline rocks, to ensure the relevance of the numerical simulations to nuclear waste disposal in crystalline rocks. Third, simulations will be performed to investigate gas bubble migration using representative pore and pore throat geometries with an emphasis on investigating the extent of interface velocity and transient pressure variations. Simulations based on idealized geometries based on morphological statistics will provide insights regarding the controls of pore morphology on gas migration. In the long run, this study will provide necessary expertise and tools for investigations that are also highly relevant to at least two other tasks within the project: (1) dynamic evolution and migration of gas bubbles in the presence of abiotic reactions and microbial activities, and (2) local pressure perturbation (dissipation and buildup) and the geomechanical responses.

8.3 Laboratory and Modeling Study on EDZ

8.3.1 Introduction

The primary objectives of the laboratory EDZ experiments are to investigate (1) the geometry of the damage around a circular excavation (tunnel/borehole breakout, tensile fracturing) within crystalline rock under high stress, (2) hydrological properties of the damage zone, and (3) the hydrological-mechanical-chemical (HMC) changes of the damage zone and the seal materials (e.g., bentonite, cement), which are expected to be caused due to diffusion and transport of pore fluid once the seal is placed within the excavation.

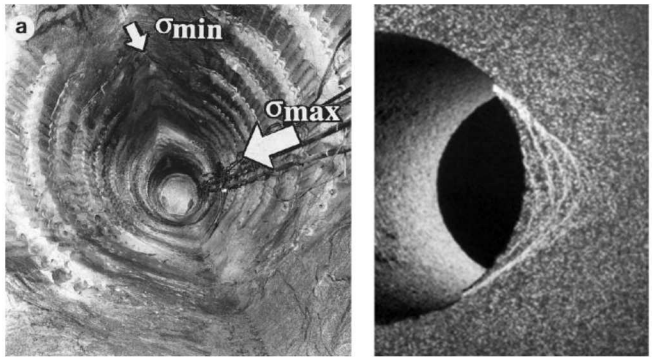

(a.) (b.)

Figure 8.6. EDZ at different scales. (a) Large-scale EDZ in a 3.5-m diameter mine tunnel (Martin, 1997); and (b) cm-scale borehole breakout (in Berea sandstone) observed in the laboratory.

One major challenge of conducting laboratory study of EDZ development is the large scale differences between laboratory samples and tunnels and boreholes produced in the field (Figure 8.6). Fracturing and breakout of rock can be strongly dependent upon the mineral grain size (e.g., Duan and Kwok, 2015) and initial flaw size distribution (e.g., Martin et al., 1994). Typical laboratory experiments using a small hole (a model of a borehole or a tunnel) with a diameter up to a few centimeters could result in underestimation of the rock strength and in possibly a wrong design of EDZ properties.

In crystalline rock, it has been found that the stress along the rock surface (tangential, or hoop stress) for initiating breakout of a circular excavation strongly depends upon the diameter. From experiments using Lac du Bonnet granite, it was found that for small, laboratory-scale boreholes, the breakout stress can be 2.5 to 3 times larger than the stress predicted by the uniaxial compression strength of the rock, and this ratio gradually reduce to 1 with increasing diameter (Figure 8.7). Comparison to the breakout of a much larger, field-scale tunnel observed at the URL (Atomic Energy of Canada Limited Underground Research Laboratory mine-by experiment at 420 level) showed the scale effect levels off for hole diameters larger than 50 to 100 mm for this granite (Martin, 1997).

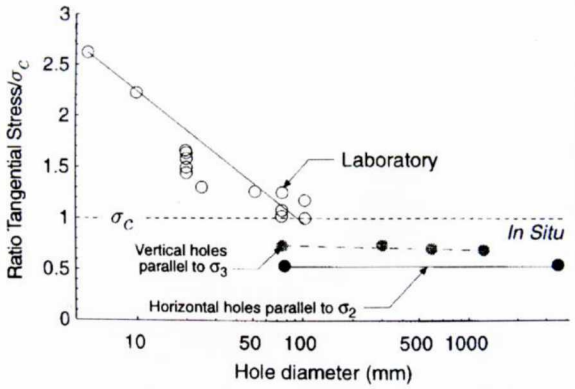

Figure 8.7. Size effect of breakout observed in the laboratory (Martin, 1997).

In FY2018, we conducted a series of laboratory EDZ formation experiments (borehole breakout study) on granite slabs with a specially designed geometry (e.g., Nakagawa and Ewy, 2008). The surface of these samples was curved, which induced stress concentration similar to a circular excavation with a diameter of ~0.5 m. Additionally, because only uniaxial loading is required to conduct these tests, very large stress (a few hundreds of MPa) was applied to the sample easily. During these experiments, acoustic emissions and seismic velocity changes caused by microcrack formation were monitored. Because the sides of these samples were either exposed or under only small confining stress, the development of the EDZ was also

visualized in real time. In the post mortem examination, more detailed seismic velocity measurements in the sample including characterization of crack-induced shear wave anisotropy, microscope observation of thin sections, and permeability measurements of subcored samples were conducted.

In the following, we will first describe the samples used in the experiments, followed by a description of the experimental procedures. Next, the results of the laboratory experiments are presented, including the visual images of EDZ development, acoustic emission history and located events, seismic velocity changes, post-mortem thin section images, and permeability measurements. Newly started effort for numerical modeling of EDZ development using TOUGH-RBSN (Rigid-Body-Spring-Network) model is also described, which will be used to interpret the laboratory experiments in the future. Lastly, the lessons learned from this study and the next research step will be provided.

8.3.2 EDZ Experiments Using Shaped Rectangular Sample

Experimental Setup

Test samples:

The rock samples used in the experiments are four shaped, fine-grained Westerly granite slabs (Figure 8.8). Only three of the four are shown in Figure 3-3. The original rectangular slabs used for the experiments were 10.24-cm tall (H), 5.08-cm wide (W), and 2.54-cm thick (T). On the sides of the slabs, concave cuts of a radius 25.4 cm were made using a diamond grinding wheel. Two-dimensional stress analysis of axial loading for samples with this geometry was performed using a 2D linear-elastic, plain-strain finite-element model (LISA ver.8.0.0. http://www.lisa-fet.com/). In the model, the rock's Young's modulus and the Poisson's ratio were assumed to be 72 GPa and 0.25, respectively. 200 MPa of axial compression was applied at the top, resulting in the distributions of vertical stress σ_{zz} and horizontal stress σ_{xx} shown in Figure 8.9. Note that the model is for one-quarter of the actual sample because of the symmetry, with zero vertical displacement at the bottom and zero horizontal displacement at the right edges of the model. Also, the compression has negative values, and tension has positive values in these plots. Note that the color scales are relative and stretched over the stress range of interest.

Figure 8.8. Photograph of shaped Westerly granite slabs used for the experiment.

Axial loading on a horizontally unconstrained sample produces large stress concentration near the curved surface, but also induces horizontal tensile stress at the top end. As will be shown in below, this causes undesirable, premature tensile fracturing of the sample. To mitigate such failure, in the experiment, the lateral deformation was constrained by attaching (gluing for a lab sample) a hard, metal footing to the ends. In the numerical model, a steel section was added to the rock model with a welded interface. Comparison of the stress distributions before and after a 2.54-cm thick alloy steel bar was attached to the sample is shown in Figure 8.10. Although this slightly reduces the stress concentration in the sample, the tensile stress in the sample (positive stress concentration in the plots) is eliminated. Comparisons between stresses along the minimum horizontal stress line (along the bottom of the model shown in Figure 8.10) of the shaped slab sample and a tunnel/borehole (theoretical Kirsch solution [Kirsch, 1898]) within an infinite medium with a far-field compressional maximum stresses ratio of (σ_{xx}^{∞} , σ_{zz}^{∞})=(100 MPa, 200 MPa) are shown in Figure 8.11. Note that, along the center line, σ_{xx}= σ_{rr} (tunnel/borehole radial stress) and σ_{zz}= $\sigma_{\theta\theta}$ (hoop stress). What

we wanted to examine here was how close the relative stress distribution in a shaped slab would correspond to conditions at a field excavation with a circular cross section. The stress concentration factor here is defined as the stress normalized by the far-field vertical stress σ_{zz}^{∞}, which is ~2.5 for the tunnel/borehole. In order to compare the distributions of the stress concentration between the shaped sample and the tunnel/borehole, for the shaped slab, the curves' vertical scales are adjusted by the same factor for both vertical and radial stresses to match the maximum stress concentration factors on the wall (at a radial distance 25.4 cm from the tunnel/borehole center). The actual maximum stress concentration factor was ~1.20 times the applied axial stress, which implies that in the laboratory 2.5/1.20=~2.1 times the far-field vertical stress is required to introduce near-wall stress state similar to a field borehole/tunnel. Based on these results it is anticipated that the stress state near the expected breakout location of the shaped slab sample can be similar to a large-diameter excavation with the same surface curvature, and that constraining the lateral deformation using a steel block on a shaped sample of granite-like rock would mitigate tensile fracturing while having only small impact on the stress concentration.

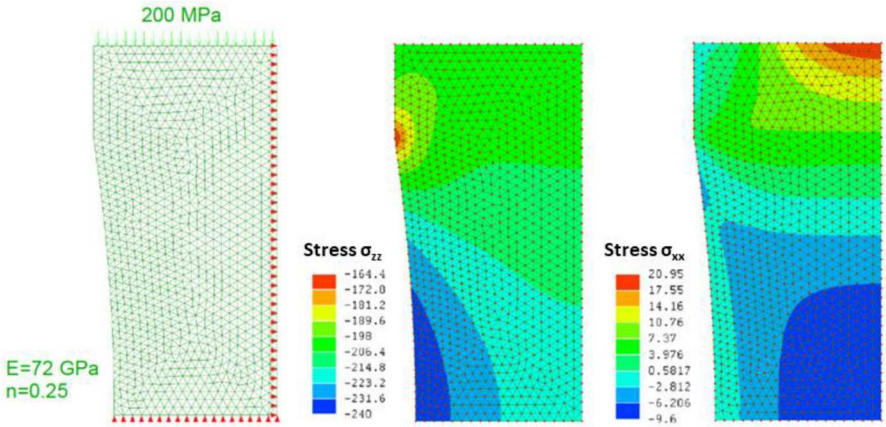

Figure 8.9. 2-D finite element stress analysis using LISA. Only one quarter of the actual sample is modeled due to the symmetry. The top boundary is not constrained, and the uniform axial stress is applied on it.

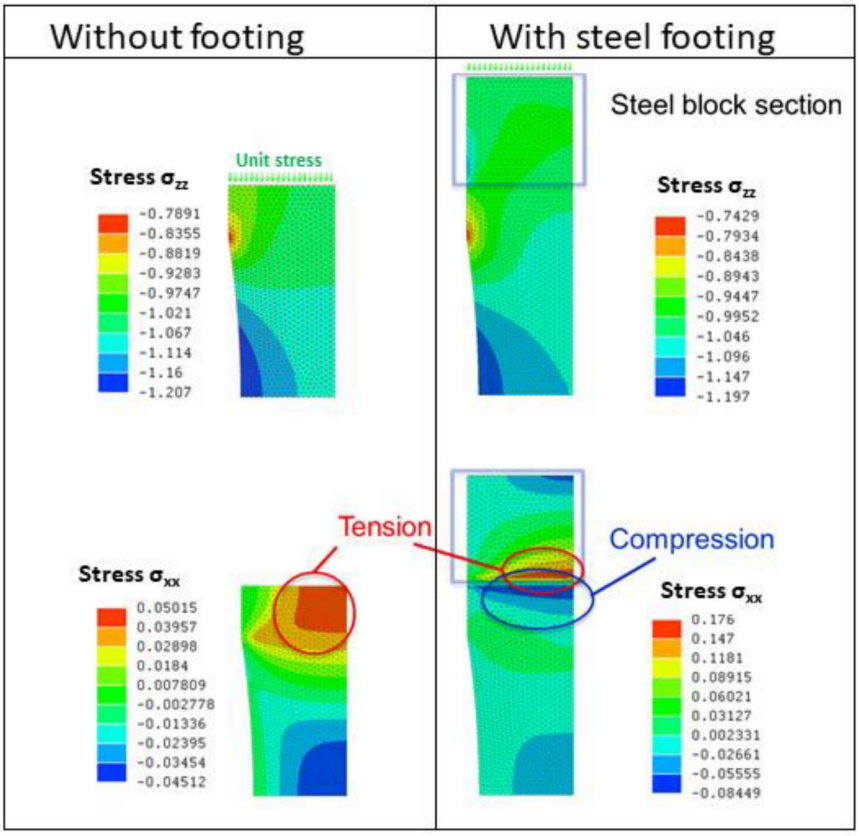

Figure 8.10. 2D finite element stress analysis of the effect of steel footing attached to the end of a shaped slab sample. The stress resulting from unit compressive stress at the top (i.e., the stress concentration) is shown.

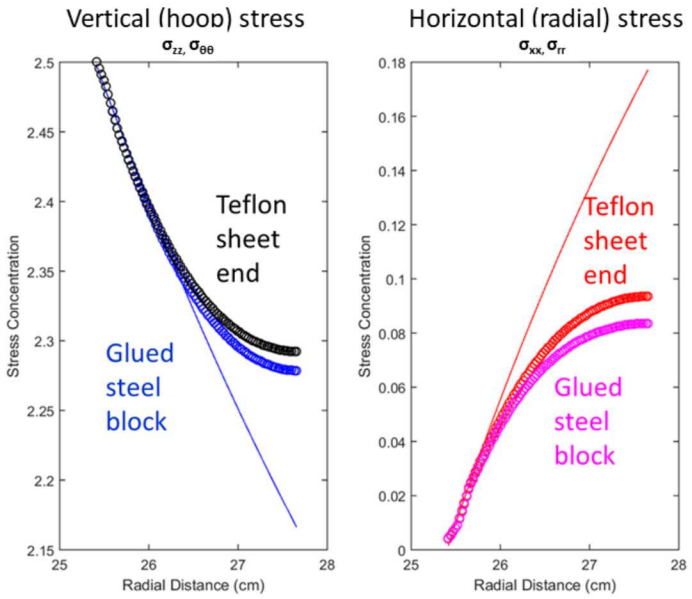

Figure 8.11. Comparisons between stresses along the minimum horizontal stress line (along the bottom of the model shown in Figure 3-5) of the shaped slab sample and a borehole within an infinite medium with a far-field compressional maximum stresses ratio of (σ_{xx}^{∞}, σ_{zz}^{∞})=(100 MPa, 200 MPa), which is represented by solid lines in plots. Note that, along the center line, $\sigma_{xx}= \sigma_{rr}$ and $\sigma_{zz}= \sigma_{\theta\theta}$. The vertical scale is adjusted for the shaped slab sample. Actual max. stress concentration factor for the slab is ~1.20 times (instead of 2.5 ×) the applied axial stress. The 'Teflon' curves represent the case when the sample top has no lateral constraints.

Test System

The experiments were conducted using a polyaxial loading system consisting of a high-loading-capacity *Z* frame and a small-capacity, lateral *X*-*Y* frame. Both of them are equipped with hydraulic cylinders to control the principal stress along each loading axis (Enerpac RSM1500 [*Z*] and Symplex R101 [*X* and *Y*], respectively) (Figure 8.12). The hydraulic fluid pressure and flow were controlled by two ISCO syringe pumps. The shaped slab samples were loaded in the *Z* direction to induce damage in the rock, while much smaller stress was applied in the *X* direction. During the tests, transparent acrylic blocks were attached to the *X* surfaces of the sample. There was no stress applied in the *Y* direction. The acrylic blocks were used to (1) transmit *X*-direction stress to the slab to provide small confining stress and to support the sides of the sample, (2) serve as an optical window for real-time imaging of the EDZ development, through a 37-mm diameter porthole in the *X*-*Y* frame, and to (3) house small acoustic emission sensors (Score Atlanta Inc, PICO Z sensors, frequency band 200 kHz-800 kHz) for acoustic emission monitoring and event location. The acrylic blocks and the sample surfaces were mediated by a thin PTFE film to minimize the friction. The Acoustic Emission (AE) transducers were placed in direct contact with the rock sample through 5mm-diameter holes in the film, with petroleum wax used to establish good acoustic coupling. The AE data collection and processing was performed in real time using an AMSY-6 acoustic emission measurement system (Vallen Systeme). The AE waveform data, when collected and stored, were later used for more careful arrival time analysis and event location.

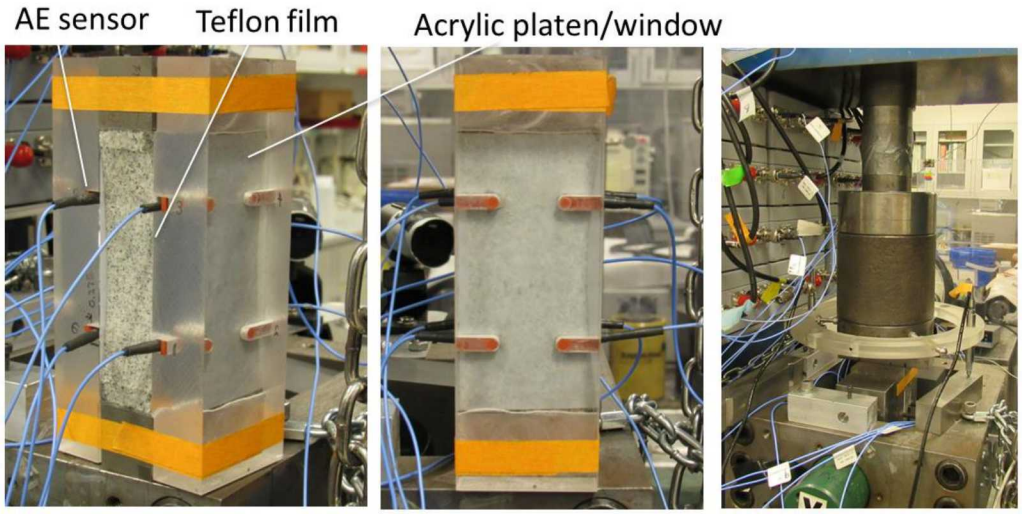

Figure 8.12. Bi-axial loading test on a shaped slab of Westerly granite. Acoustic emissions were monitored concurrently with the loading tests. 8 sensors are embedded within grooves in a pair of transparent acrylic loading platens attached to the *X* surfaces of the slab, mediated by a PTFE (Teflon) film. During the test, large axial (*Z*) stress was applied while only small confining stress in the X direction was applied and held constant.

Experimental Results

Loading Test Results

The three slab samples (Figure 8.8) were loaded under room temperature and room-dry conditions. The first Sample Z-1 was loaded with a slightly higher *X*-direction stress (σ_x=9.5 MPa) than the other two samples, and no steel footing was used (the boundary between the rock sample and *Z*-direction steel loading platens was mediated by a PTFE film). Preliminary FEM modeling indicated that this resulted in primarily axial splitting of the sample, which originated at the sample-platen boundaries. Also, the resulting ultimate strength of the sample was ~160 MPa, smaller than the other samples (Figure 8.13).

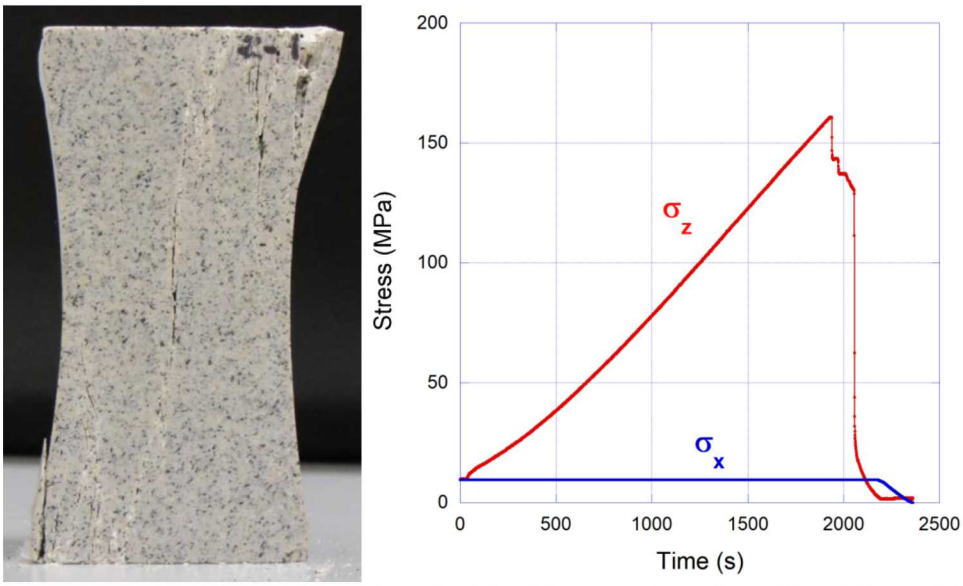

Figure 8.13. Loading test on shaped slab Sample Z-1 without steel footings. The failure of the sample was caused by axial splitting, with the ultimate strength of the sample of 161 MPa.

Next, to avoid the axial splitting, a pair of steel footings (2.54 cm × 2.54 cm × 5.08 cm) were glued to the top and the bottom ends of the remaining samples with epoxy resin. Also, the *X*-direction confining stress was reduced to 2 MPa. After a large number of acoustic emissions were detected, Sample Z-2 was temporarily unloaded from ~170 MPa to ~70 MPa a (Figure 8.14). The maximum applied stress was 208 MPa, and the sample was not brought to the ultimate failure. The photograph to the right shows a close-up view of an observed surface spalling (breakout) on one side (left edge of the sample shown in Figure 8.14 left).

The last Sample Z-3 was loaded under the same conditions as Z-2, but additional measurements were conducted, and the sample was brought to ultimate failure. During these tests, step-by-step loading was applied (Figure 8.15) to conduct active seismic velocity measurements between the sensors (note that the results are not shown in this report). The AE waveforms developed during this test were collected for conducting careful travel time determination and location analysis. Additionally, *Z*-direction deformations of the sample were measured using a pair of vertical LVDT sensors. In this experiment, after reaching the maximum axial stress of 208 MPa at the sample top, the sample started to exhibit slow plastic deformation, while the axial loading pump was stopped. Due to the compliance in the system, both the reduction in the axial stress and the increase in the compaction are seen in Figure 8.15 (between ~4,300 s and ~5,000 s). At ~5,000 s, the sample failed catastrophically. The mode of the resulting damage induced in the sample was splitting and buckling failure (Figures 8.15 and 8.16), which is typical for compression-induced

tunnel/borehole wall breakout. Still images (snapshots) extracted from a video recorded during the creep stage of the loading test are shown in Figure 8.17.

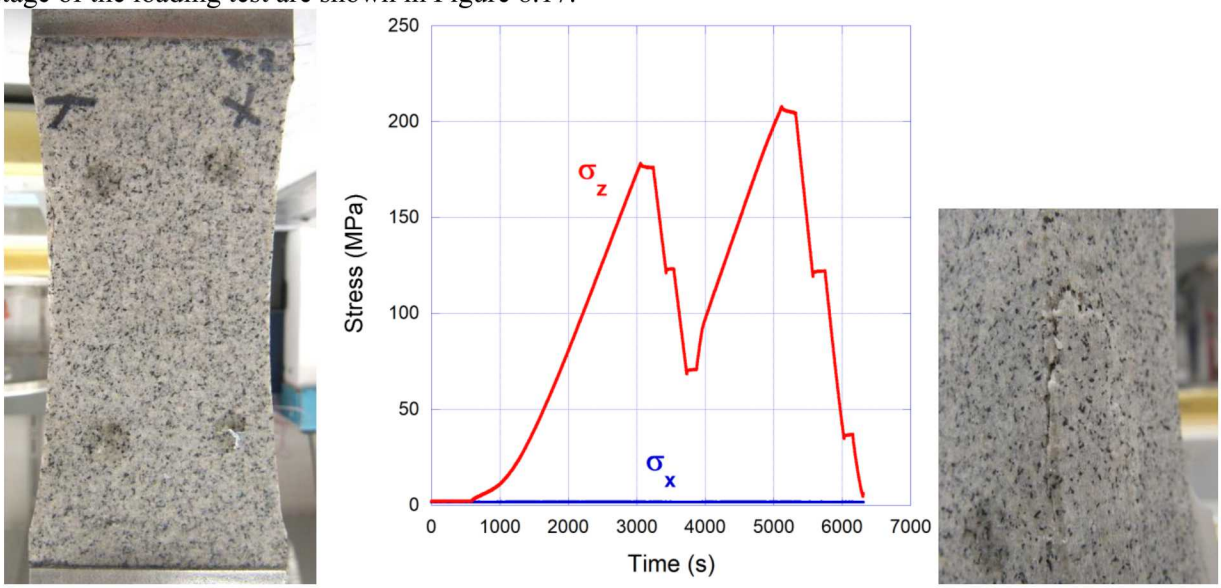

Figure 8.14. Loading test on shaped slab Sample Z-2 with steel footings. The sample was temporarily unloaded from ~170 MPa to ~70 MPa after a large number of acoustic emissions were detected at T~3,000 s. The maximum applied stress was 208 MPa, and the sample was not brought to the ultimate failure. The photograph to the right shows a close-up view of surface spalling (breakout) caused by the axial loading.

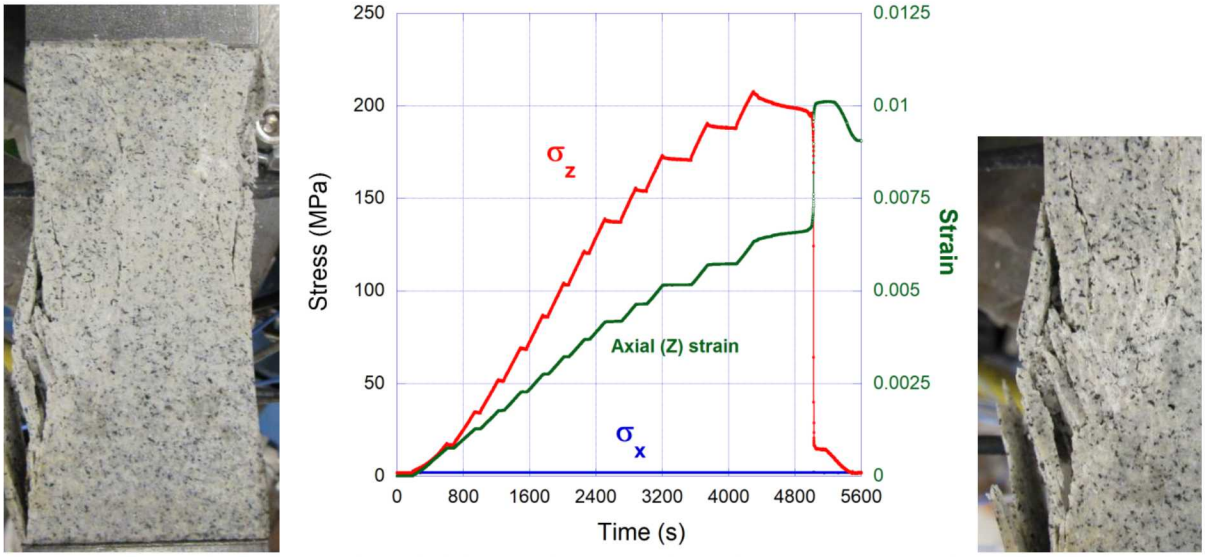

Figure 8.15. Loading test on shaped slab Sample Z-3 with steel footings: Left—the photograph of the sample before the test; middle—graphs of the stress vs time during the test; and right—the photograph of the sample loaded by steps up to ~208 MPa, when the strong, creep deformation occurred, showing a visible, continuous fracture development on the slab surface. Without further increases in load, the ultimate failure was reached at T~5,000 s. The photographs indicate axial-splitting and buckling failure, typically seen on a tunnel and borehole wall suffering EDZ development, and a diagonal shear band which led to the ultimate loss of the load-bearing capacity of the sample.

Figure 8.16. Side view of axial-splitting and buckling failure in Sample Z-3.

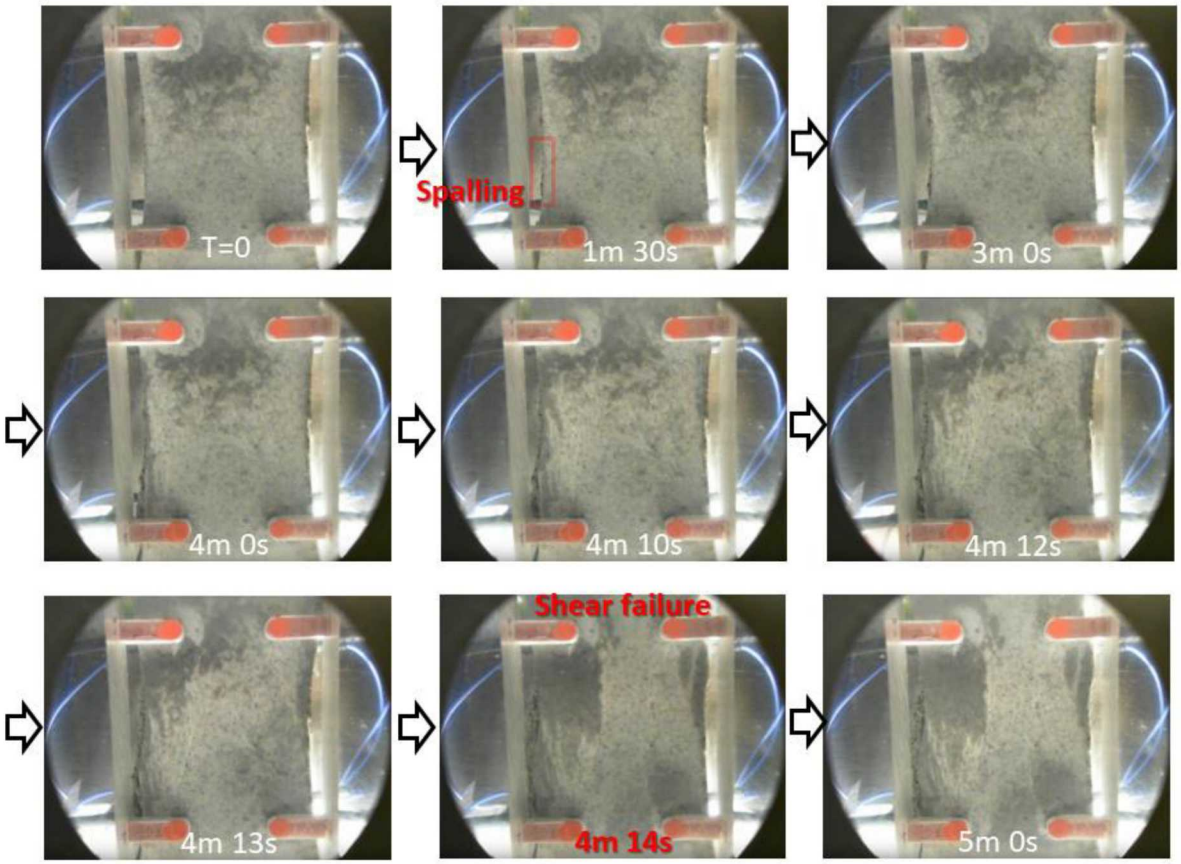

Figure 8.17. Snapshots of the EDZ (breakout) development during the slow creep deformation started at T=4,300 s. Note that the time stamps are the elapsed time after the recording was started at T=4,750s.

Geophysical (Seismic) Measurement Results

Acoustic emission measurements

Acoustic emissions, which are primarily caused by creation and extension of microcracks due to damage in the samples, were monitored during the loading tests. For Sample Z-1 (Figure 8.18), initially, the rate of AE activity increased monotonically as the axial load was increased. The AE rate apparently reduced once the rate reached ~200 counts per second (note that for this sample only two AE sensors were used). This is because the AE data acquisition system became saturated after the per-sensor count reached ~100. It typically takes a few minutes before this system recovers after the saturation, so that the following AE rate measurements become unreliable. Also, the dots shown in magenta indicate high background noise during measurements, which typically happens when the individual events cannot be distinguished from each other, because too many events are occurring close to each other. Although quantitative information cannot be obtained from such data, qualitatively, this high background noise indicates extremely strong AE activity.

The experiment on Sample Z-2 was conducted using 8 sensors. The result is shown Figure 8.19. During the initial loading, the AE activity increased rapidly at ~3,000 s. At that time σ_z~175 MPa, the loading was stopped, which resulted in immediate reductions in the AE activity. Once the sample was unloaded down to ~125 MPa, and then to ~70 MPa, the AE activity became very quiet. Upon second loading, strong AE activity did not resume until the load reached the previous level of ~170 MPa. This behavior is well known as the Kaiser effect (e.g., Lavrov, 2003). After this, the AE rate reached near or above the maximum system capacity at σ_z~208 MPa, and the activity did not decrease until the load was reduced to 125 MPa. Although the ultimate failure was not observed in this experiment, the AE activity indicated that a significant level of damage was introduced in the sample.

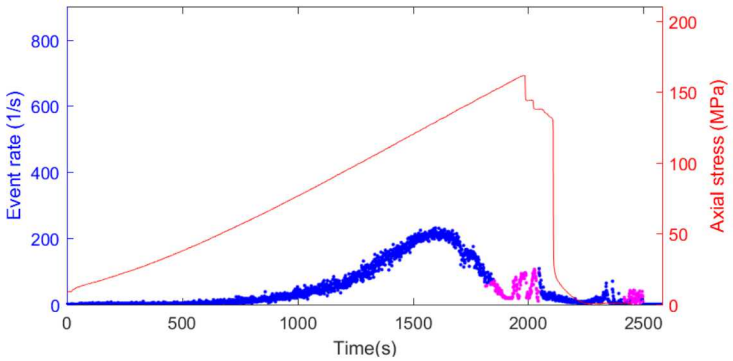

Figure 8.18 Acoustic emission event rate (number of detected events per second) history through the experiment on Sample Z-1. The corresponding axial stresses are also shown. The sudden decrease of the AE counts after reaching 200 counts per second, and the dots in magenta, indicates that the sensors and the measurement system were overwhelmed by an extremely large number of AE events which saturated the measurement capacity.

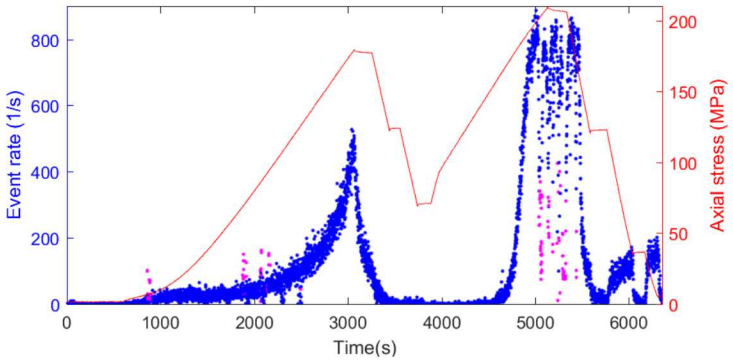

Figure 8.19. Acoustic emission event rate (number of detected events per second) history through the experiment on Sample Z-2. The corresponding axial stresses are also shown.

In the third experiment (Sample Z-3), a very large number of AE waveforms were collected at multiple time intervals for later AE wave arrival time analysis and event location (Figure 8.20). Up to the point where the system was saturated with 800 counts per second (or 100 counts per second for each sensor channel), the step loading resulted in triangle-shaped event history curves, in which the cusps corresponded to the time when the load increase was stopped. In this experiment, again, the loading was stopped at 208 MPa. At this point, extremely strong AE activity was already in progress, saturating the system (the system did not fully recover until T~4,830 s, when the ultimate failure was reached). The spatial locations of the events computed from the collected AE waveforms for each time interval are also shown in each panel in Figure 8.20. Note that the view angle is from the back side of the sample shown in Figure 8.15. The red dots indicate shear-dominant events, blue opening-closing events, and black unclassified events due to the lack of sufficient data to compute a moment tensor (which is used to classify the event type). Note that there is only a small number of the blue events occurred in this experiment compared to the others, but they are difficult to see in these figures. Surprisingly, the overall event location distribution in the sample did not change at different stages of the loading, exhibiting a diagonal band corresponding to the shear failure band seen in Figure 8.15. More events did seem to occur at and near the location of the breakout however, as indicated in Figures 8.20 (d,e).

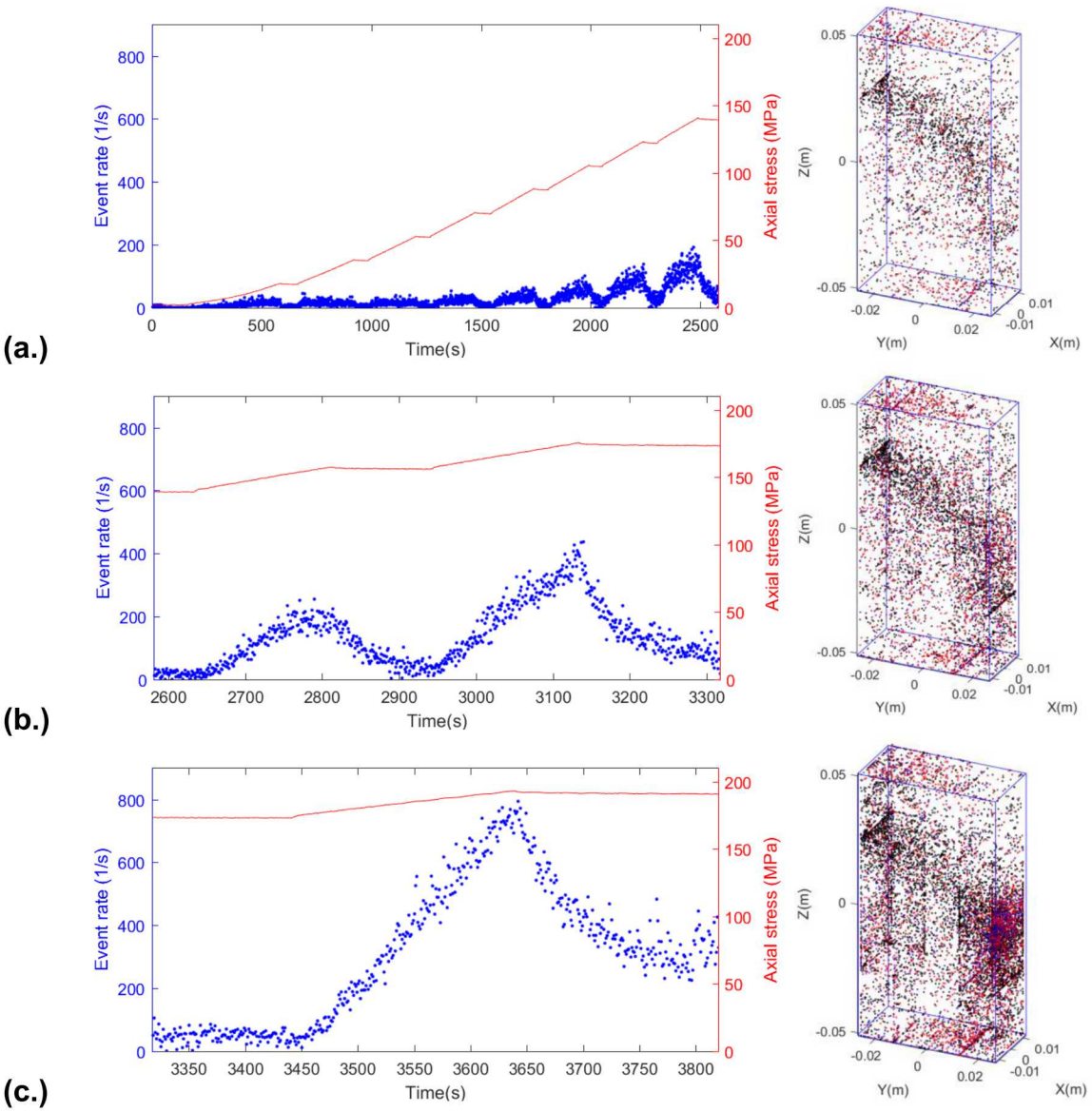

Figure 8.20. Acoustic emission event rate (number of detected events per second) history throughout the experiment on Sample Z-3. The corresponding axial stresses are also shown. Note that, compared to Figure 8.15, the view in these plots are from the back side of the sample shown in the photograph in Figure 8.15.

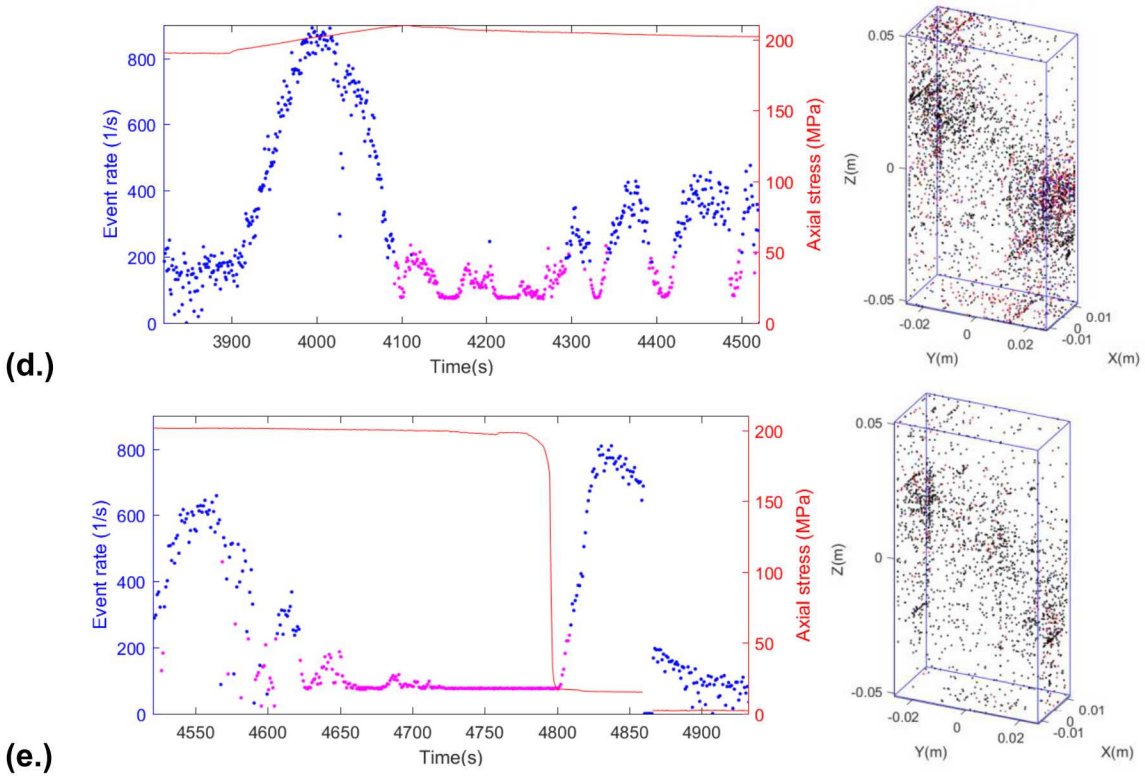

Figure 8.20. (Continued) Acoustic emission event rate (number of detected events per second) history throughout the experiment on Sample Z-3. The corresponding axial stresses are also shown. The data acquisition system saturated after ~4,000 s due to extremely strong AE activity. In the location plot, higher activity did seem to focus near the edges of a diagonal shear zone.

Post-mortem seismic velocity measurements

For Sample Z-2, seismic velocity measurements were conducted across the thickness of the slab sample using pairs of ultrasonic transducers with a central frequency of 1 MHz — Panametrics Accuscan (to measure the P-wave] and Vibroscan (to measure the S-wave). For the S-wave measurements, the direction of the wave polarization was aligned with either *Z* direction (vertical axis of the slab) or *Y* direction (horizontal axis of the slab), shown in Figure 8.21. The measurements were conducted at 1-cm intervals along three parallel lines along the *Z* axis, separated from each other by 1 cm. The determined velocities were compared to the same measurements for an intact, sister sample (Sample Z-4), which were cut from the same host block of Westerly granite, from which the other slab samples were produced.

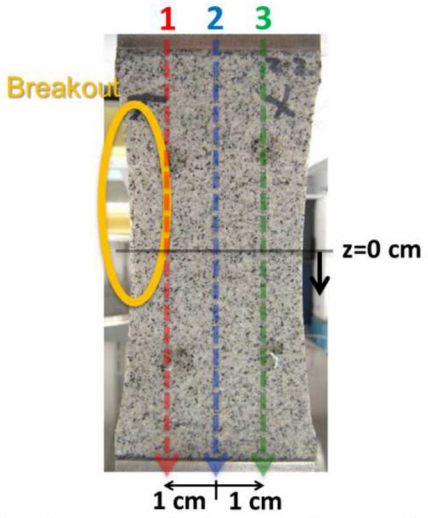

Figure 8.21. Seismic-velocity scan lines on Sample Z-2.

Seismic velocities determined for Samples Z-2 (moderately damaged) and Z-4 (intact) are shown in Figure 8.22. In Figure 8.22(a), compared to the intact sample, damaged sample exhibited very large decrease in both P and S wave velocities, particularly for Line 1 and near the location of the observed surface spalling (at from *Z*=-2 to -1 cm). It is interesting to see, however, that the seismically detected damage zone far extends into the interior of the rock, in spite of the intact exterior appearance of the sample. This result is consistent with the observation of the widely distributed acoustic emission locations in the severely damaged Sample Z-3, discussed in the previous section, even at stress levels much less than the failure strength of the sample.

The large differences in the velocities of two polarized S waves indicate the presence of cracks oriented along the *Z* axis (near parallel to the *X*-*Z* plane). In Figure 8.23, Thomsen's γ parameters (S-wave anisotropy parameter) are shown, defined by

$$\gamma = \frac{V_{S,\,\text{fast}}^2 - V_{S,\,\text{slow}}^2}{2V_{S,\,\text{slow}}^2} \tag{8.7}$$

Note that the fast S wave here is defined as the *Z*-polarized S wave, and the slow S wave is defined as the *Y*-polarized S wave (so γ can take a negative value). Consistenly with Figures 8.22(a) and (b), the damaged sample exhibited strong S-wave birefringence, with the Line 1 and the locations near the spalling, indicating larger anisotropy.

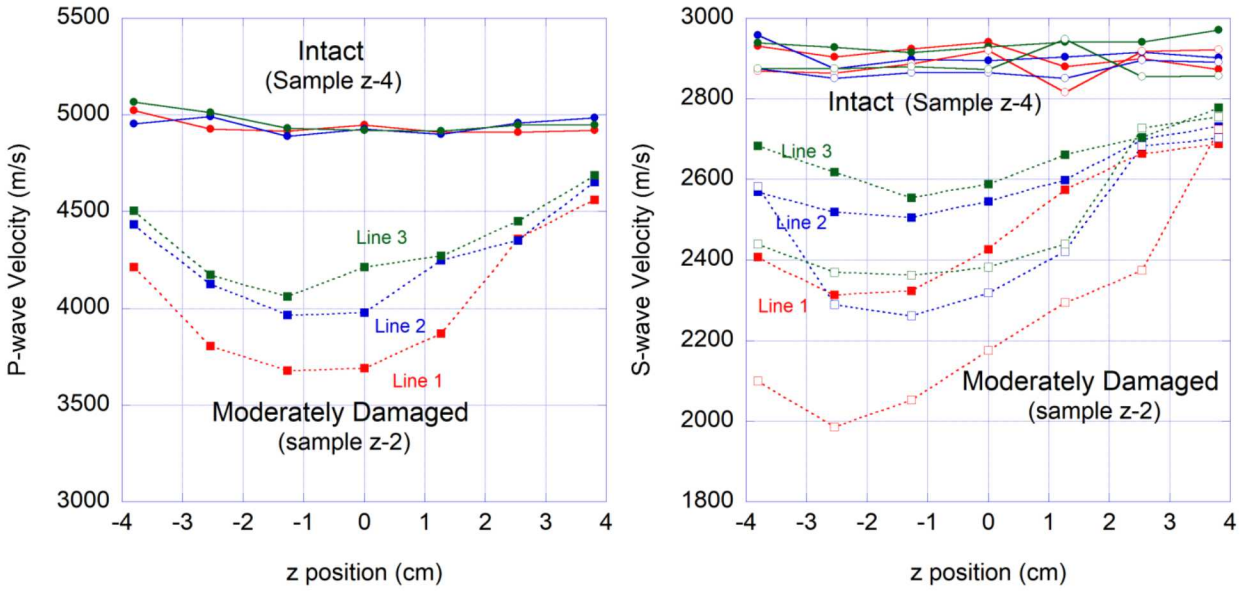

(a.) P-wave velocities

(b.) S-wave velocities (open symbols=Y polarized, closed symbols=Z polarized)

Figure 8.22. P and S-wave velocity distributions within an intact (Sample Z-4) and moderately damaged (Sample Z-2) slabs.

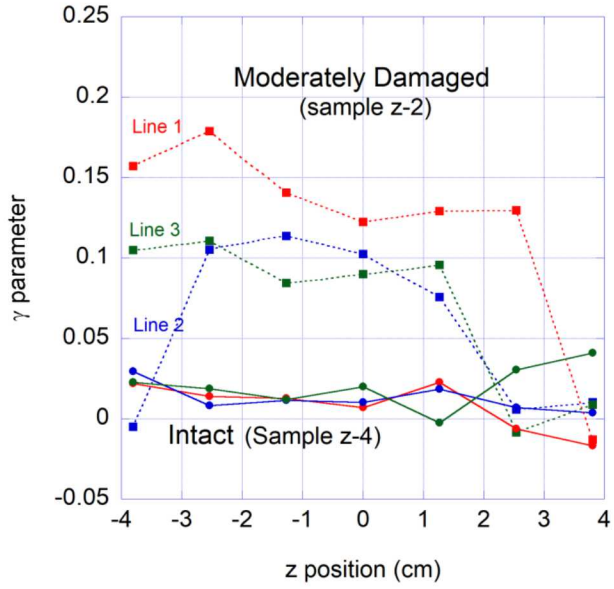

Figure 8.23. S-wave velocity anisotropy of Smple Z-2. Thomsen's γ parameter is shown.

Permeability Changes Due to EDZ Development

The acoustic measurements on Sample Z-2 indicate development of microcracks indicating an extensive damage of the rock far away from the surface, even though visually no damage was induced in the rock. To examine the actual impact of the damage on permeability of the rock, direct permeability measurements

were conducted on small core samples (diameter 13.9 mm, length 25.4 mm) taken from different locations of the slab sample (Figure 8.24). Additionally, thin section samples (sections M1, M2, and M3) were made from the remaining parts of the slab, to examine the geometry and location of the microcracks via optical microscopy.

The permeability measurements were conducted via a flow-through test using a small triaxial test cell (Figure 8.25). In this test, a small, dry cylindrical core, with stainless steel mesh placed at both ends of the sample, was jacketed and placed within a confining vessel. The cavity and the fluid line at the bottom side of the sample were saturated by water prior to the experiment. Subsequently, an axial stress of 6 MPa (884 psi) and a confining stress of 0.17 MPa (25 psi) were applied to the sample, and an upstream pressure of 0.1 MPa (15 psi) was applied to flow the water through the core. The resulting changes in the volume of the injected water were monitored over 20 to 24 hours (Figure 8.26(a)). Although we tried to maintain the pump pressure at 0.17 MPa (25 psi), imperfect servo control and possible temperature fluctuations of the system resulted in occasional temporal overpressurization (Figure 8.26(b)) due to the increased fluid volume in the system. This seems to correlate with the observed irregular changes in the injected fluid volume, which did not allow for reliable permeability estimation. Nonetheless, the high flow volumes did correlate well with the expected degree of damage of the core, with the left side of the sample (L1–L4) and the locations near the surface damage (L1–L3) exhibiting higher permeability. High accuracy estimation of permeability is not reliable because complete saturation of the cores was not assured, which can be made possible by applying higher pore pressure and via longer-term monitoring of the flow rate changes. However, if the cores are assumed to be saturated by the injected water, the values obtained from the slopes of the flow volume history range from 5.7 μD to 14.2 μD, under a pressure gradient of 6.7 MPa/m (or 25 psi/inch). The reductions in the flow volume after 20 hours for Samples R2, R3, and R4 are possibly due to thermal expansion of the fluid in the system.

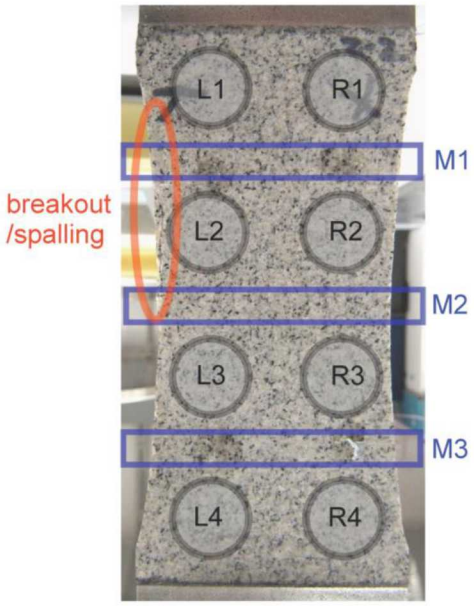

Figure 8.24. Locations of small subcores and thin section samples in Sample Z-2.

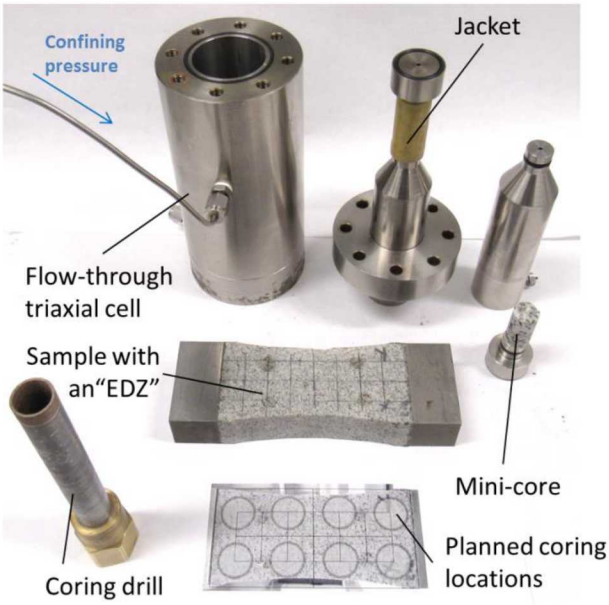

Figure 8.25. Mini triaxial test core holder used for permeability tests on the subcores.

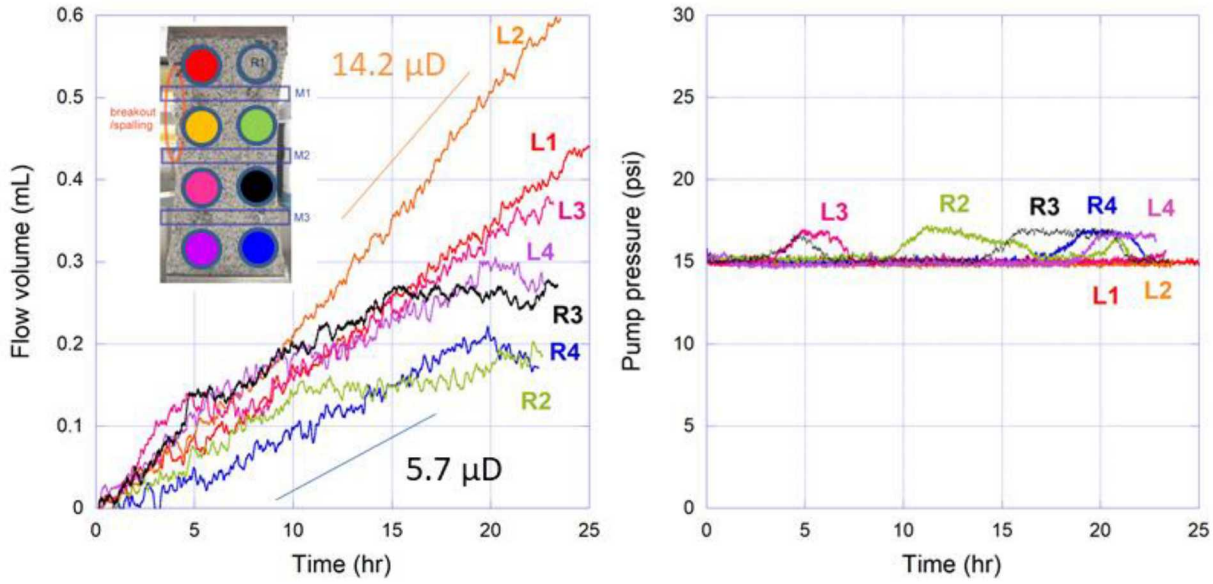

(a.) Injected fluid volume histories **(b.)** Pump pressure history

Figure 8.26. Water-injection flow permeability tests on mini cores. The overall changes in the injection rate correspond well to the expected degree of fracturing of the core samples for their locations in the moderately damaged slab Sample Z-2. Note that Sample R1 has not been tested yet.

For the locations M1, M2, and M3, indicated in Figure 3-19, thin section samples were also prepared for conducting the optical microscope study of the induced microcracks. These samples were prepared by Burnham Petrographics LLC, ID, and the samples were impregnated with blue epoxy to mark open pores and cracks in the samples (Figure 8.27). In the photograph, approximate locations of the observed area FOV1 and FOV2 are indicated.

From the image of FOV1 in Figure 8.28, intense microfractures roughly parallel to the spalled rock surface can be seen as a network of blue, epoxy filled cracks. However, once away from the surface, no clear presence of the cracks can be seen, except for a few, sparsely distributed, randomly oriented cracks (Figure 8.28). Because the seismic velocity changes—and the flow permeability measurements—indicated strong evidence of damage induced in the interior of the sample, the scarcity of the microcracks may indicate that very small aperture of the induced microcracks prevented the intrusion of the dyed epoxy.

Figure 8.27. Petrographic thin section samples made for the Sections M1, M2, and M3 shown in Figure 3-19. The width of the samples is 50.8 mm, and the height 25.4 mm. Blue boxes (FOV1 and FOV2) in the figure indicate the field of view of the magnified microscope images shown in Figure 8.28.

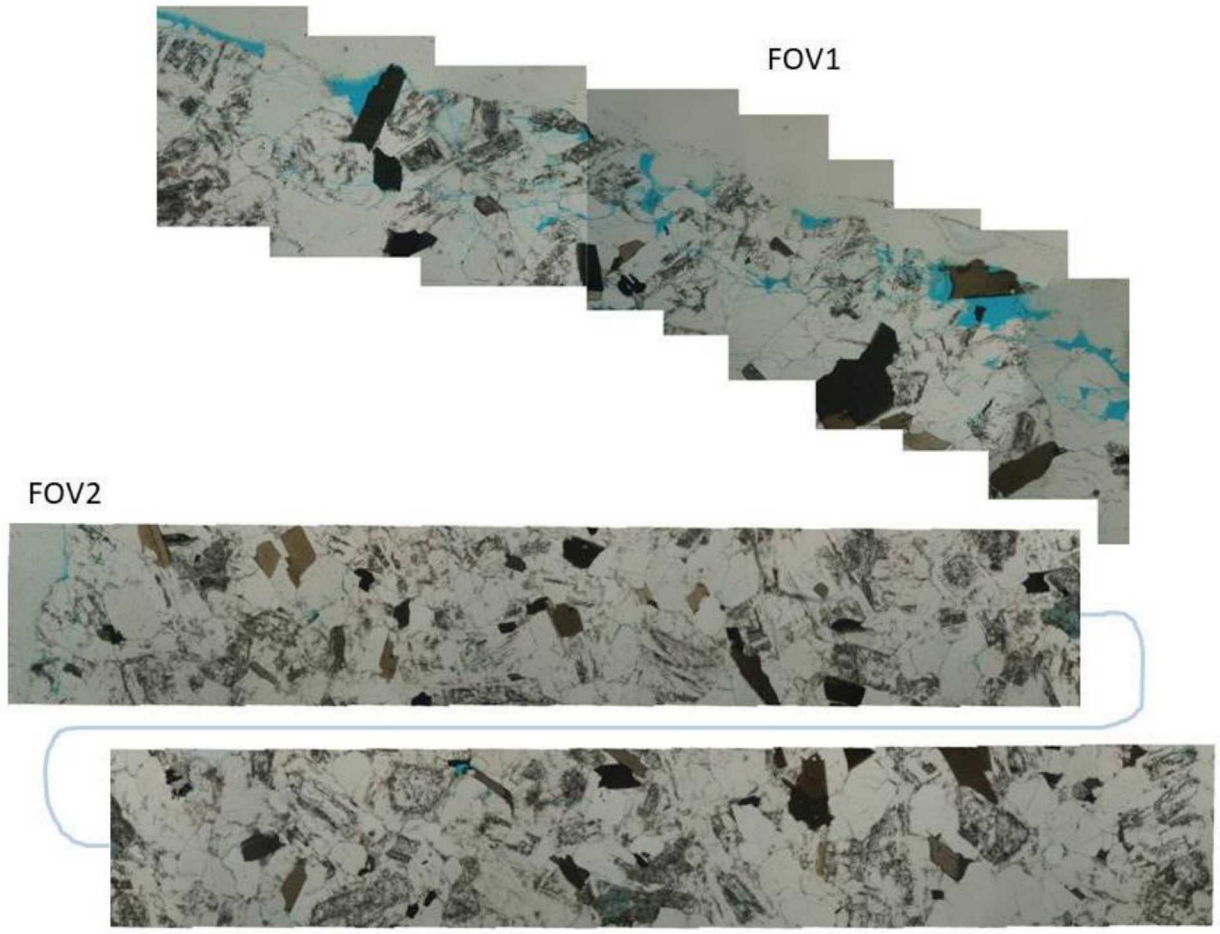

Figure 8.28. Thin-section images of FOV1 and FOV2 shown in Figure 3-22. Microcracks in the samples are mostly concentrated near the spalling observed on the surface of the sample, and much less cracks are found inside the slab samples.

8.3.3 Rigid Body Spring Network (RBSN) Modeling of EDZ Development

In order to help understand the development of microcracks due to the rock damage observed in the laboratory, we use a discrete, lattice-based approach for modeling the mechanical behavior of low-porosity crystalline rock mass with discontinuous features such as cracks and fractures. The Rigid-Body-Spring Network (RBSN), a kind of discrete modeling approach, represents the system behavior by simple two-node elements interconnected on a set of nodal points. The RBSN formulation is based on the concept of the Rigid-Body-Spring Model (RBSM), first introduced by Kawai (1978), in which the material constitution is represented as a collection of rigid bodies connected by spring sets. This section of the report presents a model setup for the compression test of shaped slab sample, the representation of Poisson effect in the RBSN formulation, followed by conclusions.

Model Setup

The RBSN model adopts the Voronoi diagram for partitioning the domain and the dual Delaunay tessellation for constructing the assembly of lattice elements. Each Voronoi cell is associated with an individual nodal point, where the kinematics of the cell is defined. The Voronoi discretization is basically carried out in three steps: nodal point generation, Delaunay tessellation, and Voronoi tessellation (Figure 8.29).

First, a set of nodal points are positioned regularly or irregularly inside the domain (Figure 3-24(a)). For random point generation, the points are sequentially generated with a minimum allowable distance l_{min} between neighboring points, which define the desired nodal density and thus controls the mesh size. Furthermore, various mesh fineness is attainable using a user-specified spatial correlation function for l_{min}. Nodal points also can be predefined at a specific position from input if necessary for the assignment of boundary geometry and other conditions.

The second step provides the Delaunay tessellation, for which a collection of tetrahedra connect the nodal points (Figure 8.29(b)). The Delaunay tessellation is constructed using the concept of a super-tetrahedron (Sloan, 1987; Taniguchi et al., 2002). The circumsphere of each tetrahedron is the smallest sphere that circumscribes the corresponding four nodal points. In general, a randomly distributed point set corresponds to a unique Delaunay tessellation, in which no two coincidental circumspheres exist. The resulting Delaunay tessellation represents the unstructured mesh of lattice elements. Each tetrahedral edge connects two adjacent nodes, by which the nodal connectivity of the lattice element is defined.

Following the Delaunay tessellation, the Voronoi tessellation is constructed with convex polyhedrons called Voronoi cells (Figure 8.29(c)). The Voronoi cell for a nodal point is a territory in which the locations are closer to the corresponding point than any other points. Locations on a cell boundary are equally close to the neighboring nodal points for which the Voronoi cells share that boundary (i.e., common cell boundary). In consequence, the domain is collectively filled with the disjoint Voronoi cells for all the nodal points. Also, the Voronoi diagram has a unique geometric correspondence with the Delaunay tessellation for a set of nodal points (Okabe et al. 2000). The geometries of the dual Delaunay-Voronoi tessellations are used for the RBSN element formulation, which will be discussed in the next subsection.

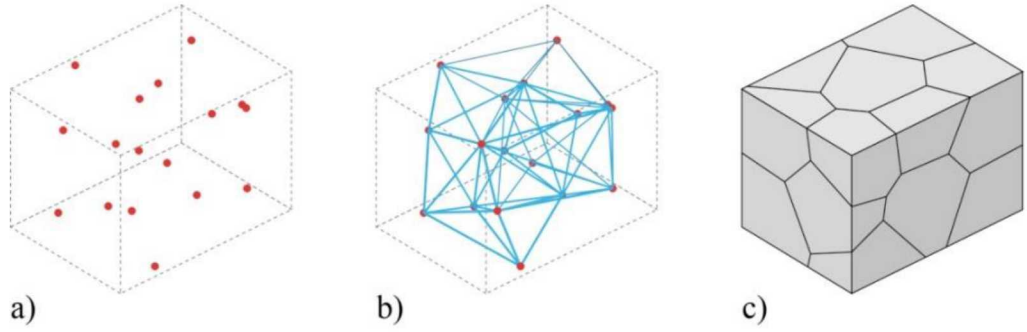

Figure 8.29. Domain partitioning process: a) nodal points; b) Delaunay, and c) Voronoi cells.

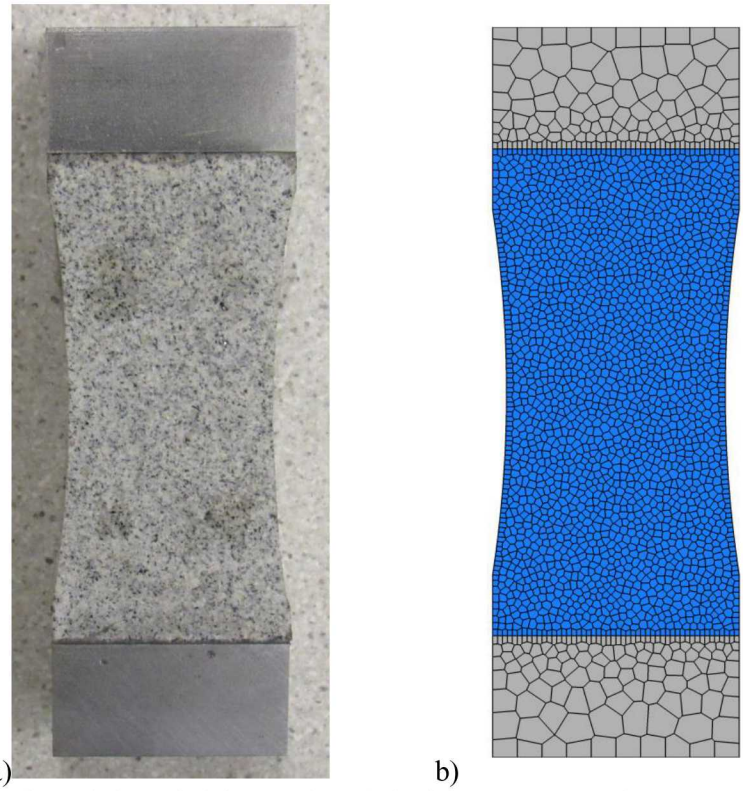

a) b)

Figure 8.29. Preparation of shaped slab samples: a) for laboratory experiments; and b) for the numerical simulations.

For simulations of the shaped slab compression test, we generated a Voronoi mesh based on laboratory experiment samples. The particular geometry of the sample involved curved surfaces on the sides of a rectangular slab, with a length of 10.2 cm, a width of 5.08 cm, and a thickness of 2.54 cm (Figure 8.29(a)). The curvature on the sides has a radius of 25 cm. Also, 2.54 × 2.54 × 5.08 cm steel blocks are attached at the top and bottom ends in order to prevent tensile fracturing of the sample. The resulting mesh, shown in Figure 8.29(b), replicates all the geometric features of the laboratory sample.

Implementation of Arbitrary Poisson's Ratio

RBSN Model Formulation

A lattice element consists of a spring set and rigid-body constraints connecting neighboring nodes. Figure 8.31 presents the formation of a lattice element for arbitrary neighboring nodes *i* and *j*. A zero-size spring set is located at position *C* (the centroid of the common Voronoi cell boundary), and rigid arms from the spring set link the neighboring nodes (Figure 8.31(b)). Each node has six degrees of freedom (three translations and three rotations) for the case of 3D modeling, and the spring set is also formed from three axial springs and three rotational springs as shown in Figure 8.31(c).

The Voronoi cell is basically considered to be rigid in the sense that it maintains its original shape during the process of loading and material deformation (assumption of small strain). The flexibility of the motion is lumped into the spring sets; therefore, the separation and interpenetration of the cells are permitted. The rigid-body constraints link the nodal degrees of freedom to the generalized relative displacements of the spring set. The spring set consists of three axial springs and three rotational springs acting independently,

with stiffnesses $\mathbf{D} = \mathrm{diag}[k_n, k_s, k_t, k_{\phi n}, k_{\phi s}, k_{\phi t}]$ in local *n-s-t* coordinates. The spring coefficients are scaled in proportion to the distance between the element length h_{ij}, and the area of the Voronoi cell boundary A_{ij}:

$$k_s = k_t = \alpha_1 k_n = \alpha_1 \alpha_2 E \frac{A_{ij}}{h_{ij}}, \quad k_{\phi n} = E \frac{J_p}{h_{ij}}, \quad k_{\phi s} = E \frac{I_{ss}}{h_{ij}}, \quad k_{\phi t} = E \frac{I_{tt}}{h_{ij}} \tag{8.8}$$

in which E is the elastic modulus, J_p, I_{ss}, and I_{tt} are the polar and two principal moments of inertia of the Voronoi cell boundary with respect to the centroid, respectively. By adjusting α_1 and α_2, according to experimental results, macroscopic modeling of both elastic constants (E and Poisson's ratio, ν) is possible. However, a local description of Poisson effect is not realized with $\alpha_1 \neq 1$. For the special case of $\alpha_1 = \alpha_2 = 1$, the Voronoi scaling of the spring coefficients enables the model to be elastically homogeneous under uniform modes of straining, albeit with zero effective Poisson's ratio (Bolander and Saito, 1998).

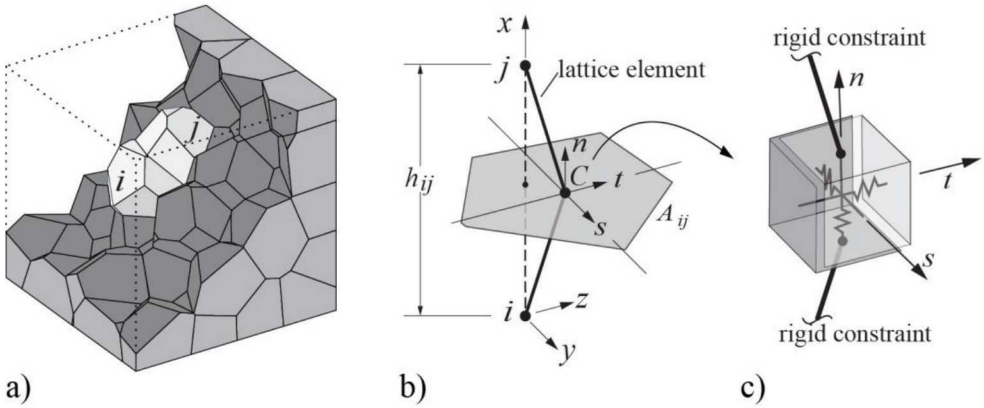

Figure 8.31. Typical RBSN lattice element ij: a) neighboring nodes i and j in a Voronoi diagram; b) isolated from the network; and c) a zero-size spring set located at centroid C of Voronoi cell boundary area A_{ij} (rotational springs have been omitted for clarity).

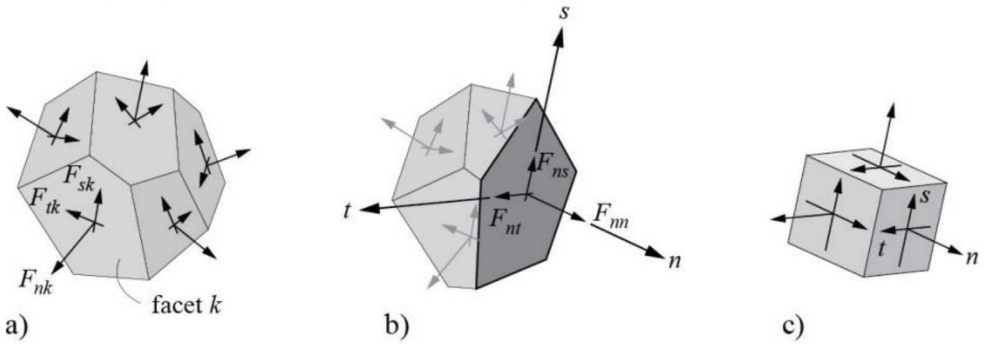

Figure 8.32. Stress tensor at a Voronoi cell node: (a) components of spring force local coordinates; (b) a set of nodal forces satisfying the equilibrium; and (c) complete stress tensor at Voronoi cell node (Adapted from Yip et al., 2005).

At each loading step, stress values are derived from the calculated spring forces. Since a lattice element is structured as a lineal connection with a determined local coordinates, the stress state is available only in the form of a vector by averaging the axial spring forces *Fn*, *Fs*, and *Ft* over the cell boundary area *Aij* (see Figures 8.31(b,c)). In order to expand the stress state to a tensor form, equilibrium conditions are considered at each Voronoi cell node. Sets of the spring forces are applied at the boundaries surrounding a Voronoi cell (Figure 8.32(a)), and nodal force components F_{nn}, F_{ns}, and F_{nt} can be calculated for an arbitrary section passing through the Voronoi cell node with its corresponding local *n-s-t* coordinates, which satisfy the equilibrium condition with all the forces acting on the remained cell boundaries (Figure 8.32(b)). Moment

contributions to equilibrium are not considered here. By dividing these force components by the cut-face area, the corresponding stress components σ_{nn}, σ_{ns}, and σ_{nt} can be obtained. By repeating this process for three mutually perpendicular sections, the full stress tensor is obtained (Figure 8.32(c)). Details are given elsewhere (Yip et al., 2005).

Fictitious Stress Approach

As described in the previous subsection, macroscopic modeling of Poisson's ratio by adjusting α_1 and α_2 in Equation (8.8) leads an irrational stress production at the local level of stress representation of lattice elements, so called the artificial heterogeneity (Bolander and Saito, 1998). To avoid that unrealistic modeling results, the fictitious (or auxiliary) stress approach has been implemented for representation of the Poisson effect. The formulation is presented as a series of steps.

Step 1: Nodal displacements are determined for the prescribed boundary conditions by solving the system equations for the case of $\alpha_1 = \alpha_2 = 1$ in Equation (8.8), which corresponds to $\nu = 0$. This condition provides an elastically homogeneous basis for introducing the Poisson effect. Principal stresses, σ_1, σ_2, and σ_3, and principal strains, ε_1, ε_2, and ε_3, are calculated at each node using the method for nodal stress calculation given in the section below. The indices 1, 2, and 3 denote the maximum, intermediate, and minimum principal values, respectively.

Step 2: At each node, an auxiliary measure of orthogonal strain is determined using the vector form of the principal strains, $\boldsymbol{\varepsilon}_P = [\varepsilon_1 \ \varepsilon_2 \ \varepsilon_3]^T$, and actual non-zero value of ν

$$\boldsymbol{\varepsilon}' = \nu \hat{\mathbf{I}} \boldsymbol{\varepsilon}_P \tag{8.9}$$

in which

$$\hat{\mathbf{I}} = \begin{bmatrix} 0 & 1 & 1 \\ 1 & 0 & 1 \\ 1 & 1 & 0 \end{bmatrix}. \tag{8.10}$$

The fictitious stress is obtained by multiplying both sides of Equation (3.3) by E

$$\boldsymbol{\sigma}' = E\nu \hat{\mathbf{I}} \boldsymbol{\varepsilon}_P = \nu \hat{\mathbf{I}} \boldsymbol{\sigma}_P \tag{8.11}$$

where $\boldsymbol{\sigma}_P = [\sigma_1 \ \sigma_2 \ \sigma_3]^T$.

Step 3: Fictitious stress is introduced into the lattice elements framing into each node i via a set of tractions, which are applied to the facets of the associated Voronoi polyhedral cell (Figure 8.33). For facet m, the traction vector is expressed by

$$\mathbf{t}_m^i = \mathbf{S}^i \mathbf{n}_m^i \tag{8.12}$$

where $\mathbf{S}^i = \text{diag}(\sigma_1', \sigma_2', \sigma_3')$ for node i, and $\mathbf{n}_m^i$ is the outward unit normal vector of facet m from node i. To facilitate explanation, but without loss of generality, the coordinate and principal directions in Figure 8.33 are assumed to be aligned. The auxiliary force acting on facet m is then

$$\mathbf{f}_m^i = \mathbf{t}_m^i A_m \tag{8.13}$$

where A_m is the area of facet *m*. This auxiliary force, resolved into normal and tangential components, is introduced into the spring set of the rigid-body-spring element associated with the facet. The set of auxiliary forces acting on the cell facets is in equilibrium.

Step 4: The introduction of auxiliary spring forces produces nodal displacements, in accordance with the prescribed boundary conditions of Step 1. The new principal stresses, $\hat{\boldsymbol{\sigma}}_P = [\hat{\sigma}_1 \ \hat{\sigma}_2 \ \hat{\sigma}_3]^T$, are calculated at each nodal site.

Step 5: Convergence of the algorithm is achieved when $\|\hat{\boldsymbol{\sigma}}_P - \boldsymbol{\sigma}_P\| < e$, where $\|\cdot\|$ is the Euclidean norm with respect to all nodal values and *e* is a predefined tolerance. Otherwise, the procedure returns to Step 2 with updated $\boldsymbol{\sigma}_P = \hat{\boldsymbol{\sigma}}_P$. Convergence is ensured since the fictitious stresses of Equation (3.5) become progressively smaller for the normal range of *v*.

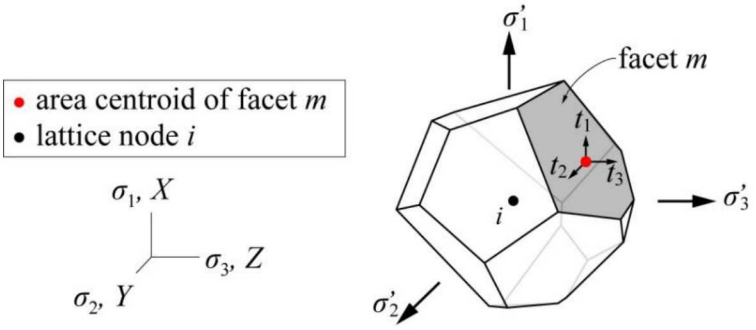

Figure 8.33. Fictitious stresses and associated traction vectors for facet *m* of Voronoi cell *i* (adopted from Asahina et al., 2017).

8.3.4 Conclusions and Future Plan

This objective of this task is to investigate a possibility of the development of excavation-induced damage zone around circular openings (i.e., boreholes and tunnels) in crystalline rock and their impact on rock's mechanical and hydrological properties. To address the issue of scale effects imposed by laboratory testing of small analogue boreholes and tunnels, rock samples with a special geometry (i.e., shaped samples with curved surfaces) have been used to induce realistic breakout on the sample surface and to evaluate a possibility of damage away from the sample surface. The use of such samples allowed us to (1) induce surface breakout, which is expected to occur in the EDZ in strong granite, (2) conduct real-time optical visualization of the EDZ development, and (3) perform acoustic visualization of microcracking in the samples via AE event location.

The acoustic measurements, both AE location and post-mortem seismic velocity measurements, indicated the development of microcracks away from the rock surface, where surface damage was observed. These observations are consistent with the results of measurements of permeability of the cores collected from the tested rock sample. However, visual inspection of the sample or examination of thin sections under a microscope did not indicate the presence of the microcracks clearly. Also, as a surface breakout grows and the failure occurs away from the curved surface, the difference between the laboratory sample and a field tunnel or a borehole grows. However, this test method can be improved to provide a tool for investigating the impact of relatively shallow breakouts on the mechanical and hydrological behavior of excavation-induced damage. Additionally, the laboratory tests can be designed to provide useful calibration data for numerical models for further upscaling.

In the newly started numerical modeling effort, we have implemented the fictitious stress approach to represent the Poisson effect without any spurious stress calculation in the lattice elements. Due to the two-node element representation of the displacement field, ordinary lattice models do not properly simulate local stress conditions for general elastic media (i.e., for arbitrary choices of E and ν). The approach described herein remedies the inabilities of regular lattice models to calculate local measures of stress. Based on tensorial representations of stress at each node, a set of fictitious forces are calculated and introduced into the lattice in a manner that correctly produces the Poisson effect. In consequence, the stiffnesses of the lattice elements are defined by the elastic constants (E and ν) without any calibration against laboratory test results. Also, we have conducted a model preparation for simulations of the shaped slab compression test. A Voronoi mesh is generated based on the geometry of laboratory test samples, which fully renders the geometric features, such as curved side cuts and steel loading blocks, in the real specimen.

For future work, we plan to test different types of rocks—including noncrystalline rocks, such as shales and carbonates—to understand the impact of rock texture and grain size on the hydrological and mechanical processes expected to occur in the EDZ. Also, we plan to test rock samples from field laboratories, including granite samples from the Grimsel and Stripa mines. Further, the hydro-mechanical-chemical interaction between the filling materials within the excavation and the EDZ is to be investigated. Concurrently, we plan to simulate the laboratory-observed EDZ development using the RBSN model, and predict the development of an EDZ in the field and its hydro-mechanical properties. A series of new modeling simulations is necessary because of nonlinear changes in the stiffness and permeability of the system resulting from progressive development of microcracks and fractures in crystalline rock.

8.4 Hydraulic Properties of Fractured Crystalline Rock Cores

8.4.1 Introduction

This section summarizes the main activities on the hydraulic characterization of fractured core samples, which were conducted at LBNL during FY18. Transmissivity of core samples were measured under laboratory conditions of controlled stress typical for field conditions. Previous reports focused on measurement technique and comparison to field results. We also analyzed the results of the evaluation of core sample transmissivity determined in FY17. Preliminary analysis of anisotropy using data collected in FY17 provided a suggestion of anisotropy, but indicated that further laboratory experiments were necessary, motivating the FY18 work. For FY18 the effort was spent on understanding anisotropy of the fractures, because flow in fractured crystalline rock in the deep subsurface takes place through a fracture network, and is dependent on fracture aperture distribution and the hydraulic head field. The main thrust of the core measurements at LBNL is to determine fracture transmissivity as a function of controlled stress under laboratory conditions. Cores were taken from the borehole COSC-1 (Collisional Orogeny in the Scandinavian Caledonides – COSC – See Chapter 5). The measurements were conducted under controlled stress conditions with fluid delivery and collection customized to directly investigate the effect of stress on fracture hydrologic behavior. A unique apparatus, described in Section 4.2.3, was constructed to enable flow through four flow channels on the fracture face, to measure multi-directional transmissivity, to assess fracture anisotropy.

8.4.2 Methodology

Description of Fractures

Four fractured core samples were chosen for the anisotropy and transmissivity measurements, and can be seen in the top four frames of Figure 4-1. Criteria for fracture selection were (1) having the correct diameter for the experimental apparatus (60 mm diameter), and (2) having a clean fracture that could be sealed on the core sides. All the cores were inspected, photographed, measured, and evaluated for usability in the experiment. All cores appear to be very tight crystalline rock, containing at least one cross-cutting fracture, and some with secondary mineralization near the fractures. Two fractured cores were selected for more detailed measurements, 211-2 and 401-1, for having the best fit to the system and the least amount of damage.

In addition to the naturally fractured cores, two artificial fractured cores were constructed and used to check the system. Several methods of artificial fracture construction were evaluated, including the use of epoxy, epoxy and sand mixtures, and other moldable compounds. It was determined that Delrin cores were the most reliable, and they were used for the experiments. One artificial core was a 60 mm diameter x 85 mm length cylinder with a horizontal hole drilled through the center. This design effectively blocks three of the flow channels and allows flow through the fourth, mainly to evaluate whether the sleeve surrounding the core properly blocks circumferential flow paths. The other artificial core had the same dimensions but was sliced in half, and an aperture distribution was created by creating a roughness on one half, as shown in the lower two frames of Figure 8.34.

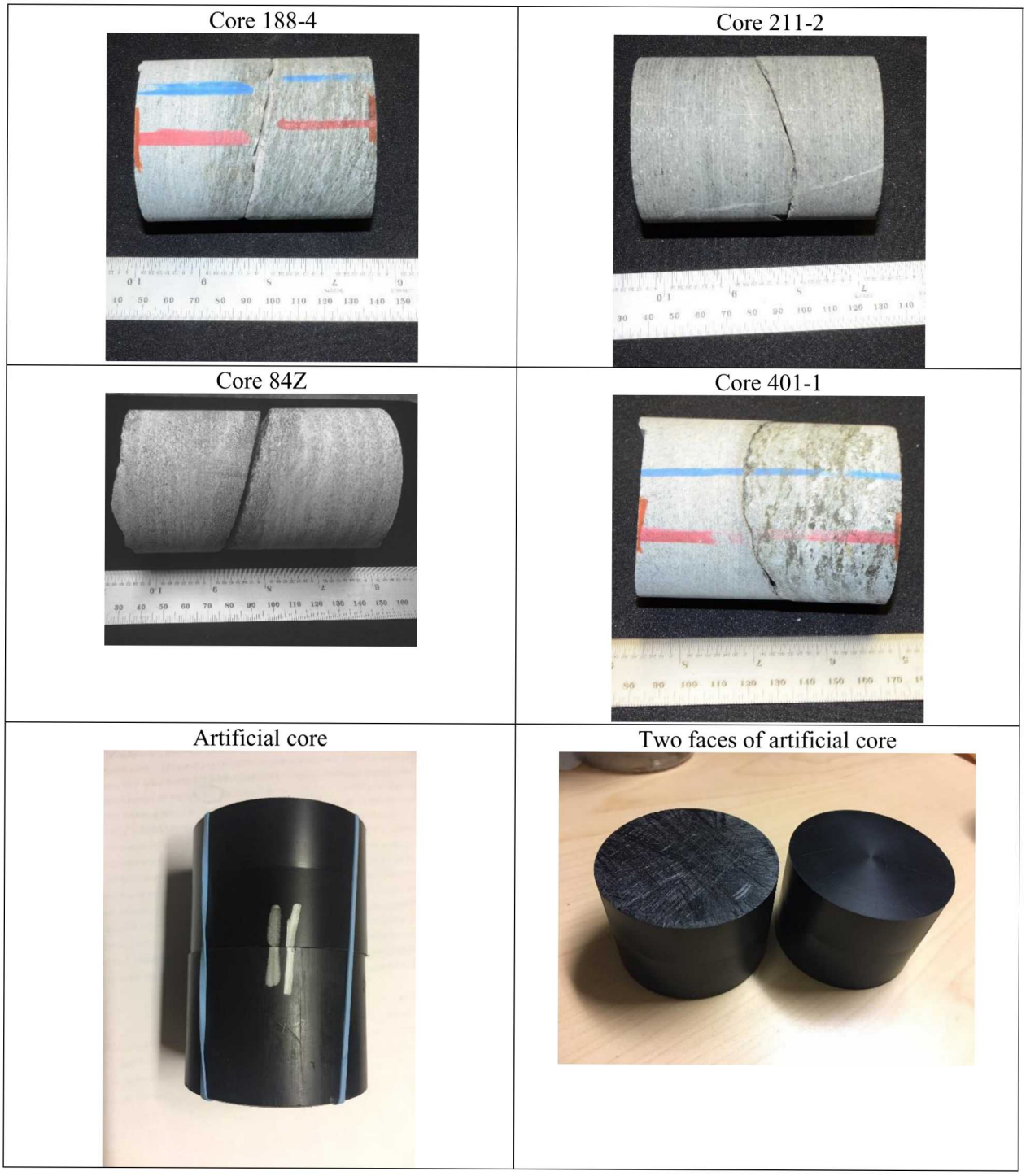

Figure 3.34. Photographs of natural and artificial cores used in this study.

Aperture Measurements

The fractured cores were CT scanned using a modified GE Lightspeed medical X-ray CT scanner before and after transmissivity measurements were made, to get a better understanding of fracture geometry and to estimate the aperture distribution. Because the cores had to be removed from the pressure vessel for scanning, scans were performed without applying the confining pressure. Figures 8.35(a) and (b) show the apertures and CT cross sections of cores 211-2 and 401-1. Figure 6.36 is an image of the sample on the table ready for CT scanning.

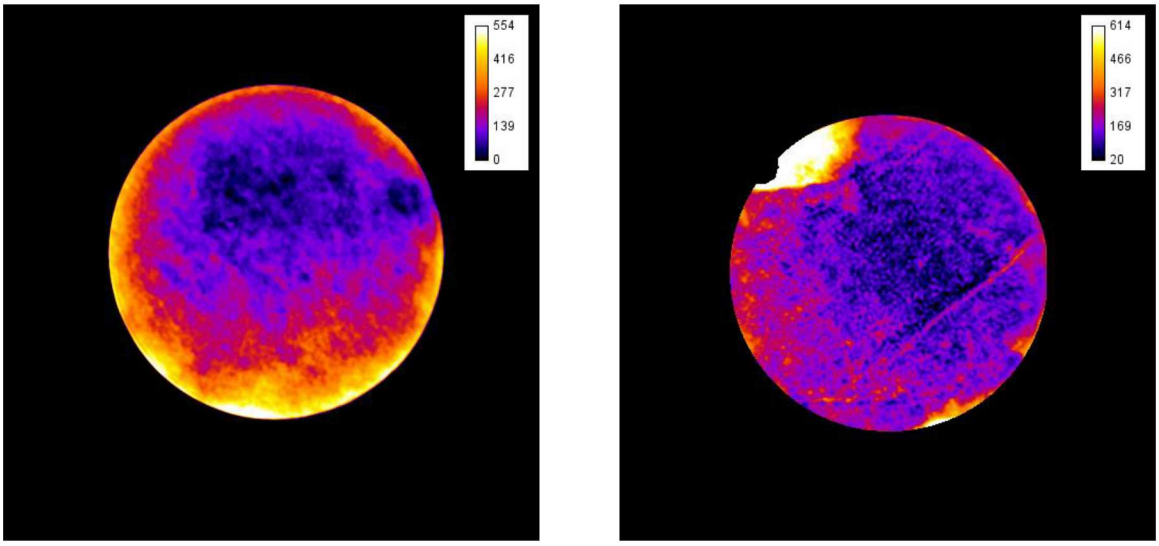

Figure 8.35(a.) Aperture maps from CT measurements for cores 211-2 (left) and 401-1 (right). Calibration scale in µm. Scans were taken on the cores with no confining pressure applied before the transmissivity measurements were made.

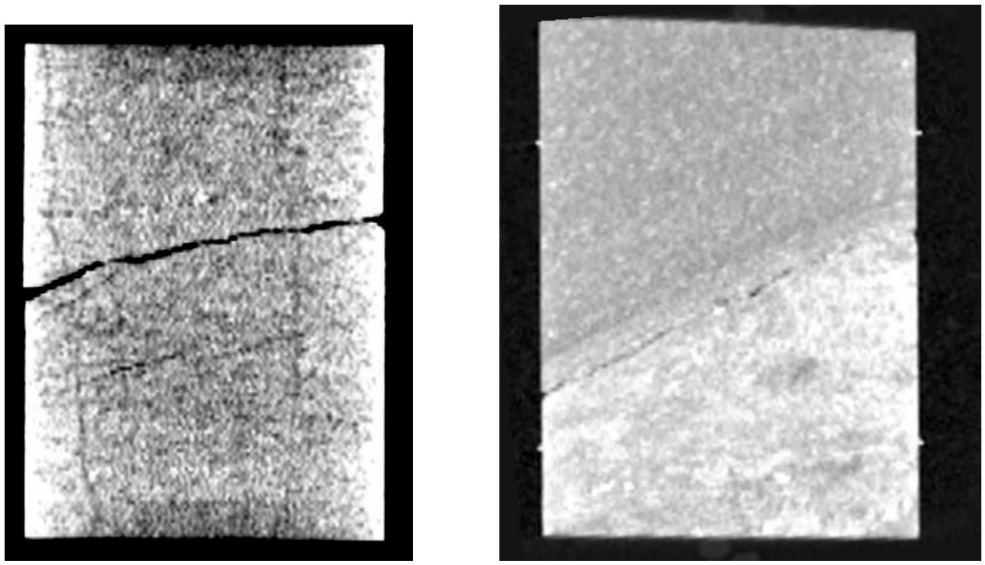

Figure 8.35(b.) Cross sections of Cores 211-2 (left) and 401-1 (right).

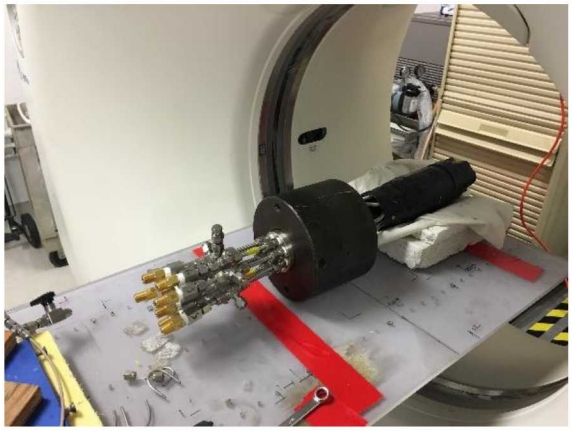

Figure 8.36. Sample on CT table ready for scanning.

In addition to the CT scanning method, a surface scan was performed using a surface profiling microscope (Keyence, Itasca, IL), and the surfaces were aligned and subtracted to estimate the aperture (Figure 8.37). The surface scans were high quality, but work is ongoing to align the faces to get the aperture maps to agree between the two measurement methods. At this time, this method is giving larger aperture values than the CT scanning method and more effort is needed to reconcile the two methods.

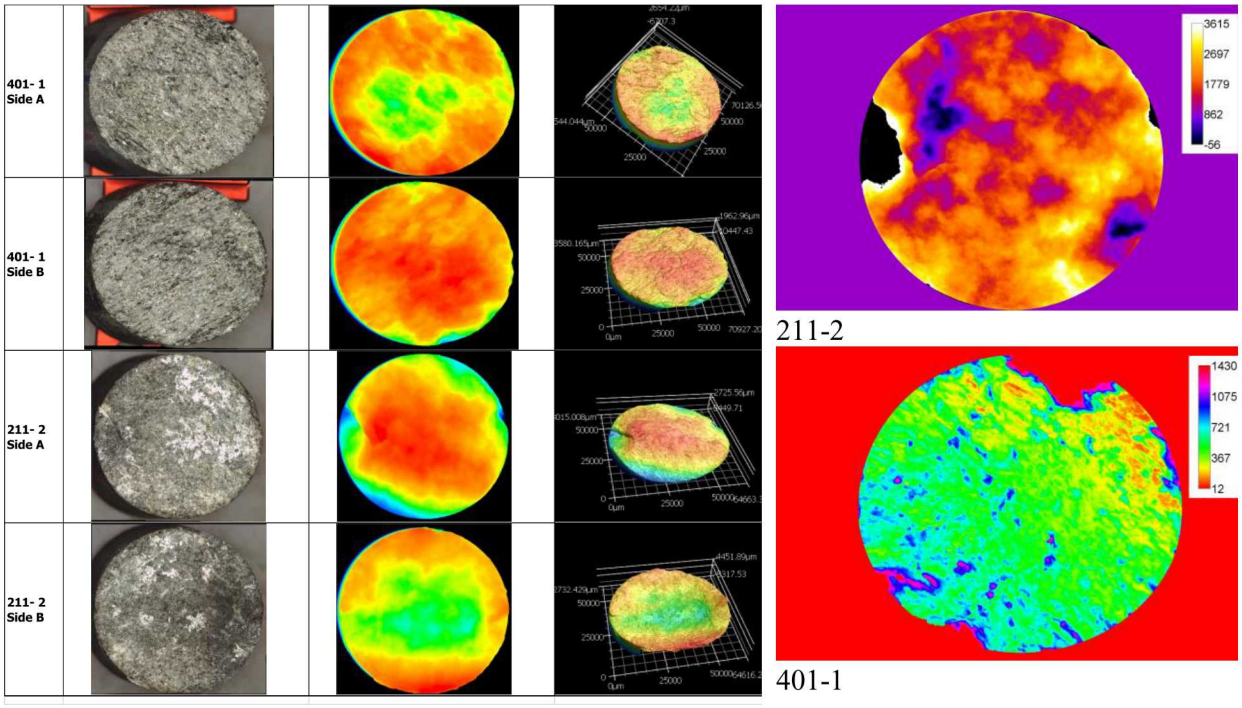

Figure 8.37. Surface profile measurements from the Keyence scanning for Cores 401-1 and 211-2. On the left is the data from the scanning scope (core photos, plan views of digital scans, perspective 3D views of scans), and on the right are estimates of the aperture after aligning and subtracting the surface maps.

Experimental Apparatus

The transmissivities were measured over a range of effective stresses from 200 to 1,100 psi. For the measurements, a custom apparatus was constructed allowing for delivery of water to any of four inlets distributed at 45-degree increments around the circumference of the core, and to extract water from an outlet opposite to the inlet (Figures 8.38 and 8.39). The inlets and outlets are half-tubes running along the length of the core to insure the contact with the fracture. A custom silicone rubber sleeve (Figure 8.39) was manufactured to fit around the core and inlet and outlet tubes to inhibit flow around the core. This sleeve was cast with silicone molding compound over a mockup of the setup to provide the proper fit.

The top inlet and outlet support is a solid Delrin (a hard plastic) hockey-puck shaped disk with holes to hold the inlet and outlet tubes on one side, and national pipe thread (NPT) fittings on the other. One-quarter inch stainless steel tubes were connected to the NPT fittings, and these were run through feed-through ports on the pressure vessel cap (Figure 8.39). Outside the pressure vessel, each tube was connected to a 20 psi pressure relief valve, and then to a five-way ball valve. Inside the pressure vessel, the tubes were connected to half round tubing that ran along the outside of the core. The ends of the half round tubing were plugged with the same silicone molding compound used for the sleeve.

A second solid hockey puck-shaped Delrin disk was placed at the bottom of the core and sleeve, and a thin Latex sleeve followed by a Viton sleeve was placed over the entire assembly to prevent leaks into the assembly from the confining fluid. The assembly shown in Figures 8.38 and 8.39 was placed in a pressure vessel (High Pressure Equipment Company TOC-31-20) with an inside diameter of 4 inches, an inside length of 20 inches and a rating of 5,000 psi. A high-pressure precision syringe pump (Isco D-series) connected to a pressure port on the bottom of the pressure vessel was used to provide controlled confining pressure.

The sleeve system surrounding the core was designed to fit tightly around the core and half round stainless tubing, to prevent circumferential flow and to guide the fluid into the fracture. Modifications were made to the silicone sleeve in FY18, mainly removing the silicone end that interfaced between the bottom Delrin puck and the rock. This was done to ensure that the confining pressure was directly applied to the core, and did not cause bowing out of the sleeve. In addition, previously a strip of copper was placed around the core under the silicone sleeve to help support the silicone sleeve and to keep the silicone from deforming into the fracture when confining pressure was applied. However, this year the copper strip was removed as the lower confining pressures used (1,100 psi max v. 4,500 psi max in previous years) did not require this extra stiffness. Also, at the lower confining pressures, the advantage of better sealing on the core surface with the silicone sleeve outweighed the benefits of the copper strip. Water penetration or adsorption into the matrix is not a factor in this experiment because the rocks are tight crystalline rock and flow occurs for such a short period of time.

At the top of the cores, at the interface between the upper Delrin disk with the feed-through flow tubing and the rock surface, a non-deformable gasket was placed to prevent flow through the top of the sample. Flow through the fracture was driven using another precision high-pressure syringe pump (Isco D-series), although flow pressures were kept below 20 psi. Initially a model 1000D pump was used for the flow, but measurement of the transmissivity for the 401-1 required lower flow rates so this was exchanged for the model 500D pump. Flow was regulated through two 5-way ball valves (1 inlet tube and 4 outlets), and the pressure difference between the inlet and outlet was measured using a Rosemount 3051 differential pressure transducer and the signal recorded with a Keithley 2701 digital multimeter using Excelinx software.

To test the apparatus, a Delrin core of the same size as the rock cores was manufactured, which was solid except for one horizontal hole 1/16” in diameter through the core center. This dummy core was placed in the system and tested with the same range of confining pressure used for the natural cores. For the channel

aligned with the through-hole, very low to no differential pressure was observed indicating that flow was not restricted. For the other three paths, no flow was observed and the differential pressure steadily climbed until nearing the pressure limit of the flow system (20 psi), indicating that no flow was occurring.

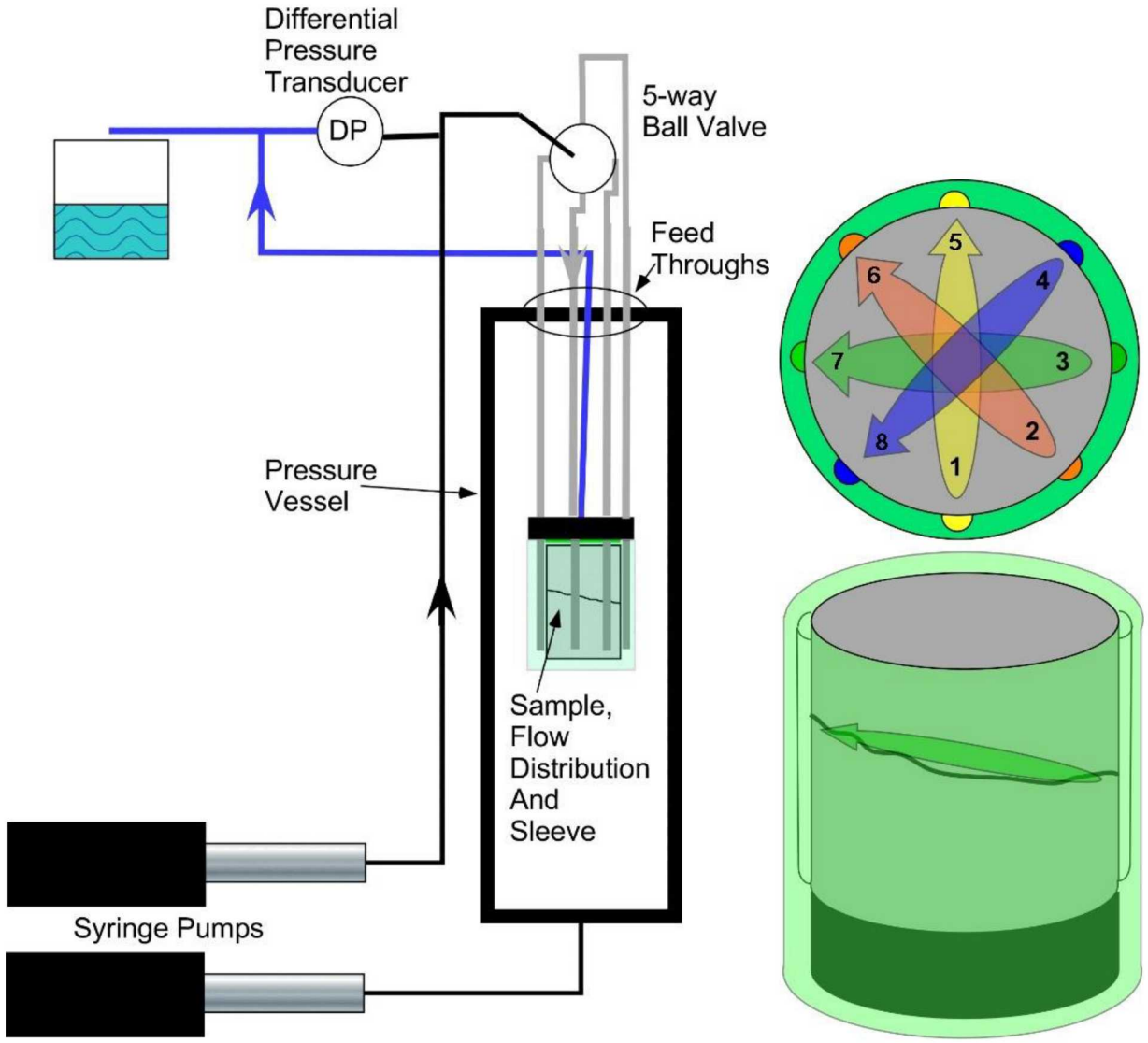

Figure 8.38. System schematic: The lower syringe pump controls confining pressure, and the upper syringe pump flows water through the core. Two 5-way ball valves (one shown) control flow to the inlet tubes (1-4) and outlet tubes (5-8).

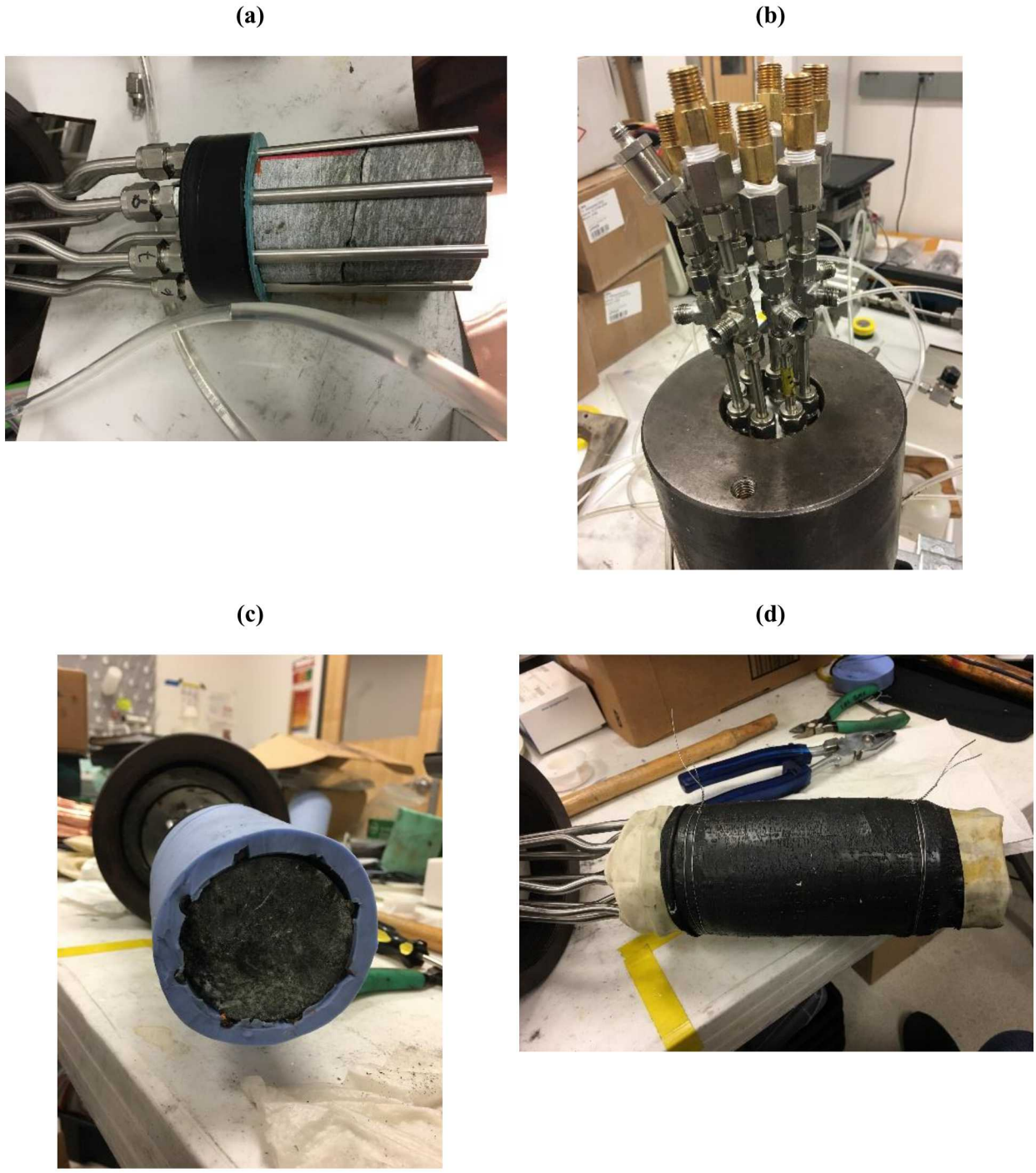

Figure 8.39. Apparatus assembly: (a) Both pieces of the fractured core are placed in between the water inlets and outlets, (b) feed-through ports on the pressure vessel cap, (c) end of core showing the Silicone rubber sleeve, and (d) view with outer sleeve in place.

Experimental Procedure

After preparing the core as described above, the core sample was placed in the pressure vessel. The vessel was filled with water and 100 psi confining pressure was applied to the core. Air bubbles in the tubing cause noise in the data and artificially increase the measured differential pressure, so any air bubbles in the flow tubing must be removed. This is an important step that cannot be omitted, even though it can be time-consuming.

Because previous experimental results showed that when confining pressure was increased for the first time, transmissivity decreased sharply and did not recover when the confining pressure was subsequently decreased, a procedure was developed to settle the fracture before beginning transmissivity measurements. After initial bubble removal, confining pressure was increased stepwise to 1100 psi, then reduced to 600 psi, and cycled two more times. After settling, differential pressure measurements were made across each of the four pathways (1-5, 2-6, 3-7, and 4-8, as shown in Figure 8.38) for at least three different flow rates. The flow rates ranged from 0.01 to 10 mL/min depending on the transmissivity of the core. When the flow measurements were completed, another confining pressure cycle was done and the measurements were repeated to assure a repeatable data set was produced. After data were collected for the flow directions (1-5, 2-6, 3-7, and 4-8), the flow directions were reversed and the measurements were repeated for directions 5-1, 6-2, 7-3, and 8-4.

Transmissivity Calculations

Differential pressure and flow rate measurements were completed on cross-cutting fractures through two core samples - Cores 211-2 and 401-1. In the case of a planar rectangular fracture with fluid inlet and outlet occurring uniformly through opposite edges, shown in Figure 8.40 (top), fracture transmissivity T (m^2/s) can be calculated from the following relationship

$$T = \frac{Q\rho g l}{h\Delta P} \tag{8.14}$$

where Q = volumetric flow rate, ρ = fluid density, g = gravity, l = fracture length, h = fracture width, and ΔP = differential pressure across the fracture.

In the case of the core geometry used in our experiments, shown in Figure 8.40 (bottom), water is applied over a finite length on opposite sides of a natural fracture, having an approximately circular area. For this core geometry we modified Equation (1), based on an analogy with the solution to a similar electrical resistance problem across a disk with finite sized electrodes (McDonald, 2000).

For the rectangular case (Figure 8.40 top), the resistance R_s across the volume is

$$R_s = \frac{l}{\sigma th} \tag{8.15}$$

and, therefore, the conductance C_s is the reciprocal

$$C_s = \frac{\sigma th}{l} \tag{8.16}$$

where σ = conductivity, t = thickness, h = height, and l = length.

For the circular case (Figure 8.40 bottom), the resistance R_c is given by

$$R_c = \frac{2}{\pi\sigma t} \ln \frac{2D}{d} \tag{8.17}$$

and the conductance is

$$C_c = \frac{\pi\sigma t}{2 \ln \frac{2D}{d}} \tag{8.18}$$

where d is the inlet/outlet length, and D is the fracture diameter. Letting l = h and dividing Equation (8.18) by Equation (8.16) yields

$$\frac{C_c}{C_s} = \frac{\pi}{2\ln \frac{2D}{d}} \tag{8.19}$$

which will be used as a factor to account for the geometric difference between the circular and rectangular geometry for all cores and paths. Therefore, Equation (8.14) is modified to

$$T = \frac{C_c}{C_s} \frac{Q\rho g}{\Delta P} \tag{8.20}$$

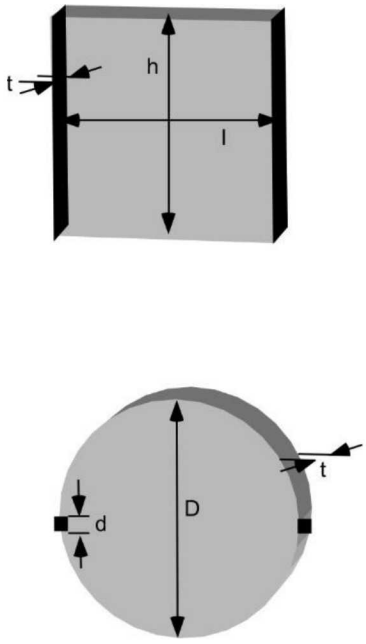

Figure 8.40. Schematic diagram of fractured core geometry used for calculations.

8.4.3 Laboratory results

For FY18 the effort was spent on understanding anisotropy of the fractures. Preliminary analysis of anisotropy using data collected in FY17 is presented first, followed by results from FY18 work.

.

Anisotropy Analysis of FY17 Experiments

Core 211-2. When all data is plotted for Core 211-2 (Figure 8.41), it is hard to see anisotropy, but individual cycles of pressure increase or decrease (Figures 8.42) consistently show anisotropy, with Paths 4-8 and 3-7 showing higher transmissivity than Paths 1-5 and 2-6. For the various cycles, anisotropy ranges from 1.7 to 2.7, with an average value of 2.2.

Core 401-1. A subset of the data collected at core 401-1, covering one cycle of confining pressure increase and decrease, is shown in Figure 8.43. Anisotropy is apparent, with Path 1-5 and Path 2-6 consistently showing greater transmissivity than Path 3-7. In this experiment, there was no flow through Path 4-8. For this core, the transmissivity values obtained in the laboratory are in the same range as the transmissivity estimated from flowing fluid electrical conductivity (FFEC) logging in the field (Doughty et al., 2017). The transmissivity variation with confining pressure (decreasing as confining pressure increases - top frame, then remaining constant as confining pressure decreases – bottom frame) is typical of the FY17 experiments conducted without the fracture-settling procedure. The anisotropy is similar for all confining pressures, with the ratio of transmissivity of the high-T paths (1-5 and 2-5) to the transmissivity of the low-T path (3-7) ranging from 2.0 to 2.9. If we include the zero permeability of Path 4-8, then the anisotropy would double, becoming 4.0 to 5.8.

The results of the core analyses can be summarized in Figure 8.44, which shows schematically the high flow and low flow directions for Cores 401-1 and 211-2.

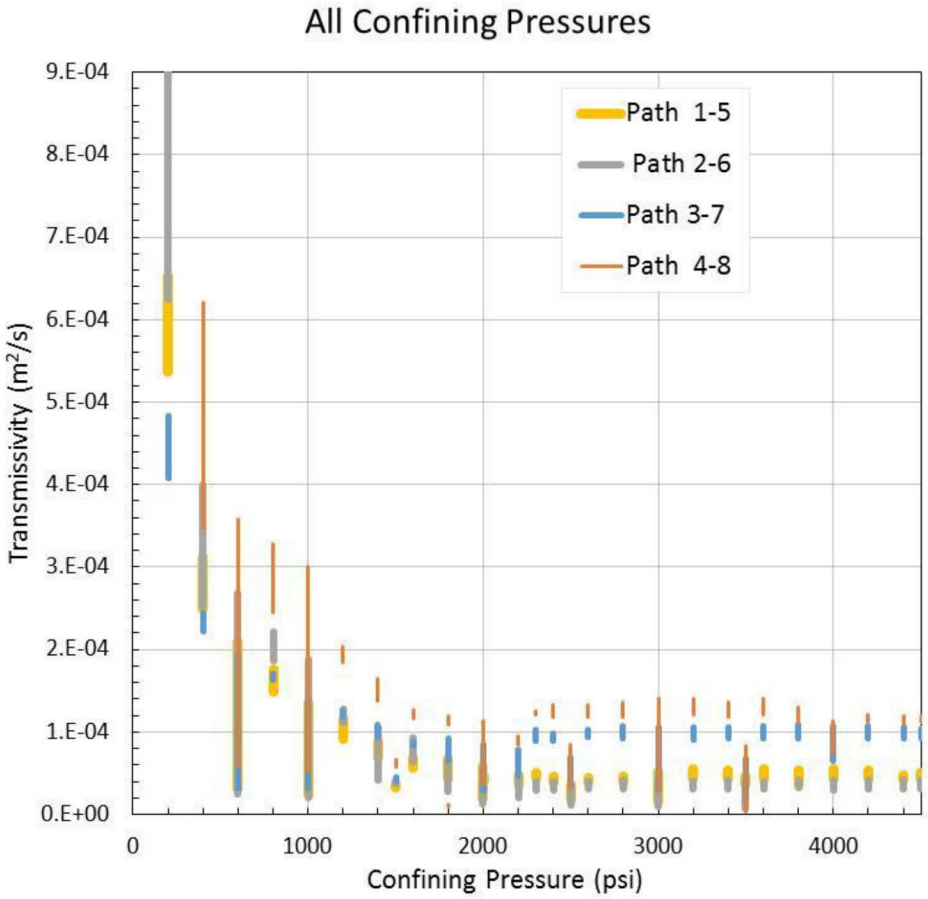

Figure 8.41. Transmissivities of various flow paths for Core 211-2 – all experiments conducted in FY17. Transmissivity for each path is shown with a different line thickness, to enable overlapping values to be seen.

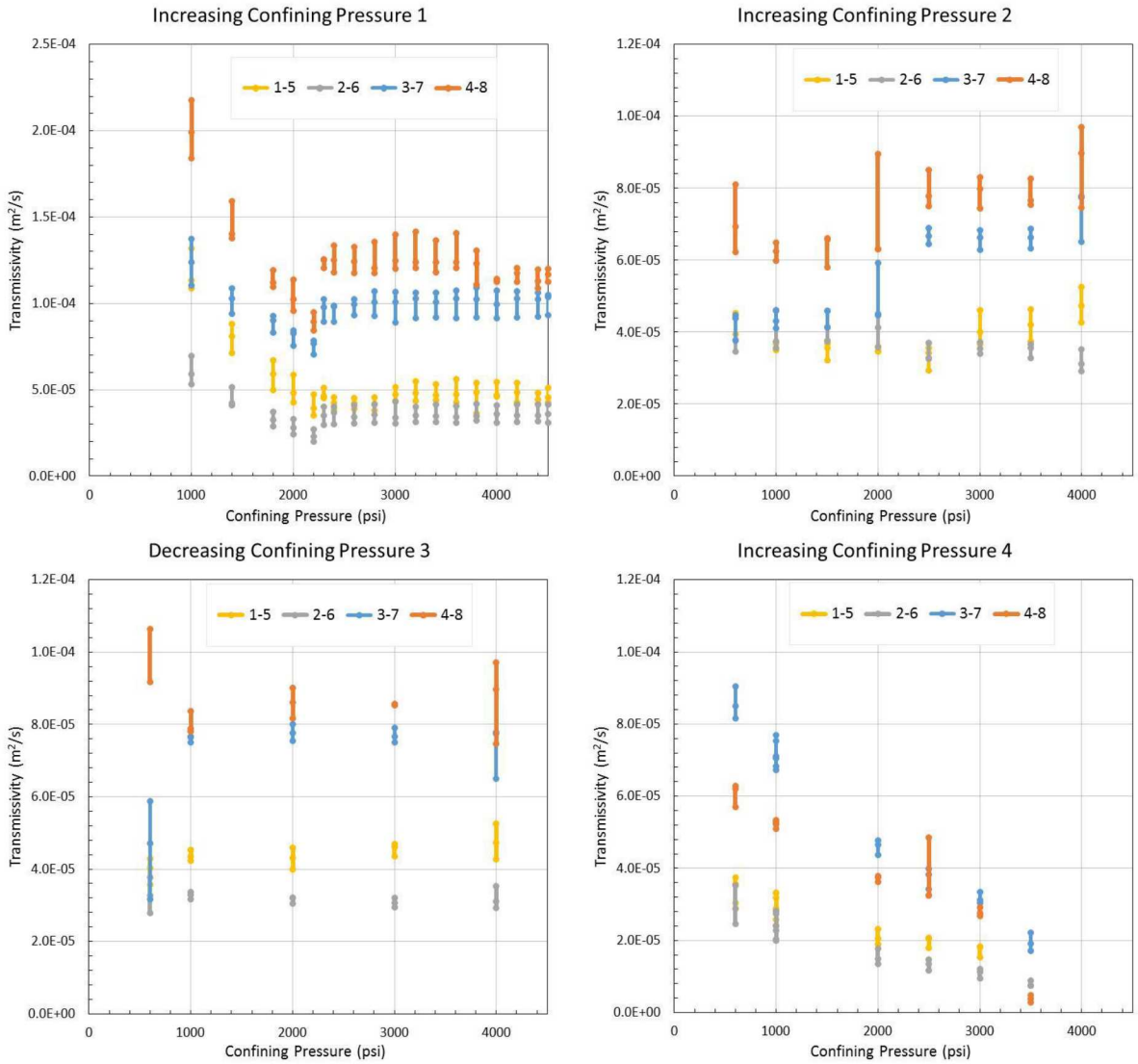

Figure 8.42. Transmissivities of various flow paths for Core 211-2 – individual cycles of FY17 data.

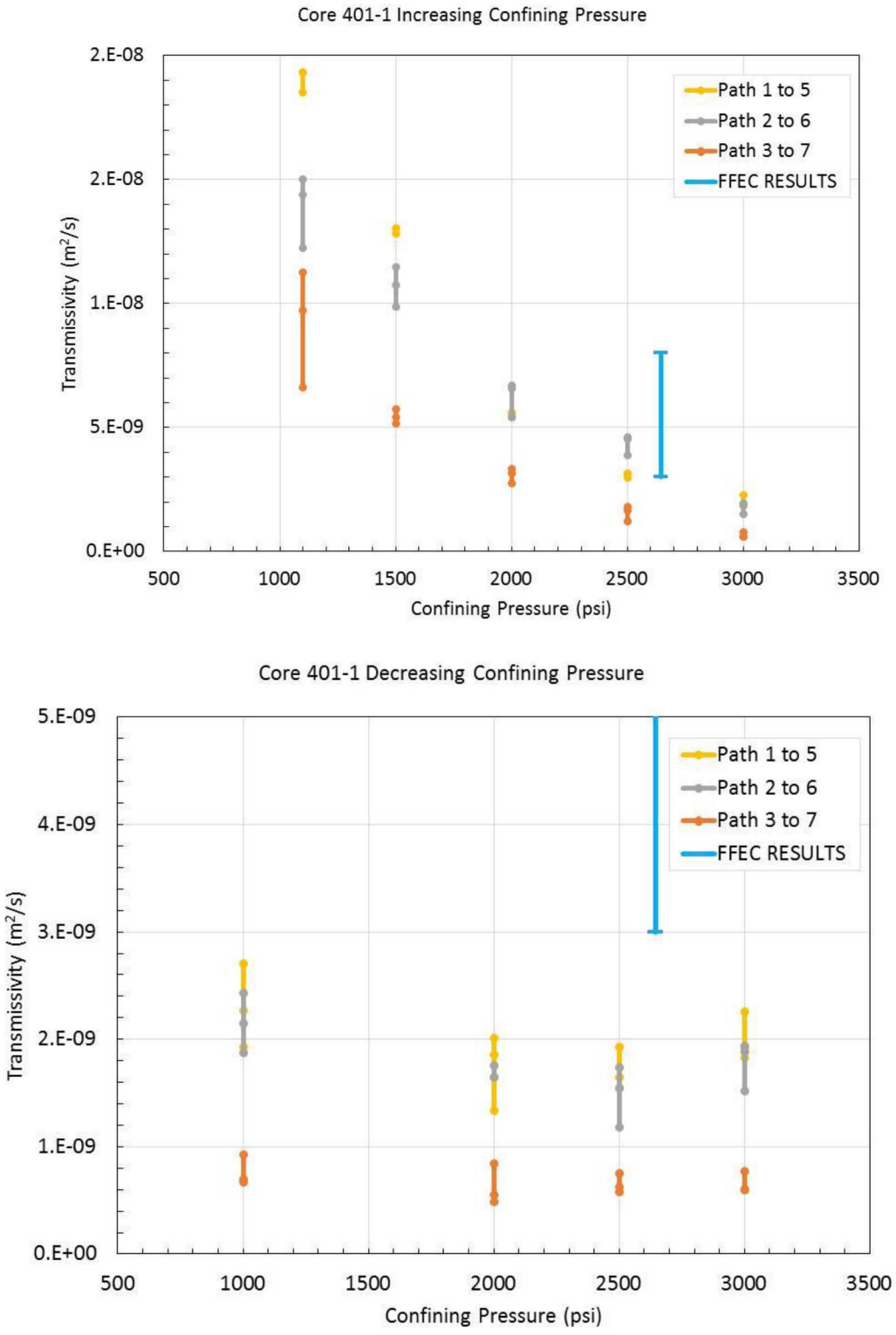

Figure 8.43. Transmissivities of various flow paths for Core 401-1 experiments conducted in FY17, and the transmissivity inferred from FFEC logging in the field. The transmissivity of Path 4 to 8 is zero.

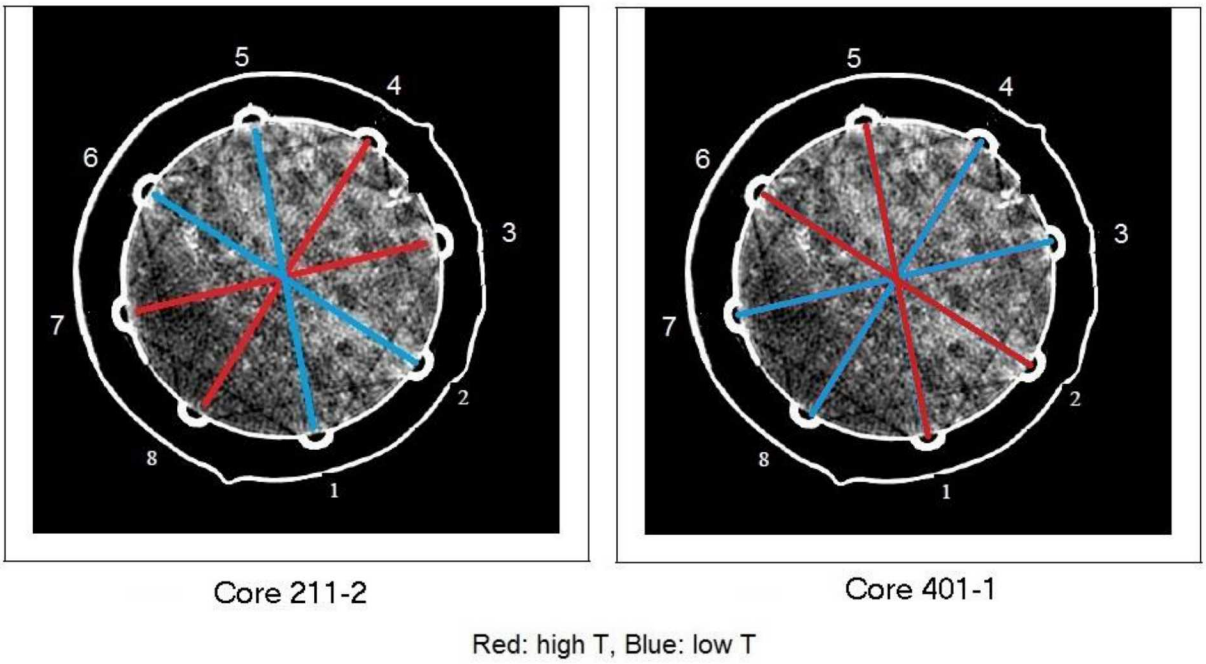

Figure 8.44. Schematic of anisotropic flow from analysis of FY17 data.

FY18 Experiments

FY18 experiments were conducted using two cores (211-2 and 401-1), which were previously investigated in FY17, and artificial fracture models with known anisotropy. The fractures are aligned so that the paths are the same each time a fracture is investigated. However, small alignment differences are unavoidable so x-ray CT scans are taken of each assembly to verify orientation.

Core 211-2. Core 211-2 was selected to simplify the experimental procedure, because it has a relatively high transmissivity, which allows it to reach a steady state quickly and makes it easier to remove trapped air bubbles. For this core, the measured transmissivity values are listed in Table 8.4 along with the standard deviation. The value for the forward direction (i.e., flow from 1 to 5, 2 to 6, 3 to 7, and 4 to 8) represents an average of 15 measurements at 4 different confining pressures (600-1,100 psi) and three flow rates (1, 5, and 10 ml/min). In the forward direction, the transmissivity values varied from 3.0×10^{-5} to 4.4×10^{-5} m^2/s. In the reverse direction (flow from 5 to 1, 6 to 2, 7 to 3, and 8 to 4) transmissivity varied from 4.2×10^{-5} to 5.7×10^{-5} m^2/s. In both cases, Path 4-8 had the highest value of transmissivity.

Table 8.4. Transmissivity of Core 211-2. All values in m^2/s

Path	Forward	Std. Dev.	Reverse	Std. Dev.
1 to 5	3.0×10^{-5}	4.3×10^{-6}	4.2×10^{-5}	3.6×10^{-6}
2 to 6	3.7×10^{-5}	1.7×10^{-6}	5.6×10^{-5}	7.4×10^{-6}
3 to 7	4.2×10^{-5}	4.6×10^{-6}	5.2×10^{-5}	6.5×10^{-6}
4 to 8	4.4×10^{-5}	1.2×10^{-6}	5.7×10^{-5}	4.4×10^{-6}

Because all the paths showed similar transmissivity values, the concern arose that fluid was flowing around the edge of the core, rather than across the center of it. Therefore, the core was removed from the apparatus and altered slightly by putting cementing compound in the larger gaps at the edge of the fracture near port 8. The purpose of this modification was to try to decrease the possibility of circumferential flow at this point to ensure that fluid is moving through the center of the core rather than around the edge. As can be seen in Table 8.5, the resultant transmissivities of Path 1 to 5 and Path 3 to 7 did not change significantly, while transmissivity for Path 4 to 8 decreased and that for Path 2 to 6 increased, possibly due to some sealing of the fracture near port 8, and propping open of the fracture near port 6. The large change in transmissivities apparent by comparing Tables 4-1 and 4-2 demonstrates that very different flow behavior can exist depending on the path through the fracture. The reverse direction flow was not measured in this system.

Table 8.5. Transmissivity of Core 211-2 altered by applying cementing compound to gaps at core edge near port 8. All values in m^2/s.

Path	Forward	Std. Dev.
1 to 5	3.0×10^{-5}	7.7×10^{-6}
2 to 6	2.7×10^{-4}	9.0×10^{-5}
3 to 7	6.6×10^{-5}	1.1×10^{-5}
4 to 8	6.7×10^{-7}	1.9×10^{-7}

Core 401-1. Core 401-1 was selected for further study because the transmissivities obtained in FY17 were comparable to those obtained in the field by FFEC logging. However, Core 401-1 has proven to be more difficult to get consistent results from, and further measurements are ongoing. Transmissivity values on this core have been previously measured as on the order of 10^{-9} to 10^{-8} m^2/s (Figure 8.43). With this small aperture, lower flow rates and longer equilibrium times are required to assure consistent measurements. In addition, complete water saturation of the fracture is required. To date, measurements in the forward direction have been completed and are shown in Table 8.6.

Table 8.6. Transmissivity of Core 401-1. All values in m^2/s.

Path	Forward	Std. Dev.
1 to 5	1.9×10^{-9}	2.1×10^{-10}
2 to 6	4.3×10^{-9}	1.7×10^{-9}
3 to 7	3.7×10^{-9}	9.6×10^{-10}
4 to 8	4.6×10^{-9}	9.0×10^{-10}

Artificial Core. An artificial core with one fracture face smooth and the other artificially roughened with sand paper has been prepared. Initial investigations suggested that the fracture transmissivity is too low to be able to complete laboratory experiments within a reasonable time frame. Therefore, work is underway to increase the relief on the roughened face to increase transmissivity.

8.4.4 Conclusions

In this work, a novel technique was developed to investigate the effect of the geometry of the fracture on anisotropic flow through fractures in rock cores. The measurements show that fracture transmissivity appears anisotropic—roughly a factor of two difference in different directions, but numerous uncertainties make this finding tentative and provide motivation for future work.

More work is ongoing to provide *T* values for forward and reverse directions on the cores for all flow paths, and also on artificial cores. Two avenues will be followed to try to support our tentative findings of observing anisotropy: use of artificial cores and numerical modeling.

For the artificial cores, we will purposefully attempt to produce fractures with anisotropic transmissivity distributions, by means of directional sanding, etching, gouging, etc. Additionally, the engineered nature of the artificial cores should minimize problems like broken edges that allow circumferential flow.

A numerical modeling component of the fracture is just getting underway. The aperture distributions shown in Figure 8.35(a) can be digitally represented by two-dimensional arrays of aperture values, each representing a 0.2 mm by 0.2 mm pixel. A 2D numerical model with grid size equal to pixel size will be constructed, with each cell having a transmissivity calculated from the aperture using the cubic law. Inlet and outlet ports will be located at their actual locations and will act as constant-rate mass sources and sinks. Differential pressure across the flow paths will be used to calibrate the model to the laboratory experiments. Previous studies comparing models and laboratory experiments conducted in transparent fracture replicas (Geller et al., 1995) indicated that subtracting a constant thickness from all aperture measurements was required to obtain a good match for the flow field. Here, direct visualization of flow paths is not possible because of the opaque core, sleeve, etc., but all the differential pressure values from the four pairs of ports should provide adequate constraints on the model.

If numerical modeling of cores 211-2 and 401-1 is promising, additional numerical models for cores 84Z and 188-4 and artificial cores may be developed.

There will be two key outputs of the numerical models:

(1) The model adjustments required to match the laboratory differential pressures will provide insight into the fracture response to confining pressure.
(2) The flow paths through the fracture will verify whether the laboratory experiments actually show anisotropic fracture flow, or whether artifacts such as circumferential flow are occurring, and what its magnitude is.

8.5 Fractures and Fluid Flow in Crystalline Rocks – Example from the COSC-1 Borehole, Sweden

8.5.1 Introduction

Low permeability crystalline rocks have long been considered as one of the important potential geologic environments for long term disposal of nuclear waste (e.g., Witherspoon et al., 1981; Bredehoeft and Maini, 1981). However, one key concern relating to this geologic disposal option is the presence of hydraulically conductive fractures that could result in transport of radionuclides (Cherry et al., 2014). Extensive field studies conducted at a number of underground research laboratories in crystalline rocks, such as the Stripa Mine in Sweden and the Grimsel Test Site in Switzerland, have revealed that often a small subset of measured fractures (Figure 8.45) is responsible for the bulk of the observed fluid flow (e.g., Witherspoon and Gale, 1982; Olsson and Gale, 1995; Carbonell et al., 2010). In the case of Stripa, three major fracture zones identified within the characterization study area accounted for 75% of the hydraulic transmissivity as measured by single-hole hydraulic tests (Olsson and Gale, 1995); the orientation of these features is correlated with both small scale fractures as well as regional lineaments.

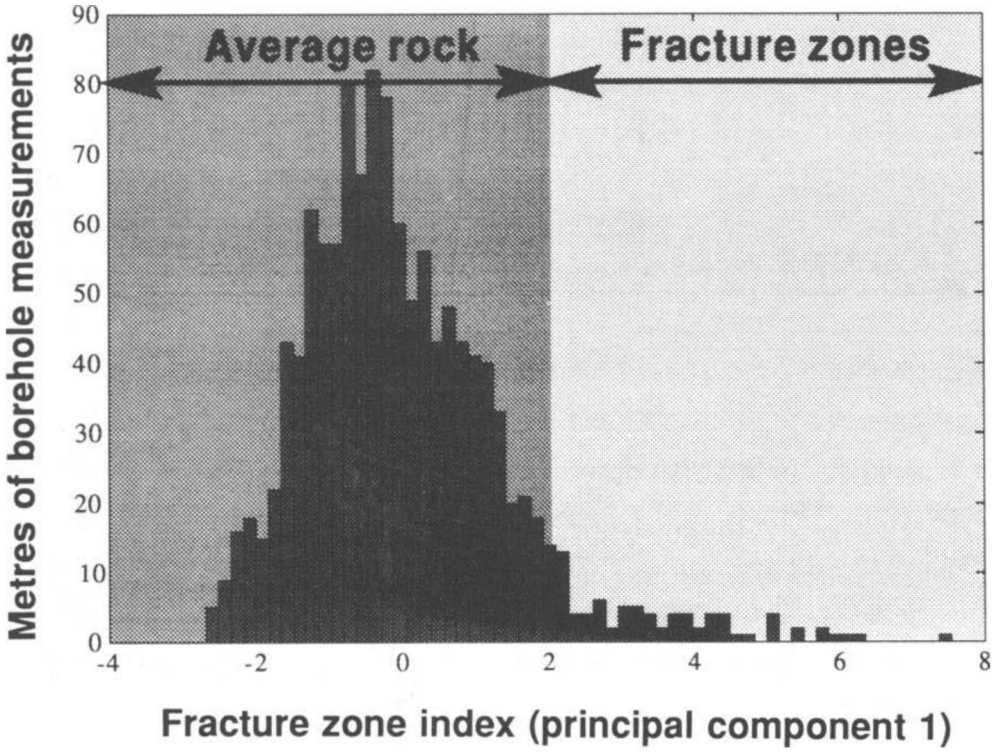

Figure 8.45. Frequency histogram of 'Fracture Zone Index (FZI)' values for 1 m long borehole intervals at Stripa. Intervals with an FZI value greater than 2 were considered part of a fracture zone. FZI was determined through a linear combination of data from borehole measurements of electric resistivity, sonic velocity, hydraulic conductivity, fracture frequency and occurrence of single-hole radar reflectors (Olsson and Gale, 1995).

Several countries are currently in the process of developing geologic repositories for spent nuclear fuel in crystalline rock: two of the most advanced projects utilizing this approach are the Forsmark site in Sweden and the ONKALO facility in Olkiluoto, Finland (Lundqvist and Hammarström, 2016; Lahti, 2016). At Fosmark, extensive field tests were conducted to develop a comprehensive conceptual model (Figure 8.46) that identified hydraulically conductive fracture systems (Lundqvist and Hammarström, 2016), which could then be used to develop hydrogeological flow models to constrain safety cases (Hartley and Joyce, 2013; Follin et al., 2014).

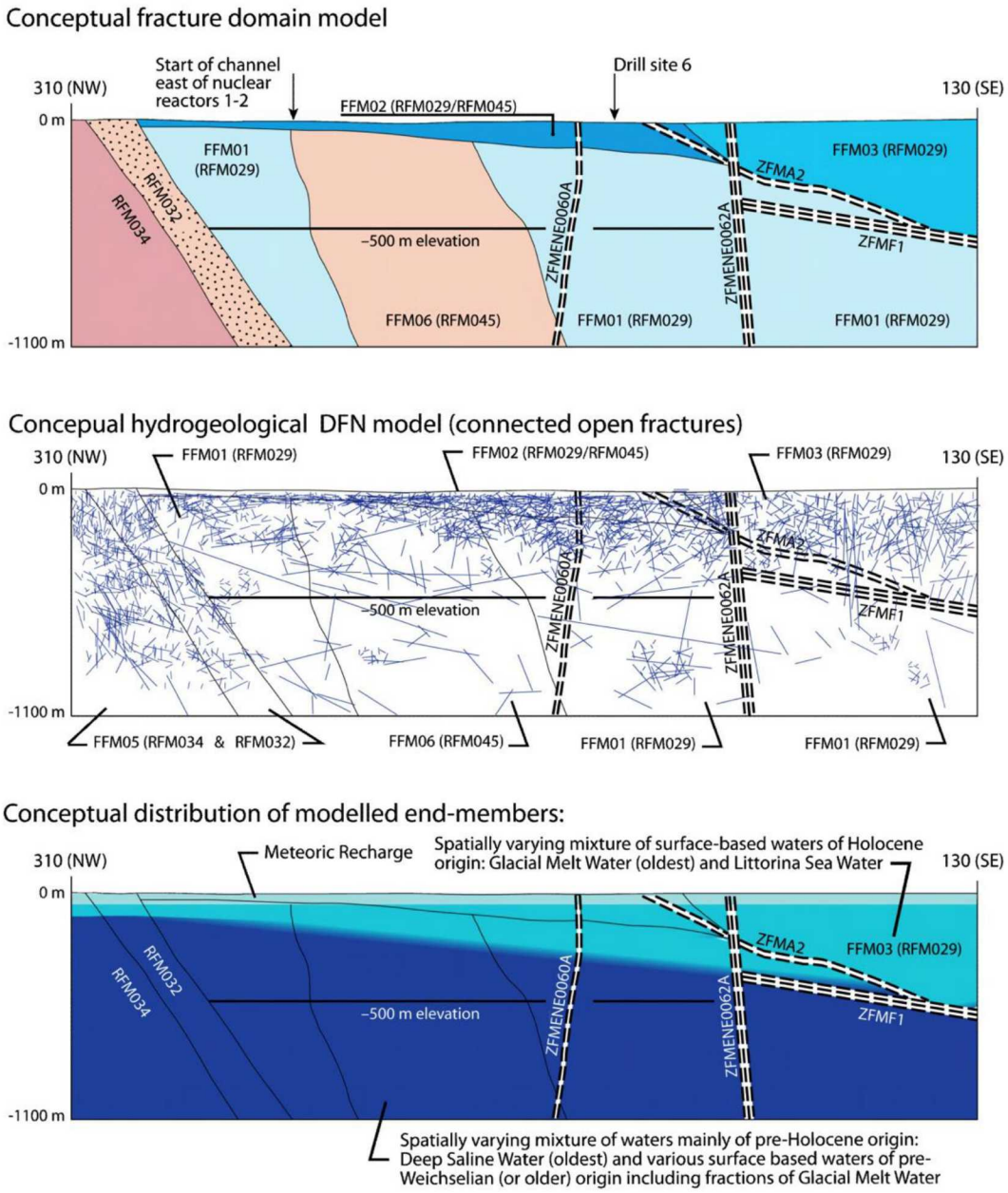

Figure 8.46. Conceptual geological-hydrogeological models, showing fracture domains, connected open fractures, and fracture end-members at Forsmark (Lundqvist and Hammarström, 2016).

Previous studies of a range of crystalline repository options (DOE, 1986) form one of the generic repository options currently under consideration (Hansen et al., 2011; Rechard et al., 2011). One key factor for this type of geologic repository is that discontinuities such as faults, joints, and fractures serve as the primary controls for groundwater flow in low permeability crystalline rocks; thus the frequency, size, orientation, and transmissivity of fractures are key attributes that need to be determined during site characterization (Patera, 1986; Rechard et al., 2011). These fracture attributes then can be used to develop discrete fracture network and equivalent continuum models for simulating flow and transport (Hadgu et al., 2017).

Thus, fracture characterization remains a critical component for evaluating the safety case for potential crystalline repositories. This report provides some insights into fracture characterization and fracture-controlled fluid flow obtained from studies conducted at a crystalline analog site in Sweden, the COSC-1 borehole.

8.5.2 Fracture Characteristics of the COSC-1 Borehole

Introduction to the COSC-1 Project

The COSC-1 borehole was drilled as part of the Collisional Orogeny in the Scandinavian Caledonides (COSC) scientific deep drilling project in central Sweden (Lorenz et al., 2015). The well was drilled to a depth of 2.5 km through the Seve Nappe, which contains high grade metamorphic rocks indicative of deep (100 km) crustal levels (Figure 8.47). The main lithologies encountered in the borehole consist of felsic gneisses, amphibolite gneisses, calc-silicate gneisses, amphibolite, migmatites, and garnet mica schists, with discrete zones of mylonite and microkarst. The primary objectives of this project were to gain insights into the tectonic evolution of the area, calibrate high quality surface geophysics through deep drilling, characterize present and past deep fluid circulation patterns, determine current heat flow to constrain climate modeling, and characterize the deep biosphere (e.g., Lorenz et al., 2015; Hedin et al., 2016; Wenning et al., 2016, 2017).

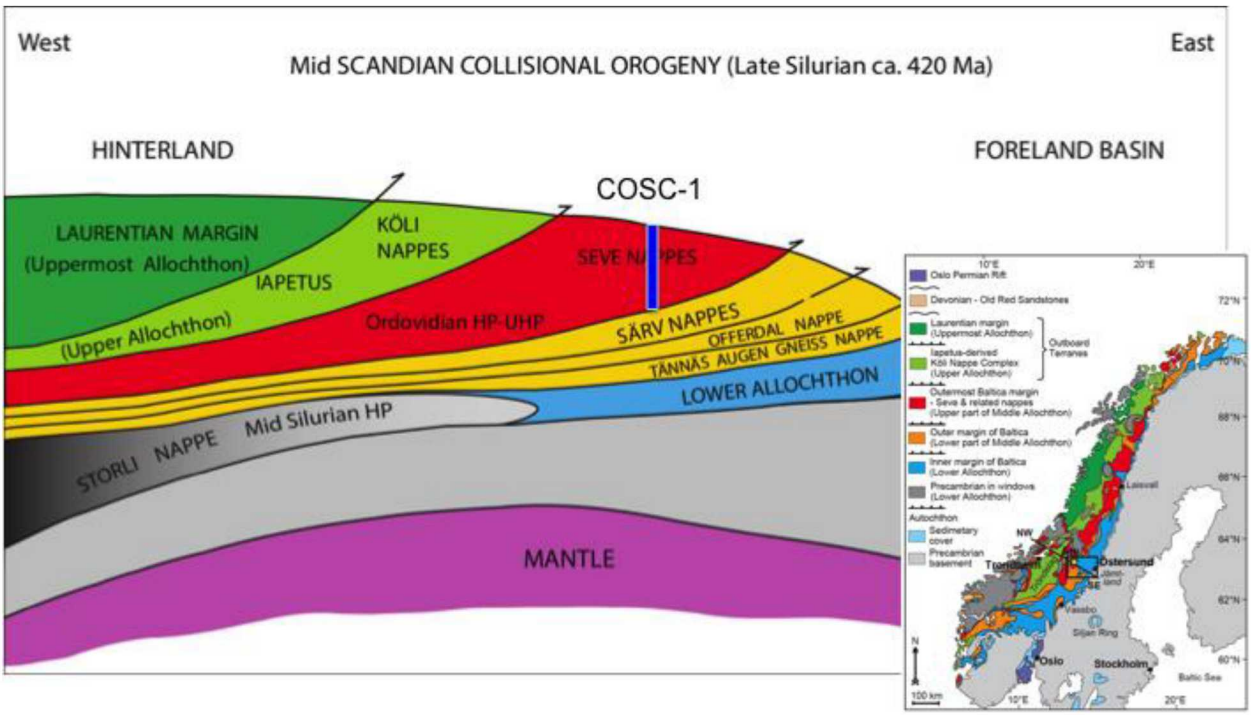

Figure 8.47. Geology and location of the COSC-1 deep borehole (Gee et al., 2013; Lorenz et al., 2015).

Our research team at LBNL has been collaborating with the COSC project to use information from this deep borehole research study as an analog for the deep borehole environment and to develop insights into fluid flow in crystalline basement rocks. Our team has previously used Flowing Fluid Electrical Conductivity (FFEC) logging as a means of identifying hydrologically transmissive fractures in the deep borehole (e.g., Tsang et al., 2016; Doughty et al., 2017). This component of our study seeks to evaluate the

correlation of these identified flow zones with potential correlative fractures observed in image logs and core samples.

Fracture Systematics of the COSC-1 Borehole

Wenning et al. (2017) conducted an extensive characterization of fractures, foliation, and in situ stress of the COSC-1 borehole through the examination of borehole acoustic televiewer image logs. They were able to characterize the *in-situ* stress through the evaluation of borehole breakout and drilling induced tensile fractures in the borehole, calculating an orientation for S_{Hmax} of 127° ± 12° based on analysis of 50 breakouts. This orientation is consistent with the regional NW-SE trend observed from boreholes, overcoring, and focal mechanisms (Wenning et al., 2017). Two main structural features were observed in the image logs – foliation and steeply dipping natural fractures (Figure 8.48). A total of 249 natural fractures were identified – they had variable orientations at depths less than 800 m, but had a consistent NW-SE strike with steep dips (> 70°) to the NE below this depth. Foliations tended to have much shallower dips and were generally parallel to lithologic contacts – their variability has been attributed to the tight recumbent folding in the Seve Nappe (Wenning et al., 2017). Fractures that were along foliations were not distinguished from foliations – thus there are likely two distinct fracture types: the steeply dipping fractures that were identified as natural fractures, and shallower dipping foliation-parallel fractures. The features recorded in the image logs do not distinguish between open and mineral-filled fractures. The orientation of the steeply dipping fractures below 800 m were interpreted by Wenning et al. (2017) to be consistent with extensional or hybrid brittle shear failure under the current stress regime.

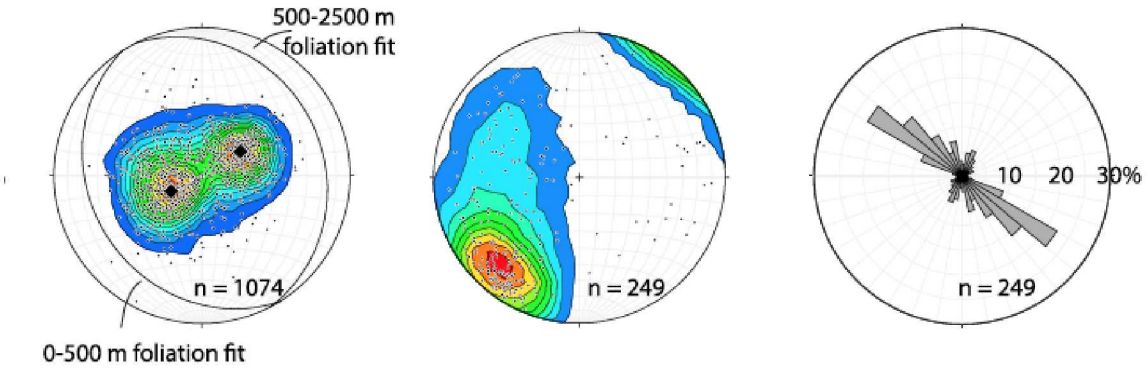

Figure 8.48. Left - Lower hemisphere Schmidt equal area projection of the poles to the foliation planes (black circles) depicting the primary shallow (0–500 m) and deep (500–2500 m) foliation trends. Center - Lower hemisphere Schmidt equal area projection of the poles (black circles) to the natural fracture planes. Right - Rose diagram of the orientation of the natural fractures. (Wenning et al., 2017).

Fractures Associated with Permeable Features Identified From FFEC Logging

Flowing Fluid Electric Conductivity (FFEC) logging is a technique that uses contrasts in wellbore and formation fluid salinities to identify permeable inflow zones in a wellbore (e.g., Tsang and Doughty, 2003). This logging method was applied first to the COSC-1 well during a break in drilling in 2014, and again in 2015 after the well had been completed (Tsang et al., 2016; Doughty et al., 2017). Analysis of the results of these logging runs indicated the presence of fluid entry points in the boreholes at depths of 228, 338-339, 507-508, 553-554, 696, 1214, 1243-1245, 2300, and 2380 m. Selected core samples that appeared to contain fractures that roughly corresponded to these depth intervals were obtained by Chin-Fu Tsang and

sent to LBNL for further study. A subset of these core samples was used to determine fracture transmissivities under controlled confining stress conditions (Dobson et al., 2017; Section 8.4, this study). One of the objectives of these measurements was to compare the field scale fracture transmissivities obtained from the FFEC studies with the core scale fracture measurements. However, one key concern was whether the core sample fractures actually corresponded to the permeable features that were detected in the boreholes. Thus, the core samples and the FFEC entry points reported by Doughty et al. (2017) were compared to fractures and foliations that were identified in the acoustic televiewer image logs by Wenning et al. (2017); these results are summarized in Table 8.7.

One aspect of this correlation work is that the depths reported for the core samples, FFEC logging, and image log data may be slightly off due to a number of technical reasons at the field site. Benoît Dessirier, a member of the COSC team at Uppsala University, used gamma log data from the downhole surveys as well as rock density and magnetic susceptibility data from both the rock core data as well as the downhole surveys to cross-correlate depths between these measurements and bring them into agreement. The offsets appear to be constant down to 1600 m depth (Figure 8.49; Dessirier et al., 2018). This comparison indicates that most of the core samples that were examined are not correlative with the actual FFEC inflow zones, and that neighboring samples might be more appropriate for analysis – these samples are indicated in the right-hand column of Table 8.7. In one specific instance (the FFEC peak at 506 m), the studied core (144-2) appears to be at the correct depth interval.

Table 8.7. FFEC peak locations, corresponding core samples, and fractures and foliations in the COSC-1 borehole.

FFEC peak depth (m) (2017 paper)	Corrected FFEC peak depth[1] (m)	Core sample studied	Core sample depth[2] reported (m)	Corrected sample depth[3] (m)	Closest image log fractures (m) *	Closest image log foliations (m) *	More likely core sample
1243	1242	401-1	1242.06	1239.5	1238.62	1241.43 1242.51	401-4
1214	1212	393-3	1219.85	1217	1211.83 1212.68	1211.45	391-2 391-4 392-2
696	694.4	211-2 209-3	702.38 698.0	695.5	696.72	693.98	209-1 209-2
638.5[+]		**188-4**	638.39		618.68	639.16	
553	552.5				543.41	553.49	159-4
508	505.9	**144-2** 144-1	507.33 506.13	506 505	513.69	504.56	144-2
338	337.2	84-3	340.31	338.5	334.17	335.11 340.95	84-1
288	287				275.37	285.53	

[1]Corrected peak depths taken from estimated mid-point depth of FFEC curve peaks corrected by B. Dessirier – these peaks are often are more than 1 m in height.
[2]Sample depths (for midpoint of core sample) determined from COSC-1 core archive sheet, using MBSF as reference point.
[3]Approximate sample depth based on gamma log depth correction made by B. Dessirier.
* Fracture and foliation data obtained from supplemental data tables, Wenning et al. (2017)
[+]Minor FFEC peak – not analyzed.
Samples shown in **bold** have fracture mineralization.

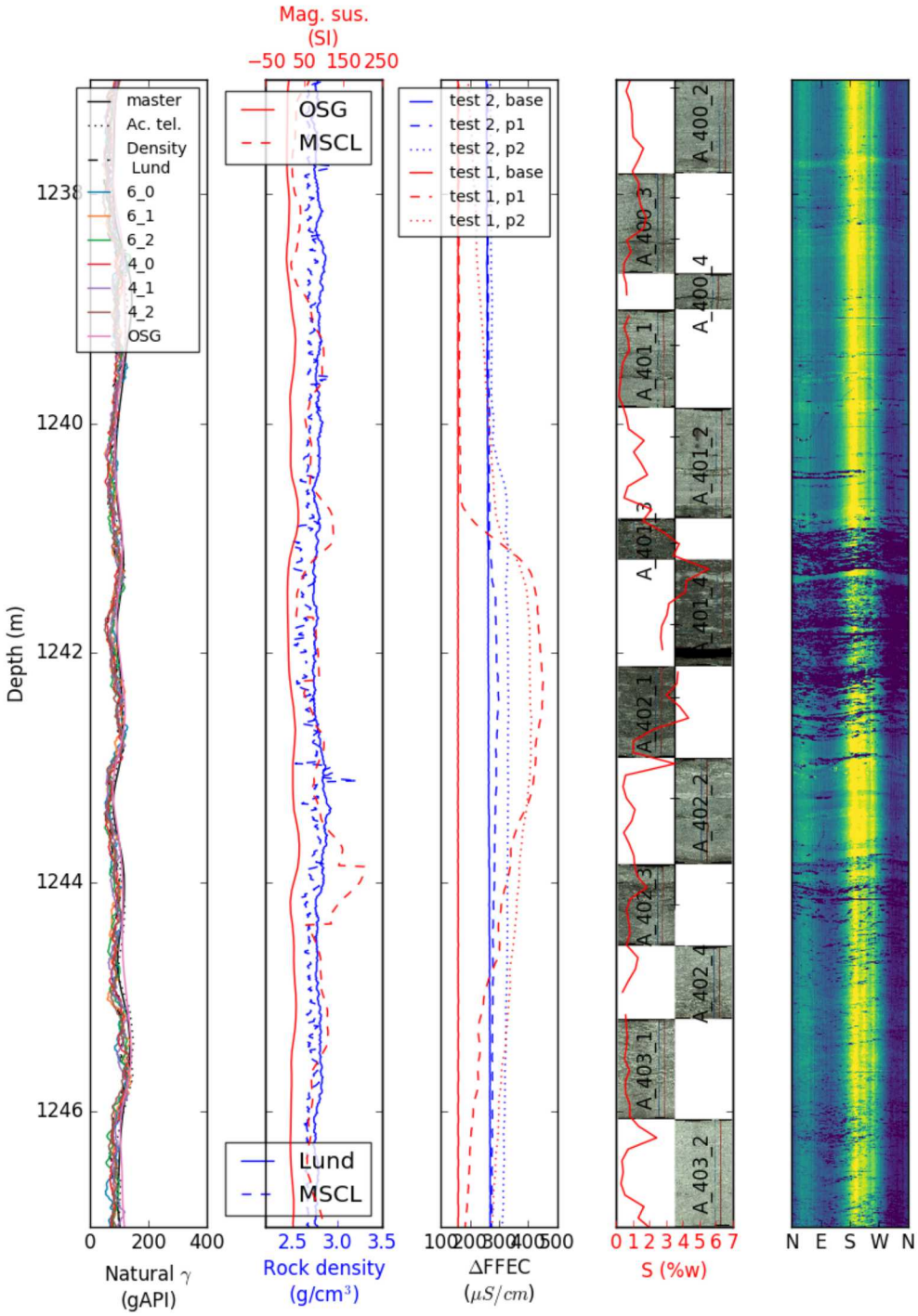

Figure 8.49. Correlation at 1237-1247 m in COSC-1 borehole between natural gamma and rock density/magnetic susceptibility logs used for depth matching (left two columns), the peaks obtained using the FFEC method identifying approximate location of flowing fractures (central column), and the unrolled core image, the sulfur content (wt. %), and the amplitude of the televiewer image (right two columns). Correlation conducted by B. Dessirier, Uppsala University.

The core samples listed in the table above were all examined to provide more details on the nature of the fracture (Tables 8.8 and 8.9). All but one of the samples have shallow dipping fractures (or core breaks), parallel to the foliation. Many of the core samples do not have a close-fitting match between the core pieces, casting doubt that they truly represent actual fractures, but instead may be core breaks along foliation that were then damaged in the core barrel, resulting in the poor mating of the samples. Three of the samples (393-3, 188-4 and 144-2) have mineralization on the fracture surface, suggesting that these samples indeed do represent mineralized fractures.

Table 8.8. Photos of COSC-1 core samples.

Core sample	Photo of core pieces	Photo of fracture surface
401-1		
393-3		
211-2		

209-3		
188-4		
144-2		
144-1		

84-3		

Core samples are 60 mm in diameter. White material seen on core faces 211-2 and 209-3 is sealing material introduced to core during fracture flow experiments and not natural mineralization. White material seen on core faces 188-4 and 144-4 is mineralization (see Table 8.9).

Table 8.9. Observations of fractures in COSC-1 core samples.

Core sample	Rock type	Dip of fracture (geometric)	Dip of fracture (goniometer)	Parallel to foliation?	Fitting of core pieces	Fracture mineralization
401-1	Gneiss / microkarst	25		Yes	Good	No
393-3	Microkarst	>80		No	Good	Yes
211-2	Amphibolite	12	12	Yes	Moderate	No
209-3	Gneiss / amphibolite	6	10	Yes	Poor	No
188-4	Gneiss	13	14	Yes	Moderate	Yes
144-2	Gneiss	11	15	Yes	Poor	Yes
144-1	Gneiss	4	6	Yes	Moderate	No
84-3	Gneiss	21	18	Yes	Moderate	No

Fracture dips were estimated using two approaches. The height to the fracture top and bottom of the cores were used together with the core diameter to calculate the dip angle. A goniometer was also used to estimate the steepest dip angle of the core.

Analysis of Fracture Mineralization of Selected Core Samples Using X-Ray Diffraction (XRD)

Samples of secondary mineralization were collected by scraping the fracture surface with a steel razor blade. The collected fragments were then reduced into powder using an agate mortar and pestle. A small amount of powder was deposited onto a glass slide placed in an aluminum sample stage. Samples were spinned during the data collection to improve counting statistics. The instrument used was a Rigaku SmartLab®, and data were collected from 5° to 72° of 2θ, using Kα radiation (instrument operating at 40kV and 44 mA). After manual identification of the mineral phases, a Rietveld analysis of the collected X-ray powder diffraction (XRPD) profile (e.g. Young, 1993) was performed on both samples to obtain weight fractions and to further validate the correctness of the phase identification procedure.

The mineral coating on the fracture face of sample 144-2 consisted of a white platy coating that was observed on a small portion of the fracture. The Rietveld analysis of this sample (Figure 8.50) shows thaumasite ($Ca_3Si(OH)_6(CO_3)(SO_4)\cdot 12H_2O$) as the most abundant mineral phase (85% by weight), a

mineral from the group of micas, fitted using a muscovite structure, as the second most abundant phase (12%), and the third phase was identified as aerinite ($Ca_4(Al,Fe,Mg)_{10}Si_{12}O_{35}(OH)_{12}CO_3 \cdot 12H_2O$) (3%).

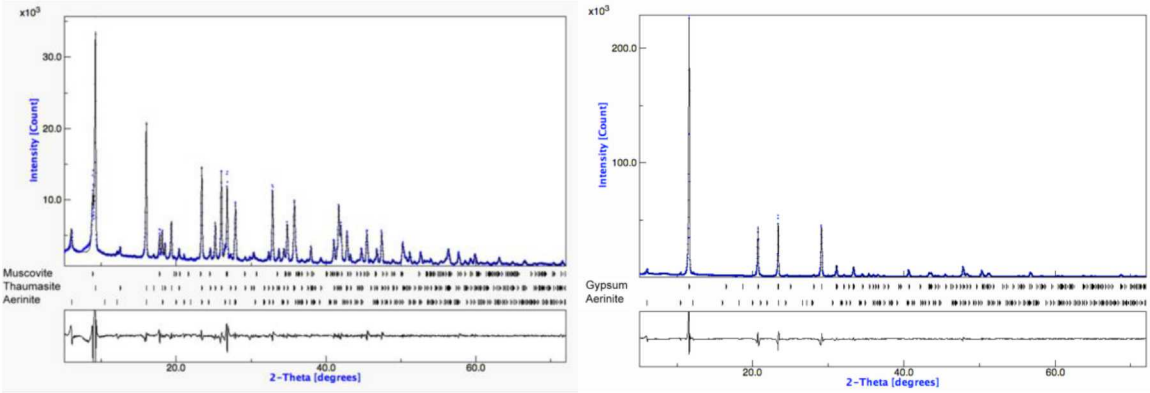

Figure 8.50. X-ray powder diffraction profile for fracture mineralization for samples 144-2 (left) and 188-4 (right), where the blue dots are the measured data and the black line is the Rietveld model. The peak positions for each phase are marked at the bottom.

The fracture coating sampled from 188-4 is composed almost exclusively by gypsum (Figure 8.50). It is observed coating one of the two fracture faces, present as white and glassy mineralization. Small (<1%) but clear traces of aerinite are still present. The presence of gypsum ($CaSO_4 \cdot 2H_2O$) in this sample is of particular interest. The COSC group at Uppsala (Dessirier et al., 2018) noted a correlation between increased S contents of core samples and the presence of fluid flow zones (Figure 5-5, fourth column). If these fractures have gypsum mineralization, this would help explain this correlation. The waters that were sampled from the COSC-1 borehole are primarily Ca-SO_4-HCO_3 waters (Figure 5-7) (Dobson et al., 2016), so that gypsum could be expected as a potential mineral precipitating from such fluids. Thaumasite (the main mineral phase of the mineralized fracture in sample 144-2) also contains SO_4, so it could also be an indicator of flowing (and sealed) fractures.

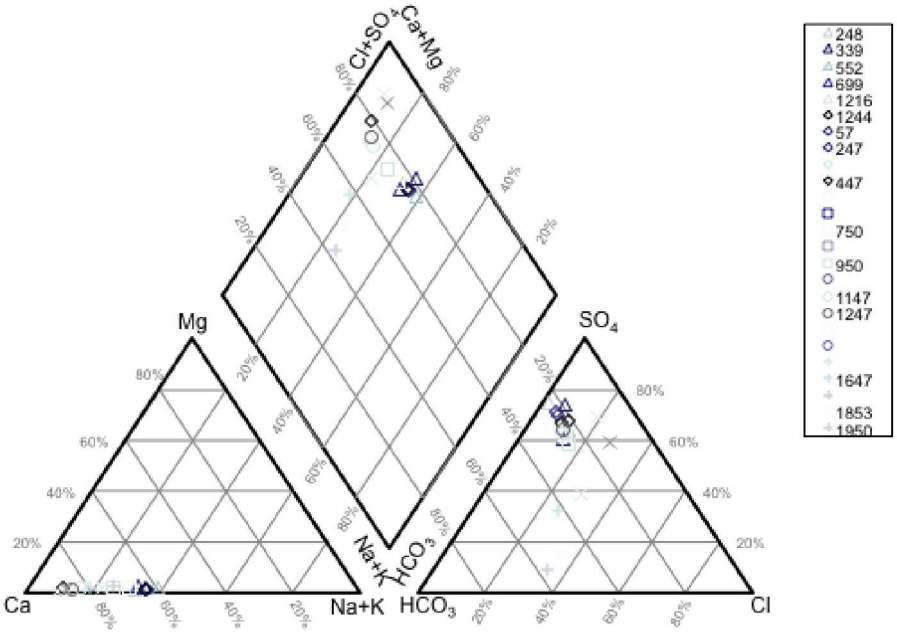

Figure 8.51. Piper diagram of borehole waters from COSC-1 well (Dobson et al., 2016).

8.5.3 Correlation of FFEC Flow Zones with Fracture Features and Future Work

While many of the core samples that were examined do not appear to spatially correlate with the FFEC inflow zones (Table 8.7) due to the recalibration of the core and logging depths, these zones do not appear to correspond to steeply dipping fracture features that were identified in the acoustic televiewer image logs either (Wenning et al., 2017). This observation was somewhat surprising, given that the steeply dipping fractures appear to be features that crosscut the foliation and would seem to be better candidates for hosting fluid flow within the low permeability crystalline rock. Using the core to FFEC log correlations developed by Benoît Dessirier, in most cases, foliation-parallel fractures are observed adjacent to the FFEC log peaks. Because most of the FFEC peaks are quite extensive (over 1 m), in many cases, there are multiple fracture/foliation features that may correspond to the inflow zones. The presence of increased sulfur contents in the core samples that are associated with some of the fractures in the vicinity of the flow zones may suggest the presence of a sulfate-bearing fracture mineral phase, such as gypsum or thaumasite, on the fracture surface. A number of additional core samples with fractures have been identified as possible candidates for hosting these flow zones. Two of the main fluid flow regions that were identified by the FFEC logging (1212 and 1242 m) also appear to be associated with a microkarstic region – localized dissolution may also enhance fluid flow in this region. It would be helpful to revisit additional core samples using the revised depth correlation (Table 8.7) to see if any additional fracture features are observed, and whether these also have sulfur-bearing secondary mineralization. It would also be helpful to see if the steeper dipping fractures identified in the televiewer logs have been sealed by mineralization.

8.6 Summary of FY2018 Progress and Future Work

According to the Used Fuel Disposition Disposal R&D roadmap, based on an analysis of key features, events, and processes, which are important to the safety case for radioactive waste disposal, the main research priorities relevant to the evaluation of the possibility of disposal in crystalline rock include the

evaluation of host rock properties, flow and transport pathways and processes in crystalline media, and the excavation disturbed zone.

The LBNL R&D activities during FY18 related to crystalline disposal addressed the following key issues: preliminary numerical simulations of the impact of gas bubble generation and migration on fracture growth and radionuclide migration, laboratory experiments and numerical simulations of how the excavation disturbed zone could impact local fluid flow properties in crystalline rocks, and the use of a crystalline basement analog site in Sweden to evaluate core-scale fracture transmissivity and to compare identified flow zones with different fracture sets observed from acoustic televiewer logs and core studies.

In particular, a new modeling activity was initiated during FY18 to simulate gas bubble migration. Gas bubbles, which are known to be produced by metal corrosion, radiolysis of trapped water, or by microorganisms, could impact the migration of radionuclides and could also cause fracturing of the crystalline rock mass if sufficient overpressures are generated. The preliminary modeling work was conducted to evaluate the migration of gas bubbles within different synthetic pore structures, and directions of research are identified to evaluate the potential impact of gas migration on radionuclide migration.

During FY18, a series of laboratory experiments were conducted on granite slabs with a special geometry to replicate the stresses and rock deformation responses that are expected to occur in larger circular excavations of the excavation damage zone (EDZ) in a mined crystalline repository. Specifically, microcracks generated by applying stress to the shaped rock samples were observed both visually and through a pronounced decrease in seismic velocity. The stressed samples were also used to assess the changes in rock permeability as an indicator how these microcracks could affect hydraulic properties of rock in the EDZ. Preliminary modeling studies of flow and transport coupled process and the effects of the rock deformation on hydrological and transport properties were initiated using a rigid body spring network modeling approach.

The final two sections of the report are based on the results of investigations of rock samples and data from a crystalline basement analogue site in central Sweden, the 2.5 km deep “Collisional Orogeny in the Scandinavian Caledonides” (COSC) scientific borehole. This study is aimed at gaining insights into the flow characteristics of crystalline basement rocks. The first part of this task included a series of laboratory experiments on fractured cores that were selected based on the correlation with the borehole inflow zones identified from flowing fluid electrical conductivity (FFEC) logs. These core flow measurements were conducted using a unique laboratory apparatus that can measure multi-directional transmissivity to assess fracture anisotropy under confining stress conditions. One challenge that was observed is that some of the core appears to have been damaged during recovery from the borehole, so that the core transmissivity measurements are significantly higher than the field scale values calculated from the FFEC logging runs. The second part of this task involved the evaluation of the nature of the fractures that appear to be linked to the borehole inflow zones, which were identified from the FFEC field measurements. Acoustic borehole televiewer images of the COSC-1 borehole indicated that there were two distinct sets of fractures: (a) steeply dipping fractures that were generated by current tectonic stresses, and (b) shallow fractures parallel to rock foliation. Based on new depth correlations of the core and well log datasets, it appears that the majority of the inflow zones are associated with the foliation-parallel fractures.

Based on the LBNL FY18 results, we have identified a number of areas that merit additional study in FY19. The initial results of the gas bubble migration study will be extended to perform simulations of bubble transport in fractures. The EDZ laboratory experiments are planned to be conducted on samples from the Grimsel URL, such as the FEBEX experiment. The COSC-1 analogue study will be completed in FY19; we may request some additional core samples to evaluate the spatial correlation with the actual FFEC inflow

zones. The results of the COSC-1 analogue study will be included in a paper to be submitted to a peer-reviewed journal.

8.7 References

Abu-Al-Saud, M. O., Riaz, A., Tchelepi, H. A. (2017) Multiscale level-set method for accurate modeling of immiscible two-phase flow with deposited thin films on solid surfaces. Journal of Computational Physics 2017, 333, 297-320.

Adrian, M. S., Hisham, B. M., Andrew, J. K. (2016) Comparison of Two-Phase Pipe Flow in OpenFOAM with a Mechanistic Model. IOP Conference Series: Materials Science and Engineering, 121, (1), 012018.

Armstrong, R. T., Evseev, N., Koroteev, D., Berg, S. (2015) Modeling the velocity field during Haines jumps in porous media. Advances in Water Resources, 77, 57-68.

Asahina, D., Aoyagi, K., Kim, K., Birkholzer, J.T., and Bolander, J.E. (2017) Elastically-homogeneous lattice models of damage in geomaterials, Computers and Geotechnics, 81, 195– 206.

Berg, S.; Ott, H.; Klapp, S. A.; Schwing, A.; Neiteler, R.; Brussee, N.; Makurat, A.; Leu, L.; Enzmann, F.; Schwarz, J. O.; Kersten, M.; Irvine, S.; Stampanoni, M. (2013) Real-time 3D imaging of Haines jumps in porous media flow. Proceedings of the National Academy of Sciences of the United States of America, 110, (10), 3755-3759.

Birkholzer, J.; Houseworth, J.; Tsang, C. F. (2012) Geologic Disposal of High-Level Radioactive Waste: Status, Key Issues, and Trends. Annual Review of Environment and Resources, Vol 37 2012, 37, 79-106.

Blunt, M. J.; Bijeljic, B.; Dong, H.; Gharbi, O.; Iglauer, S.; Mostaghimi, P.; Paluszny, A.; Pentland, C. (2013) Pore-scale imaging and modelling. Advances in Water Resources, 51, 197-216.

Bolander, J.E. and Saito, S. (1998) Fracture analyses using spring networks with random geometry, Eng. Fract. Mech., 61, 569–91.

Bredehoeft, J.D., and Maini, T. (1981) Strategy for radioactive waste disposal in crystalline rocks. Science 423 (4505), 293–296.

Bultreys, T.; Boone, M. A.; Boone, M. N.; De Schryver, T.; Masschaele, B.; Van Hoorebeke, L.; Cnudde, V. (2016) Fast laboratory-based micro-computed tomography for pore-scale research: Illustrative experiments and perspectives on the future. Advances in Water Resources, 95, 341-351.

Carbonell, R., Pérez-Estaún, A., Martínez-Landa, L., Martí, D., and Carretero, G. (2010) Geophysical and geological characterization of fractures within granitic pluton. Near Surface Geophysics 8 (3), 181–193.

Chang, C.; Ju, Y.; Xie, H. P.; Zhou, Q. L.; Gao, F. (2017) Non-Darcy interfacial dynamics of air-water two-phase flow in rough fractures under drainage conditions. Scientific Reports, 7.

Cherry, J.A., Alley, W.M., and Parker, B.L. (2014) Geologic disposal of spent nuclear fuel – An earth science perspective. The Bridge, Spring 2014, 51–59.

Christensen, H.; and Sunder, S. (2000) Current state of knowledge of water radiolysis effects on spent nuclear fuel corrosion. Nuclear Technology, 131, (1), 102-123.

Cihan, A.; and Corapcioglu, M. Y.(2008) Effect of compressibility on the rise velocity of an air bubble in porous media. Water Resources Research, 44, (4).

Claret, F., Marty, N., and Tournassat, C, (2018) Modeling the Long-term Stability of Multi-barrier Systems for Nuclear Waste Disposal in Geological Clay Formations. Reactive Transport Modeling.

Deshpande, S. S.; Anumolu, L.; Trujillo, M. F. (2012) Evaluating the performance of the two-phase flow solver interFoam. Computational Science and Discovery, 5, (1).

Dessirier B., Hedayati, M., Tsang, C.F., and Niemi, A. (2018) A study of correlating hydraulically transmissive zones at the COSC deep borehole with geological, geophysical and geochemical logging data from downhole surveys and core samples, in preparation.

Dobson, P., Tsang, C.F., Doughty, C., Ahonen, L., Kietäväinen, R., Juhlin, C., Rosberg, J.E., Borglin, S., Kneafsey, T., Rutqvist, J., Zheng, L., Xu, H., Nakagawa, S., and Nihei, K. (2017) Deep borehole

field test activities at LBNL 2017. US DOE Spent Fuel and Waste Science and Technology, SFWD-SFWST-2017-000046, LBNL Report 2001043, 118 p.

Dobson, P., Tsang, C.F., Kneafsey, T., Borglin, S., Piceno, Y., Andersen, G., Nakagawa, S., Nihei, K., Rutqvist, J., Doughty, C., and Reagan, M. (2016) Deep Borehole Field Test Research Activities at LBNL. Prepared for U.S. Department of Energy Used Fuel Disposition Campaign, FCRD-UFD-2016-000438, LBNL Report LBNL-1006044.

DOE (1986) Draft area recommendation report for the crystalline repository project. U.S. Department of Energy Office of Civilian Radioactive Waste Management, Crystalline Repository Project Office, DOE/CH-15(O), DE87 012335.

Doughty, C. Tsang, C-F., Rosberg, J-E., Juhlin, C., Dobson, P.F. and Birkholzer, J.T. (2017) Flowing fluid electrical conductivity logging of a deep borehole during and following drilling: estimation of transmissivity, water salinity and hydraulic head of conductive zones, Hydrogeol J 25:501–517 DOI 10.1007/s10040-016-1497-5

Doughty, C., Tsang, C.F., Rosberg, J.E., Juhlin, C., Dobson, P.F., and Birkholzer, J.T. (2017) Flowing fluid electrical conductivity logging of a deep borehole during and following drilling: estimation of transmissivity, water salinity and hydraulic head of conductive zones. Hydrogeology Journal 25, 501–517.

Duan, K. and Kwok, C.Y. (2015) Evolution of stress-induced borehole breakout in inherently anisotropic rock: Insights from discrete element modeling, J. Geophys. Res., Solid Earth, 121, 2361-2381, DOI:10.1002/2015JB012676.

Follin, S., Hartley, L., Rhén, I., Jackson, P., Joyce, S., Roberts, D., and Swift, B. (2014) A methodology to constrain the parameters of a hydrogeological discrete fracture network model for sparsely fractured crystalline rock, exemplified by data from the proposed high-level nuclear waste repository site at Forsmark, Sweden. Hydrogeology Journal 22, 313–331.

Gaboreau, S., Robinet, J. C., Pret, D. (2016) Optimization of pore-network characterization of a compacted clay material by TEM and FIB/SEM imaging. Microporous and Mesoporous Materials, 224, 116-128.

Gee, D.G., Janák, M., Majka, J., Robinson, P., and van Roermund, H. (2013) Subduction along and within the Baltoscandian margin during closing of the Iapetus Ocean and Baltica-Laurentia collision, Lithosphere 5, 169–178.

Geller, J.T., Doughty, C., Long, J.C.S. and Glass, R.J. (1995) Disturbed zone effects: Two-phase flow in regionally water-saturated fractured rock: FY94 Annual Report, Rep. LBL-36848, Lawrence Berkeley Lab., Berkeley, CA,.

Hadgu, T., Karra, S., Kalinina, E., Makedonska, N., Hyman, J.D., Klise, K., Viswanathan, H.S., and Wang, Y. (2017) A comparative study of discrete fracture network and equivalent continuum models for simulating flow and transport in the far field of a hypothetical nuclear waste repository in crystalline host rock. Journal of Hydrology 553, 59–70.

Hansen, F.D., Hardin, E., and Orrell, A. (2011) Geologic disposal options in the USA. Proceedings, International High Level Radioactive Waste Management Conference 2011, Albuquerque, NM, 932–940.

Hartley, L., and Joyce, S. (2013) Approaches and algorithms for groundwater flow modeling in support of site investigations and safety assessment of the Forsmark site, Sweden. Journal of Hydrology 500, 200–216.

Hedin, P., Almqvist, B., Berthet, T., Juhlin, C., Buske, S., Simon, H., Giese, R., Krauß, F., Rosburg, J.-E., and Alm, P.-G. (2016) 3D reflection seismic imaging at the 2.5 km deep COSC-1 scientific borehole, central Scandinavian Caledonides. Tectonophysics 689, 40–55.

Hoang, D. A.; van Steijn, V.; Portela, L. M.; Kreutzer, M. T.; Kleijn, C. R. (2012) Modeling of low-capillary number segmented flows in microchannels using OpenFOAM. AIP Conference Proceedings, 1479, (1), 86-89.

Jasak, H., (2009) OpenFOAM: Open source CFD in research and industry. International Journal of Naval Architecture and Ocean Engineering, 1, (2), 89-94.

Kawai, T. (1978) New Discrete Models and their Application to Seismic Response Analysis of Structures, Nuclear Engineering and Design, 48, 207–229.

Kim, J.-S.; Kwon, S.-K.; Sanchez, M.; Cho, G.-C. (2011) Geological storage of high level nuclear waste. KSCE Journal of Civil Engineering, 15, (4), 721-737.

Kirsch, E.G. (1898) Die Theorie der Elastizität und die Bedürfnisse der Festigkeitslehre. Zeitschrift des Vereines deutscher Ingenieure, 42, 797–807.

Lahti, M. (2016) Chapter 7: Towards Implementation of the Spent Nuclear Fuel Repository in Finland. In: International Approaches for Deep Geological Disposal of Nuclear Waste: Geological Challenges in Radioactive Waste Isolation – Fifth Worldwide Review, B. Faybishenko, J. Birkholzer, D. Sassani, and P. Swift, Eds., Lawrence Berkeley National Laboratory and Sandia National Laboratories, LBNL Report 1006984, pp. 7-1–7-12.

Lavrov, A. (2003) The Kaiser effect in rocks: principles and stress estimation techniques, Int. J. Rock Mech. & Min. Sci., 40, 151-171.

LISA ver.8.0.0. http://www.lisa-fet.com/

Lorenz, H., Rosberg, J.E., Juhlin, C., Bjelm, L., Almqvist, B.S.G., Berthet, T., Conze, R., Gee, D.G., Klonowska, I., Pascal, C., Pedersen, K., Roberts, N.M.W., and Tsang, C.F. (2015) COSC-1 – drilling of a subduction-related allochthon in the Palaeozoic Caledonide orogen of Scandinavia, Scientific Drilling 19, 1–11.

Lundqvist, B., and Hammarström, M. (2016) Chapter 20: Licensing of the KBS-3 concept for spent nuclear fuel in Sweden. In: International Approaches for Deep Geological Disposal of Nuclear Waste: Geological Challenges in Radioactive Waste Isolation – Fifth Worldwide Review, B. Faybishenko, J. Birkholzer, D. Sassani, and P. Swift, Eds., Lawrence Berkeley National Laboratory and Sandia National Laboratories, LBNL Report 1006984, pp. 20-1–20-25.

Martin, C.D. (1997) Seventeen Canadian Geotechnical Colloquium: The effect of cohesion loss and stress path on brittle rock strength, Canadian Geotechnical Journal, 1997, 34(5): 698-725, https://doi.org/10.1139/t97-030

Martin, C.D., Martino, J.B. and Dzik E.J. (1994) Comparison of borehole breakouts from laboratory and field tests, SPE 28050, SPE/ISRM Rock Mechanics in Petroleum Engineering Conference, Delft, The Netherlands, August 29-31, 183-190.

McDonald, K.T. (2016) Resistance of a Disk, Joseph Henry Laboratories, Princeton University, Princeton NJ, www.physics.princeton.edu/~mcdonald/examples/resistivedisk.pdf, *accessed June 30, 2016)*

Meakin, P.; and Tartakovsky, A. M. (2009) Modeling and simulation of pore-scale multiphase fluid flow and reactive transport in fractured and porous media. Reviews of Geophysics, 47, (3), n/a-n/a.

Nakagawa S. and Ewy, R. (2008) Shaped-Core Uniaxial Compression Test for Studying Borehole Breakout in Rocks, In Proceedings of 42nd US Rock Mechanics Symposium, ARMA-08-158, 29 June-2 July, San Francisco, CA.

Nieves-Remacha, M. J.; Yang, L.; Jensen, K. F., (2015) OpenFOAM Computational Fluid Dynamic Simulations of Two-Phase Flow and Mass Transfer in an Advanced-Flow Reactor. Industrial & Engineering Chemistry Research, 54, (26), 6649-6659.

Okabe, A., Boots, B., Sugihara, K., and Chiu, S.N. (2000) Spatial Tessellations: Concepts and Applications of Voronoi Diagrams, 2nd ed., Wiley, NYC, 696 pages.

Olsson, O., and Gale, J.E. (1995) Site assessment and characterization for high-level nuclear waste disposal: results from the Stripa Project, Sweden. Quarterly Journal of Engineering Geology 28, S17–S30.

Patera, E.S. (1986) United States Crystalline Repository Project – Key research areas. Materials Research Society Symposium Proceedings, v. 50, 17–21.

Pedersen, K. (1999) Subterranean microorganisms and radioactive waste disposal in Sweden. Engineering Geology, 52, (3-4), 163-176.

Pedersen, K., (1996) Investigations of subterranean bacteria in deep crystalline bedrock and their importance for the disposal of nuclear waste. Canadian Journal of Microbiology, 42, (4), 382-391.

Raeini, Q. A. J., Blunt, M.; Bijeljic, B. (2012) Modelling two-phase flow in porous media at the pore scale using the volume-of-fluid method; Vol. 231, p 5653–5668.

Rechard, R.P., Goldstein, B., Brush, L.H., Blink, J.A., Sutton, M., and Perry, F.V., (2011) Basis for identification of disposal options for research and development for spent nuclear fuel and high-level waste. Fuel Cycle Research & Development, U.S DOE Used Fuel Disposition Campaign, FCRD-USED-2011-000071, 54 p.

Roman, S., Abu-Al-Saud, M. O., Tokunaga, T., Wan, J. M., Kovscek, A. R., Tchelepi, H. A. (2017) Measurements and simulation of liquid films during drainage displacements and snap-off in constricted capillary tubes. Journal of Colloid and Interface Science, 507, 279-289.

Sloan, S.W. (1987) A fast algorithm for constructing Delaunay triangulations in the plan, Advances in Engineering Software, 9(1), 34–55.

Taniguchi, T., Yamashita, Y., and Moriwaki, K. (2002) Generation of arbitrary 3-dimensional domain from nodes on its surface, 8th Conference on Numerical Grid Generation, Hawaii, USA.

Tsang, C. F.; Neretnieks, I.; Tsang, Y. (2015) Hydrologic issues associated with nuclear waste repositories. Water Resources Research, 51, (9), 6923-6972.

Tsang, C.F. and Doughty, C. (2003) Multirate flowing fluid electric conductivity logging method. Water Resources Research 39(12), 1354–1362, doi:10.1029/2003WR002308

Tsang, C.F., Rosberg, J.E., Sharma, P., Berthet, T., Juhlin, C., and Niemi, A. (2016) Hydrologic testing during drilling: application of the flowing fluid electrical conductivity (FFEC) logging method to drilling of a deep borehole. Hydrogeology Journal 24, 1333–1341.

Wan, J. M. and Wilson, J. L. (1994) Visualization of the Role of The Gas-Water Interface on the Fate and Transport of Colloids in Porous-Media. Water Resources Research, 30, (1), 11-23.

Wenning, Q.C., Almqvist, B.S.G., Hedin, P., and Zappone, A. (2016) Seismic anisotropy in mid to lower orogenic crust: Insights from laboratory measurements of Vp and Vs in drill core from central Scandanaivan Caledonides. Tectonophysics 692, 14–28.

Wenning, Q.C., Berthet, T., Ask, M., Zappone, A., Rosberg, J.-E., and Almqvist, B.S.G. (2017) Image log analysis of in situ stress orientation, breakout growth, and natural geologic structures to 2.5 km depth in central Scandinavian Caledonides: Results from the COSC-1 borehole. Journal of Geophysical Research Solid Earth 122, 3999–4019.

Witherspoon, P.A., and Gale, J.E. (1982) Hydrogeological testing to characterize a fractured granite. Bulletin of the International Association of Engineering Geology 26, 515–526.

Witherspoon, P.A., Cook, N.G.W., and Gale, J.E. (1981) Geologic storage of radioactive waste: Field studies in Sweden. Science 211 (4485), 894–500.

Xu, T. F., Senger, R. and Finsterle, S. (2008) Corrosion-induced gas generation in a nuclear waste repository: Reactive geochemistry and multiphase flow effects. Applied Geochemistry, 23, (12), 3423-3433.

Yip, M., Mohle, J., and Bolander, J. (2005) Automated modeling of three-dimensional structural components using irregular lattices, Computer-Aided Civil and Infrastructure Engineering, 20, 393–407.

Young, R.A., (ed.) (1993) The Rietveld Method. Oxford University Press, Oxford, England, 298 p.

9. SUMMARY

Significant progress has been made in FY18 in both experimental and modeling arenas in evaluation of used fuel disposal in crystalline rocks, especially in model demonstration using field data. The work covers a wide range of research topics identified in the R&D plan. The major accomplishments are summarized below:

- **Model development for spent fuel degradation and its coupling with metal corrosion:** The fuel matrix degradation (FMD) model that calculates the degradation rate of spent UO_2 fuel is being developed to predict radionuclide source term values based on fundamental electrochemistry and thermodynamics. The FMD model has been implemented in a manner that facilitates its integration with the geologic disposal safety assessment (GDSA) model. A preliminary integrated FMD-GDSA model has been successfully tested. The specific focus of on-going work is to accurately and quantitatively represent the generation of H_2 in a breached waste package and model its effect on the degradation rate of the spent fuel so that this key process can be accurately represented in PA models. A recent sensitivity analysis shows that the dissolved H_2 concentration is the dominant environmental variable affecting the UO_2 spent fuel dissolution rate. The anoxic corrosion of metallic engineering materials will be the main source of H_2 in crystalline rock repository systems, including stainless steel and carbon steel internal waste package components and possibly the Zircaloy fuel cladding. A steel corrosion module has been added to the FMD model to account for these H_2 sources and couple the H_2 generation rate with fuel degradation processes. There is a need for experimental data from electrochemical corrosion experiments with relevant steel, Zircaloy and UO_2 electrodes to parameterize and validate the steel corrosion module in the FMD model with regard to key environmental variables and alloy compositions.
- **Model development for glass waste form degradation:** The reactivity of silicate glasses and minerals is important to numerous engineering applications including nuclear waste disposal. Silicate dissolution exhibits complex temporal evolution and rich pattern formations. In FY17, we showed how observed complexity could emerge from a simple self-organizational mechanism: dissolution of the silica framework in a material could be catalyzed by the cations released from the reaction itself. This mechanism enables us to systematically predict many key features of a silicate dissolution process including the occurrence of a sharp corrosion front (vs. a leached surface layer), oscillatory dissolution and multiple stages of the alteration process (e.g., an alteration rate resumption at a late stage of glass dissolution). In FY18, through a linear stability analysis, we showed that the same mechanism could also lead to morphological instability of an alteration front, which, in combination with oscillatory dissolution, could potentially lead to a whole suite of patterning phenomena, as observed on archaeological glass samples as well as in laboratory experiments, including wavy dissolution fronts, growth rings, incoherent bandings of alteration products, and corrosion pitting. The result thus further demonstrates the importance of the proposed self-accelerating mechanism in silicate material degradation.
- **Understanding radionuclide interaction with metal corrosion products:** The main interest in radionuclide sequestration by corrosion products stems from (1) the potential for this process to significant inhibit radionuclide release during canister breaching and (2) from the absence of such processes in most repository performance assessments. The objective of this work is to quantify radionuclide sequestration as a result of canister breaching and near field corrosion processes. In FY18, molecular and crystallographic behaviors of Pu associated with ferrihydrite and goethite iron oxide phases were investigated. It was shown that the timing of Pu release and ferrihydrite corrosion product formation could lead to differences in Pu association: formation of PuO_2 versus coprecipitated Pu. Alteration of amorphous ferrihydrite to a more crystalline goethite phase would retain Pu association with the solid phase. However, the nature of Pu association would be affected

by the characteristics of Pu associated with the precursor ferrihydrite. The molecular nature of Pu association with iron oxide phases affects the leaching behavior of Pu. EXAFS and TEM data confirm that in Pu association with goethite as a surface precipitate is more labile than the coprecipitate. This has implications to the longterm stability of Pu associated with corrosion products.

- **Understanding colloid-facilitated Cs transport:** Batch and column transport experiments were conducted to interrogate the effects of colloid aging on colloid-facilitated transport of ^{137}Cs through crushed analcime columns. The batch experiments were conducted to quantify the effect of colloidal aging on Cs partition coefficients and characterize the colloids injected into the columns. The column experiments were designed to characterize the desorption of Cs from strong sites on colloids. This was accomplished by using a very low concentration of total Cs (~10^{-10} M) so that ^{137}Cs would preferentially sorb to the fewer but stronger sorption sites. The first set of column experiments involved spiking a solution of FEBEX colloids with ^{137}Cs and letting the colloids age for a few hours, whereas the second set of experiments let the colloids age for 1200 hours prior to injecting through the analcime column. For both sets of column experiments, the eluent that passed through a first analcime column was collected and injected into a second fresh analcime column. The sequential injection method allows characterization of the ^{137}Cs bound to the strong sites on the colloid, and the use of a strongly sorbing column material (analcime) promotes desorption from the colloids. Both batch and column experiments demonstrate analcime's ability to outcompete colloids for ^{137}Cs sorption. In the presence of analcime, 12-23% of ^{137}Cs sorbed to the colloids and only 2-6% was in the dissolved phase, with the remainder sorbed to the analcime. The partitioning of ^{137}Cs between colloidal and dissolved phases in the absence of analcime was approximately 60:40. The column experiments had a much lower ratio of solid to liquid and demonstrated even greater loss of the Cs to the analcime. The ^{137}Cs eluted through the first column of the first set of experiments was only about 5%, and through the second column, no measureable ^{137}Cs eluted. Conversely, through the first column of the second set of experiments (aged colloids), only ~2% of the initially injected ^{137}Cs was recovered through the column, but ~10% was recovered through the second column. Additionally, the second set of experiments also showed greater colloid recovery (~40%) through the second column compared to the second column (~20%) from the first set of experiments. These results suggest that aging the colloids prior to injection through analcime columns allows the ^{137}Cs to find the strong sorption sites on the colloids. Compared to previous batch experiments, the experiments of the present study report a higher K_d value for sorption of Cs onto colloids owing to the lower total Cs concentration and aging effects. Additionally, the present batch experiments demonstrate that the sorption rate onto the strong sorption site of the colloid is very slow compared to the sorption rate onto the weaker colloid sorption site. Furthermore, the desorption rate constant of the strong colloid sorption site had to be lowered for the aged colloid column experiment relative to the un-aged column experiment, suggesting that with a progressively smaller Cs concentration, the remaining Cs is proportionally more sorbed to the stronger sites. This work also suggests that there are greater than 2 sorption sites with progressively stronger affinity for Cs but less abundant.
- **Micro Fracture Flow Simulation Using Discrete Fracture Network Model:** The main focus of this year fracture simulation work was to simulate the Long-Term Sorption Diffusion Experiment (LTDE), conducted at the Äspö Hard Rock. The field test characterized tracer transport in the stagnant pore water of the rock matrix. A cocktail of both sorbing and non-sorbing tracers were allowed to contact fractured surface, as well as the unaltered rock matrix, for a time period of 200 days. The penetration profiles obtained by 1D simulation of tracer diffusion and measured during experiment do not agree and show different behavior. A Discrete Fracture Network (DFN) model was used to validate the hypothesis, which states that LTDE results were strongly influenced by heterogeneity in the micro-structure and the major diffusion of injected tracer into crystalline rock occurs through multiple micro fractures, which are observed in the rock samples. The DFN simulations of micro-fractures were performed using the dfnWorks simulation tool. Three

numerical experiments were performed, where micro fracture intensity in DFN configurations varied representing different microstructure at the experimental sample. In each DFN configuration steady state pressure solution was evaluated and transport was evaluated through particle tracking transport. Time Domain Random Walk technique was used to simulate tracer movement through micro fractures, where a particle's travel time is controlled by both processes, advection and diffusion. The simulated penetration profile of particles shows similar behavior with LTDE experimental penetration plot when the advection term plays a significant role in the TDRW simulations. The conclusion from the performed numerical simulations is that microstructure is present in the experimental sample and the injected tracer is driven by both, diffusion and advection.

- **Flow-transport model demonstration using Mizunami site data:** Through the Development of Coupled Models and their Validation against Experiments (DECOVALEX-2019) project, we obtained a comprehensive set of hydrologic and chemical data from a research tunnel at 500 m depth, at the Japan Atomic Energy Agency (JAEA) Mizunami Underground Research Laboratory (MIU). The objectives of this work are to develop a general workflow or methodology to synthesize field observations and measurements into a flow and transport model. In FY18, modeling analyses were conducted for DECOVALEX19, Task C, Step 2a and Step 2b. For Step 2b, the analysis was based on a larger domain to reduce boundary effects. The analysis also included fracture characterization using the new domain. The fracture model produced 10 DFN realizations which were upscaled to a continuum mesh for use in flow and transport. Boundary and initial conditions specified by the project were applied to flow and transport simulations for Step 2b. Project experimental data of excavation progress were also used. The simulation method previously developed to simulate excavation progress by continuously removing material from the excavated area was utilized. The DAKOTA statistical analysis and optimization code and the PFLOTRAN numerical flow and transport code were used. Predictions of inflow into the inclined drift for the 10 realizations are reasonable when compared with the experimental data. Inflow of the combined inclined drift and Closure Test Drift (CTD) were largely overpredicted. The simulations provided statistical data with uncertainty range. Future simulations will attempt to improve the predictions by using additional fracture data from Borehole 13MI38. Step 2b preliminary flow modeling was also conducted to simulate water filling of the plugged CTD and pressure recovery. The excavation process resulted in pressure drawdown in the vicinity of the experimental area. An experiment was conducted with the aim of pressure recovery by closing the CTD using a concrete plug and water filling. Preliminary blind simulations were carried out using project data with initial conditions at the CTD and 6 observation points in Borehole 12MI33. The simulation results were compared with project experimental data. The pressure predictions at the CTD and the observation points did not match the experimental data. Further modeling will incorporate the leakage.
- **Multi-Scale Characterization of Crystalline Rocks:** A series of laboratory experiments were conducted on granite slabs with a special geometry to replicate the stresses and rock deformation responses that are expected to occur in larger circular excavations of the excavation damage zone (EDZ) in a mined crystalline repository. Specifically, microcracks generated by applying stress to the shaped rock samples were observed both visually and through a pronounced decrease in seismic velocity. The stressed samples were also used to assess the changes in rock permeability as an indicator how these microcracks could affect hydraulic properties of rock in the EDZ. Preliminary modeling studies of flow and transport coupled process and the effects of the rock deformation on hydrological and transport properties were initiated using a rigid body spring network modeling approach. In addition, rock samples and data were collected from a crystalline basement analogue site in central Sweden, the 2.5 km deep "Collisional Orogeny in the Scandinavian Caledonides" (COSC) scientific borehole. This study is aimed at gaining insights into the flow characteristics of crystalline basement rocks. The first part of this task included a series of laboratory experiments

on fractured cores that were selected based on the correlation with the borehole inflow zones identified from flowing fluid electrical conductivity (FFEC) logs. These core flow measurements were conducted using a unique laboratory apparatus that can measure multi-directional transmissivity to assess fracture anisotropy under confining stress conditions. One challenge that was observed is that some of the core appears to have been damaged during recovery from the borehole, so that the core transmissivity measurements are significantly higher than the field scale values calculated from the FFEC logging runs. The second part of this task involved the evaluation of the nature of the fractures that appear to be linked to the borehole inflow zones, which were identified from the FFEC field measurements. Acoustic borehole televiewer images of the COSC-1 borehole indicated that there were two distinct sets of fractures: (a) steeply dipping fractures that were generated by current tectonic stresses, and (b) shallow fractures parallel to rock foliation. Based on new depth correlations of the core and well log datasets, it appears that the majority of the inflow zones are associated with the foliation-parallel fractures.

We have also made significant progress in FY18 in other research topic areas such as the study of smectite-to-illite transformation and the development of next generation buffer materials. Such work will be reported in future milestone reports.

APPENDIX A. SFWST R&D FOR SPENT DISPOSAL IN CRYSTALLINE ROCKS: CURRENT STATUS AND PERSPECTIVES

The key research topics for spent disposal in crystalline rocks for the SFWST program were identified in a R&D plan formulated in FY2014 (Wang et al., 2014). In this appendix, we briefly summarize the major accomplishments over the past five years and provide a perspective for future research for each research topic area.

System level R&D topics:

Topic #S1
Title: Evaluation of potential impacts of disposal options on fuel cycles
Description: The DOE is now reconsidering its nuclear waste disposal policy and re-evaluating alternative options to the current once-through open fuel cycle. This policy shift creates a unique opportunity for exploring new concepts and ideas that can potentially lead to the development of transformational technologies for an efficient and clean nuclear fuel cycle. The choice of waste disposal environments may potentially impact the development of upstream processes of the fuel cycle. Such impacts have not been fully explored and evaluated. This research topic will focus on new concept development. Specific activities will include:

- Comparative study of different disposal environments
- Identification and evaluation of potential impacts of different disposal environments on waste separation and waste form development.
- Capability of crystalline rocks for disposal waste packages of multiple sizes, especially for large dual-purpose canisters (DPCs)

Anticipated results: New concept development

Major accomplishments:

- Both analytical and numerical models were developed for near field thermal evolution calculations.
- It has been shown that repository performance is in general insensitive to waste forms, and therefore certain existing constraints on the upstream of the fuel cycle could potentially be relaxed.
- Work on borate solubility limits in a near-field environment was initiated. This work will help develop a realistic waste package and fuel degradation model for post closure criticality evaluation, especially for DPCs.

Perspective:

- Closely interact with fuel cycle activities such as waste separation and waste form development programs to seek new ideas and concepts that can optimize the whole fuel cycle.
- Develop realistic scenarios for waste package and fuel degradation for a post-closure criticality evaluation.

Topic #S2
Title: Disposal concept development
Description: As explicitly identified in the UFDC R&D roadmap (DOE, 2011), there is a need for developing a range of generic disposal system design concepts. This research topic will support the overall UFDC effort on the development of disposal system design concepts by cataloging possible combinations and geometries of both host rock and far-field media (e.g., mineral and chemical compositions, physical dimensions, hydrologic properties). The task will define a generic set of key parameters (e.g., water chemistry) for other UFDC activities. Specific activities will include:

- Literature review

- Concept development
- Development of reference cases for crystalline media

Anticipated results: Generic representations of various disposal environments

Accomplishments:

- A reference case for spent disposal in crystalline rocks was developed.

Perspective:

- The reference case needs to be refined with respect to the engineered barrier system.

Topic #S3
Title: Disposal system modeling
Description: Disposal system modeling is crucial for the whole life cycle of repository development. Such modeling tools will be essential for management decisions on project priority and resource allocation. This research will serve two purposes: (1) supporting the development of the Generic Disposal System Analysis (GDSM) models as well as the development of higher-fidelity performance assessment models, and (2) developing a comprehensive subsystem model for natural system performance evaluation. The subsystem model will include (1) detailed thermal-hydrologic-mechanical-chemical (THMC) process models (with appropriate levels of fidelity) for flow field and radionuclide transport calculations and (2) probabilistic performance assessment capabilities. This subsystem model will be used for integration and prioritization of relevant natural system evaluation activities. Specific activities will include:

- Selection of flow and radionuclide transport codes
- Improvements to the selected codes
- Wrapping the selected process codes with a Monte-Carlo simulation tool
- Performing Monte-Carlo simulations for total system and subsystem evaluation.

Anticipated results: Enhanced process understanding; probabilistic performance assessment tools for natural system evaluation, which will allow for taking more credit for natural system performance; laboratory and field data for model validation and parameterization

Accomplishments:

- A generic reference case for crystalline disposal media was established. The reference case specifies the emplacement concept, waste inventory, waste form, waste package, backfill/buffer properties, EBS failure scenarios, host rock properties, and biosphere.
- Based on the reference case, a preliminary GDSA model was developed.

Perspective:

- Continue refining the GDSA model, especially with the improvement to the statistical representation of effective porosity and permeability fields.
- Refine the thermal-hydrological-chemical evolution of the near-field.

Topic #S4
Title: Development of a centralized technical database for crystalline disposal system evaluation
Description: Given the quantity of data already accumulated through various repository programs and also the data to be collected from the UFDC R&D activities, it is essential for future repository development to archive and categorize these data in an appropriate manner so that they can be easily accessible to UFDC participants and has appropriate quality assurance enforced. This task will focus on the database development for natural system evaluations. The data to be collected will include thermodynamic data for radionuclide speciation and sorption, groundwater chemistry, hydraulic and mechanical property data, mineralogical and compositional data of representative host and far-field media, spatial distributions of potential host formations, etc. To support site screening and selection, there is a need to develop tools for spatial data analysis and visualization (e.g., a geographic information system). Specific activities will include:

- Collection of user requirements
- Database design
- Retrieval of relevant data that was generated by previous DOE research studies on shale, salt, and crystalline basement repository rocks
- Data collection from UFDC experimental activities
- Database population and maintenance.

Anticipated results: Database. This database will serve as a knowledge management system for all system evaluation activities. It will serve a part of the technical database supporting the parameter database development for total system performance assessments.

Accomplishments:

- Representative site characterization data were collected for a generic repository in crystalline rocks. The data include the distribution of crystalline rocks, fracture distributions, water chemistry, rock compositions, sorption data (Kd values), etc.
- A significant portion of thermodynamic data was collected.
- A data management plan was developed but not implemented.
- Regional geologic data have been collected and managed using a geographic information system.
- A relationship with NEA thermodynamic database development was established.

Perspective:

- Need to develop a centralized data storage for the project.

Topic #S5

Title: Evaluation of state of the art of site characterization techniques

Description: Site characterization techniques evolved and improved both in the U.S. and other nations as geologic repository programs progress. Advances both in the disposal science and other geotechnical fields (e.g., oil and gas industry, mineral mining, geothermal exploration, and carbon sequestration) may lead to improved site characterization techniques that could be applied to future site characterization efforts. This activity will evaluate and identify potential field survey techniques that may prove useful for site characterization. The effort will be equally divided into four areas: geophysical techniques, geochemical techniques, hydrological testing techniques, and rock mechanics techniques. Specific activities will include:

- Literature review
- Gap analysis
- Recommendations for future technique development

Anticipated results: Information needed for planning further development of site characterization techniques.

Accomplishments:

- A series of laboratory experiments were conducted on granite slabs with a special geometry to replicate the stresses and rock deformation responses that are expected to occur in larger circular excavations of the excavation damage zone (EDZ) in a mined crystalline repository.
- Use of flowing fluid electrical conductivity (FFEC) logs to identify borehole inflow zones was demonstrated using the 2.5 km deep “Collisional Orogeny in the Scandinavian Caledonides” (COSC) scientific borehole in central Sweden.

Perspective:

- Continue development of in-situ detection techniques.

Topic #S6
Title: Development and demonstration of geophysical techniques for site characterization
Description: Existing non-invasive geophysical techniques are adequate for characterizing large-scale subsurface features and physical properties, but continued advances could help achieve high-resolution images of time-varying properties and structural changes that may be important during the site selection or characterization stages. For example, high-resolution seismic imaging of subsurface faults under development for oil and gas exploration purposes could advance to the point where sub-meter sized features can be more easily resolved and high-angle (near vertical) reflectors can be directly imaged. Similarly, advances in seismic imaging could allow the direct detection of fluids and their migration through fractures. Laboratory experiments and waveform modeling approaches could be pursued to develop and test new seismic methods for fluid monitoring. Strategies may be needed to integrate multiple geophysical techniques to optimize information gathering in host-rock and geologic environments. This task will focus on the development of new geophysical techniques that can provide unprecedented high spatial resolutions. Specific activities will be formulated based on the results from Topic #S5.
Anticipated results: Improved geophysical techniques for site selection and site characterization.

Accomplishments:
- A comprehensive literature review was performed on geophysical characterization of fracture media.
- Use of flowing fluid electrical conductivity (FFEC) logs to identify borehole inflow zones was demonstrated using the 2.5 km deep "Collisional Orogeny in the Scandinavian Caledonides" (COSC) scientific borehole in central Sweden.
- Preliminary streaming potential testing was conducted in collaboration with Korean Atomic Energy Research Institute (KAERI).
- A packer test was initiated with KAERI but not further pursued.

Perspective:
- Continue development and demonstration of geophysical techniques for site characterization. One particular area to look into is a possibility of using acoustic wave to characterize fractures in a DRZ.

Topic #S7
Title: Identification of the needs for using Underground Research Laboratories (URLs)
Description: Underground research laboratories (URLs) can be used to conduct experiments designed to address the issues that require field-scale testing and demonstration. Experimental activities conducted in URLs (and operations-related surface facilities) can potentially help improve public confidence through demonstrating fundamental understanding of disposal and operational concepts. If the U.S. foregoes repository siting for an extended period of time, studies in a domestic URL could help maintain repository development expertise. However, there may be reasons (e.g., cost) not to develop URLs in the U.S. unless they are in geologic media where one does not currently exist elsewhere. Domestic R&D needs could potentially be met by gaining access to URLs in other countries working in relevant geologic media through collaborative studies and experiments. This research topic will (1) identify potential areas in which the UFDC can benefit the most from international collaboration on the URL research and (2) formulate a strategy for domestic URL development. Specific activities will include:
- Identification of the needs for URLs
- Formulating URL development strategy, especially the international collaboration approaches.

Anticipated results: Information needed for developing an international collaboration plan. Actual collaboration will be carried out in individual research topic areas.

Accomplishments:

- Through international collaborations, site characterization data have been collected from Korean Underground Research Tunnel (KURT), Czech Bedrichov Tunnel, Japanese Mizunami site, and Swedish underground facility.

Perspective:

- Continue site characterization data through international collaborations and make fully use of the data for modeling development and validation.

Topic #S8
Title: Natural analogue studies
Description: Natural analogues such as uranium deposits preserve information about physical and chemical processes that may be relevant to nuclear waste isolation in a geologic repository. This information could be useful for repository performance assessment model validation and confidence building. Natural analogues are also needed to identify potential effects of geologic processes that may be relevant to waste disposal in a given geologic medium. Identification of such processes is critical for site screening. Current hydrogeologic modeling practices tend to assume that the system will be static other than changes induced by the repository itself. This is an assumption that needs to be investigated and analogues are the best way for testing this assumption. In a study of analogues for argillaceous rock, a variety of geologic processes have been found that can significantly affect flow and transport pathways through otherwise very low-permeability materials. Specific activities will include:

- Literature review
- Systematic evaluation of the uses of natural analogue data for repository development
- Data compilation and synthesis

Anticipated results: An overview report with compiled data; enhanced process understanding

Accomplishments:

- Ancient Roman glass has been used for an analog to borosilicate glass.

Perspective:

- Data from geothermal sites may provide useful information about subsurface fracture distribution and fluid flow in crystalline rocks.

Process-level R&D topics:

Topic #P1
Title: Development of discrete fracture network (DFN) model
Description: There is a need to develop improved modeling tools to represent fractures or fracture sets as discrete features. Experience in Sweden and Finland suggests that DFN models offer advantages over continuum models for sparsely fractured media such as fractured crystalline basement rock, especially when fracture networks or network statistics are well characterized. There is also a need for DFN studies for argillaceous host rock in the disturbed rock zone (DRZ). DFN modeling capability would provide an alternative to continuum codes and would also be invaluable for numerically determining effective parameters for use in existing continuum codes. This task will develop a DFN code for modeling multiple-scale, three-dimensional fracture networks. The specific activities will include:

- Review of state of the art of DFN model development
- DFN code development
- Code verification and validation
- Code demonstration

- Better understanding of fracture distribution, fracture closure and opening, and fluid flow and transport in individual fractures in subsurface.

Anticipated results: Theory, computer code and validation data for modeling sparsely fractured geologic media; enhanced process understanding

Accomplishments:

- A simulation tool (dfnWorks) for fracture network generation and for simulating fluid flow and transport in discrete fracture network was developed. This simulation tool won a R&D100 award.
- The discrete fracture network model was used to simulate the Long-Term Sorption Diffusion Experiment (LTDE) conducted at the Äspö Hard Rock.
- A fully coupled thermal-hydrological-mechanical-chemical model for fracture opening and closure was formulated by explicitly accounting for the stress concentration on aperture surface, stress-activated mineral dissolution, pressure solution at contacting asperities, and channel flow dynamics.

Perspective:

- Continue model demonstration using field data.
- Develop a reduced order model based DFN simulations for total system performance assessments.
- Expand the existing discrete fracture model to account for the dynamic evolution of fractures.

Topic #P2

Title: Parameter estimation and uncertainty quantification of field testing

Description: Parameters used in the assessment of groundwater flow and radionuclide transport in saturated media are determined from a wide range of laboratory and field-scale testing. Laboratory measurements are generally conducted under controlled conditions and the uncertainty for parameters from these experiments related to instrumental errors is relatively small. In contrast, field testing such as hydraulic testing in fractured media and tracer testing in the subsurface is analyzed with imperfect knowledge of the hydrogeological system at depth. Consequently, there are often issues of nonuniqueness and significant uncertainties in the parameter values derived from this testing. In the past these uncertainties typically have been evaluated using simple statistical analyses or professional judgment for propagation to total system performance assessments. This task will assess the use of advanced methods in parameter estimation and uncertainty analysis in the interpretation of field testing in saturated media. The task will also address the issues related to flow localization and the associated diffusion into immobile water. Specific activities will include:

- Literature review of state of the art in hydrologic parameter estimation
- Formulation of new techniques (e.g. new optimization techniques)
- Demonstration of new techniques.

Anticipated results: New methodology and related software for uncertainty quantification of field testing results; enhanced process understanding

Accomplishments:

- Flow and transport in a hypothetic fracture network were performed using both particle tracking and advection-diffusion approaches. As expected, the particle tracking method generates a sharper breakthrough peak.
- Preliminary analysis was performed on the minimal samples needed for a stable statistical representation of fracture networks. The results show that, depending on the actual fracture distribution parameters, a relative large number of realization may be needed in order to obtain a stable statistical representation for flow and transport in a fracture medium.
- PFLOTRAN code was coupled with DAKOTA for Monte-Carlo simulations.

Perspective:

- Further understand the uncertainty in radionuclide transport associated with different modeling approaches.

Topic #P3

Title: Development of a new theory for preferential flow in unsaturated porous media

Description: Groundwater recharge associated with the unsaturated zone is an important factor for characterizing any repository site and for evaluating its performance. In a water-saturated environment, because thermal effects, multiphase-flows (similar to unsaturated flow) may also occur near the drift in the host formation of a given repository. Preferential flow is a common flow mechanism in the unsaturated zone and has been described as one of the most frustrating processes in terms of hampering accurate predictions of flow and transport in the unsaturated zone as a result of its complexity. This work attempts to apply an optimal principle (that water flow resistance is minimized for the entire flow domain) to steady-state unsaturated flow processes. Specific activities will include:

- Formulation of new preferential flow model
- Comparison of model results with laboratory measurements of fingering flow (available in the literature) and the existing models.

Anticipated results: New theory and modeling tools with improved capability of modeling near-field flow and transport; enhanced process understanding

Accomplishments:

- A new model based on the minimal flow resistance principle was developed and Model results were compared well with laboratory measurements.

Perspective:

- The same approach may be applicable to near-field multi-phase fluid flows.

Topic #P4

Title: Investigation of water movement and transport in low permeability media (clay materials)

Description: Low permeability geologic formations such as clay formations are considered as effective media for waste isolation. Understanding water movement in such media is crucial for the performance assessment of a waste isolation system. It was recently discovered that water advection and chemical diffusion in low-permeability media may not follow traditional linear laws such as Darcy's law and Fick's law. This task will systematically study water flow regimes and their transport behaviors in clay formations as a function of clay formation texture and pore geometry. New methodologies will be developed for modeling these non-traditional flow and transport behaviors. Specific activities will include:

- Selection and characterization of clay samples
- Experimental testing of flow regimes in clay samples
- Experimental testing of diffusion regimes in clay samples
- Development of modeling capabilities
- Prediction of water movement and chemical species diffusion in clay formations

Anticipated results: New formulations for water flow and transport in clay formations, with supporting experimental data; enhanced process understanding

Accomplishments:

- Model was developed for gas migration in a water saturated compacted clay material, using the gas injection data obtained from the British Geological Survey. Both data and model analysis show that gas migration in such media exhibits rich nonlinear dynamics.
- Non-Darcian flow model in clay formations was formulated.

- Using small-angle neutron scattering techniques to characterize pore structure and water movement in clay was explored.

Perspective:

- Refine the existing model to better match experimental data.
- Understand a potential thermal effect on Non-Darcian flow.

Topic #P5 (not applicable to crystalline media)
Title: Investigation of water movement and transport in low permeability media (salt formations)
Description: Low permeability geologic formations such as salt beds are considered as effective media for waste isolation. Understanding of water movement in such media is crucial for the performance assessment of a waste isolation system. Significant gaps exist in predicting moisture movement along salt grain boundaries under stress and temperature gradient. This task will establish constitutive relationships for moisture movement in the near-field of a salt repository through laboratory analysis, field testing and modeling. Specific activities will include:

- Experimental testing of water movement in consolidated salt
- Experimental testing of chemical species diffusion in salt
- Development of modeling capabilities
- Prediction of water movement and chemical species diffusion in salt formations.

Anticipated results: New formulations for water flow and transport in salt formations, with supporting experimental data; enhanced process understanding

Topic #P6
Title: Investigation of water movement and transport in deep borehole disposal environments
Description: In the deep borehole disposal concept, high level nuclear waste will be emplaced in the depth interval of 3 to 4 km below the surface, based on the premise that water movement at that depth would be minimal. Characterization of water flow in such environments is a technical challenge. This task will first collect relevant information of deep ground water movement and formulate a strategy for developing field characterization strategies for deep borehole disposal. The information to be collected will include those obtained from continental drilling programs. The task will then focus on the development of novel techniques for characterizing deep ground water movement (e.g., using isotopic signatures). Specific activities will include:

- Literature review on water movement in deep subsurface environments
- Development of novel techniques for deep ground water movement
- Extending the existing groundwater flow models to deep subsurface environments.
- Understanding fracture distribution with depth – an important issue for both crystalline disposal and deep borehole disposal concepts.

Anticipated results: Novel field survey techniques and modeling capability for characterizing deep ground water movement; enhanced process understanding; relevant field data

Accomplishments:

- Data collected from deep boreholes about fracture distribution have been used for the development of the reference case for spent fuel disposal in crystalline rocks.

Perspective:

- None

Topic #P7
Title: Novel in-situ techniques for groundwater chemistry characterization
Description: An understanding of the repository far-field geochemical system is critical to understanding repository performance. Geochemical conditions and the characteristics and composition of the ground water in the repository far field govern the mobility and solubility of radioactive elements. In addition, the

chemistry of water flowing from the far field into the near-field environment is an important control on the near-field chemical environment, which, in turn, affects engineered barrier degradation rates. There is a need for developing chemical sampling techniques to characterize initial fluid composition in shale and salt. This activity will explore and develop novel techniques for characterizing groundwater chemistry. The emphasis will be given to the techniques that can provide fast, accurate, in-situ and high spatial resolution measurements (e.g., in boreholes) with minimum human perturbations. The techniques that can characterize flow localization and the associated chemical heterogeneity is particularly of interest. Specific activities will include:

- Literature review
- Development of high resolution in-situ characterization techniques
- Field demonstration of new techniques

Anticipated results: A set of demonstrated techniques ready for field demonstration; relevant lab and field data

Accomplishments:

- Streaming potential tests have performed on a sand box with different solution chemistry.

Perspective:

- One of the focus areas for future work is down-borehole microsensors.

Topic #P8

Title: Reactive transport modeling of groundwater chemistry evolution and radionuclide transport

Description: This task will aim at improving the existing reactive transport modeling tools for simulating groundwater chemistry evolution and radionuclide migration along the flow path from the DRZ, to the far field and ultimately to the boundary of a repository. Radionuclide transport modeling remains a computationally challenging task. Except for the extreme situation of diffusion-dominated conditions, transport models are more sensitive than flow models to numerical grid effects and small-scale heterogeneity. Relatively fine grids are needed to avoid numerical dispersion when traditional finite-difference or finite-element methods are employed. Multiple radionuclides linked through decay chains need to be considered, and the simulation time steps are thus limited by the most mobile (least retarded) radioelement. In addition, transport modeling to assess geosphere performance typically requires parametric uncertainty to be addressed, which places a premium on fast execution time of modeling codes. This task will focus on the following improvements to the existing reactive transport modeling capability:

- Incorporation of interfacial reactions (e.g., surface complexation), microbially mediated reactions, colloid-facilitated transport, and radionuclide decay and ingrowth
- Improved representation of spatial heterogeneity of chemical and transport properties
- Coupling of radionuclide transport with evolving water chemistry along a transport pathway (e.g. alkaline plumes)
- Robustness of numerical algorithms for coupling chemical reactions with solute transport
- Explicit consideration of structural complexity of the media in the solute transport (e.g. the fracture-matrix system in DRZ or the micro, macro-pores system for host clay rock)

Anticipated results: Modeling tools that will go beyond the traditional Kd approach for modeling radionuclide partitioning between pore water and solid substrates

Accomplishments:

- The module for calculating radionuclide decay and ingrowth was added to PFLOTRAN.
- Fluid flow and tracer transport at Bedrichov Tunnel (Czech Republic) were simulated and modeling simulations were compared with field measurements.

Perspective:

- Future work may include additional chemical processes other than a simple Kd-based sorption-desorption process.
- A future model should also consider the of multiple scale heterogeneities and more robust uncertainty quantification.

Topic #P9

Title: Evaluation of the effects of spatial heterogeneity on radionuclide transport

Description: Some key parameters that control radionuclide transport in natural system generally vary spatially. Existing repository performance assessments try to capture this variability with model input parameter uncertainty, which inevitably lead to a significant overestimate of total radionuclide release. This task will develop modeling capabilities to capture the effects of the spatial heterogeneity (e.g., Kd values) on radionuclide transport in natural systems. The work will include two parts: the modeling capabilities for realistic representation of spatial heterogeneity and the experimental technique for quantification of this heterogeneity. The work will significantly reduce both the predicted total radionuclide release from a repository and the associated uncertainty through improved performance prediction of the natural barrier system. Specific activities will include:

- Representation of spatial heterogeneity in reactive transport models
- Development of characterization techniques for quantification of spatial heterogeneity
- Model validation and demonstration.

Anticipated results: New modeling approaches and characterization techniques for capture the effect of spatial heterogeneity on radionuclide transport.

Accomplishments:

- Using the DFN model, dispersion and mixing within three-dimensional fracture networks were simulated. The result shows that, as hydraulic heterogeneity increased, both longitudinal and traverse dispersion increases; the less mechanical dispersion observed in the structured network appears to be linked to the higher levels of connectivity than in the poorly connected random network; for moderate levels of hydraulic heterogeneity, fracture network structure is the principal control on transport times and dispersion within fracture networks.
- The effect of spatial heterogeneity in Kd was evaluated, showing the effect is significant.

Perspective:

- Future DFN simulations need to be performed on more realistic fracture networks.
- Incorporate the effect of spatial heterogeneity in Kd into the GDSA model.

Topic #P10

Title: Better understanding radionuclide interaction with geomedia

Description: As they move through the natural system, radionuclides released from the engineered barrier will experience a complex set of physical and chemical interactions with the geologic media. Existing models generally assume that radionuclide retention in the natural system could be described with a linear, equilibrium Kd approach. The reality may be much more complex. This task will develop key experimental techniques and modeling tools in the following areas:

- Thermodynamics and kinetics of radionuclide sorption onto or desorption from representative mineral substrates (e.g. different clay minerals)
- Radionuclide behaviors in high rock/water ratio environments, especially in confined environments such as nanopores and interlayers
- Coupling of redox reactions with radionuclide sorption
- Complexation of radionuclides with natural organic matter
- Radionuclide sorption in the presence of competing species, high ionic strength media, or at elevated temperatures

- Extrapolation from simple system measurements to complex systems
- Radionuclide transport in low permeability media (e.g., membrane effect of clay formation).

Anticipated results: Key technical data for the development of next generation (more predictive) radionuclide transport models; enhanced process understanding; relevant laboratory data

Accomplishments:

- The effect of bentonite heating on U(VI) adsorption was investigated using bentonite samples from the FEBEX *in situ* experiment. The adsorption seems to decrease with the heating but the actual mechanism is not clear.
- A new surface complexation model (SCM) was developed for U(VI) adsorption onto clay materials. The model specifically accounts for the 'spillover' of the electrostatic surface potential of basal cation exchange sites on the surface potential of neighboring edge sites.
- Short-term (< 35 days) study of uranium sorption and diffusion in bentonite was conducted. The results indicate a relevance of so-called anion exclusion effects, the full or partial exclusion of anionic U(VI) solution species from clay interlayer spaces.
- Long-term (6 years) study of uranium diffusion in bentonite was conducted. The Kd values obtained from the long-term experiment is one order of magnitude lower than those from batch sorption measurements. The apparent U(VI) diffusion coefficient determined from the long-term experiment is about two orders lower than obtained from short-term experiments, which may be attributed to a reduction of clay porosity.
- A study of Pu sorption and desorption in bentonite was performed. The result suggests the importance of montmorillonite phases in controlling Pu sorption/desorption reactions on FEBEX bentonite.
- An analysis was performed to examine the consistency of macroscopic measurements, electrical double layer (EDL)-based models, and molecular-scale simulations of clay media for adsorption and diffusion of trace levels of calcium (Ca^{2+}), bromide (Br^-), and tritiated water (HTO) in a loosely compacted, water-saturated Na-montmorillonite.
- The concept of the control of nanopore confinement on radionuclide interaction with compacted clay materials was explored and applied to iodide sorption. The work shows that iodide can potentially interact with interlayer sites of a clay material.

Perspective:

- Further mechanistically understand a potential effect of heating on radionuclide adsorption on bentonite materials.
- Test the model for other radionuclides.

Topic #P11
Title: New perspective of colloid-facilitated radionuclide transport
Description: Colloid facilitated transport (CFT) may have been overestimated in previous performance assessments because many aspects of CFT are not well constrained, thus making pessimistic bounding assumptions necessary. CFT is also an important issue for confidence building of a performance assessment model. Important uncertain processes and parameters associated with CFT include: desorption processes and rates, colloid immobilization processes and associated parameters, the degree to which colloids behave as heterogeneous populations in the subsurface, the role of chemical and flow transients in mobilizing and immobilizing colloids, and colloid generation processes. This task will focus on two key aspects of the CFT: (1) colloid particle formation and transport in porous geologic media and (2) radionuclide partitioning among pore water, colloid particles, and stationary substrates. In recent years, much progress has been made in nanoscience and nanotechnology. Such progress allows re-examining CFT in a new perspective, for example, understanding the size dependence of particle surface chemistry and radionuclide sorption

capability. This work will involve laboratory measurements, model development, and field testing. Novel in-situ colloid characterization techniques will be explored. Specific activities will include:

- Literature review
- Better understanding colloid-radionuclide-stationary mineral phase interactions
- Development of novel in-situ techniques for characterizing CFT
- Development of modeling capabilities for simulating CFT.

Anticipated results: New modeling and experimental tools as well as key technical data for predicting CFT; enhanced process understanding; relevant laboratory and field data; laboratory and field measurement techniques

Accomplishments:

- A comprehensive literature review and data synthesis was conducted on colloid-facilitated radionuclide transport, and a scheme for the implementation of the transport model in performance assessment was proposed.
- A multiple site and multiple rate colloid-facilitated transport model was developed and was applied to the data obtained at the Grimsel Test Site.
- Batch and column transport experiments were conducted to interrogate the effects of colloid aging on colloid-facilitated transport of ^{137}Cs in granitic environments.
- The reactivity of three different types of intrinsic Pu colloids in the presence of montmorillonite at 25 and 80°C under atmospheric conditions. Pu oxides calcined at 300 and 800 °C and intrinsic Pu colloids produced from acidic solution are quite stable under our experimental conditions. Predicted Pu concentrations calculated using dissolution rate constants obtained from intrinsic Pu colloids formed in alkaline solution are much higher than the measured Pu concentrations, suggesting that these three types of intrinsic Pu colloids are more stable, thus less reactive than the ones formed in alkaline solution.
- A study of the dissolution of intrinsic colloids in the presence of montmorillonite at different temperatures was completed using a dialysis device. The results show that the kinetic constants for dissolution are one to two orders of magnitude lower than the apparent diffusion rates across the dialysis membranes. Thus, the dissolution process was the rate-limiting step. The presence of clay tends to stabilize dissolved Pu species and drive intrinsic Pu colloid dissolution and the formation of more stable pseudo-colloids.
- New data on Pu colloid formation on iron oxide substrates were collected.

Perspective:

- The colloid aging effect on radionuclide mobility needs to be considered in a CFT model in a performance assessment.
- Implement the developed CFT model in performance assessments. It is preferable that the future CFT model would also be able to account for colloid phase stability.

Topic #P12

Title: Upscaling of key hydrological and geochemical parameters

Description: It is known that some key parameters (e.g., dispersion coefficient, matrix diffusion coefficient) controlling radionuclide transport in geologic media are scale-dependent. Capture of this scale dependence is crucial for predicting radionuclide transport in a geologic repository environment. This task will systematically evaluate the existing techniques for upscaling key hydrologic and geochemical parameters, identify the gaps in upscaling, and develop new methodologies for bridging the identified gaps. The parameters of interest include matrix diffusion coefficients, sorption coefficient, chemical reaction kinetics, etc. The laboratory and field experiments of various scales will be explored for conceptual model development and validation. Specific will activities include:

- Literature review on hydrological and geochemical upscaling
- Data collection and multiple scale testing

- Model development for hydrological and geochemical upscaling.

Anticipated results: Constitutive relationships for predicting radionuclide transport in natural systems; enhanced process understanding; relevant field data

Accomplishments:

- Using both discrete fracture network model and fracture continuum model, a general work flow was developed to synthesize field fracture distribution data to generate effective permeability and porosity fields for fluid and transport simulations.
- The methodology was successfully applied to Japanese Mizunami site.
- A comprehensive comparison was performed between discrete fracture and equivalent continuum approaches for modeling flow and transport in fractured media**.**

Perspective:

- Continue model demonstrations using other field data, for example, using Swedish data.

Topic #P13

Title: Evaluation of biological processes

Description: Transport of dissolved radionuclides in the host rock and other geologic units is affected by microbial activity in the host rock and other geologic units (non-host-rock). The effects of biological processes include the formation of complexants, the formation of microbial colloids, the biodegradation of organic compounds, and the bioaccumulation of radionuclides. Similar to purely inorganic complexants, there is a potential for enhanced transport of radionuclides associated with organic complexants. There are fundamental gaps in the methods of characterizing biological processes and their effects on the repository system, and fundamental gaps in available data. This activity will develop better techniques for quantifying microbial activity in a subsurface environment and improve the existing methodology for evaluating microbial impacts on water chemistry and radionuclide transport. Specific activities will include:

- Literature review
- Development of new techniques for characterization of microbial activity in subsurface environments
- Upgrading the existing biogeochemical modeling capability for evaluating microbial activity and its impact on radionuclide transport.

Anticipated results: New techniques for characterizing microbial population; an improved methodology for evaluating microbial impacts on radionuclide transport in natural system; enhanced process understanding

Accomplishments:

- The complexation constants of uranyl with oxalate under different ionic strength was constrained.

Perspective:

- Future work may examine the potential effect of biological activity, especially metabolites, on radionuclide sorption in a far field.

Topic #P14

Title: Technical basis for thermal loading limits

Description: The repository thermal loading limits are of concern for thermal-mechanical effects on engineered materials and host rocks. Thermal expansion, tensile and compressive stresses, and altered properties of fractures, faults, and the rock matrix are possible. There can also be thermal-chemical alteration of the materials, including, mineral precipitation, dissolution, alteration of minerals with attendant volume changes, and altered properties of fractures, faults, the rock matrix, and the formation of near-field chemically altered zones (rind). This task will systematically examine the technical basis for the thermal

limits of various disposal media (i.e., the maximum wall temperature allowed). Specific activities will include:

- Literature review
- Examination of technical basis for thermal limits of various disposal media, including certain thermal-hydrologic-mechanical-chemical calculations.

Anticipated results: Technical basis for the thermal limits of various disposal media

Accomplishment:

- Preliminary tests show that no significant phase transition would occur at temperature below 500 ^{o}C.
- A significant understanding was obtained about the controlling factors for smectite-to-illite transformation. The transformation seems highly dependent on water rock ratio.

Perspective:

- Further mechanistically understand the illitization process. This understanding may lead to design a buffer material with much high thermal stability.

Topic #P15 (probably applicable to clay buffer materials in the EBS)

Title: Modeling of disturbed rock zone (DRZ) evolution (clay repository)

Description: There is a need for improved understanding and representation of the evolution of disturbed rock zone characteristics as a result of thermal-mechanical-hydrological-chemical changes in clay environments, including the coupled evolution of near-field host rock and any backfill/buffer materials that would be used in the design of the repository. This task will address the following specific issues associated with the DRZ:

- Improved methods for representing the complex coupling of processes (physical, chemical, thermal, mechanical), including the coupling of the engineered and natural systems
- Improved methods for representing near- and far-field interface chemistry (perturbation & transient phenomena, repository operation, thermal effect)
- Quantifying gas generation and representing potential impacts (gas displacement and leakage)
- Evaluating the effects of excavation and ventilation-induced fracturing in clay/shale environments
- Better understanding of fracture initiation and healing (re-compaction as a function of environment)
- Improved understanding of heterogeneity and anisotropic properties in the DRZ and their impacts
- Evaluating the potential for the development of fast transport pathways that could bypass the natural or engineered system and associated impacts
- Development of model tools for capturing these processes/issues mentioned above.

Anticipated results: Constitutive relationships and computer codes for modeling thermal-mechanical-hydrological-chemical coupling in the near field of a clay repository; enhanced process understanding; relevant laboratory and field data

Accomplishments:

- A rigid body spring network (RBSN) model for DRZ evolution was developed and used for the simulation of fracture initiation and propagation around a excavation area.
- Through an international collaboration, the requirements for Ca-bentonite as a buffer material was collected.

Perspective:

- Further test the RBSN model against field measurements.

Topic #P16 (not applicable to crystalline media)

Title: Modeling of DRZ evolution (salt repository)

Description: Evolution of the DRZ in salt is very sensitive to the stress state and exhibits steep transient deformation behavior that evolves into steady-state deformation. This behavior can be understood in terms of plastic dislocation mechanisms in salt crystals. Hence, creep closure of underground openings in salt at

ambient temperature can be understood at a mechanistic level. Based on studies at WIPP, the nature of the DRZ can be adequately described for engineering and analysis purposes in terms of stress invariants, which is conducive to finite element calculations. Long-term behavior including healing can be assessed by tracking the stress state within the structural calculation. For the long-term disposal of high level wastes, a better understanding of rock salt creeping and fracture sealing around the DRZ at elevated temperatures and in the presence of moisture is required. This work will develop the needed tools for testing and simulating salt repository room closure, salt creeping and fracture healing in the presence of moisture at elevated temperatures. Specific activities will include:

- Literature review
- Laboratory and field testing on salt creeping and fracture healing
- Model simulation and data integration.

Anticipated results: Constitutive relationships and computer codes for modeling thermal-mechanical-

Topic #P17
Title: Modeling of DRZ evolution (deep borehole disposal)
Description: For deep borehole disposal, simulation of multi-borehole arrays should be undertaken for a system consisting of 10 to 100 individual boreholes. Such investigations could evaluate the potential for communication between boreholes, thermal or hydrologic interactions, and large-scale responses to borehole arrays. Performance assessments are needed to establish a better sense of the potential performance variability that might be expected in multiple implementations of borehole disposal fields. This activity will simulate the coupled thermal-hydrological-mechanical-chemical processes around a single borehole and multiple boreholes as well. Specific activities will include:

- Literature and data collection
- Thermal-hydrological-mechanical-chemical calculations.

Anticipated results: Constitutive relationships and computer codes for modeling thermal-mechanical-hydrological-chemical coupling in a deep borehole disposal environment; enhanced process understanding; relevant laboratory and field data

Topic #P18
Title: In-situ testing of DRZ development
Description: In situ testing could prove quite valuable for proof-of-principle testing. A field test provides an opportunity to observe anticipated phenomenology, validate modeling capabilities, and fine tune design options. This task will focus on full-scale heating testing for the DRZ evolution. In situ testing will confirm the predictive ability of repository models and provides a range of expected parameters and rock mass response. Full-scale heater tests will determine:

- Extent and properties of the disturbed zone
- Fracture healing characteristics
- Changes in permeability and porosity
- Thermomechanical response of compacted backfill
- Water migration and influx rates (where applicable)
- Moisture behavior (e.g., partial vapor pressure)
- Compositional changes; all for heated conditions representative of repository conditions.

Anticipated results: Experimental data for model validation

Accomplishments:

- A series of laboratory experiments were conducted on granite slabs with a special geometry to replicate the stresses and rock deformation responses that are expected to occur in larger circular excavations of the excavation damage zone (EDZ) in a mined crystalline repository.

Perspective:

- One future research area is to examine a possibility of using acoustic wave to characterize fractures in a DRZ.

Topic #P19
Title: Development of waste form degradation model
Description: Currently, in a performance assessment calculation, waste form degradation is modeled with fractional degradation rates. Such models are not able to predict waste form degradation for a wide range of physical/chemical conditions. In this effort, we propose to develop a new generation waste form degradation model that is able to account for complex physical/chemical processes involved in waste form degradation under wide range of disposal conditions. This model will explicitly incorporate potential impacts of radiolysis. The work includes:

- Extensive literature search and data collection
- Formulation of a complex chemical reaction model
- Implementation of the model in a performance assessment calculation.

Anticipated results: New model for performance assessments

Accomplishments:

- The fuel matrix degradation (FMD) model was developed based on fundamental electrochemistry and thermodynamics.
- A recent sensitivity analysis with the FMD model shows that the dissolved H_2 concentration is the dominant environmental variable affecting the UO_2 spent fuel dissolution rate.
- A simplified version of the FMD model was implemented in the GDSA model.
- A new glass degradation model was developed by considering the nonlinear dynamics of involved glass dissolution processes.

Perspective:

- Continue the integration of waste form degradation models with the GDSA model.
- Optimize the waste form degradation models to speed up the total system performance simulations.
- Continue model parameter estimation and uncertainty quantification using experimental data.

Topic #P20
Title: Development of new waste package concepts and models for evaluation of waste package performance for long-term disposal
Description: Waste packages are an important layer of an engineered system for waste isolation, especially for a repository in fractured crystalline rocks. This effort will include two parts: (1) new materials and new concepts for waste package design and (2) improved models for predicting the long-term performance of waste packages in a crystalline repository. One aspect to be examined is the potential interactions of waste packages with buffer materials in the EBS.
Anticipated results: New models and experimental data for model parameterization and validation

Accomplishments:

- Electrochemical test was initiated to measure the corrosion rates of metallic packaging materials.

Perspective:

- Continue development of a waste package degradation model.
- Incorporate the model into a GDSA model.

Topic #P21
Title: Backfill and seal materials design
Description: This effort will focus on designing new buffer/backfill and seal materials for effective isolation of waste in a repository. The new design will fully take into account the capabilities of the materials as a hydrologic barrier (low permeability to a fluid flow) and a reactive barrier (high radionuclide

sorption capacity). It will also consider the availability of the materials and their compatibility with repository environments.
Anticipated results: Experimental data and new design concepts

Accomplishments:

- The work on the development of next generation buffer materials was initiated and significant progress has been made. The work shows that the performance of the existing bentonite-based materials can be much improved using a material engineering technique. A technical advance is to be filed.
- A thermal-hydrological-mechanical-chemical model was developed and applied to the analysis of coupled EBS processes in bentonite-backfilled repositories.

Perspective:

- Continuing progress in materials science and technology opens new opportunities for buffer material design and improvement.
- Development a subsystem model that can be used to evaluate the effectiveness of new buffer materials for waste isolation.

Topic #P22
Title: Modeling radionuclide transport in engineered barrier system
Description: This effort will focus on the development of a reactive transport model for radionuclide transport with an engineered barrier system. The model considers (1) radionuclide speciation, precipitation and dissolution in an evolving near-field physical/chemical conditions and (2) radionuclide transport from degraded waste form, to buffer/backfill materials, and to the disturbed rock zone.
Anticipated results: Experimental data, new models

Accomplishments:

- Molecular and crystallographic behaviors of Pu associated with ferrihydrite and goethite iron oxide phases were investigated. It was shown that the timing of Pu release and ferrihydrite corrosion product formation could lead to differences in Pu association: formation of PuO_2 versus coprecipitated Pu.

Perspective:

- Continue the investigation of radionuclide interaction with metal corrosion products, especially with anoxic corrosion products.
- Develop a new radionuclide partitioning model by considering irreversible radionuclide sorption/desorption processes.

Wang Y. et al., (2014) *Used Fuel Disposal in Crystalline Rocks: Status and FY14 Progress*, FCRD-UFD-2014-000060, SAND2014, Sandia National Laboratories, Albuquerque, NM.